INFORMATION TO USERS

This reproduction was made from a copy of a document sent to us for microfilming. While the most advanced technology has been used to photograph and reproduce this document, the quality of the reproduction is heavily dependent upon the quality of the material submitted.

The following explanation of techniques is provided to help clarify markings or notations which may appear on this reproduction.

1. The sign or "target" for pages apparently lacking from the document photographed is "Missing Page(s)". If it was possible to obtain the missing page(s) or section, they are spliced into the film along with adjacent pages. This may have necessitated cutting through an image and duplicating adjacent pages to assure complete continuity.

2. When an image on the film is obliterated with a round black mark, it is an indication of either blurred copy because of movement during exposure, duplicate copy, or copyrighted materials that should not have been filmed. For blurred pages, a good image of the page can be found in the adjacent frame. If copyrighted materials were deleted, a target note will appear listing the pages in the adjacent frame.

3. When a map, drawing or chart, etc., is part of the material being photographed, a definite method of "sectioning" the material has been followed. It is customary to begin filming at the upper left hand corner of a large sheet and to continue from left to right in equal sections with small overlaps. If necessary, sectioning is continued again–beginning below the first row and continuing on until complete.

4. For illustrations that cannot be satisfactorily reproduced by xerographic means, photographic prints can be purchased at additional cost and inserted into your xerographic copy. These prints are available upon request from the Dissertations Customer Services Department.

5. Some pages in any document may have indistinct print. In all cases the best available copy has been filmed.

University Microfilms International
300 N. Zeeb Road
Ann Arbor, MI 48106

Dagen, Aaron J.

SPECTRAL AND TEMPORAL PROPERTIES OF THE ALPHA AND BETA SUBUNITS AND (ALPHA BETA) MONOMER ISOLATED FROM NOSTOC SP. USING PICOSECOND LASER SPECTROSCOPY

City University of New York PH.D. 1985

SPECTRAL AND TEMPORAL PROPERTIES OF THE α AND β SUBUNITS AND (αβ) MONOMER ISOLATED FROM NOSTOC sp. USING PICOSECOND LASER SPECTROSCOPY

by

AARON J. DAGEN

A dissertation submitted to the Graduate Faculty in Physics in partial fulfillment of the requirements for the degree of Doctor of Philosophy, The City University of New York

1985

This manuscript has been read and accepted for the Graduate Faculty in Physics in satisfaction of the dissertation requirements for the degree of Doctor of Philosophy.

Robert R Alfano

date

Chairman of Examining Committee

4/28/87

Executive Officer

Robert Gulfanda

Barbara A. Zilinskas

Shirley Papa

Supervisory Committee

The City University of New York

Abstract

SPECTRAL AND TEMPORAL PROPERTIES OF THE α AND β SUBUNITS AND (αβ) MONOMER ISOLATED FROM NOSTOC sp. USING PICOSECOND LASER SPECTROSCOPY

by

Aaron J. Dagen

Adviser: Professor Robert R. Alfano

The fluorescence decay profiles, relative quantum yield and transmission of the α, β and (αβ) complexes from phycoerythrin isolated from the photosynthetic antenna system of Nostoc sp. and measured by single picosecond laser spectroscopic techniques is studied. The fluorescence decay profiles of all three complexes are found to be intensity independent for the intensity range investigated ($\sim 4 \times 10^{13}$ to $\sim 4 \times 10^{15}$ photons-cm^{-2} per pulse). The apparent decrease in the relative quantum yield of all three complexes as intensity increases is offset by a corresponding increase in the relative transmission. This evidence, along with the intensity independent fluorescence kinetics, suggests that exciton annihilation is absent in these complexes. The decay profiles are fit to models assuming energy transfer amongst fluorescing chromophores. The intraprotein transfer rate is found to be 100 ps in the α subunit, 666 ps in the β subunit. Constraining these rates to be identical in the monomer results in explaining the monomer kinetics by an increase in the nonradiative rate of the f_β chromophore, an apparent result of aggregation effects.

ACKNOWLEDGMENTS

I wish to express my sincere thanks to my thesis advisor, Professor R. R. Alfano for his continuing interest and support of my research.

I thank Professor B. A. Zilinskas for preparing the samples and offering her biological expertise to the research.

I also wish to thank the members of my committee, Professors J. Gersten, R. Callender and S. Rapps, for their assistance.

My thanks and appreciation to my parents and family for their support and encouragement.

TABLE OF CONTENTS

LIST OF FIGURES

LIST OF TABLES

Chapter 1

INTRODUCTION

Over the last thirty years, the energy transfer dynamics of excited electronic states have been extensively studied and applied to a wide range of processes in biological and chemical systems.[1-8] The study of biological energy transfer schemes has concentrated on photosynthetic organisms. Photosynthesis is the process by which chlorophyll containing plants convert solar energy into photochemical energy. In organisms higher than bacteria, and in the cyanobacteria, the solar energy is used to drive the charge transferring reaction that converts carbon dioxide and water into oxygen and carbohydrates. In these organisms, the primary energy conversion occurs in specialized Chl a molecules known as reaction centers. The reaction centers, which are located on specialized membranes called thylakoids, receive the energy used to effect the charge transfer from the plant's light harvesting complex or antenna system. It is the antenna system of light-harvesting pigment-proteins that absorbs the solar energy. This energy is then efficiently transferred to the reaction centers.

It is the supramolecular pigment-protein aggregates known as the phycobilisomes which serve as the primary light-gathering antennae in red algae and in cyanobacteria (blue-green algae).[9-17] These aggregates, composed primarily of phycobiliproteins, absorb light over most of the visible spectrum, and play an important role in light-limiting conditions. Organisms adapt to restricted light conditions by

increasing their total phycobiliprotein content or by specifically producing the phycobiliprotein type capable of absorbing the prevalent available wavelengths.

There are three main classes of phycobiliproteins: phycocyanins (PC), phycoerythrin (PE) and allophycocyanins (APC). The PE absorbance maxima range from 500 nm to 568 nm, the PC maxima occur around 620 nm and the APC have several wavelength-absorbing forms ranging from 618 nm to 673 nm, with the 650 nm being the most common. Energy transfer occurs along the following pathway: PE → PC → APC → reaction centers.[11]

Each phycobiliprotein consists of open chain tetrapyrrole chromophores covalently bound to apoproteins.[12,13] Ultrastructural (or electron microscopic) studies indicate that the trimer form of the biliprotein is disc shaped, 12 nm in diameter and 3 nm thick. Their basic building block is an ($\alpha\beta$) protein monomer of 30,000-40,000 daltons. The monomer consists of two dissimilar polypeptide chains, the α and β subunits. The α polypeptides (12,000-20,000 daltons) are generally smaller than the β polypeptides (15,000-22,000 daltons). From 1-4 chromophores (open-chain tetrapyrroles) are covalently bound to each polypeptide, with APC having the lowest number and PE the highest. The distinctive spectroscopic properties of each phycobiliprotein are a consequence of the chemical structure of the attached chromophore and of the influence of the conformation and aggregation state of the protein on the spectra of these prosthetic groups.

The role of the phycobiliproteins as the antenna system for the capture of radiant energy was discovered by Engelmann.[14,31,32] He

projected light in the region of absorption of the biliproteins of the Oscillatoria filament and noted the consequent evolution of oxygen. Subsequent action spectra for oxygen evolution performed with many red algae and cyanobacteria confirmed that biliproteins are highly efficient light absorbers. The highly efficient transfer of energy to APC from other phycobiliproteins was demonstrated when the fluorescence emission maximum of 675-680 nm with a quantum fluorescence yield of 0.60 in the intact phycobilisome was shown to be similar to that of isolated APC. This characteristically high fluorescence emission only occurs when the phycobilisomes are intact and energetically well coupled. Experiments showing the drop of APC emissions and the increase in the emissions from the other biliproteins in dissociated phycobilisomes further showed that APC is the terminal pigment in the transfer chain. The low degree of polarized fluorescence (±0.02) in intact phycobilisomes is another indication of the high efficiency of energy migration in these aggregates.[15]

Porter et al.[8] showed that energy transfers from PE → PC → APC occurs on a ps time-scale. Their time resolved measurements of fluorescence in Porphyridium cruentum resulted in reported fluorescence lifetimes of 70 ps from PE, 118 ps from APC and 175 ps for the lifetime of chlorophyll in the intact algae. The dramatic shortening of the lifetimes of these pigment-proteins from their normal fluorescence lifetimes in solution of nanoseconds indicates that the transfer efficiency between these pigment-proteins is almost 100%.

The physical arrangement of the phycobiliproteins in the phycobilisomes is consistent with the energy transfer scheme. The first

determination of the biliprotein arrangement was made by observing the progressive release of phycobiliproteins during the dissociation of the phycobilisomes of Porphyridium cruentum.[16] The order of release of PE followed by PC and the APC led to the proposed models of phycobilisomes consisting of a centrally located APC core surrounded by PC and PE on the periphery. The isolation of rods from the dissociated phycobilisomes in Rhodella violacea provided further evidence of the peripheral location of PC and PE.[17] These and electron microscopic observations of blue-green algae led to the particular model of phycobilisomes in cyanobacteria consisting of 6 stacked rods, containing PC and PE, fanning out from the APC core (Figure 1.1). Each rod consists of 3-4 double discs. The double discs are the hexamer forms of the biliproteins. Each disc, which is the trimeric form of the biliprotein is 12 nm in diameter and 3 nm thick.

Teale and Dale[18,19] used steady state techniques to determine the fluorescence lifetimes, absolute quantum yields, absorption, fluorescence emission and polarization spectra of a number of phycobiliproteins. They discovered that the polarization spectra were complex, showing low values within the absorption bands, then rising steeply to maximum positive values at the absorption limit. These complex polarization spectra indicate the presence of different chromophore types, those that absorb at shorter wavelength ('s' type) sensitizing those that absorb and emit ('f' type) at longer wavelengths. Further evidence for the presence of 's' and 'f' chromophores was provided when

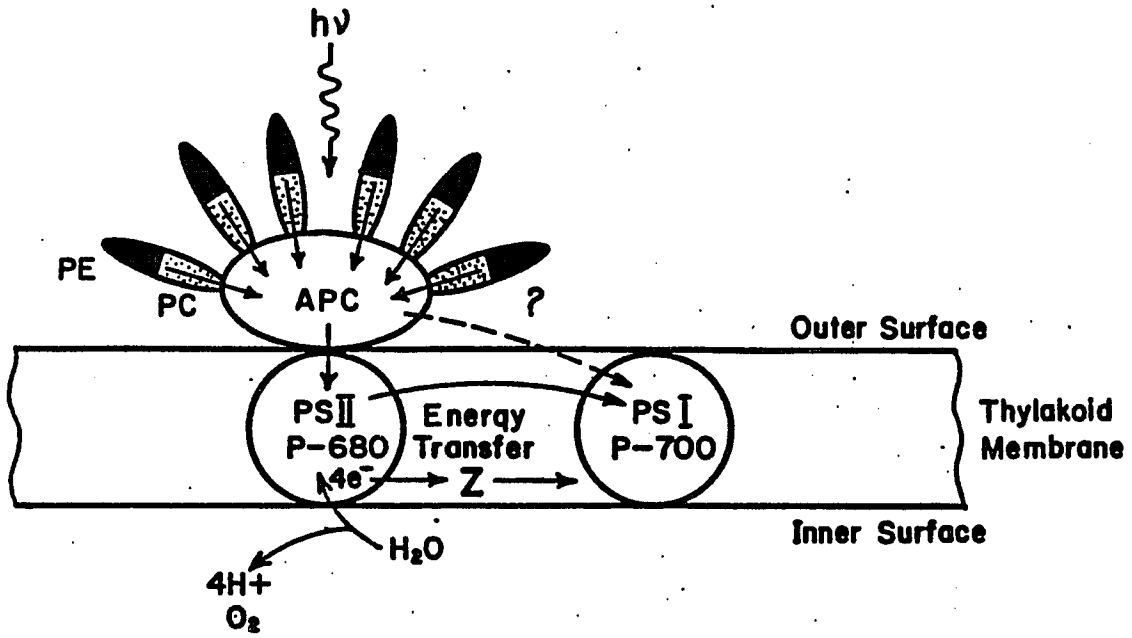

Figure 1.1: The Phycobilisomes and Reaction Centers.

it was shown that the excitation and absorption spectra of the biliproteins were not coincident. They used their data to calculate the number of different types of chromophores, sensitizing and fluorescing, per chromoprotein and to deconvolute the absorption spectra of each type. Glazer et al.[20] concluded from their study of the spectroscopic properties of C-PC and its α and β subunits that the α subunit contains the 'f' type of chromophore. They characterized the single β chromophore as being of the 's' type.

The assigning of the 's' chromophore to the β subunit and the 'f' chromophore to the α subunit has not met universal approbation. Zickendraht-Wendelstadt et al.[21] used their steady state fluorescence emission, polarization, and absorption spectra measurements to propose the 's' and 'f' chromophores appear in both subunits. They also contend that the 's' chromophores also fluoresce. As a result, their concept of s → f transfer includes the possibility of energy transfer within each subunit, as opposed to the simplified scheme of transfer from the s chromophore of the β unit to the f chromophore of the α subunit. Picosecond time resolved measurements of s → f transfer are also scarce and contentious. Kobayashi et al.[22] contend to have measured energy transfer from s → f chromophores in the monomer occurring between 32 and 85 ps. Wong et al.[23] concluded from their measurements on the trimer form of the algae that if such energy transfer does take place, it occurs within 12 ps.

Though steady state studies have resulted in the concept of s → f transfer in the subunits, few picosecond time resolved studies have

been performed, until recently, on the α and β subunits of biliproteins. Most picosecond studies have concentrated on the intact algae or higher aggregate forms of the phycobiliproteins. In addition to Porter's work mentioned previously, Searle et al.[24] studied energy transfer in phycobilisomes isolated from the red alga, Porphyridium cruentum. They noted an excitation intensity independent (10^{13} to 10^{15} photons/cm^2) decay time of 70 ps for PE. The relaxation time of APC decreased from 4 to 2 nsec over this intensity range, with a more complex exponential behavior occurring at higher intensities. They attributed this change to singlet-singlet exciton annihilation.

Wong et al.[23] measured the decay kinetics of the isolated phycobiliproteins (trimer) of Nostoc sp. They found a single exponential decay with a lifetime of 1552 ± 31 ps for C-PE (<10^{14} photons/cm^2). At higher excitation intensities, they fit the decay to a double exponential with lifetimes 130 ± 23 ps and 1477 ± 29 ps. They also found a significant decline in the relative fluorescence quantum yield at higher intensities. The kinetics of C-PC were fit to single exponential curves with the lifetimes declining from a value of 2111 ± 83 ps to a value of 1376 ± 24 ps as intensity increased from 3 x 10^{13} photons/cm^2 to 1.3 x 10^{15} photons/cm^2. APC forms I, II, III and B did not display the characteristics of exciton annihilation displayed by the other two biliproteins. Their intensity independent lifetimes were measured to be 1932 ± 165, 1870 ± 90, 1816 ± 88 and 2577 ± 121 ps, respectively, and the relative fluorescence quantum yields remained flat over the measured intensity range. Absorption measurements by Doukas et al.[25] corroborated the results and conclusions of Wong et al.

Pellegrino et al.[26] continued the work of Wong et al. in the intact phycobilisomes of Nostoc sp. They found the decay time of the PE component was 31 ± 4 ps. The risetime of the PC + APC component was a similar 34 ± 13 ps, indicating energy transfer from PE to PC + APC occurs within this time. Fitting the decay kinetics of the PC + APC component to a double exponential decay, they found the fast component decreased from 212 ps to 83 ps, while the long component decreased from 1174 ps to 716 ps over the intensity range (2.7×10^{13} photons/cm^2 to 2.7×10^{15} photons/cm^2). The fluorescence quantum yield for the PC + APC component decreased by a factor of 13 over the intensity range, indicating considerable singlet-singlet annihilation occurring in APC. This was attributed to a higher affective absorption for APC in phycobilisomes resulting from the efficient funneling of energy from the PE to the APC component.

Other investigators have measured the decay kinetics from the phycocyanin pigments. Switalski et al.[27] showed that the α, β and (αβ) forms of C - PC from Anabaena variabilis displayed nonexponential decays, with components of 1 ns and 300-500 ps. Their steady state polarization data indicated the existence of energy transfer in the β and (αβ) units. The α subunit, however, contains only one chromophore. They speculate that the observed two exponential decay in the α subunit may be due to conformational changes in the chromophore environment. Hefferle et al.[28] also saw a two component decay in a one chromophore α system. They speculate the existence of contaminants or different aggregation states in their sample. Holzwarth et al.[29] found 1 ns and 300-500 ps components in the decay kinetics of C - PC from

Chroomonas sp. They attributed the fast component to chromophore-chromophore interaction. They also found a 15 ps component in the kinetics, which they attributed to s → f transfer. Wendler et al.[30] conducted a study similar to Porter's on the phycobilisomes of Porphyridium cruentum. They used a tunable laser to selectively excite each pigment. Though they found similar decay and rise times to those of Porter's, they could not fit the kinetics to a $t^{1/2}$ decay. To this date, no one has provided a detailed mathematical study of energy transfer in these biological systems.

The goal of this dissertation is to expand the work of Wong, Doukas and Pellegrino to include the α, β and [(αβ)] forms of the PE pigment of the blue-green alga Nostoc sp. In so doing, we will provide the first study of the absorption, fluorescence emission spectra, picosecond time resolved fluorescence kinetics, relative quantum yield and transmission data of the basic subunits, α and β, and the basic building block of the biliproteins, (αβ) of PE, in Nostoc sp. The purpose of the study is to understand the possible models that explain the energy transfer mechanisms and pathways in these sub-components of the biliprotein. As these are representative of the basic building blocks of the antenna system of Nostoc sp., understanding and contrasting the mechanisms in these forms and the forms in which they appear in nature (trimer and hexamer in the intact PBS and isolated biliprotein) should prove of great interest to the scientific community.

In order to understand the energy transfer mechanisms in the α, β and (αβ) components of phycoerythrin in Nostoc sp., research was conducted into:

1. The time-resolved fluorescence kinetics as a function of intensity of the 3 compounds. In so doing, we wanted to see whether change of lifetime over the given intensity range occurs as it does in the higher aggregates, indicating the possibility of the occurrence of exciton annihilation.

2. The measurement of the relative quantum yields of the 3 units and the complementary measurement of the relative transmission data. These measurements helped us determine the appropriateness of fitting the data to present exciton annihilation theories.

3. Steady-state measurements of the absorption and fluorescence spectra of the 3 components. The β subunit contains 4 chromophores and the deconvolution of its absorption spectra is more difficult. In the α subunit, which contains only 2 chromophores, the absorption spectra data and the mirror image of the fluorescence spectra were used to provide a detailed scheme of the energy levels of the two chromophores. By comparing the spectra of the 3 units, we were able to notice whether any significant conformational changes occur when the α and β subunits aggregate together into the (αβ) monomer. This helped us postulate possible energy pathways in the monomer.

4. Computer simulations of the possible energy transfer pathways in the alga was conducted. These simulations showed that the kinetics could be fit by assuming $s \rightarrow f$ transfer and allowed us to obtain the appropriate rate parameters. In the simpler α subunit, we were able to correlate the kinetic parameters with steady state measurements of the absolute quantum yield and the polarization anisotropies.

5. In addition, the theoretical curves of annihilation theory were generated. These quantum yield and fluorescence kinetic curves will help other investigators determine if annihilation is occurring in their samples. In addition, our experimental results have helped us define the experimental techniques required to check for the existence of annihilation, and led us to suggest that transmission data also be measured.

This dissertation is divided into seven chapters. Chapter 2 describes the experimental setup including the laser system, detection system and data storage and analysis system. It includes a discussion of the Nd:glass laser system, single pulse selection and second harmonic generation. The streak camera system is amply described, as is the newly installed PMT-integrator system used to measure the quantum yield and transmission data.

Chapter 3 provides the details of the many theoretical models that might be appropriate to our data. These include the $t^{\Delta/s}$ dependence for the decay kinetics (where Δ = the strength of interaction and s = number of dimensions over which energy transfer occurs); Paillotin's theory of the effect of domain size on exciton annihilation and Fayer's theory of the effects of a small domain on fluorescence kinetics are also included. It is, in essence, a summary of the most important theories presently used in the study of energy transfer in photosynthetic organisms and a nice detailing of the experimental results and limits over which each is appropriate.

Chapters 4, 5 and 6 present the results, analyses and discussions of the energy transfer mechanisms in the α and β subunits and [($\alpha\beta$)]

monomer of PE from Nostoc sp. Chapter 7 is the summary and conclusion of the investigation and provides details of further research that will emanate from this work.

The computer programs used in our research are presented in the Appendix.

Notes

1. Huber, D. L. (1979). Phys Rev., 20, 2307; 20, 5333.

2. Blumen A., & Manz, J. (1978). J. Chem. Phys. 68, 1879.

3. Forster The. (1949). Z. Naturforsch, 40, 321.

4. Knox, R. S. (1975). In Govindjee (Ed.), Bioenergetics of Photosynthesis, pp. 183-221. New York: Academic Press.

5. Hahn, S. W., & Zwanig, R. (1978). J. Chem. Phys., 68, 1889.

6. Loring, R. F., Anderson, H. C., & Fayer, M. D. (1982). J. Chem. Phys., 76, 2015.

7. Lu, P. Y., Yu, Z. X., Alfano, R. R., & Gersten, J. I. (1982). Phys. Rev., A26, 3610.

8. Porter, G., Tredwell, C. J., Searle, G. F. W., & Barber, J. (1978). Biochem. Biophys Acta, 501, 232.

9. Barber, J. (1978). Rep. Prog. Phys. 41, 78.

10. Gantt, E. (1981). Ann. Rev. Plant Physiol., 32, 327.

11. Grabowski, J., & Gantt, E. (1978). Photochem. Photobiol., 28, 47.

12. Brigand, D. A., Guglielmi, G., deMarsac, N. T., Castets, A. M., & Cohen-Bazire, G. (1979). Arch. Microbiol., 123, 113.

13. Glazer, A. N. (1977). Mol. and Cellular Biochem., 18, 125.

14. Clayton, Roderick K. (1980). Photosynthesis: Physical Mechanisms and Chemical Patterns. Cambridge: Cambridge University Press.

15. Grabowski, J., & Gantt, E. (1978). Photochem. Photobiol. 28, 39.

16. Gantt, E., Lipschultz, C. A., & Zilinskas, B. (1976). Biochemica et Biophysica Acta, 430, 375.

17. Morschel, E., Koller, K.-P., Wehrmeyer, W., & Schneider, H. (1977). Cytobiologie, 16, 118.

18. Teale, F. W. J., & Dale, R. E. (1970). Biochem. J., 116, 161.

19. Dale, R. E., & Teale, T. W. J. (1970). Photochem. Photobiol., 12, 99.

20. Glazer, A. N., Fang, S., & Brown, D. M. (1973). Journal of Biological Chemistry, 248, 5679.

21. Zickendraht-Wendelstadt, B., Friedrich, J., & Rudiger, W. (1980). Photochem. Photobiol., 31, 367.

22. Kobayashi, T., Degenkolb, E. O., Bersohn, R., Rentzepis, P. M. MacColl, R., & Berns, D. S. (1979). Biochemistry, 18, 5073.

23. Wong, D. F., Pellegrino, F., Alfano, R. R., & Zilinskas, B. A. (1981). Photochem. Photobiol., 33, 651.

24. Searle, G. F. W., Barber, J., Porter, G. & Tredwell, C. J. (1978). Biochimica et Biophysica Acta, 501, 246.

25. Doukas, A. G., Stefancic, V., Buchert, J., Alfano, R. R., & Zilinskas, B. A. (1981). Photochem. Photobiol., 34, 505.

26. Pellegrino, F., Wong, D.,Alfano, R. R., & Zilinskas, B. A. (1981). Photochem. Photobiol., 34, 691.

27. Switalski, S.C., & Sauer, K. (1981). Photochem. Photobiol. 40, 423.

28. Hefferle, P., Nies, M., Wehrmeyer, W., & Schneider, S. (1983). Photobiochem. Photobiophys. 5, 325.

29. Holzwarth, A. R., Wendler, J., & Wehrmeyer, W. (1983). Biochimica et Biophysica Acta, 724, 388.

30. Wendler, J., Holzwarth, A. R., & Wehrmeyer, W. (1984). Biochimica et Biophysica Acta, 765, 58.

31. Engelmann, T. W. (1881). Bot. Zeitung, 39, 441.

32. Engelmann, T. W. (1884). Bot. Zeitung, 41, 81.

Chapter 2

EXPERIMENTAL TECHNIQUES

The invention of the mode-locked laser was the first step in opening a new field of spectroscopy by permitting the exploration of molecular dynamics in the time range of 10^{-9} to 10^{-12} sec. The picosecond pulse produced by these lasers serves as the appropriate clock needed to study such events as energy transfer in various fields including photobiology. The single short pulse also eliminates many experimental artifacts, such as triplet formation and longer measured lifetimes, associated with multiple excitations and long pulses. The development of sophisticated temporal resolution equipment, such as the streak camera to measure light emitting events on the order of picoseconds, was the next crucial step to letting the picosecond laser reach its full potential use in experimental studies. In this chapter, we discuss the experimental techniques and setup used in our study. The chapter is divided into sections on the laser, single pulse selection system, second harmonic generation, the PMT integrator system, the streak camera system and the computer analysis section.

2.1 Experimental Setup

The experimental setup[1] used in picosecond time resolved fluorescence kinetic studies is shown in Figure 2.1. It consists of a

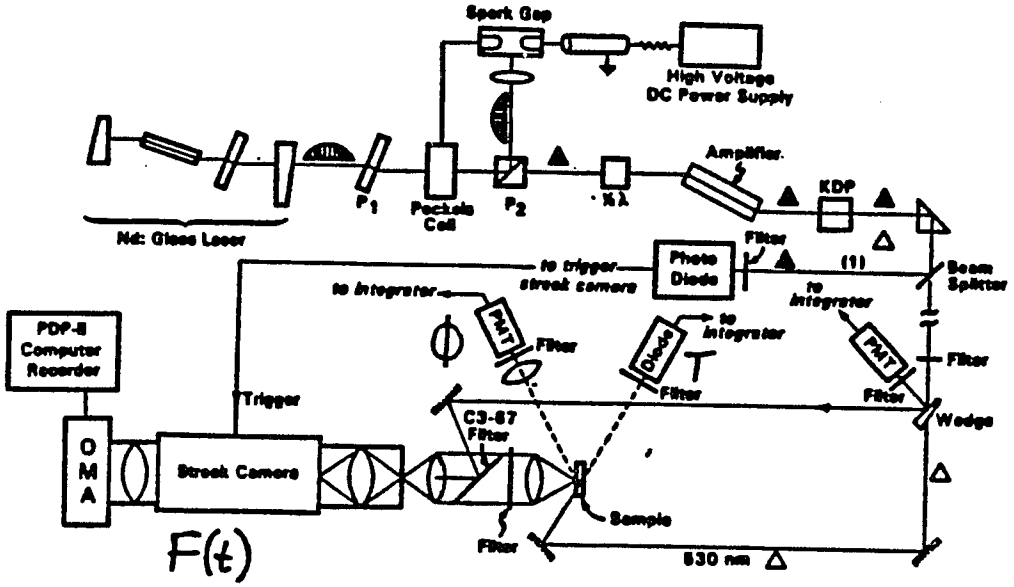

Figure 2.1: Experimental Apparatus.

laser system with single pulse selection, a single pass amplifier, a second harmonic generator, a detection system including a streak camera for temporal resolution, a PMT above it to measure the intensity of the fluorescent light and a diode behind the sample to measure transmitted light and a data storage and analysis system. The PMT, diode and another PMT calibrated to measure the intensity of the incident pulse are connected to an electronic integrator simplifying the measurement of all related intensities and resulting in extremely accurate quantum yield data. The laser is described in the next section.

2.2 The Nd^{3+}:Glass Laser

The laser oscillator consists of an Nd^{3+}:glass laser rod with both ends cut at Brewster angle and a cell of bleachable dye between two wedged mirrors separated by distance L aligned parallel to each other and perpendicular to the axis of the resonator as shown in Figure 2.2. A flashlamp around the glass rod provides the energy for exciting the laser medium and producing the atomic population inversion necessary for lasing action. The rod and 5 inch Xenon flashlamp are mounted in a liquid cooled laser head enclosure and a 1/4" diameter aperture placed between it and the saturable absorber. The rod is 1/2" in diameter and 7-1/2" in length. The center of the laser rod faces from the rear and output mirrors are 18 and 45 cm, respectively. The ends of the rods are optically polished to $\lambda/10$ and cut at Brewsters angle to reduce multicavity modes and reduce reflection losses. The rear mirror is curved and 100% reflecting at 1.06 μm, while the flat

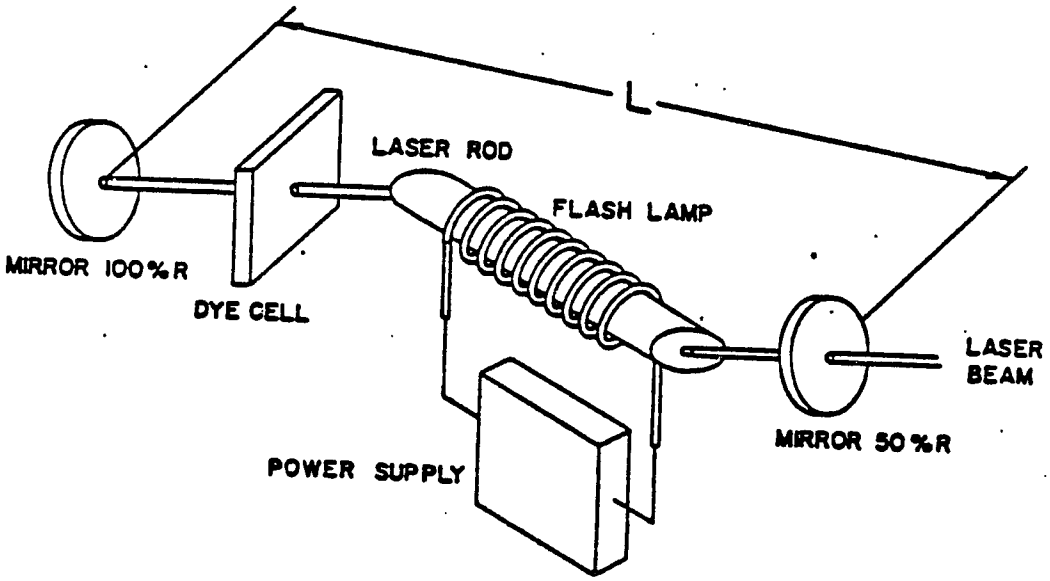

Figure 2.2: Optical resonator cavity configuration from Grant et al.

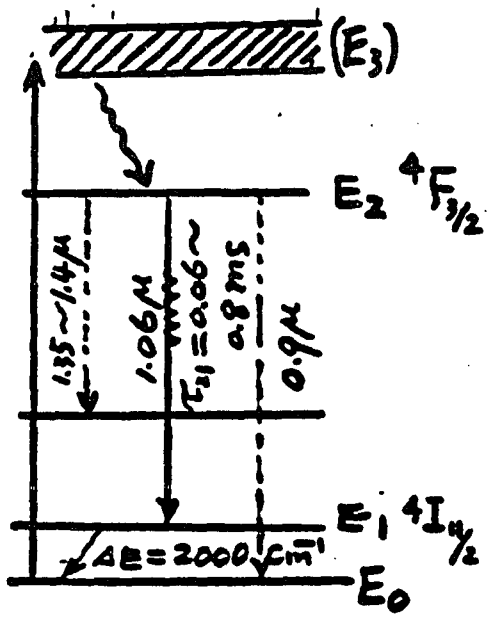

Figure 2.3: Energy level of Nd:glass laser.

output mirror has 50% reflection at 1.06 μm. The dielectric coated mirrors, obtained from the Laser Energy Co., are mounted in Lansing mounts with micrometer positioning controls. The output mirror is wedged $1/2^{o}$ to eliminate multiple cavity modes.

The Nd^{3+}:glass laser is a four level laser.[2] As opposed to a three level laser in which the energy difference between the terminal laser level and the ground state is small compared to kT, its lower laser level is approximately 1950 cm^{-1} above the ground state. As a result, the thermal population of the lower lasing level is negligible. This reduces the pumping rate required to create a certain population inversion compared to a three level laser which has considerable thermal population in its lower lasing level. The fluorescent emission is centered at λ_o = 1.06 μm and has a linewidth of approximately 300 cm^{-1} caused by the amorphous structure of glass resulting in individual Nd^{3+} ions seeing differing surroundings and thus varying their energy splittings. The different ions radiate at slightly different frequencies, causing a broadening of the spontaneous emission spectrum.

It is necessary to create a population inversion in order to amplify the fluorescence due to the spontaneous emission. The photons, due to this emission, bounce back and forth between the mirrors in the laser cavity. As they travel through the laser rod, they stimulate more excited atoms to emit photons of the same frequency, phase and direction. The stimulated emission rate, which is proportional to the population density of the excited state, competes with the stimulated absorption rate which is proportional to the population density of the lower lasing level. Causing a population inversion by firing the

flashlamp results in a net amplification of the light until the excited state population is depleted. The pumping voltage from the power supply is set 10v to 30v above the threshold voltage for laser action. It is found that this results in a single reproducible train without satellite pulses and multiple trains. The flashlamp is fired by discharging a 400 uf capacitor, through the trigger circuit of a Korad K-1 5 KV power supply. Cooling the rod helps prevent thermal population of the lower lasing level which would decrease the necessary population inversion for a given pump rate. A Korad KWC-3 temperature controlled cooler provides cooling for the laser rod, flashlamp and housing at a rate of 2 gal/min at a pressure of 7 psi at 22°C. Distilled de-ionized water is used in the cooling system with a deionizer in the KWC-3 cooler maintaining the low ionic concentration required to prevent shorting of the electrodes at the flashlamp contacts.

2.2.1 Cavity Configuration and Mode-Locking

In addition to the fluorescence bandwidth and quantum yield of the lasing material, the configuration of the laser cavity plays a crucial role in determining the light emitted by the laser.[2] Of all the frequencies emitted and amplified by the lasing material only some, called modes, are allowed by the laser cavity. These modes are determined by solving the wave equation in a lenslike media between two mirrors subject to the self-consistency condition. This condition requires that a stable eigenmode of the system reproduces itself after one round trip. Solution of the equation results in two types of

resonator modes: longitudinal modes which differ from each other only in frequency, and transverse modes which differ from each other in the distribution of the field as well as the frequency. The self-consistency condition also requires that the rear mirror be curved to obtain a stable resonator configuration. The TEM_{xy} modes are directly related to the Hermite Polynomials; a $TEM\phi\phi$ mode has a uniform field distribution about the laser axis distribution while a TEM_{mn} field distribution has m nodes in the x direction and n nodes in the y direction. The 1/4" diameter aperture placed between the rod and saturable dye support only those fields nearest the axis--thus only the preferred lower modes, in particular, the uniformly distributed TE_{oo} modes are allowed in the cavity.

The longitudinal modes allowed in the resonator are determined by the condition that the field inside the resonator forms a standing wave. These modes satisfy $n\lambda_j/2 = L$ where L is the optical length of the cavity λ_j is the wavelength of an allowed mode and n is an integer. The output mirror is wedged 1/2° in order to eliminate multiple cavity modes. The ends of the rod are optically polished and cut at Brewster's angle, also to eliminate multiple cavity modes. These modes are equally spaced in frequency with $\Delta f = c/2L$ a matter of great importance for mode-locking. Clearly, only the allowed modes within the bandwidth, $\Delta f'$, of the gain envelope of the lasing material will be amplified. The number of such modes, $N' = (2L/c)\Delta f'$ is on the order of 10^4 in our cavity, which has an optical path length, L = 84 cm.

The mode-locking[3-5] of these 10^4 modes, achieved by the saturable dye, is required to achieve intense, picosecond pulses. If the

10^4 longitudinal modes were allowed to oscillate simultaneously with random phases, the pulse width of the laser output would be on the order of milliseconds, about the duration of the flashlamp, and its intensity would have the characteristics of thermal noise, hardly a useful laser for the study of fast phenomena. Mode-locking is the final crucial factor in determining the output of the laser: a train of about one hundred 1.06 μm pulses, the first few pulses typically 8 ps in duration with those towards the end of the train lasting about 20 ps. The pulses are separated by the round trip time of the cavity, 5.54 ns. The total energy in a typical train is 177 mJ and each pulse is 1.77 millijoule. The beam of light is $\sim$ 1 cm in diameter and the typical power density is 2.2×10^8 watts.

The central idea behind mode-locking is the more modes that oscillate in phase, the shorter the duration of the pulse. This follows immediately from the relationship $\Delta f \Delta t > k$ where Δt is the duration of the pulse, Δf the bandwidth of the modes oscillating in phase and k is a number on the order of unity whose exact value depends on the pulse shape. For a Gaussian transform-limited pulse k = 0.441.

Mode-locking is accomplished by the saturable dye, Kodak dye A9860 (Eastman Co.) dissolved in 1,2-dichloroethane (Eastman Co.) until the solution transmits 65-70% at 1.06 μm. To achieve good mode-locking a dye must have the following characteristics: (a) nonlinear absorption dependent on intensity. Generally, bleaching occurs above 50 MW/cm^2, (b) strong absorption of the laser wavelength 1.06 μm and for the extent of its bandwidth ($\sim$ 260Å), (c) the recovery time after each absorption of light by the dye is much smaller than the round trip

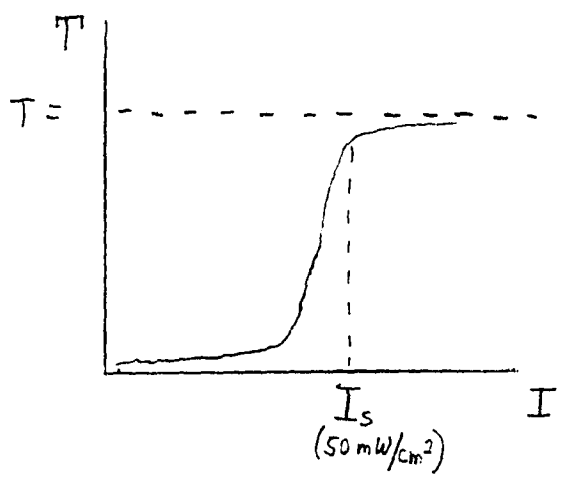

Figure 2.4: Transmission characteristics of saturable absorber dye A9860.

time 2L/c. The Kodak 9860 dye has an absorption peak close to 1.06 μm, an absorption bandwidth of about 200 Å and its recovery time is 10 ps, meeting all the requirements for a saturable dye.

Two popular theories have been developed to explain the production of the very short pulses. The noise theory is akin to the survival of the fittest concept. Initially, there is only spontaneous fluorescence inside the cavity consisting of random noiselike signal. Because of the nonlinear absorbance of the dye, noise pulses above the background are absorbed less in the dye. As the pulse bounces back and forth in the cavity, it is amplified more than the low-intensity pulses. When the pulse increases above 50 MW/cm^2, the absorber starts to bleach shortening the lower intensity wings of the pulse and increasing its bandwidth. The pulse decreases after the population of the excited state is depleted.

Alternatively, the dye cell can be considered an optical shutter actuated by the oscillating pulse. This results in the modes of the pulse being modulated at the round trip time c/2L resulting in the creation of sidebands locked in phase and separated in frequency by c/2L. Fortunately, this is also the intermode separation frequency; that is, the resonator shape permits these modes to oscillate in the cavity. As a result, the electric fields of all the oscillating modes become coupled together, resulting in a shorter, more intense pulse.

The positioning and size of the dye cell is important. Satellite pulses can arise when a weak pulse oscillates in the cavity that though not strong enough to bleach the dye, may sneak through it by passing through it at the same time as a strong bleaching pulse. The 1 cm long

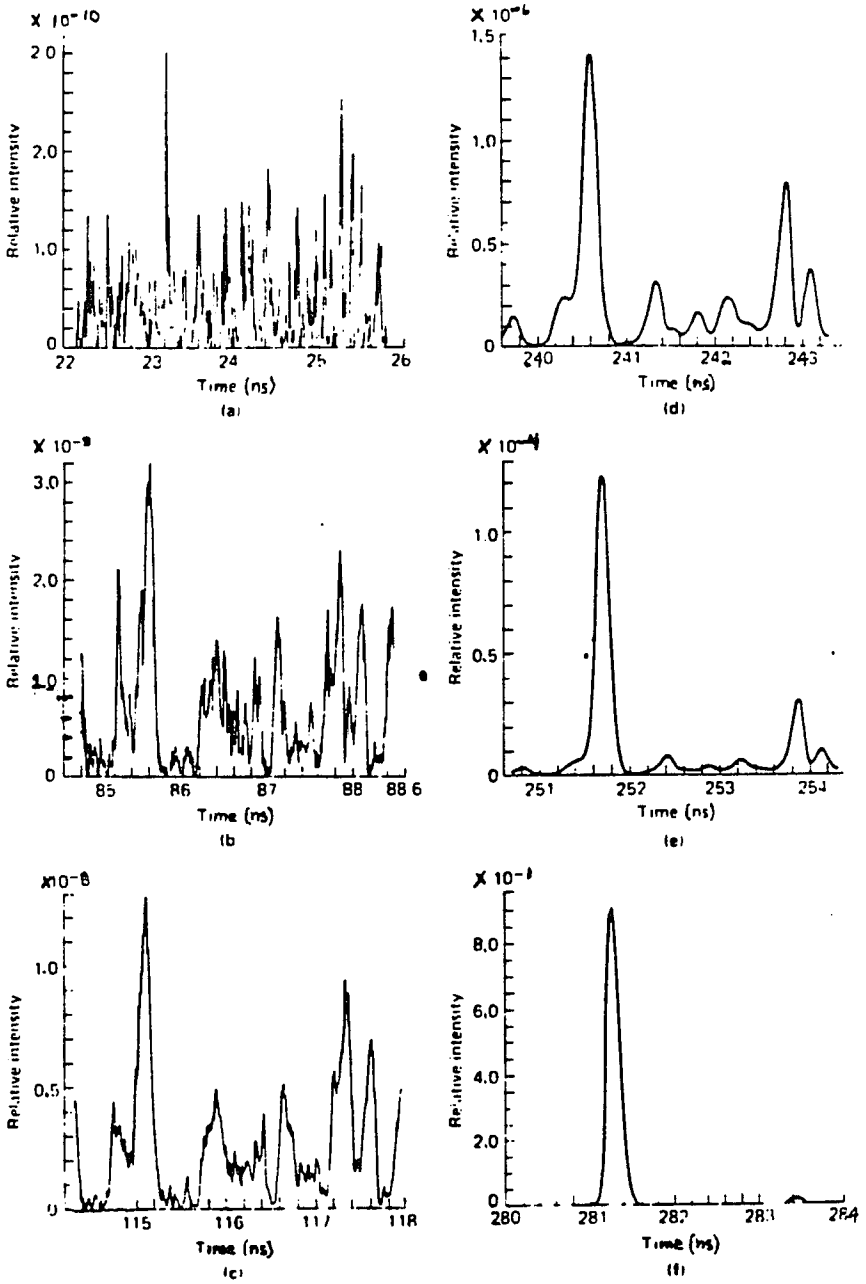

Figure 2.5: Computer simulation of the development of a mode-locked pulse from noise (from Fleck).

dye cell used obviates this problem because its optical path length, 50 ps, is long enough to entirely absorb a weak 10 ps pulse even if it coincides with a larger pulse at some point in the dye. The surface of the dye cell is, like the lasing rods, oriented at the Brewster angle to prevent reflection loss and the creation of multicavity modes. The creation of secondary cavities would reduce the bandwidth of the laser frequency and result in a longer pulse. This would happen because the standing wave requirement must be met for the secondary cavity as well, reducing the allowed modes in the cavity. The Brewster angle orientation of all the major optical components of the cavity insures that only light with the electric field parallel to the plane of incidence, will be entirely transmitted. The perpendicular polarized light is reflected out of the cavity. As a result, multicavity modes are not created and no reflection losses occur for the modes with electric field parallel to the table--which is the polarization of the output train.

The laser pulse train is monitored with a Hadron 105c (Hadron Division of ITT) photodiode with S-1 photodetector surface operated at 2.0 KV. The output of the diode is displayed on a Tektronix 519 (Tektronix, Beaverton, Oregon) oscilloscope with 1 G H Z bandwidth. The typical risetime of the photodetector is 300 ps so that the 4.4 ns spacing between pulses can be easily resolved.

2.3 Single Pulse Selection

The selection of a single pulse from the beginning of the train of pulses is necessary to prevent effects, such as triplet formation,

which occur due to multiple excitations of the sample and which complicate the study of our samples. The pulses at the beginning of the train are the shorter, better mode-locked pulses on the order of 8 ps.

Single pulse selection is achieved by placing a Pockell Cell (Lasermetrics Co., Teaneck, NJ) connected to a spark gap between two cross polarizers. The first polarizer allows the train of pulses to pass through it. The Pockell cell, a uniaxial crystal, serves as a retardation plate when under the stress of an electric field. The retardation, caused by the birefringence of the crystal, is independent of crystal dimensions and, for a given wavelength of light, directly proportional to the voltage applied across the crystal optic axis. The amount of birefringence without an external field is insignificant. As a result, in the absence of such a field the pulses cannot pass through the cross polarizers. By applying the 1/2 wave point voltage, the output beam is linearly polarized and rotated by 90° with respect to the incoming beam. To select one pulse, it is necessary that the retardation last for only a single pulse; that is the birefringence must last for less than the round trip time of 5.4 ns.

The first polarizer is polarized along the polarization direction of the laser fundamental and is used as a precaution to avoid reflections from the Pockell cell or other components in the setup from returning to the oscillator cavity. Such feedback ruins the mode-locked output because, in effect, a second cavity has been created. The second polarizer acts to reject the laser output insuring that only the pulse rotated by the Pockell cell is allowed to pass through the

Glen-Air prism polarizer. The train pulse rejected by this second polarizer is focused between the electrodes of a Nitrogen pressurized spark gap cells. Ionization of the Nitrogen atoms in the spark gap by the first few pulses in the rejected laser trains causes an avalanche breakdown across the electrodes, providing a conductive path for the voltage pulse. This pulse is a preformed 17 KV, 5 ns pulse that is on a transmission line connected to the input electrode of the spark gap. The 5 ns duration of the pulse is less than the 5.4 ns round trip time insuring single pulse selection. The transmission line is a standard 125Ω doubly sheathed cable with a 10 MΩ resistor providing current limiting for the 3.3 ft length of cable (2L/c for L = 3.3 ft is 5 ns). The output of the Pockell cell transmission line is dumped into a 50Ω resistor after passing through 15 ft of cable in order to prevent reflections from returning to the Pockell cell. It was found that a pressure of 100 psi at a voltage of 17 KV provided extremely good selection. Selection is checked by directing the rejected pulse train to a Hadron 105-C photodiode and displaying the output on a Tektronix 519 oscilloscope. Sweep speed is 5 ns/cm. An example of the output indicating proper selection with a gap in the train indicating the selected pulse, is shown in Figure 2.6A. A signal to noise ratio of better than 600:1 was measured for a single 530 nm pulse relative to the noise leakage through the single pulse selection apparatus.

Figure 2.6A: The picosecond laser pulse train with one pulse selected.

(B) The selected laser pulse.

2.4 Second Harmonic Generation

The biological samples we studied have considerable absorption at 530 nm, in the green region of the visible spectrum. They do not absorb the 1.06 μm laser fundamental. As a result, the nonlinear optical effect known as second harmonic generation[6-11] is used to convert the laser fundamental into a useful 530 nm pulse. A carefully aligned, negative uniaxial crystal, KDP (Potassium Dihydrogen Phosphate), is used to generate the second harmonic. When properly phase matched, a maximum of 10% power conversion from 1.06 μm to 530 nm is obtained. The pulse width of the 530 nm pulse is $\sqrt{2}$ shorter than that of the fundamental, lasting for about 4 ps.

Second harmonic generation is a nonlinear effect resulting from the polarization vector in a crystal being related to the electric field by $P_i^{2w} = d_{ijk}\, E_j^{2w} E_h^{W} E_h^{W}$ and serving as a source term in Maxwell's wave equations equations. The nonlinear polarization term, P_i^{2w}, oscillates at frequency 2w because of its relationship to the E_j^{w} terms, which are the electric field terms oscillating at the fundamental frequency w. Solution of Maxwell's equations using the expression for P_i^{2w} results in expressions indicative of a 3-wave mixing phenomenon that generates a photon at twice the fundamental frequency from two photons at the fundamental frequency, thus conserving energy.

The expression for the ratio of the power conversion of the second harmonic to the fundamental is:

$$\frac{I^{2w}}{I^{w}} = 2\left(\frac{u}{\varepsilon}\right)^{3/2} \frac{w^2}{n^3} d^2 l^2 \frac{I^{w}}{A} \frac{\sin^2\left(\frac{\Delta KL}{2}\right)}{\left(\frac{\Delta KL}{2}\right)^2} \qquad (2.4.1)$$

where

w = fundamental frequency

2w = second harmonic frequency

A = area of incident light beam at fundamental frequency

u,E = permeability and dielectric constant of free space respectively

n = index of refraction of crystal

L = optical path length

$$\Delta k = k_{2w}^{j} - k_{w}^{i} - k_{w}^{k}$$

$$k_{w}^{i} = (n^{w} c/w) i$$

The superscripts of the k vector give the direction of the propagation vector.

As Equation 2.4.1 indicates, maximum power conversion is obtained when the phase matching criteria, $\Delta k = 0$, is met. This may be rewritten as $\Delta k = 2w/c\ (n^{2w} - n^{w}) = 0$. In order to obtain phase matching, one takes advantage of the natural birefringence of anisotropic crystals. In such crystals, the phase velocity of a wave propagating along a given direction depends on the direction of its polarization. In such crystals, propagation along a given direction can be sustained only for light of 2 possible polarizations, each of which faces a different index of refraction. In a uniaxial crystal, one finds that the direction of polarization and the index of

refraction of one wave varies with the angle between the optic axis and the direction of propagation--this is the extraordinary wave. The other wave, the ordinary wave, remains polarized along the same direction with the same index of refraction independent of θ.

Because in a normally dispersive material the index of refraction of both polarizations of a wave increases with w, phase matching is possible only if the second harmonic propagates as an extraordinary wave, while the fundamental propagates as an ordinary wave. To insure the fundamental propagates as an ordinary wave, the notches of the KDP are placed so that the direction of polarization of the incident beam is parallel to the crystal edge between the two notches.

The relationship between the index of refractions of the ordinary and extraordinary beams as a function of the angle θ between the optic axis and direction of propagation is:

$$\frac{1}{n_e^2(\theta)} = \frac{\cos^2\theta}{n_o^2} + \frac{\sin^2\theta}{n_e^2}$$

Finding the angle θ, at which $n_e^{2w}(o) = n_o^{w}$ is the final step in achieving phase matching. For the KDP crystal, used in our setup because of its ability to generate the second harmonic of the entire bandwidth of the laser fundamental, the phase matching angle is 41° 12'. Correct positioning of the KDP's angular orientation was determined by maximizing the 530 nm output of the crystal. A Laser Precision Co. RK P-335 probe and PK-3230 readout system with 1-75 and 4-96 filters to block out the 1.06 μm fundamental was used in the alignment procedure.

The frequency doubled and fundamental pulses now begin a carefully laid out journey over two optical tables encompassing one-half of a major sized room. Apertures, when placed at carefully selected points, assure the pulses are following the proper path. The itinerary of the 30 ns trip includes diversion, by beam splitters, of fractions of the pulses to a diode to trigger the streak camera and a different diode to trigger the discriminator used in conjunction with the integrator. After passage through 4-96 and 1-75 filters that pass only the 530 nm pulse, a beam splitter diverts part of the frequency doubled pulse to an RCA 7102 PMT whose output is calibrated to the intensity of the pulse at the sample site. The surviving portion of the 530 nm pulse is then directed, by mirrors, over the home stretch until it reaches the sample site. The intensity of the resulting fluorescence from the sample is measured by a PMT (RCA 7265), while the time resolved fluorescence kinetics is captured by a streak camera, digitized on an Optical Multichannel Analyzer (OMA) and recorded for posterity on the floppy discs of a PDP 11/03 minicomputer and on paper by an x-y recorder. The outputs of both the PMT (RCA 7102) measuring the intensity of the pulse at the sample site and the PMT (RCA 7265) measuring the intensity of the fluorescence, are connected to the electronic integrator whose digital readout provides easy recording of the data. The integrator, in particular, greatly simplifies the accumulation of data for the relative quantum yield measurements. The ability to accumulate more raw data, as well as the fact that each measurement is more accurate, provides for extremely accurate measurements of the relative quantum yield, a significant improvement over the

previous method that required measuring the height of a pulse from an oscilloscope recorded on film.

2.5 PMT Integrator System

Measurements of the intensity of the excitation pulse and fluorescence of the sample, used to calculate the relative quantum yields, were made by PMTs whose outputs were connected to a LeCroy Research Systems Model 227G Integrator. The integrator, in conjunction with the LeCroy Research Systems Model 62IL Discriminator, provided digital readout of the intensities.

The LRS Model 227G Quad Gated Integrator (Figure 2.7) provides four identical pulse integrator and storage channels which produce an output amplitude proportional to the area of an input pulse contained within an externally generated gate interval. The gate interval is provided by the LRS Model 62IL Discriminator (Figure 2.8). The full-scale of each channel of the integrator is 5.0 volt-ns. A pulse with area of 5 volt-ns will produce 10 volts at the Test Point BNC (TP) of the integrator. A digital voltmeter connected to the Test Point BNC provides a readout of the voltage at the (TP).

The gate interval is supplied to the integrator by the LRS Model 62IL discriminator. The output durations of the discriminator are continuously adjustable from 5 ns to 1000 ns and are highly stable and independent of the input amplitude and duration which is supplied by a trigger diode. The trigger diode is connected to the IN connector of the discriminator. The trigger diode was placed at the end of the delay path when it was determined that this length of cable would delay the start of the gate sufficiently in order that the output of both

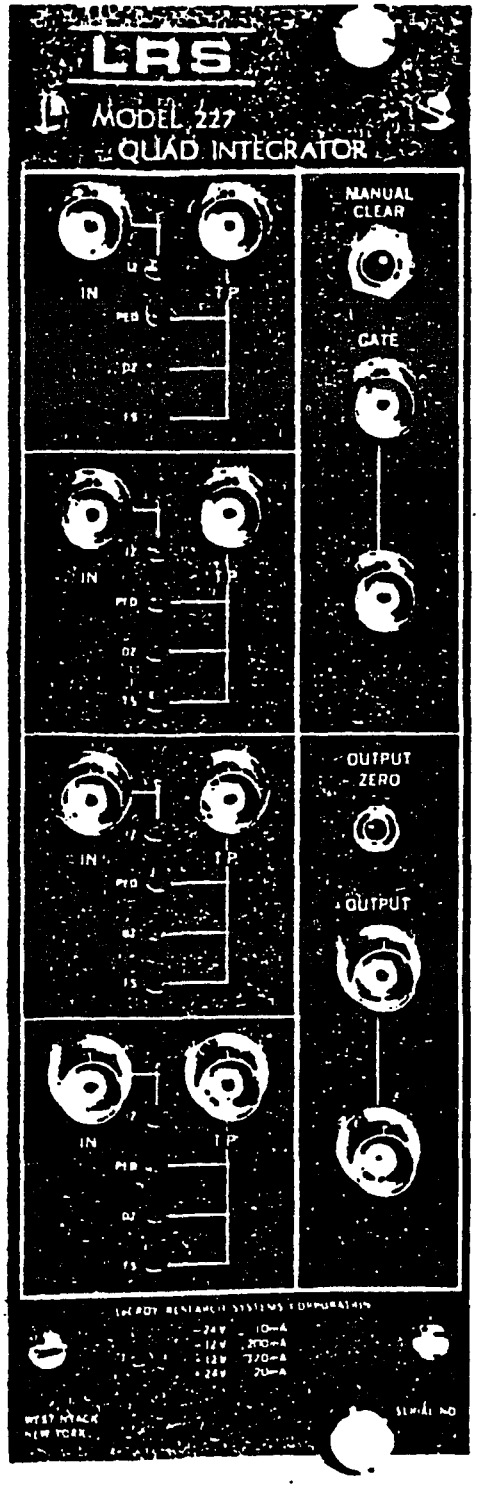

Figure 2.7: LRS Quad Integrator.

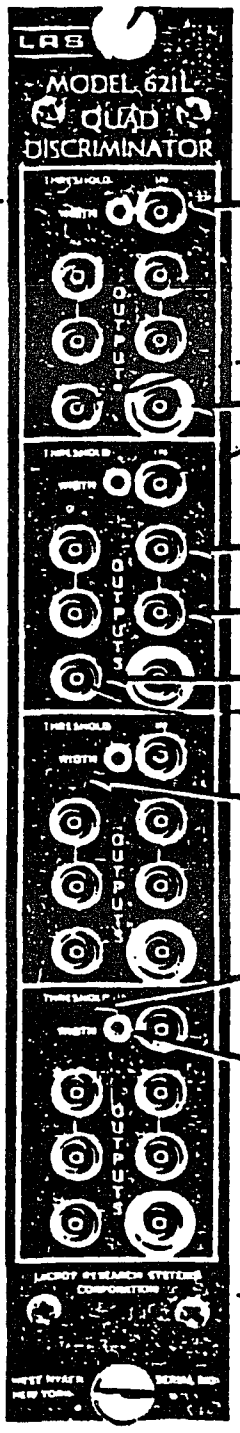

NIM Model 621L

Quad Discriminator

50 Ω input, < 2% reflections.

1 complementary 50 Ω output
(quiescently, -16 mA; logical 1, 0 mA).

2 pairs bridged 50 Ω outputs
(quiescently, 0 mA; logical 1, -32 mA per pair).

1 normal 50 Ω output
(quiescently, 0 mA; logical 1, -16 mA).

Continuous width adjust, 5 ns to 1 us.

Threshold adjust, -30 mV to -1 volt;
stability, < 0.2%/°C.

Threshold monitor point; reads 10X
actual threshold.

Standard AEC/NIM packaging, in conformance
with AEC Report TID-20893, No. 1 width module.

Figure 2.8: LRS Quad Discriminator.

PMTs would be within the gate. The gate length was set at 80 ns in order to insure that the entire output of both PMTs would always be within the gate interval, even allowing for jitter. The gate length was kept as short as possible to reduce the conduction of noise to the readings. The initial setup was done with an oscilloscope which displayed the positioning of the gates and PMT outputs.

The trigger diode is connected to the IN connector of the discriminator. The gate output comes from the output of the discriminator and is connected to the GATE Input BNC of the integrator. The output of the PMT's, measuring excitation pulse intensity and sample fluorescence intensity, are connected to the IN BNC connectors of the top 2 channels of the integrator. Digital voltmeters are connected to the Test Point BNC connectors of the top two channels to provide readings proportional to the area of the output pulses of the PMTs. A pin diode located behind the sample and an RCA 7265 PMT above the streak camera, both connected to the electronic integrator, measured the intensities of the transmitted and fluorescent beams respectively. The intensity of the excitation fluence at the sample site was determined by an RCA 7102 connected to an electronic integrator. A Jarrel Ash energy meter placed at the sample site was used to calibrate the digital reading with the intensity of the excitation pulse, as explained in the next paragraph.

The appropriate amount of neutral density filters were placed in front of the RCA 7102 PMT to insure that the highest intensity pulse registered 10 volts on the integrator. A plot of energy measured at the sample site by the Jarrel Ash energy meter, against volts measured on the integrator, showed a linear response between 2 and 10 volts.

As a result, pulses which registered less than 2 volts on the integrator were rejected. The slope of the response curve was shown to be 6.0×10^{-6} Joules/volt. Using the fact that the energy of one 530 nm photon ($\hbar\omega$) is 3.78×10^{-19} Joules, we obtained that each volt on the integrator corresponded to 1.59×10^{13} photons. In other words, the number of photons per volt, N, is equal to $\frac{6.0 \times 10^{-6} \text{ Joules/volt}}{3.7 \times 10^{-19} \text{ Joule/photon}}$. We then divided N by the area of the pulse at the sample site (whose measurement is discussed in the next paragraph) to obtain the calibration number of 8×10^{15} photons/cm^2 per volt measured on the integrator. In other words, the calibration number, or the incident fluence measured in photons/cm^2 per volt read on the integrator, equals $\frac{1.59 \times 10^{13} \text{ photons/volt}}{2 \times 10^{-2} \text{ cm}^2}$. The intensity of the incident fluence at the sample site was varied by placing appropriate neutral density filters in the excitation pathway. Its value was obtained by multiplying the volts on the integrator by the calibration number times the transmission of the neutral densities.

The spot size of 2×10^{-2} cm^2 at the sample site was obtained by collimating the excitation beam to an elliptical spot size of uniform density at the sample position. The spot size is determined by photographing the image at the sample size using appropriate neutral density filters in front of the film until the excitation pulse is just visible on the film. In addition to determining the spot size, this technique insures the absence of hot spots in the laser pulse.

The transmission data were obtained by dividing the intensities of the transmitted beam (measured by a diode located behind the sample)

per incident intensity with that ratio recorded at low fluence. Similarly the quantum yield data were obtained by dividing the readings obtained by the RCA 7265 per incident intensity with the ratio recorded at low fluence. Quantum yield measurements of known samples, such as erythrosin, spinach and the trimer form of the PE were taken to ensure the integrity of the system. We discovered the need to cover the outputs of the PMTs with aluminum foil and shielding, and to place as long a length of them as possible in a protective, metal ash tray to reduce electromagnetic noise radiating from the equipment in the lab. We also discovered the need to determine the exact transmission of each ND filter at each wavelength. We discovered that the slight difference in transmission of similar ND's, as well as the variation in transmission of each ND filter as a function of wavelength, produced inaccurate quantum yield measurements. ND filters were placed on the PMT measuring the fluorescent intensity to keep the output of that PMT within the 5 volt-ns limit that the integrator can measure. Transmission data of known samples, such as erythrosin, water and no sample at the sample site, were used to insure the integrity of the system.

The result of this carefully laid out system was extremely accurate measurements of the quantum yields of the samples and the first conclusive experimental evidence that bleaching, and not exciton annihilation, is responsible for the apparent decrease in quantum yield of the lower aggregate forms of PE. We have also been able to obtain data indicating exciton annihilation can be seen in the trimer and higher aggregates.

2.6 Streak Camera System

2.6.1 The Camera

The streak camera used to provide the time resolved fluorescence kinetics of our samples is a prototype manufactured by the Hamamatsu Corporation (Middlesex, NJ).[12-17] A schematic diagram describing its operation is shown in Figure 2.9.

The photoelectrons generated by light incident on the photocathode are accelerated by an accelerating mesh and deflected by an applied voltage ramp in time. The microchannel plate within the streak tube (n 895) produces photoelectrons through secondary emission processes in the microchannel plates. The result of the sweeping voltage ramp in time is to provide a temporal profile of an event along a spatial axis which is divided into channels. The secondary electrons impinge upon a phosphor screen to form the streak image in different channels, with the intensity distribution of the space dependent profile representing the temporal profile of the original signal. Four streak rates are available on the Hamamatsu camera. The nominal sweep ranges are 10, 5, 2, and 1 nanoseconds over the 15 mm length of the output slit. The streak image on the phosphor screen can be recorded by polaroid film, by an electronic readout video or as in our case, by a photodiode array device.

The Optical Multichannel Analyzer (OMA) which records the streak image of the camera consists of a model 1205 D detector head with an S-20 photodetector surface and 1205 A console. Efficient transfer of the streak output is assured by the peak spectral response of the photodetector surface nearly matching the peak spectral output of the

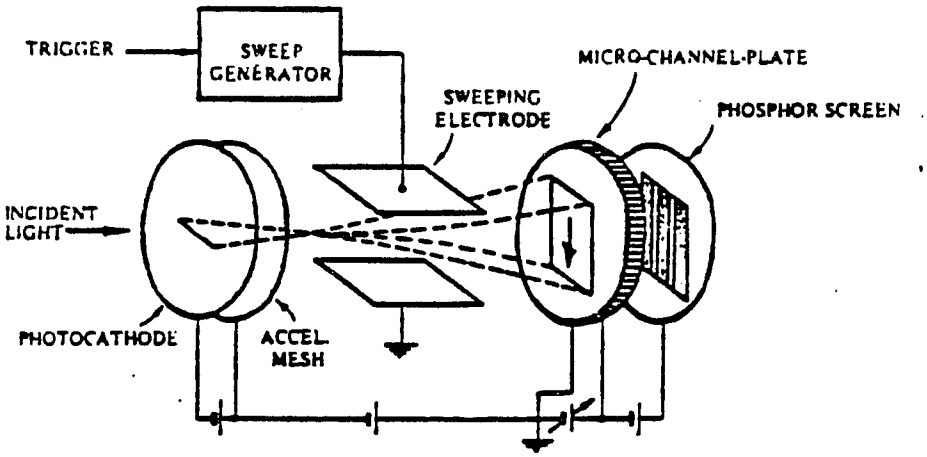

Figure 2.9: Schematic diagram of streak tube operation.[15]

streak camera P-11 phosphor (465). The OMA detector surface consists of a 1" diameter photocathode with a 2.5 mm x 12.5 mm active area. Photoelectrons are focused onto a thin layer of silicon which is internally scanned by an electron beam. This active photosensitive area is divided into 500 regions, or channels of resolution, which are scanned at the rate of 64 us per channel. The amount of charge deposited by the beam is proportional to the amount of charge depleted by the photoelectric effect induced by light striking the outer surface of the detector head. The output signal of the diode array is obtained by capacitative coupling to the scanning electron beam. The signal from 5 scans of the tube target face was accumulated in measurements involving the OMA to ensure the reading of at least 97% of the signal charge. The reading of most of the charge from the tube target face is necessitated by the need to obviate problems caused by lag. Lag is the residual signal charge left on the target face after three scans of the active area, and is a nonlinear function of the incident intensity. Lag may vary by as much as 400% for a ten-fold change in incident illumination. As a result failure to read out most of the charge from the target face would result in distorted representations of the intensity of the incident light.

Operation of the streak camera requires proper electronic triggering of the deflection voltage prior to the arrival of the signal on the streak tube detector surface. The camera is triggered by beam splitting a portion of the laser pulse into a pin diode which provides a 2-10 volt trigger signal into the 50Ω trigger input of the camera. Prior triggering is required by the fact that the streak camera uses

avalanche transistors (possessing an inherent delay of 35 ns) to generate the deflection voltage ramp. The optical delay path travelled by the pulse after part of it triggers the camera, ensures the simultaneous occurrence of the arrival of the fluorescence signal and actual sweeping of the voltage at the streak tube.

2.6.2 Calibration of Streak Rate and Intensity

The streak camera must be calibrated for streak rate linearity, which affects both time base and intensity calibration.[16] A 6 ps, 530 nm laser pulse and an etalon were used to calibrate the streak rate. The etalon consists of two 92% R (8% T) dielectric coated mirrors at 5300 nm, with reflective coated surfaces facing one another, and separated with a cylindrical aluminum spacer machined to 10^{-3} inch accuracy. The etalon is placed in front of the camera and the time separation between two adjacent pulses arising from the round trip reflection from the dielectric mirror on the etalon is 2d/c where d is the length of the aluminum spacer. The ratio of intensity of these two adjacent pulses is $(1 - T)^2$.

The exponentially decreasing sequence may be expressed as $I_k = I_o \exp(t_k/\Delta t\ I_n(1 - T)^2)$. An illustration of the peaks, which appear periodically across the 500 channels of the OMA, appear in Figures 2.10A and B. If the ramp voltage were constant in time, the plot of $\Delta T/\Delta X$ as a function of channel would be a horizontal line, or equivalently, the distance between peaks on the OMA would be the same. By definition, to obtain $\Delta T/\Delta X$ as a function of channel X, one

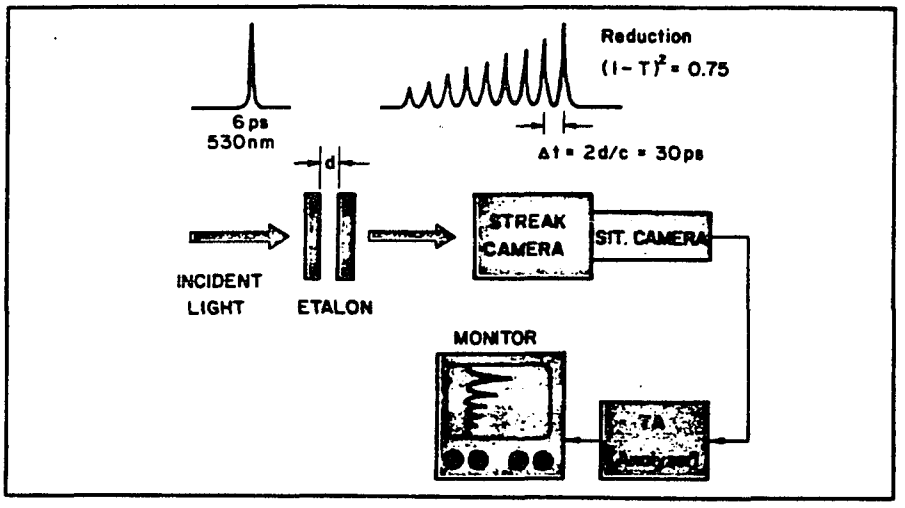

Figure 2.10: Schematic diagram of calibration technique of a streak camera system (from Schiller, Dagen, & Alfano).[17]

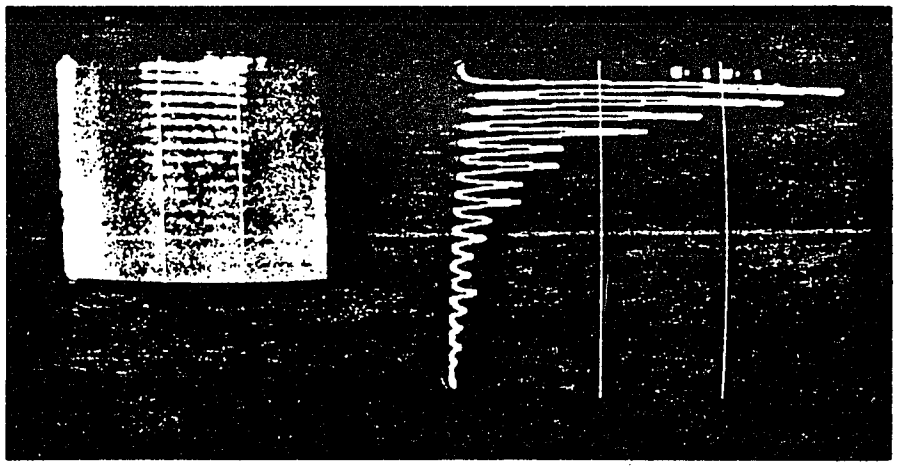

Figure 2.11: Graphic representation of the intensity profile for a 6 ps laser pulse passing through a 300 ps etalon. (From Schiller, Dagen, & Alfano).[17]

calculates ΔT, divides by the number of channels between peaks and assigns that value of $\Delta T/\Delta X$ to the channel midway between the two peaks. By taking several shots, one can form a complete graph of $\Delta T/\Delta X$ versus channel. Noting that $t = (\Sigma \Delta T/\Delta X)\Delta X$ where the sum is over the channels up to the point of interest, one can determine the time to which each channel corresponds.

With the time axis thus calibrated, one must now calibrate the intensity axis, taking into account the streak rate $\Delta T/\Delta X$ just calculated. The need for this calibration is clear as soon as one appreciates the fact that the intensity at a particular channel, $I(X)$, is not the same as $I(t)$, the true intensity at the time corresponding to that channel. To see that this is so, let us assume that I at one channel is larger than at a later channel; that is the voltage ramp is such that the deflected electron beam excites phosphor at the first channel longer than at the second channel to which it is deflected. Let us also assume the light intensity is constant in time. Clearly, while in reality the light intensity at both times are equal, more intensity will be indicated at the first channel than at the second channel, because the first channel collected the electrons for a longer time.

To correct the data, taking into account the nonlinear streak rate, one sets $I(t)dt = I(X)dX$ or, equivalently $I(t) = I(X)\, dX/dt$ because $I(X)dX$ is the total intensity measured in the immediate vicinity of channel X, and $I(t)dt$ is the total intensity measured in the immediate vicinity of time t; the equation simply requires that the total intensity at X equal the total intensity measured for the

corresponding time. By multiplying I(X) measured at each channel X, by $\Delta X/\Delta T$ of that channel, we obtain the intensity as a function of time.

2.6.3 Trigger and Jitter

The applied deflecting voltage for the streak camera requires a triggering voltage of about 2-10V into 50 ohms. Streaking begins 10-100 ns after triggering depending on sweep rate. The trigger delay time varies for different sweep settings. In order to synchronize the arrival of the light signal with the beginning of the deflection sweep, a portion of the laser pulse is split off to a PIN diode to produce the trigger pulse, while the pulse to be investigated is sent along a delay path so that it arrives at the camera when streaking begins. It is useful to note that light takes approximately 3.3 ns to go 1 meter in air. In addition to the optical delay path, an electronic delay unit is necessary as a means of making incremental changes in the delay time. This fine tuning is necessary in order to compensate for jitter, as well as provide the necessary change in delay time needed when changing streak speeds.

Trigger jitter, which largely depends on the characteristics of the trigger pulse, is the difference in time from shot to shot between the arrival of the trigger signal at the streak camera and the beginning of streaking. Typically, trigger jitter ranges from a few ps to tens of nanoseconds. In general, the sharper the risetime of the triggering pulse, the less the jitter. The jitter of our streak camera is not more than 15 channels.

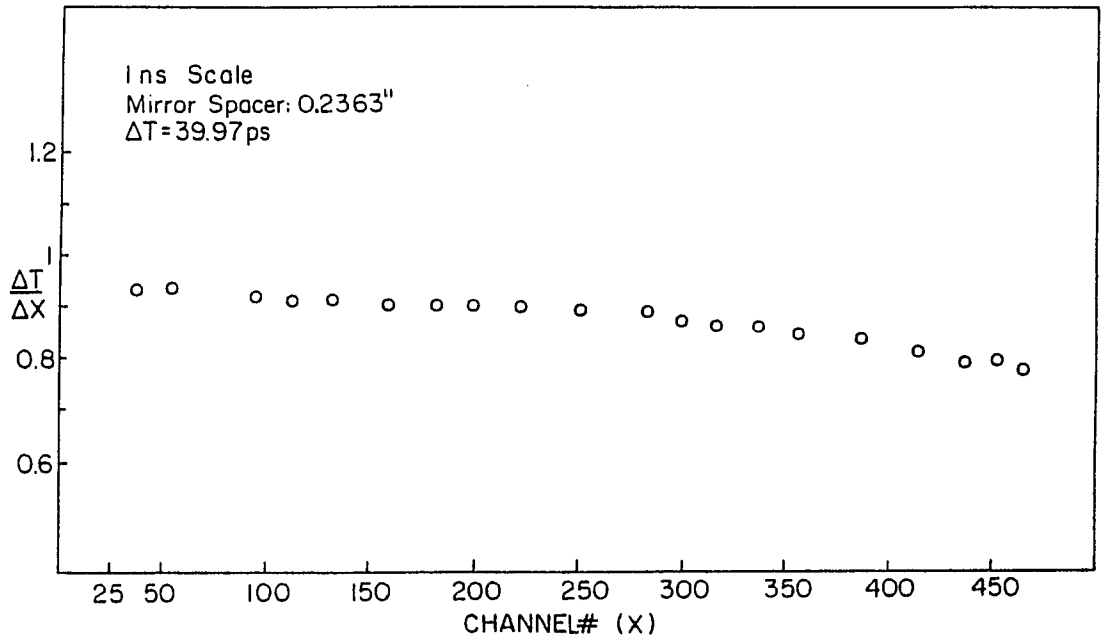

Figure 2.12A. ΔT/ΔX Versus channel number for 1 ns scale.

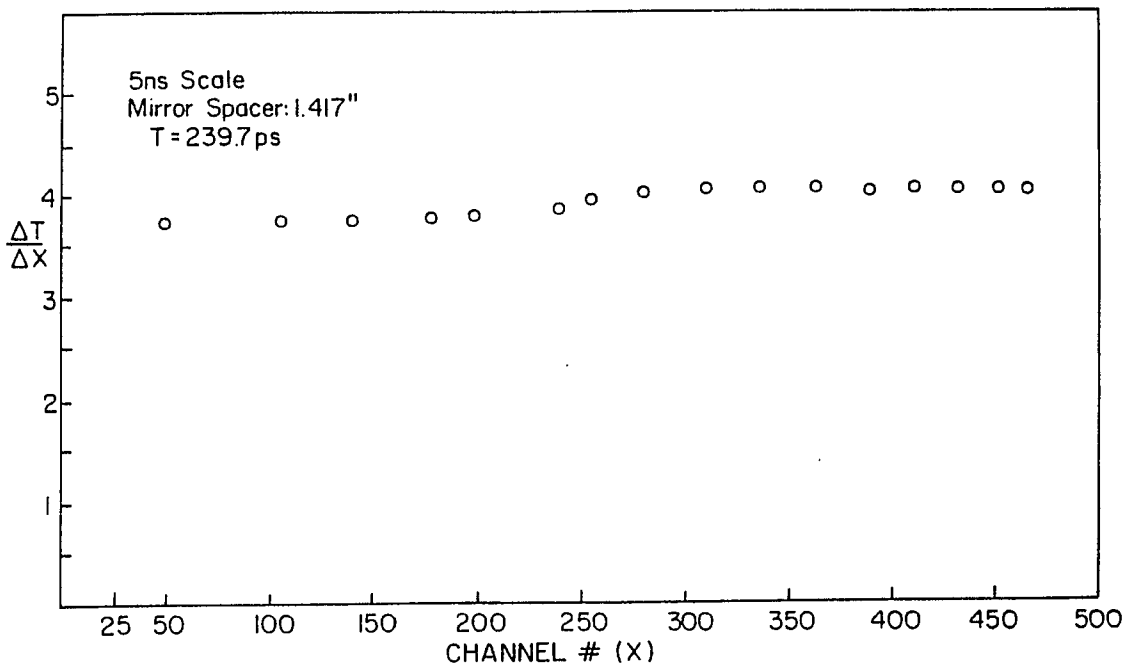

Figure 2.12B. ΔT/ΔX Versus channel number for 5 ns scale.

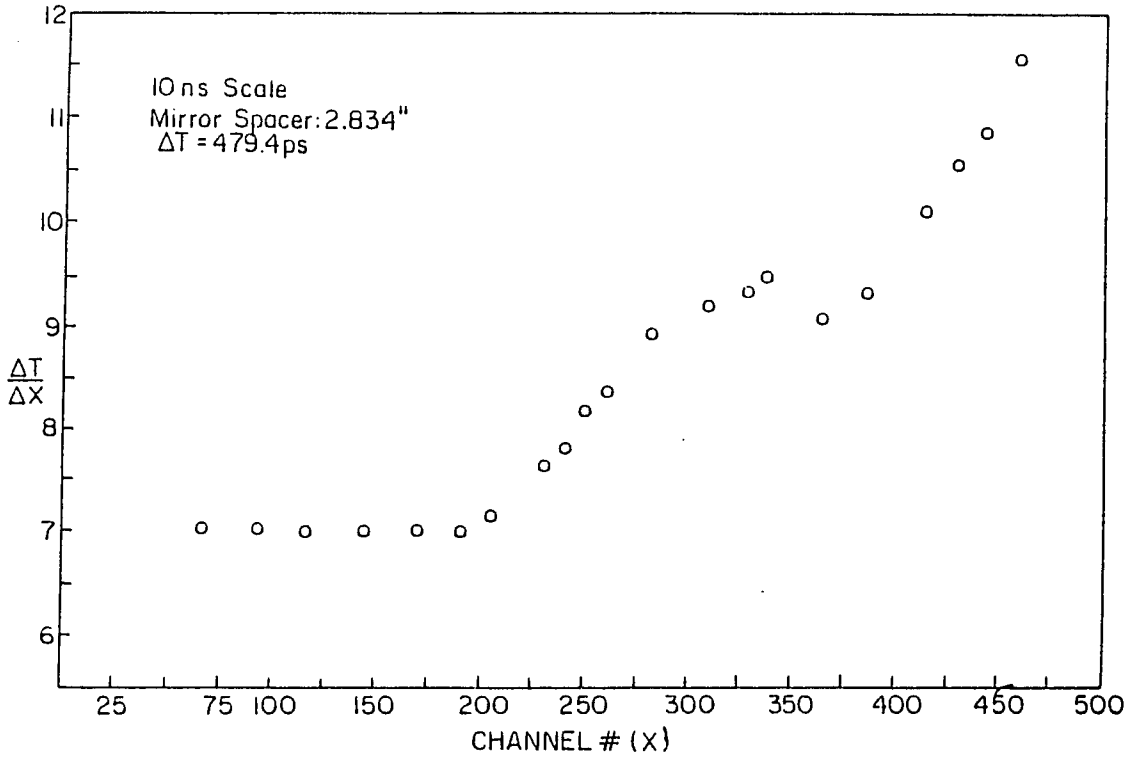

Figure 2.12C. ΔT/ΔX Versus channel number for 10 ns scale.

2.6.4 Time Resolution

The time resolution of a streak camera is determined by: the spread of the photoelectron transit times, Δt_1, the spread in the time related to the spatial resolution of the slit Δt_2, and the deflection field Δt_3. The time spread in the arrival at the phosphor screen of electrons that were simultaneously emitted from the photocathode, Δt_1, is determined by the initial velocity distribution.[15,16] This spread is mainly developed close to the photocathode where the electrons are moving slowly. To develop an expression for Δt_1, one makes use of the fact that the time for a photoelectron of initial energy, eV_o, emitted normal to the photocathode, to travel a distance χ along the tube axis is given by $t = \sqrt{m/2e} \int dx/\sqrt{v_o + v(X)}$ where V(X) is the axial potential distribution and e and m are the electron charge and mass, respectively. If $V(\chi)$ varies linearly with distance from the photocathode, and the initial photoelectron velocity spread is Δv, it can be shown that $\Delta t_1 = m\Delta v/eE$ where E is the electric field strength near the photocathode. The planar, fine-mesh-high potential electrode close to the tube photocathode improves the time resolution by increasing E.

The value of Δv depends on the response of the particular photocathode and the wavelength of the illuminating light. The wish to choose a photocathode that will minimize Δv for the wavelengths to be studied and thus improve the time resolution, may conflict with the desire to have the camera exhibit high sensitivity over a wide spectral range.

The time spread Δt_2 caused by the spatial spread of the slit width is given by: $\Delta t_2 = W/V$ where W is the FWHM of the slit image

formed on the phosphor screen in the (non-streaking) focus mode and V is the streak speed. The time spread Δt_2 corresponds to the time it takes the electron to sweep (when the camera is streaking) from the bottom to the top of the image formed on the phosphor screen when the camera is in the focus mode. A moment's reflection should convince the reader that Δt_2 is the uncertainty in time of an event caused by the slit width.

The time spread at Δt_3 is caused by the deflection electric field on the photoelectron beam and depends on the length of the deflecting plates, the beam spot size in the deflection plates, the deflection electric field and the axial direction velocity of the electron. By taking the convolution of the three resolution times, assuming distributions Gaussian in time, the total time resolution Δt_r of the streak camera is given by $\Delta t_r = (\Delta t_1^2 + \Delta t_2^2 + \Delta t_3^2)^{1/2}$. The measured pulse duration, Δt_m for a Gaussian laser pulse of duration Δt_p is:

$$\Delta t_m = (\Delta t_r^2 + \Delta t_p^2)^{1/2}.$$

Typically, the values of Δt_1, Δt_2, and Δt_3 are on the order of 1 picosecond. The response time of the detection system is the convolution of the real laser pulse and the resolution of the streak camera. For an ideal Gaussian pulse, Δt_m of above is about 10 ps on the fast sweep rate scale (15 mm/ns or nominal 5 ns scale). For decays that are on the order of the resolution of the camera, the response time of the system must be deconvoluted from the experimental data to obtain the actual decay time. This fact was used in our research on the α subunit.

2.6.5 Data Storage and Analysis System

A DEC PDP 11/03 minicomputer with 28 Kb MOS memory, a dual floppy disk storage system with 256K bytes storage per disk, A/D converter, D/A converter and graphics VT-55 terminal was used to store and analyze the data. A Fortran program synchronized data transmission between the OMA 1205A console and the computer.

Fortran programs were also used to construct the data files and correct for streak rate and intensity. The collected data was normalized in a way to ensure that the peak was at the top of the computer screen. Programs were then constructed to compare the corrected experimental data with various theories (explained in next chapter). Where necessary, a program averaging many experimental curves together was used to generate a composite curve. Also, where necessary, numerical deconvolution of the data with the response time of the detection system was performed.

A VAX 11/780 computer was also used in data analysis. The IMSL Library provided numerical solutions to the differential equations. These programs are described in the Appendix.

2.7 Materials

Nostoc sp. (strain Mac) was grown in a 14 liters fermentor with pink or cool white fluorescent light as described by Zilinskas and Howell.[19] Phycobilisomes were isolated from these cells according to the protocol of Troxler et al.[20] Phycoerythrin was obtained from dissociated phycobilisomes by use of calcium phosphate chromatography and sedimentation on linear gradients, as detailed by Zilinskas and

Howell.[19] The smallest phycoerythrin aggregate so obtained [trimer, $(\alpha\beta)_3$] was removed from the gradient, dialyzed exhaustively against 1 mM potassium phosphate, pH 5.0, containing 0.02% sodium azide, and was then lypophylized. This sample was dissolved at ∿ 10 mg/ml in 8.0 M urea, 0.01M potassium phosphate, pH 8.0 and 0.01 M β-mercaptoethanol and incubated at 37°C for 2 hours. The denatured phycoerythrin was then applied to a DEAE-Sephacel column preequilibrated with the denatured solution. The α and β subunits were then eluted (in that order) with a linear gradient of increasing NaCl in equilibrating solution. The peak fractions were pooled separately, dialyzed against 0.1M potassium phosphate, pH 5.0, to effect renaturation, and their identities assessed by absorption, sedimentation on linear gradients of sucrose, and electrophoresis on SDS - polyacrylamide gels.

In all but two such isolations, the α and β subunits of phycoerythrin were clearly separated from each other during chromatographic elution, and analyses showed that these were purified to homogeneity. However, for two (out of a total of eight) isolations, for reasons not yet understood (but probably relating to unobvious differences in phycoerythrin layered on the DEAE-Sephacel column), clear separation of the two subunits was not obtained. Rather, a major fraction was eluted from the column which had equimolar quantities of α and β subunits, as judged by SDS gel electrophoresis, which after renaturation, sedimented as a monomer, and whose absorption and circular dichroism spectra approximated the summation of equimolar amounts of both subunits.[19]

Absorption spectra were measured on a Cary 17D spectrophotometer. Fluorescence emission spectra were determined on an SLM 4800S spectrofluorimeter with corrections made for the grating and photomultiplier tube efficiency. Samples were diluted to an absorbance of 0.1 at the absorption maximum and excited at 530 nm. The excitation and emission monochromator bandwidths were 8 and 2 nm, respectively. Fluorescence polarization spectra were measured with an Aminco-Bowman spectrofluorimeter equipped with a R446S (Hamamatsu TV) photomultiplier tube and two Glan-Thompson prism polarizers. Measurements and calculation of the degree of polarization were done as described by Grabowski and Gantt.[22] The excitation and emission monochromator band passes were 2.7 and 5.5 nm, respectively and the observation wavelength was at 585 nm. Samples were diluted to an absorbance of 0.17 at the absorption maximum with 0.1M potassium phosphate buffer, pH 5.0.

For the quantum yield measurements, rhodamine B in ethanol was used as a standard; its quantum yield is 0.94, as measured by Dale and Teale.[23] The sample and standard were adjusted to an absorbance of 0.07 at the excitation wavelength (530 nm). Fluorescence was measured with the SLM 4800s spectrofluorimeter.

Notes

1. Lu, P. Y., Ho, P. P., & Alfano, R. R. (1979). IEEE J. of Quan. Electron, QE-15, 406.

2. Yariv, A. (1975). Quantum Electronics, 2nd ed. New York: John Wiley.

3. DeMaria, A. J., Glenn, Jr., W. H., Brienza, M. J., & Mack, M. E. (1969). Proceed. of IEEE, 57, 2.

4. Klauder, J. R., Duguay, M. A., Giordmaine, J. A., & Shapiro, S. L. (1968). Applied Physics Letters, 13, 174.

5. Smith, P. W., Duguay, M. A., & Ippen, E. P. (1975). Process in Quan. Electron., 3, 107.

6. Yariv, A. (1976). Optical Electronics, 2nd ed. New York: Holt, Rinehart and Winston.

7. Conwell, E. M. (1973). IEEE J. of Quan. Electron, QE-9, 867.

8. Shapiro, S. L. (1968). Applied Physics Letters, 13, 19.

9. Kleinman, D. A. (1962). Physical Review, 128(4), 1761.

10. Green, B., Liu, J. C., Alfano, R. R. (1977). Optics Communications, 22, 119.

11. Green, B., & Alfano, R. R. (1977). Optics Communications, 20, 305.

12. Bradley, D. J., Higgins, J. F., & Key, M. H. (1971). Applied Physics Letters, 16, 53.

13. Bradley, D. J., Liddy, B., & Sleat, W. E. (1971). Optics Communications, 2, 391.

14. YaShelev, M., Richardson, M. C., & Alcock, A. J. (1971). Applied Physics Letters, 18, 354.

15. Schiller, N. H., Tsuchiya, Y., Inuzuka, E., Suzuki, Y., Kamiya, K. Iida, H., & Alfano, R. R. (1980). Opt. Spec., 14, 55.

16. Dagen, A., Alfano, R. R., & Schiller, N. H. (1982). Picosecond Streak Cameras. International Encyclopedia of Optical/Electro-Optical Laser Technology.

17. Schiller, N. H., Dagen, A., & Alfano, R. R. (1982). Photonics, 16(1), 56.

18. Fleck, J. A. (1970). Phys. Rev. B1, 128, 84.

19. Zilinskas, B.A., & Howell, D. A. (1983). Plant Physiol., 71, 379-385.

20. Troxler, R. R., Greenwald, L. S., & Zilinskas, B. A. (1980). J. Biol. Chem., 255, 9380-9387.

21. Grant, M., Schiller, N. H., & Alfano, R. R. (1977). Physics Teacher, 15, 369.

22. Grabowski, J., & Gantt, E. (1978). Photochem. Photobiol., 28, 39.

23. Dale, R. E., & Teale, F. W. J. (1970). Photochem. Photobiol., 12, 99.

Chapter 3

THEORETICAL FOUNDATIONS

3.1 Introduction

Chapter 3 presents the theoretical foundations used in this dissertation. Section 3.2 describes the Paillotin-Swenberg annihiliation theory. This theory explains the fluorescence decay curves and quantum yield curves ϕ/ϕ_o resulting from a sample, in which bimolecular interactions occur, hit by an intense laser pulse. The laser pulse creates excitons within the sample. No assumptions concerning the dimensions of the volume through which the excitons migrate, also known as the domain, are made. Relative sizes of domains may be estimated, however, by comparing the theoretically calculated and experimentally attained, quantum yield and fluorescence decay curves.

Sections 3.3 and 3.5 describe systems in which no bimolecular interactions occur. Instead, these two sections deal with excited molecules, randomly located throughout the domain, which either fluoresce or transfer energy to each other. Section 3.3 addresses the problem of a finite domain, while section 3.5 assumes an infinite domain.

Section 3.4 illustrates the effects of energy transfer on the fluorescence decay viewed through polarizers placed in front of the

monitoring system. In particular, it derives the expressions for fluorescence viewed with the polarizer placed parallel (I_{11}) and perpendicular (I_{+}) to the polarization of the excitation pulse, and for the experimentally measured $I_{11} + I_{+}$ in the small domain theory.

3.2 Paillotin-Swenberg Annihilation Theory

The Paillotin-Swenberg annihilation theory is the most comprehensive description of the fluorescence temporal decay curves F(t), and fluorescence quantum yield, ϕ/ϕ_o, obtained from systems in which bimolecular processes occur.[1,2] No assumptions concerning the actual dimensions of the domain size of migration of the exciton, that is the active volume through which they move, are made. The theory does allow one to estimate relative domain sizes by comparing theoretically calculated and experimentally obtained quantum yield and fluorescence kinetic curves. The integrity of the theory has been assured by comparing the results in the two limits of domain size, very large and very small, with previous theories developed for those specific cases. In addition to fitting the Swenberg-Campillo theory in large domains, and the Mauzerall theory in small domains, the originators of the theory found the appropriate limits for which the curves are fit by the expression $e^{-a\sqrt{t}-kt}$. During the course of our research, we found the limit corresponding to decays of the form $e^{-kt^{1/3}-kt}$. As explained in section 3.5, these decays are also expected from molecules, with fluorescence lifetimes $\tau = 1/k$, which transfer energy to each other and are randomly located in an infinite lattice. The $t^{1/2}$ decay law is

appropriate for a three dimensional lattice; the $t^{1/3}$ law derives from a two dimensional lattice.

The drudgery associated with actually solving the differential equation describing the system belies the simple, elegant logic and clarity of thought that serves as the foundation of this, as well as any other good, comprehensive theory. The theory considers a single domain containing (i) excitons at time t. These excitons decay in time by monomolecular, as well as bimolecular, processes. The theory examines the probability, $P_i(n,t)$, of having these (i) excitons in the domain at time (t), given that (n) excitons were created at time t = o. After developing the differential equation for $P_i(n,t)$, the theorists solve the equation for $\langle i(t) \rangle$, the average number of excitons at time t, given that n excitons were created at time t = o. The fluorescence is proportional to $\langle i(t) \rangle$ and quantum yield is obtained by integrating the fluorescence over time.

It is important to remember that to this point the expressions for fluorescence $F_n(t)$, and its related quantum yield, ϕ_n/ϕ_o have been developed from $\langle i(t) \rangle$; that is these expressions are appropriate for a domain in which n excitons were created at time t = o. In an actual experiment, one can only determine the average number of excitons created at time t = o. Denoted by y, the average number of excitons created by a pulse of intensity I is given by

$$y = \sigma I \qquad (3.2.1)$$

where σ is the absorption cross section. Equation (3.2.1) is the definition of absorption cross section and reflects the fact that a pulse of intensity I which strikes many similar domains will actually create a different number of excitons in each domain. We can experimentally determine only the average number of excitons created. The probability of a particular number of excitons being created, given that the average number determined from Equation (3.2.1) is known, is best described by Poisson statistics.[3,4] The probability of having n excitons if y is the average number is,

$$P(n/y) = \frac{y^n e^{-y}}{n!} \tag{3.2.2}$$

Equation (3.2.2) describes the probability[3,4] of having n of any outcome, such as heads of a coin or excitons in a domain, when many cases are examined (flipping the coin thousands of times or looking at thousands of domains), there is only one other possible outcome (tails on the coin, the absence of an exciton in the domain) and the average number of positive outcomes (the average number of heads or excitons that will appear), is relatively small, can be determined and is denoted by y. For excitons y is determined from Equation (3.2.1), for coins y would be the number of flips of the coin multiplied by the probability of getting heads on one flip.

Because the experimental situation meets the criteria appropriate for Poisson statistics, the expressions for $F_n(t)$ and ϕ_n are then weighted by that distribution to obtain the physical observables F(t) and ϕ, as in Equation (3.2.3)

$$F(t) = \sum_{n=o}^{\infty} P(n/y)(nF_n(t))$$

$$\phi = \frac{1}{y} \Sigma\ P(n/y)(n\phi_n) \qquad (3.2.3)$$

Equation (3.2.3) describes the actual experimental condition: a certain probability exists that there will be n excitons created at time t = 0 given that y is the average number of excitons created. This probability is multiplied by the fluorescence and quantum yields, $F_n(t)$ and ϕ_n, that result in the particular situation where n excitons are created at t = o. Each product is in turn multiplied by the number of excitons n to create the weighted average. It is the weighted average of ϕ_n and $F_n(t)$ that are experimentally observed.

In developing the differential equation from which expressions for the physical observables are obtained, often called the master equation because deriving the correct results is dependent on and hence subservient to writing the correct equation, the theory makes the following four assumptions:

1. The exciton distribution randomization time is very short and is smaller than the characteristic exciton annihilation time.

2. The depletion of ground state molecules is negligible.

3. The exciton coherence time is extremely short so that memory effects can be neglected.

4. There are no active reaction centers.

The state of a particular domain is defined by the number (i) of excitons it contains at a particular time (t). These (i) excitons

decay in time by radiative and nonradiative processes. The monomolecular processes are characterized by the rate constant K, where

$$K = k_f + k_{Is} + K_D \tag{3.2.4}$$

k_f is the radiative decay constant, k_{Is} is the intersystem crossover rate constant and k_D is a nonradiative term describing the decay from the first excited singlet, S_1, to the ground state S_o.

In addition to monomolecular processes, the excitons decay through bimolecular processes. In a domain in which several excitons migrate, the most significant bimolecular deactivation process is singlet-singlet exciton annihilation. Annihilation is the interaction of two molecules, both initially in the first excited state, which results in either one or both molecules decaying to a lower triplet or the ground state. Two rate constants δ^1 and δ^2 characterize annihilation, describing the possible outcomes of the process:

$$\begin{aligned} S_1 + S_1 &\xrightarrow{\delta^1} S_1 + S_o \\ S_1 + S_1 &\xrightarrow{\delta^2} T_1 + S_o \\ & \qquad\quad T_1 + T_1 \\ & \qquad\quad S_o + S_o \end{aligned} \tag{3.2.5}$$

T_1 represents the lower triplet state.

In general, bimolecular processes cause a domain of (i) excitons to decay to a state of (i-1) or (i-2) excitons, with decay constants δ^1 and δ^2, respectively. When the number of pairwise interactions that (i) excitons can have is taken into account, the decay of an (i) state to an $(i - \alpha)$ state for $\alpha = 1,2$ is described by

$$T^{\alpha}(i \rightarrow i-\alpha) = \binom{i}{2}\delta^{\alpha} = \frac{i}{2}(i-1)\delta^{\alpha} \qquad (3.2.6)$$

T^{α} is the bimolecular decay rate resulting from one or both excitons decaying to a lower state. $\binom{i}{2}$ is the standard shorthand for the permutation of 2 particular objects in a domain consisting of (i) objects in all, and describes the number of pairwise interactions (i) excitons can undergo. α denotes whether one or both excitons decay.

The monomolecular decay rate, T^{mono}, is given by

$$T^{mono}(i \rightarrow i-1) = Ki \qquad (3.2.7)$$

where K is described in Equation (3.2.4). It describes the probability of (i) excitons decaying to (i-1) excitons due to monomolecular processes.

If $p_i(n,t)$ is the probability of (i) excitons existing at time t in a domain in which n excitons were created by a delta function excitation pulse at time t = o, the differential equation describing $p_i(n,t)$, also known as the master equation, is:

$$\frac{dp_i(n,t)}{dt} = T^{mono}(i+1 \rightarrow i)p_{i+1}(n,t) - T^{mono}(i \rightarrow i-1)p_i(n,t) + \sum_{\alpha=1,2}\left[T^{\alpha}(i+\alpha \rightarrow i)p_{i+\alpha}(n,t) - T^{\alpha}(i \rightarrow i-\alpha)p_i(n,t)\right] \qquad (3.2.8)$$

The first two terms describe the monomolecular decay. The first term is a source term, a domain of (i+1) excitons decaying to a domain containing (i) excitons. The second term, on the other hand, is the loss term caused by a domain of (i) excitons decaying to a state containing

(i-1) excitons. Similarly, the third and fourth terms describe the source and decay channels resulting from bimolecular processes in which either one or both excitons are deactivated. The (i+1) and (i+2) states feed the (i) states, while the (i) states decay to (i-1) and (i-2) states.

Substituting the expressions for T^{mono} and T^{α} from Equations (3.2.6) and (3.2.7) into Equation (3.2.8), one obtains

$$\frac{dp_i(n,t)}{dt} = K(i+1)p_{i+1}(n,t) + \delta^1 \frac{i}{2}(i+1)p_{i+1}(n,t) + \delta^2 \frac{(i+1)(i+1)}{2} \times$$

$$p_{i+2}(n,t) - [Ki + \delta^1 \frac{i}{2}(i-1) + \delta^2 \frac{i}{2}(i-1)]p_i(n,t) \qquad (3.2.9)$$

The average number of excitons is defined as:

$$\langle i \rangle = \sum_{i=1}^{n} i\, p_i(n,t) \qquad (3.2.10)$$

where $\langle i \rangle$ is the weighted average with the probability of having (i) excitons if n were initially created. Multiplying each term in Equation (3.2.9) by (i) and performing the summation, Equation (3.2.9) reduces to:

$$\frac{d\langle i \rangle}{dt} = -K\langle i \rangle - (\delta^2 + \frac{\delta^1}{2}) \langle i(i-1) \rangle \qquad (3.2.11)$$

In the case of a large domain where the exciton density can be treated as a continuous variable, $\langle i(i-1) \rangle \sim \langle i \rangle^2$. This case is identical to the Swenberg-Campillo[5,6] continuum model, and it is comforting to note that Equation (3.2.10) reduces to the equation appropriate for that model. That this identity is reflected in the physical observables will be displayed later.

As previously described, $F_n(t)$, the fluorescence profile obtained in a domain in which n excitons were initially created is proportional to <i>. When normalized to unity at t = o, the proper expression is:

$$F_n(t) = \frac{1}{n} \sum_{i=1}^{\infty} i p_i(n,t) = \frac{\langle i \rangle}{n} \qquad (3.2.12)$$

The quantum yield is obtained by integrating the fluorescence over time:

$$\phi_n = k_f \int_o F_n(t)dt \qquad (3.2.13)$$

Equations (3.2.12) and (3.2.13) correspond to a domain in which n excitons were initially created. In an actual experiment, there are many domains, each absorbing a different number of photons. Experimentally, one may only determine the mean number of excitons created per domain. This number is obtained from $y = \sigma I$ where σ is the absorption cross section of the domain and I the intensity of the excitation pulse. The probability that a given domain contains (n) excitons at t = o is described by a Poisson distribution.

The measurable physical observables are the weighted average of the fluorescence resulting from a domain initially containing (n) excitons with the probability of (n) excitons being initially created. The fluorescence and quantum yields are thus described by:

$$F(t) = \frac{1}{y} \sum_{n=o}^{\infty} \left(\frac{y^n e^{-y}}{n!}\right) [nF_n(t)]$$

$$\phi = k_f \int_o^{\infty} F(t)dt \sum_{n=1}^{\infty} \frac{1}{y} \left(\frac{y^n e^{-y}}{n!}\right) [n\phi_n] \qquad (3.2.14)$$

where the parenthesis bound the Poisson distribution of (n) excitons being created when the average number created is (y), and the brackets are the expressions accruing from a domain in which (n) excitons were initially created.

F(t) and ϕ are obtained by solving Equation (3.2.9) for $p_i(n,t)$, using Equations (3.2.12) and (3.2.13) to obtain the partial expressions and substituting those expressions into Equation (3.2.14) to obtain the actual measured quantities. Solution of Equation (3.2.9) is obtained by a standard generating function method, and the final results are:

$$F(t) = \sum_{p=0}^{\infty} A_p \, (-1)^p \exp[-(p+1)(p+r)\tau]$$

where

$$A_p = \sum_{k=p}^{\infty} \frac{(-1)^k \, k! Z^k \, (r+1+2p)}{p!(k-p)!(r+p+1)\ldots(r+p+k+1)} \qquad (3.2.15a)$$

and

$$\tau = \left(\frac{\delta^1 + \delta^2}{2}\right)t$$

$$\frac{\phi}{\phi_o} = r \sum_{k=o}^{\infty} \frac{(-1)^k Z^k}{r(r+1)\ldots(r+k)} \frac{1}{k+1} \qquad (3.2.15b)$$

ϕ_o is the fluorescence quantum yield at low intensities. The parameters used in Equations (3.2.15a) and (3.2.15b) are defined as:

$$\delta = \delta^1 + \delta^2 \quad r = \frac{2k}{\delta} \quad \varepsilon = \frac{\delta^2}{\delta} \quad Z = y(1+\varepsilon) \quad y = \sigma I \qquad (3.2.16)$$

δ is the total bimolecular rate constant due to one or both excitons decaying to a lower energy level. r is the ratio of double the mono-

molecular decay rate to the total bimolecular decay constant, and is thus related to domain size. In a large domain, the Swenberg-Campillo limit, $\delta << 2K$ because excitons have so much volume over which to migrate that monomolecular processes dominate. As a result, $r \to \infty$ corresponds to the large domain, continuum limit. On the other hand, in a small domain where the restricted confines crowd the excitons and increase the chances of annihilation, the bimolecular processes dominate, $2K << \delta$. This limit, described by $r \to 0$, is similar to the conditions assumed by Mauzerall.[7,8] Y is the average number of hits per domain, or the average number of excitons created at $t = o$. Z is therefore proportional, within a factor of two, to the number of hits per domain.

It is comforting to note that the expressions for $F(t)$ and ϕ/ϕ_o, in Equations (3.2.15a) and (3.2.15b) reduce to the expressions expected in the appropriate limits,

$$F(t) = \frac{1}{e^{kt}\left[1 + \frac{Z}{r}\right] - \frac{Z}{r}} \qquad (3.2.17)$$

$$\frac{\phi}{\phi_o} = \frac{r}{Z} \ln\left(1+\left(\frac{Z}{r}\right)\right)$$

for the continuum $r \to \infty$ limit, and

$$F(t) = \left(1 - \frac{e^{-Z}}{Z}\right) e^{-kt} \qquad (3.2.18)$$

$$\frac{\phi}{\phi_o} = \frac{1 - e^{-z}}{Z}$$

in the small domain, $r \to o$ limit. One should note that

$$_{\delta}\text{PAL-Swenberg V} = {}_{\delta}\text{Swenberg-Campillo}$$

where V is the volume of the domain, and is simply a result of the different dimensions used in the two models.

The programs used to generate the theoretical curves for F(t) and ϕ/ϕ_o use the expressions described by Equations (3.2.15a) and (3.2.15b), and are listed in the Appendix. The curves for representative values of r and z are shown in Figures 3.1 and 3.2. Table 3.1 lists the coefficients, A_p, used in the temporal fluorescence profiles for representative values of r and z. For each value of r, corresponding to a particular domain size, the fluorescence is best described by a single exponential for small values of z; the exact value of z for a single exponential fit depends on r. As z increases, for each value of r, the decay becomes more nonexponential, as expected. Examination of the theoretical curves shows the decay curves, for each value of r, is noticeably sensitive to changes in z. Quantum yield curves have basically the same shape for $r > 5$, but the shapes of the ϕ curves are sensitive to changes in r for $r < 1$. It has been shown that r = 2-5 fluorescence kinetics curves correspond to the $e^{-at^{1/2}} - kt$ decay law. We discovered that fluorescence curves for r = 0.05 to 0.5 can be fit to curves of the form $e^{-bt^{1/3}} - kt$. These relationships are displayed in Figures 3.3A and 3.3B.

As described in section 3.5, the $\sqrt{t}$ and $t^{1/3}$ decay laws can also be explained, respectively, by a three- or two-dimensional, infinite lattice containing randomly located, fluorescing molecules. To ascertain that annihilation processes are occurring, and that the

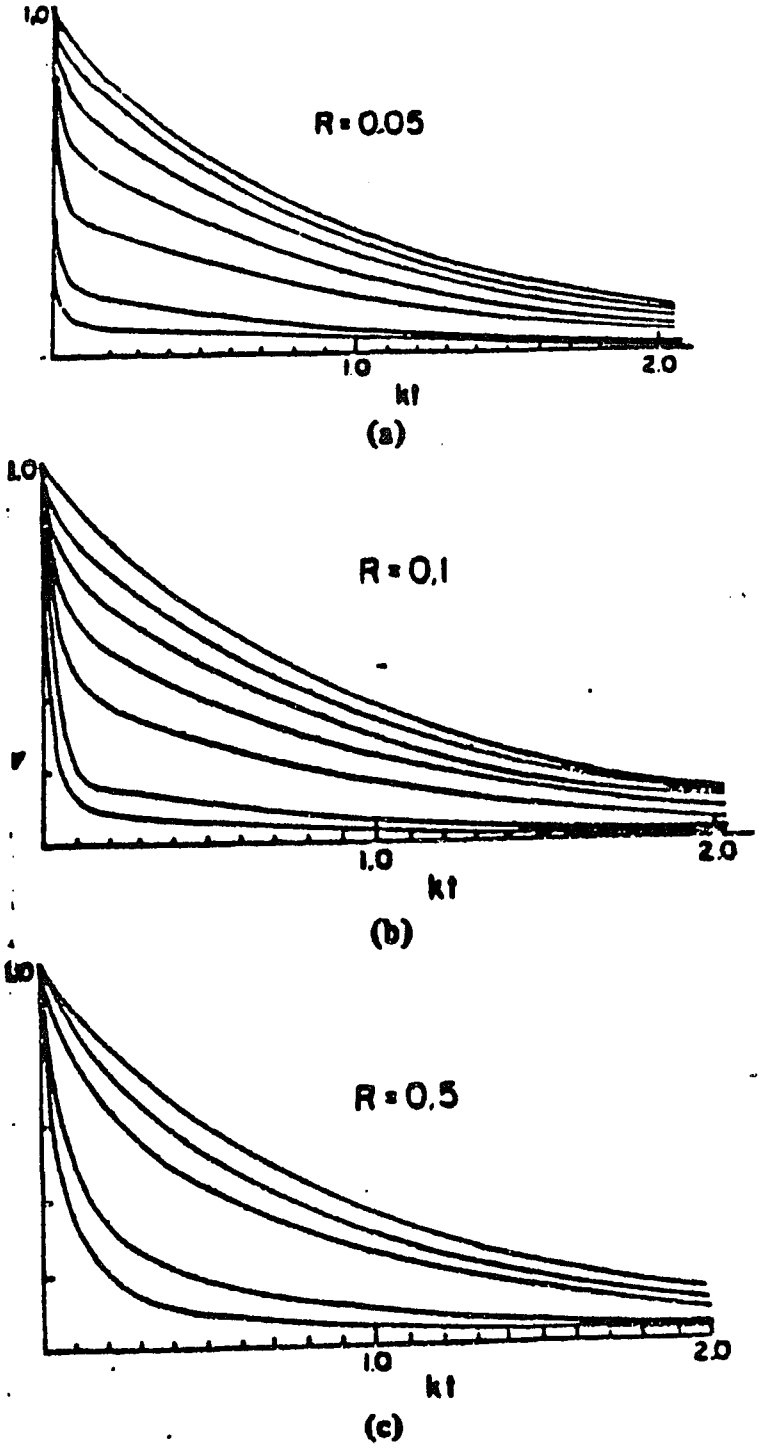

Figure 3.1: Fluorescence curves for representative values of R and Z versus Kt in annihilation theory (from Dagen et al.) In descending order: (a) r = 0.05, Z = 0.1, 0.2, 0.5, 1.0, 2.0, 5.0, 10.; (b) r = 0.1, Z = 0.005, 0.2, 0.5, 1.0, 2.0, 5.0, 10.; (c) r = 0.5, Z = 0.05, 0.5, 1.0, 5.0, 10.;

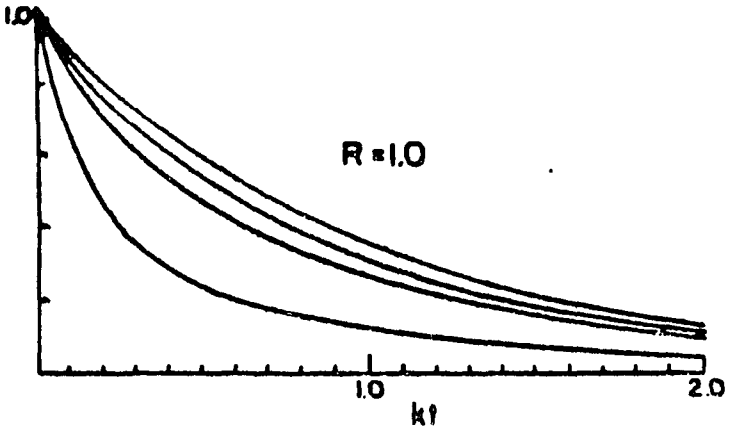

(d)

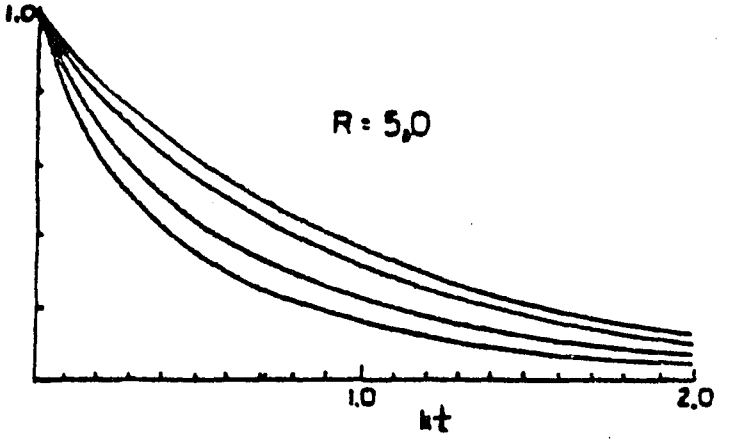

(e)

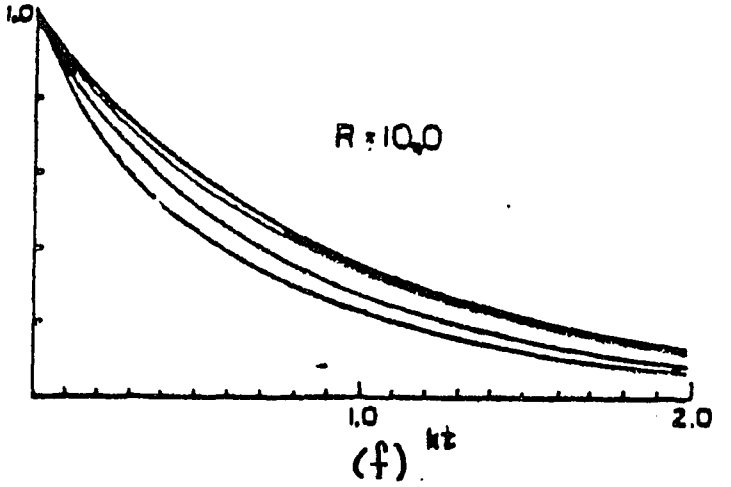

(f)

Figure 3.1: (continued): Fluorescence curves for representative values of R and Z versus Kt in annihilation theory. In descending order: (d) r = 1.0, Z = 0.05, 0.5, 1.0, 5.0;
(e) r = 5.0, Z = 0.05, 1.0, 5.0, 10.0;
(f) r = 10.0, Z = 0.05, 1.0, 5.0, 10;

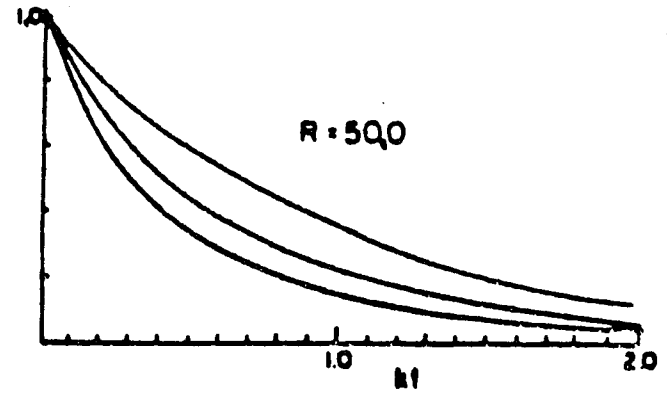

(g)

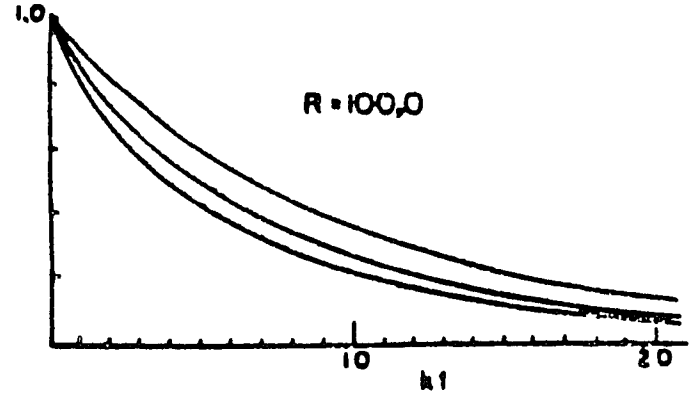

(h)

Figure 3.1 (continued): Fluorescence curves for representative values of R and Z versus Kt in annihilation theory. In descending order

(g) r = 50.0, Z = 5.0, 50.0, 100;
(h) r = 100.0, Z = 5.0, 50.0, 100.0.

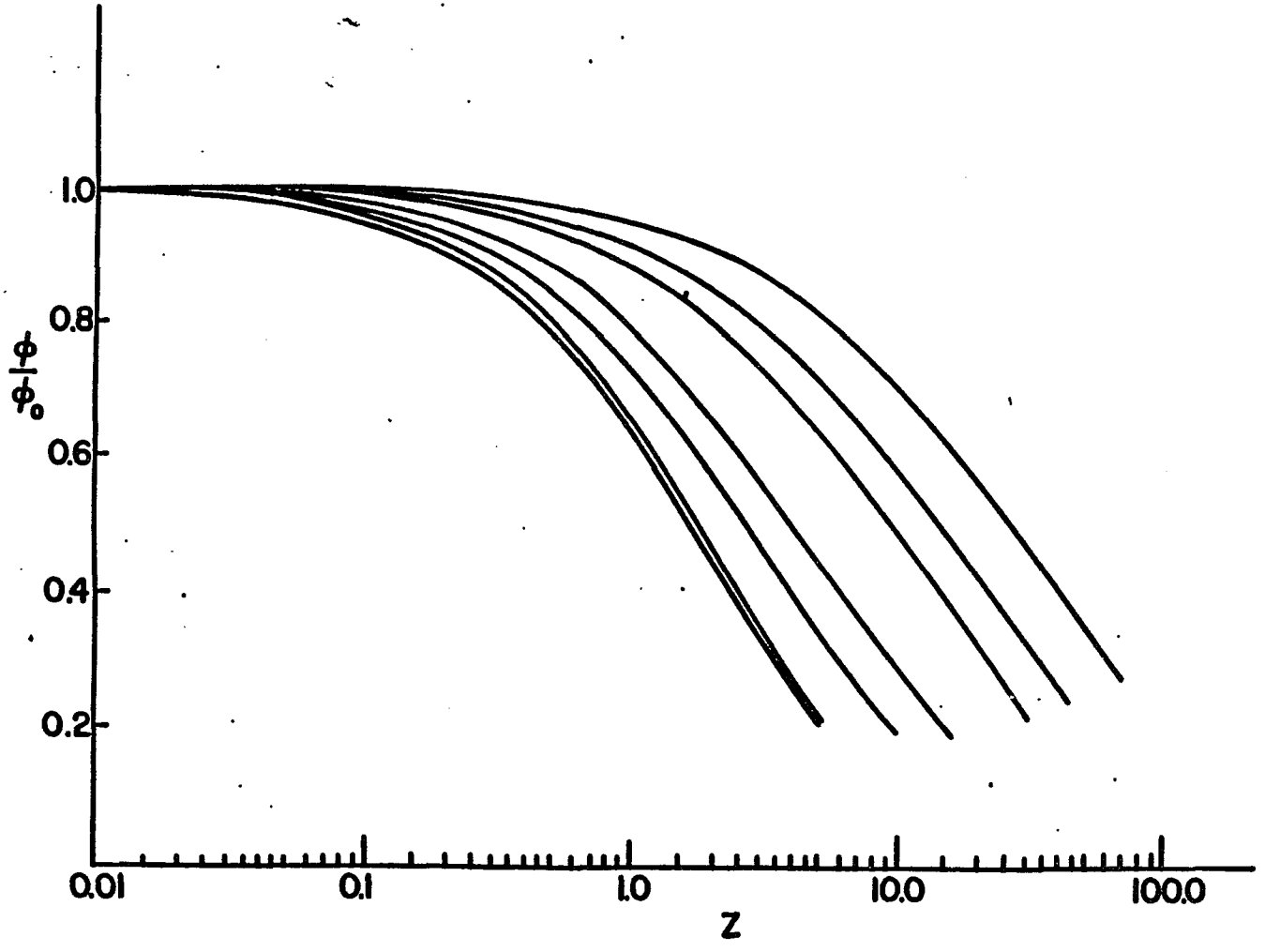

Figure 3.2: Quantum yield ϕ/ϕ_o versus number of hits Z. Curves for smaller values of r break sooner (from Dagen et al.). The curves shown are for r = 0.05, 0.1, 0.5, 1.0, 3.0, 5.0, 10.0.

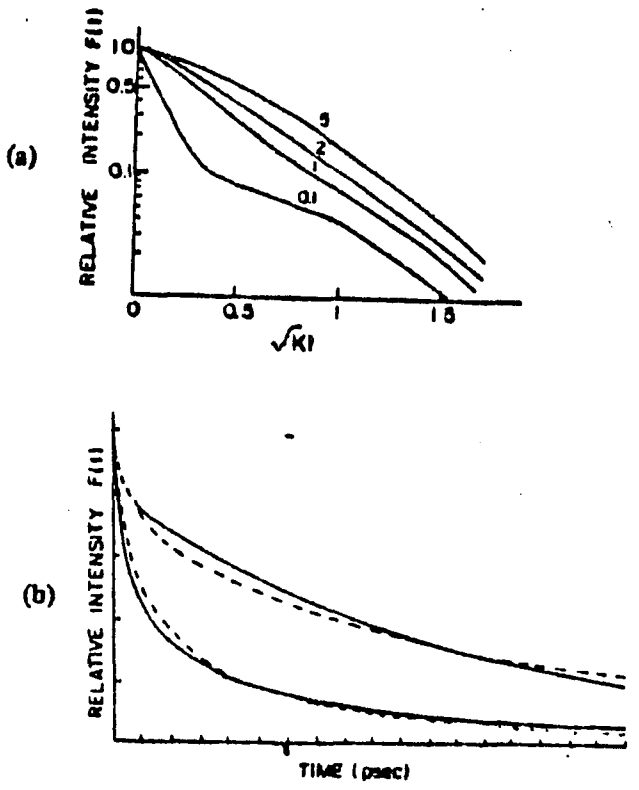

Figure 3.3A: Plot of log F(t) versus $\sqrt{kt}$ for Z = 10 and representative r values showing resemblance of r = 2-5 curves to $\sqrt{t}$ decay law.

B. Plot of annihilation theory curves (solid lines) and $F(t) = \exp(-at^{1/3} - kt)$ curves (dashed curves) versus time in picoseconds. Upper curve: Solid: r = 0.05, Z = 0.5, $k = 7.5 \times 10^8\ s^{-1}$; dashed: $a = 0.63 \times 10^3\ s^{-1/3}$, $k = 3.75 \times 10^8\ s^{-1}$. Lower curve: Solid, r = 0.5, z = 5.0, $k = 1 \times 10^9\ s^{-1}$; dashed: $a = 1.43 \times 10^3\ s^{-1/3}$, $k = 1.0 \times 10^9\ s^{-1}$.[19]

Table 3.1

Magnitude of Coefficients A_p in Expressions for F(t)

Listed Versus R and Z

R	Z	A_o	A_1	A_2	A_3	A_4	A_5	A_6
.05	.001	.9995	.0005					
.05	.100	.953	.046	.00077				
.05	.500	.792	.192	.015				
.05	1.00	.639	.305	.050	.005			
.05	5.00	.206	.365	.259	.118	.039	.011	.002
.05	10.00	.104	.242	.259	.194	.113	.054	.002
.100	.005	.9976	.0023					
.100	.100	.954	.045					
	.500	.796	.180	.065				
.100	1.0	.646	.1996	.049	.005			
.100	5.0	.213	.364	.256	.116	.099	.010	
.100	10.0	.109	.243	.258	.192	.112	.054	.02
.500	.05	.980	.02					
.500	.50	.823	.161	.013				
.500	1.00	.693	.262	.041	.004			
.500	5.00	.265	.357	.233	.101	.033	.008	
.500	10.00	.142	.254	.250	.179	.101	.047	.02
1.0	.05	.984	.016					
1.0	.50	.852	.137	.010				
1.0	1.00	.736	.228	.033	.003			
1.0	5.00	.321	.349	.208	.086	.027	.007	.001
1.0	10.00	.180	.264	.240	.163	.087	.041	.011
5.0	.05	.993	.007					
5.0	.50	.933	.064	.003				
5.0	1.0	.873	.115	.011	.001			
5.0	5.0	.569	.282	.107	.032	.008	.002	
5.0	10.0	.390	.289	.174	.087	.038	.014	

Table 3.1 Continued

R	Z	A_o	A_1	A_2	A_3	A_4	A_5	A_6
10.0	.05	.996	.004					
10.0	.50	.960	.039	.013				
10.0	1.00	.923	.073	.005				
10.0	5.0	.701	.223	.059	.014	.003		
10.0	10.0	.536	.273	.121	.047	.016	.005	.001
50.0	0.05	.999	.001					
50.0	1.0	.981	.019					
50.0	5.0	.912	.061	.007	.001			
50.0	10.0	.838	.137	.021	.003			
50.0	50.0	.507	.256	.126	.060	.028	.013	
50.0	100.0	.339	.231	.155	.102	.065	.042	.026
100.0	1.0	.9995	.0004					
100.0	5.0	.953	.045	.002				
100.0	10.0	.911	.082	.007				
100.0	50.0	.610	.222	.073	.023			
100.0	100.0	.504	.253	.126	.061	.029	.014	

Paillotin-Swenberg theory is appropriate as opposed to a different model yielding similar results, accurate quantum yield measurements must be taken in addition to obtaining the temporal decay profiles as a function of intensity. We used a PMT-integrator system to obtain quantum yield measurements. As described in the experimental section, the accuracy and simplicity of the system, which gives one the ability to take many shots in each intensity range, resulted in extremely small error bars in the measurements. Such accurate results can then be fit to the theory to find the appropriate value of r for the system, and the value of Z corresponding to a given value of I. As explained previously, Z is proportional to I and while experimental results are plotted against I, the theoretical curves are plotted against Z. After fitting the ϕ curves, the decay kinetics can be fit. The values of r and Z that fit the decay kinetics should correspond to those obtained by fitting the quantum yield measurements.

In addition, we recommend that experiments also measure transmission data vs. intensity. This insures that a drop in quantum yield is due to annihilation processes and not bleaching. We found that the apparent drop in quantum yields in our α, β, and $(\alpha\beta)$ samples was offset by an increase in transmission. This, in addition to the fact that our decay curves did not change shape with increasing intensity of the excitation pulse, led us to conclude that annihilation processes are absent in these samples. We explained the apparent drop in quantum yield to be caused by bleaching.

3.3 Small Domain Theory

Ediger and Fayer[9,10] were the first to address the problem of excited state energy transportation when the chromophores are constrained to a volume of microscopic dimensions. Use of their theory permits one to explain fluence independent nonexponential decay curves by attributing the particular shape of the curves to the effects of energy transfer in a small domain. Annihilation processes, and the attendant fluence dependent decay curves, are absent in this theory.

To understand the concept of the effect energy transfer has on fluorescence, one must remember that the intensity of fluorescence at a particular time is proportional to the number of excited state molecules at that time. As the population of these excited state molecules decreases, so does the intensity of fluorescence. As a result, the more decay channels available to a molecule, the shorter is its lifetime. For example, if the fluorescence decay rate is described by k_f, and the decay due to energy transfer by k_{et}, the total rate of decay is described by $K = k_f + k_{et}$. In the absence of energy transfer, the decay time is $\tau = k_f^{-1}$; the addition of the energy transfer decay path decreases the decay time to K^{-1}.

The problem of excited state transport in systems of molecules randomly located in solution has been the subject of extensive work. Though most of these works have assumed the extent of these systems to be infinite,[11-14] recent works by Ediger and Fayer[9-10] have pointed out the effects the finite size of a domain has on the fluorescence. In the case of a lattice, infinite or finite, where pairwise energy

transfer rates are equal, the energy rates cancel each other out, resulting in a single exponential total fluorescence decay. This can be clearly seen by example, and is discussed after Equation (3.3.19). For any particular configuration of molecules, the decay is a single exponential.

When transfer occurs between molecules randomly located in a lattice, the ensemble average of the fluorescence over all configurations must be considered. The result of the averaging of these different configurations, is a nonexponential decay. As shown in section 3.5, in the case of an infinite lattice one obtains a $t^{\Delta/6}$ decay, where Δ is the dimension of the lattice. The dimensionality comes into play, as shown in that section, because the summation, which is approximated by an integral, depends on the differential volume element at each point. This volume element is, of course, dependent on the dimension of the lattice.

In the case of an infinite lattice, only the dimension is important; the configuration surrounding each molecule is identical. In a finite volume, however, the configuration around each molecule is different. In particular, molecules near the edge of the volume have fewer numbers of neighboring chromophores than those near the center. As a result, the transport time away from the originally excited molecule averaged over all starting positions and chromophore configurations is slower than in an infinite volume of the same chromophore density. Because this channel of deexcitation of the molecule is different, the fluorescence profile from a finite lattice is distinct from that of an infinite lattice.

The model assumed in the small domain theory is a spherical volume of randomly distributed and oriented molecules. The sphere has radius R, volume Ω and N donor molecules with no traps. The configuration of the system, K, is characterized by the location of the N molecules (r_1, r_2, ... r_3). The probability $p_j(K,t)$ that the j^{th} molecule is excited at time t in configuration K, is governed by the differential equation:

$$\frac{dp_j'}{dt} = -\frac{p_j'}{\tau} + \sum_{i=1}^{N} w_{ji}[p_i'(K,t)-p_j'(K,t)] \qquad (3.3.1)$$

τ is the measured excited state lifetime, assumed to be the same for all the chromophores. w_{ji} is the transfer rate between molecules j and i ($w_{ji} = 0$). Dipole-dipole interactions are assumed, so $w_{ji} = 1/\tau(R_o/r_{ji})^6$ where R_o is the Forster radius. The first term is a loss term due to the fluorescence lifetime in the absence of energy transfer, while the second and third terms are source and loss terms, respectively, describing energy transfer to and from all the other molecules p_j. One should note that the size of the domain is not taken into account until the basic solution to this equation is integrated over the various configurations.

The transformation $p_j = p_{je}'^{-t/\tau}$ eliminates the lifetime decay term and allows Equation (3.3.1) to be rewritten as

$$\frac{d\vec{p}}{dt} = W \cdot p \qquad (3.3.2)$$

where $W_{ji} = w_{ji} - \delta_{ij} w_{i\ell} \sum_{\ell}$

$\vec{W}$ is a matrix with components w_{ji} as defined in Equation (3.3.2). This equation is solved using standard Laplace transformation techniques. The innovation of the theory is averaging the results over all possible configurations over a finite volume.

To solve the equation,[15] one takes the Laplace transform of both sides of Equation (3. .2), obtaining

$$s\vec{P}(s) - \vec{p}(o) = \vec{W}\vec{P}(s) \tag{3.3.3}$$

or

$$(s\vec{I} - \vec{W})\vec{P}(s) = \vec{p}(o) \tag{3.3.4}$$

Multiplying both sides of Equation (3.3.4) by $(s\vec{I}-\vec{W})^{-1}$ yields

$$\vec{P}(s) = (S\vec{I} - \vec{W})^{-1}\,\vec{p}(o) \tag{3.3.5}$$

where $\vec{p}(o)$ is the vector containing the initial conditions and $\bar{p}(s)$ is the Laplace transform of the solution vector describing the decay of the molecules. Taking the inverse Laplace transform of $\vec{P}(s)$ yields expressions for the decay of the molecules.

The following expression for the inverse matrix is then substituted into Equation (3.3.5).

$$(sI-W)^{-1} = \frac{\vec{B}(s)}{\det(sI-W)} \tag{3.3.6}$$

where $\det(sI-w) = d(s) = s^n - d_1 s^{n-1} - d_2 s^{n-2} \ldots\ldots - d_n$

$$\vec{B}(s) = \vec{B}_o s^{n-1} + \vec{B}_1 s^{n-2} + \ldots \vec{B}_{n-2} s + \vec{B}_{n-1} \tag{3.3.7}$$

and

$$\vec{B}_o = \vec{I}$$

$$\vec{B}_1 = \vec{W}-d_1\vec{I}$$

$$\vec{B} = \vec{W}\vec{B}_1-d_2\vec{I}$$

$$\vec{B}_k = WB_{k-1}-d_k\vec{I}$$

Substituting Equations (3.3.6) to (3.3.8) into Equation (3.3.5) yields the Laplace transform of the solution. The solution is given by

$$\vec{P}(s) = \tilde{G}(s,N,\Omega,r,r')p(o) \qquad (3.3.9)$$

where p(o) is the initial conditions vector and $\tilde{G}(s,N,\Omega,r,r')$ is the Laplace transform of the Green's function of the system. The diagonal terms of G are called $\tilde{G}^s$ and the off diagonal terms are called $\tilde{G}^m$. $\tilde{G}^s$ is related to the probability that the excitation is on the originally excited molecule. The finite volume of the domain has still not been considered.

To further appreciate $\tilde{G}^s$ and $\tilde{G}^m$, we will define the Green's function from another approach and use a simple example of the two molecules to illustrate their significance. The solution to Equation (3.3.2) is

$$\vec{p}(t) = e^{t\vec{W}}\vec{p}(o)$$

where again, $\vec{p}(t)$ is the column vector containing the solution and $\vec{p}(o)$ is the column vector containing the initial conditions of the system. The Green's function of the system is defined as follows.

If $P(N,\Omega,r,t)$ is the ensemble average density of excitations then

$$P(N,\Omega,r,t) = \int dr' G(N,\Omega,r,r',t)\ P(N,\Omega,r',o) \tag{3.3.11}$$

where

$$G(N,\Omega,r,r',t) = G^{s}(N,\Omega,r,r',t) + G^{m}(N,\Omega,r,r',t) \tag{3.3.12}$$

$$G^{s}(N,\Omega,r,r',t) = \Omega\langle\delta(r_1-r)\ \delta(r_1-r')[\exp(tW)_{11}]\rangle \tag{3.3.13}$$

$$G^{m}(N,\Omega,r,r',t) = (N-1)\Omega\langle\delta(r_2-r)\delta(r_1-r')[\exp(tW)_{12}]\rangle \tag{3.3.14}$$

The brackets indicate the ensemble average

$$\langle A(K)\rangle = \frac{1}{\Omega^{n}} \int_{\Omega} dr_1 \ldots \int_{\Omega} dr_n\ A(K) \tag{3.3.15}$$

As before, $G^{s}(N,\Omega,r,r',t)$ is the term that appears on the diagonal of the solution matrix. $G^{m}(N,\Omega,r,r',t)$ are the off diagonal terms. One then defines $G^{s}(N,\Omega,t)$ by:

$$G^{s}(N,\Omega,t) = \frac{1}{\Omega} \int dr \int dr'\ G^{s}(N,\Omega,r,r',t) \tag{3.3.16}$$

One obtains after integrating over both spatial variables $G^{s}(N,\Omega,t)$. Because this term is from the diagonal of the solution matrix it is the

probability that the excitation is on the originally excited molecule at time t. Similarly, integrating $G^m(N,\Omega,r,r',t)$ over the spatial coordinates gives the probability that the excitation is not on the originally excited molecule. Though defined by Equation (3.3.13) $G^s(N,\Omega,r,r',t)$ is more easily obtained by taking the inverse Laplace transform of the diagonal terms of $G(s,N,\Omega,r,r')$ in Equation (3.3.9). In either case, the effect of the small domain comes into play in Equation (3.3.16) where the integration is over the volume of interest. It is helpful to remember that up to the integration, the small domain theory is a standard approach to the solution of a system of basic rate equations. Its uniqueness is in the integral used to average the fluorescence over all configurations in the domain.

A further understanding of G^s and G^m may be obtained by looking at Equation (3.3.2) for the simple case of two molecules. In this case, Equation (3.3.2) can be written as

$$\frac{d\begin{pmatrix} p_1(t) \\ p_2(t) \end{pmatrix}}{dt} = \begin{pmatrix} -w_{12} & w_{12} \\ w_{12} & -w_{12} \end{pmatrix} \begin{pmatrix} p_1(o) \\ p_2(o) \end{pmatrix} \qquad (3.3.17)$$

Where $p_i(t)$ describes the decay of the i^{th} molecule and $p_i(o)$ is the initial condition of the i^{th} molecule. Solving the differential equation by using equations (3.3.5) to (3.3.8) and taking the inverse Laplacian of Equation (3.3.9), one obtains:

$$\begin{pmatrix} P_1'(t) \\ \\ P_2'(t) \end{pmatrix} = e^{-t/\tau} \begin{pmatrix} \frac{1}{2} + \frac{1}{2} e^{-2w_{12}t} & \frac{1}{2} - \frac{1}{2} e^{-2w_{12}t} \\ \\ \frac{1}{2} - \frac{1}{2} e^{-2w_{12}t} & \frac{1}{2} + \frac{1}{2} e^{-2w_{12}t} \end{pmatrix} \begin{pmatrix} P_1'(o) \\ \\ P_2'(o) \end{pmatrix} \tag{3.3.18}$$

Here the transformation $p_j = p_j e^{t/\tau}$ has been used to put back the effect of the fluorescence decay of both molecules. By definition, G^s is the diagonal terms and G^m the off diagonal terms. Hence

$$G^s = \frac{1}{2} + \frac{1}{2e^{-2w_{12}t}} \tag{3.3.19}$$

$$G^m = \frac{1}{2} - \frac{1}{2e^{-2w_{12}t}}$$

Because $G^s(t)$ appears on the diagonal of the solution matrix, it describes the probability of the initially excited molecule retaining its excitation at time t. The small domain aspect of the theory comes into play when the expressions in Equation (3.3.19) are integrated for the various configurations over the finite volume. An examination of the total solution of Equation 3.3.18, shows that the total fluorescence, $p_1(t) + p_2(t)$, for this particular configuration is a single exponential. This is a simple illustration of the previously stated claim that the total fluorescence for a particular configuration is a single exponential.

In actuality, expressions like Equation (3.3.19) are not integrated over the finite volume. It is easier to deal with the Laplace transform, $\tilde{G}^s(N,\Omega,r,r',s)$, integrate over the finite volume and

then use an algorithm[16] to numerically calculate the inverse Laplace transform to obtain $G^s(N,\Omega,t)$. If one uses Equations (3.3.5) to (3.3.8) to get the inverse Laplace of G^s as defined in Equation (3.3.9), one obtains

$$G_s(N,\Omega,s) = \frac{1}{s} - \frac{N-1}{\Omega^2} \int_\Omega dr_1 \int_\Omega dr_2 \frac{w_{12}}{s(s+2w_{12})} - \frac{(N-1)(N-2)}{2\Omega^3} \int d^3r \tag{3.3.20}$$

$$\left[\frac{sw_{12} + w_{12}w_{13} + w_{13}w_{23} + w_{12}w_{23}}{s[s^2 + 2s(w_{12} + w_{13} + w_{23}) + 3(w_{12}w_{13} + w_{12}w_{23} + w_{13}w_{23})]} - \frac{w_{12}}{s(s + 2w_{12})} \right]$$

where the particles are labeled 1, 2, 3. One should again note that the terms in the integral are the diagonal terms appearing in the matrix in Equation (3.3.9). The integrations are taken over the finite volume Ω.

Neither of the integrals in Equation (3.3.20) can be performed analytically. Both integrals can be solved numerically as functions of a one dimensional parameter $\beta = \left(\frac{R}{R_o}\right)^3 \frac{\sqrt{st}}{2}$. The results of the numerical integration results in Equation (3.2.20) being written as:

$$\tilde{G}^s(N,\beta,s)_L = \frac{1}{s} \left[1 - \frac{N-1}{(\sqrt{2})\beta} f_2(\beta) + \frac{(N-1)(N-2)}{2\beta^2} f_3(\beta) \right] \tag{3.2.21}$$

The functions $f_2(\beta)$ and $f_3(\beta)$ contain the solutions to the numerical integration. They can be fit to analytical functions using a polynominal fitting routine. These analytical functions aid in performing the numerical inverse Laplace transform of $\tilde{G}^s(N,\beta,s)$. The effects of the finite volume are contained in $f_2(\beta)$ and $f_3(\beta)$.

Equation (3.3.21) is the exact solution for three or less particles, and a reasonable solution for more particles. It can be shown that the exact solution for a large number of particles is:

$$\tilde{G}^s(N,\beta,s) = \frac{1}{s} /\{1 + \frac{C_D}{\sqrt{s\tau}} (1 - \frac{1}{N}) f_2(\beta) + \frac{C_D^2}{s\tau} (1 - \frac{1}{N}) [(1 - \frac{1}{N}) (f_2(\beta))^2 - (1 - \frac{2}{N}) f_3(\beta)]\} \qquad (3.3.22)$$

where $C_D = N(\frac{R_o}{R})^3$. It has been shown that the small domain theory reduces to the expected results when the dimensions are assumed to be infinite.

The expressions for $f_2(\beta)$ and $f_3(\beta)$ appear in the appendix. These expressions were substituted in Equation (3.3.22) and an algorithm[16] to numerically compute the inverse Laplace transform was used to compute $G^s(N,\beta,t)$. This algorithm also appears in the appendix. The values of $G^s(N,\beta,t)$ were used, as explained in the research section of the dissertation, in the expression developed in the next section to explain the decay curves of the α, β, and $(\alpha\beta)$ units.

3.4 Geometry of Small Domain Theory

Depolarization[17,18] of the fluorescence occurs in the small domain theory because a fluorescent molecule, which absorbs light at time t, transfers its excitation to other fluorescent molecules whose emission dipoles are randomly oriented. The net result is of a rotation, in time, of the transition dipole of the fluorescing molecule.

As shown in Figure 3.4, the experimental conditions consist of a fluorescent molecule placed at the origin of the fixed coordinate system x, y, z. The exciting light travels along the x axis, polarized in the z direction. The fluorescence, polarized along the z axis, (I_{11} (t)), and along the x axis, (I_{+} (t)), are observed along the y axis. The u is the transition dipole of the fluorescent molecule and its orientation molecule and its orientation to the x, y, z axes are defined by (θ,ϕ). The absorption and emission dipoles are assumed to be parallel. The expressions for I_{+} (t) and I_{11} (t), as well as I_{+} (t) + I_{11} (t) which is the observed fluorescence in the absence of polarizers, may be obtained by the following argument.

For any one particular orientation of the molecules, the observed fluorescence is:

$$J_{11} = P(t)(u.\hat{z})^2 = u^2\cos^2\theta P(t)$$
$$J_{+} = P(t)(u.\hat{x})^2 = u^2\sin^2\theta P(t) \qquad (3.4.1)$$

where P(t) is the fluorescence decay law for the molecule. We are, however, interested in looking at the fluorescence from many samples whose dipoles are randomly oriented averaged over all possible initial configurations. Taking into account the average over all orientations, of the dipole.

$$I_{11} = \int\int \sin\theta d\theta d\phi J_{11}(\theta,\phi)\ W(\theta,\phi,t)$$
$$I_{+} = \int\int \sin\theta d\theta d\phi J_{+}(\theta,\phi)\ W(\theta,\phi,t) \qquad (3.4.2)$$

where $W(\theta,\phi,t)$ is the probability that the transition dipole is oriented along θ and ϕ at time t. This probability, $W(\theta,\phi,t)$ however, arises by averaging the probability of a dipole aligning along (θ,ϕ), given a certain initial configuration, over all possible <u>initial</u> configurations. In short,

$$W(\theta,\phi,t) = \int_0^{2\pi} d\phi_o \int_0^{\pi} \sin\theta_o d_o\theta_o W(\theta_o\phi_o)G(\theta_o\phi_o|\theta,\phi,t) \qquad (3.4.3)$$

where $W(\theta_o\phi_o)$ is the initial (t = o) distribution of the orientations of u and $G(\theta_o\phi_o|\theta,\phi,t\}$ is the evolution function of $W(\theta_o,\phi_o,t)$. That is, if u is oriented at (θ_o,ϕ_o) at t = o, then $G(\theta_o\phi_o|\phi,\theta,t)$ is the probability it will be oriented at (θ,ϕ) at time t.

Since the probability of a photon polarized along z being absorbed by a dipole u at time t = o is proportional to $(u.z)^2 \sim u^2\cos^2\theta$, and $W(\theta_o\phi_o) \sim A\cos^2\theta_o$, the normalized initial distribution is

$$W(\theta_o\phi_o) = \frac{3}{4\pi}\cos^2\theta_o = \frac{1}{4\pi}(1 + 2P_2(\cos\theta_o)) \qquad (3.4.4)$$

where P_2 is the Legendre polynomial of order 2.

If one expands $G(\theta_o\phi_o|\theta\phi t)$ in terms of surface harmonics:

$$G(\theta_o\phi_o|\theta,\phi,t) = \sum_{\ell=o}^{\infty} \sum_{m=-\ell}^{\infty} C_{\ell m}(t)\, Y_{\ell m}(\theta_o\phi_o)Y_{\ell m}(\theta\phi) \qquad (3.4.5)$$

with boundary condition

$$G(\theta_o\phi_o|\theta,\phi,o) = \delta(\cos\theta - \cos\theta_o)\delta(\phi-\phi_o) = \sum_m \sum_\ell Y_{\ell m}(\theta_o\phi_o)Y_{\ell m}(\theta\phi) \qquad (3.4.6)$$

one obtains

$$C_{oo}(t) = 1 \text{ for all } t \qquad (3.4.7)$$

$$C_{\ell m}(o) = 1 \text{ for all } \ell, m$$

Substituting Equations (3.4.4) and (3.4.5) into Equation (3.4.3) subject to the constraints of Equation (3.4.7) and using orthonormality relations, one obtains

$$W(\theta,\phi,t) = \frac{1}{4\pi}\left[1 + 2C_{20}(t)\ P_2(\cos\theta)\right] \qquad (3.4.8)$$

$W(\theta,\phi,t)$ is the probability that $\vec{u}$ is oriented along a particular θ, ϕ at time t. Equation (3.4.6) is the expression for the fluorescence from this particular orientation. To obtain the observed fluorescence, however, one must average over all possible final configurations as in Equation (3.4.2).

Substituting Equation (3.4.8) and Equation (3.4.1) into Equation (3.3.2) and using orthonormality relations one obtains:

$$\begin{aligned} I_{11} &= \left(\frac{1}{3} + \frac{4}{15} C_{20}(t)\right) P(t) \\ I_{+} &= \left(\frac{1}{3} - \frac{2}{15} C_{20}(t)\right) P(t) \end{aligned} \qquad (3.4.9)$$

Equation (3.4.9) can be rewritten as

$$\begin{aligned} I_{11} &= \frac{1}{3}\left(1 + \frac{4}{5} C_{20}(t)\right) P(t) \\ I_{+} &= \frac{1}{3}\left(1 = \frac{2}{5} C_{20}(t)\right) P(t) \end{aligned} \qquad (3.4.10)$$

and then

$$I_{11} = \frac{1}{3}\,(1 + 2\tilde{C}_{20}(t))\;P(t)$$
$$I_{+} = \frac{1}{3}\,(1 - \tilde{C}_{20}(t))\;P(t) \qquad (3.4.11)$$

where $\tilde{C}_{20}(t) = C_{20}(t)$ and

$$C_{20}(t) = \langle P_2[\hat{u}(o)\;\hat{u}(t)]\rangle = \frac{1}{4\pi}\int d\Omega \int d\Omega_o\; P_2(u(o)\cdot u(t))\; W(\theta_o \phi_o)\,|G(\theta_o \phi_o\,|\theta\phi t) \qquad (3.4.12)$$

In Equation (3.4.12) $\vec{u}(t)$ is the direction vector of the transmission dipole at time t.

To obtain the final expressions for $I_{11}(t)$ and $I_{+}(t)$, one defines $\tilde{C}_{20}(t) = kG_s(N,\Omega,t)$. This definition may be understood by examining Equations (3.4.5) and (3.4.8). The term $C_{20}(t)$ is the first term related to the angular rotation of the transition dipoles. The theory makes the simple assumption that this term is proportional to the probability that the excitation is on the initially excited molecule which is, in essence, the source of these rotated dipoles.

The final expressions for $I_{11}(t)$ and $I_{+}(t)$, are

$$I_{11} = e^{-t/\tau}\;[1 + 2kG_s(N,\Omega,t)] \qquad (3.4.13)$$

$$I+ = e^{-t/\tau}\;[1 - kG_s(N,\Omega,t)]$$

where P(t), the molecule decay law is assumed to be a simple exponential.

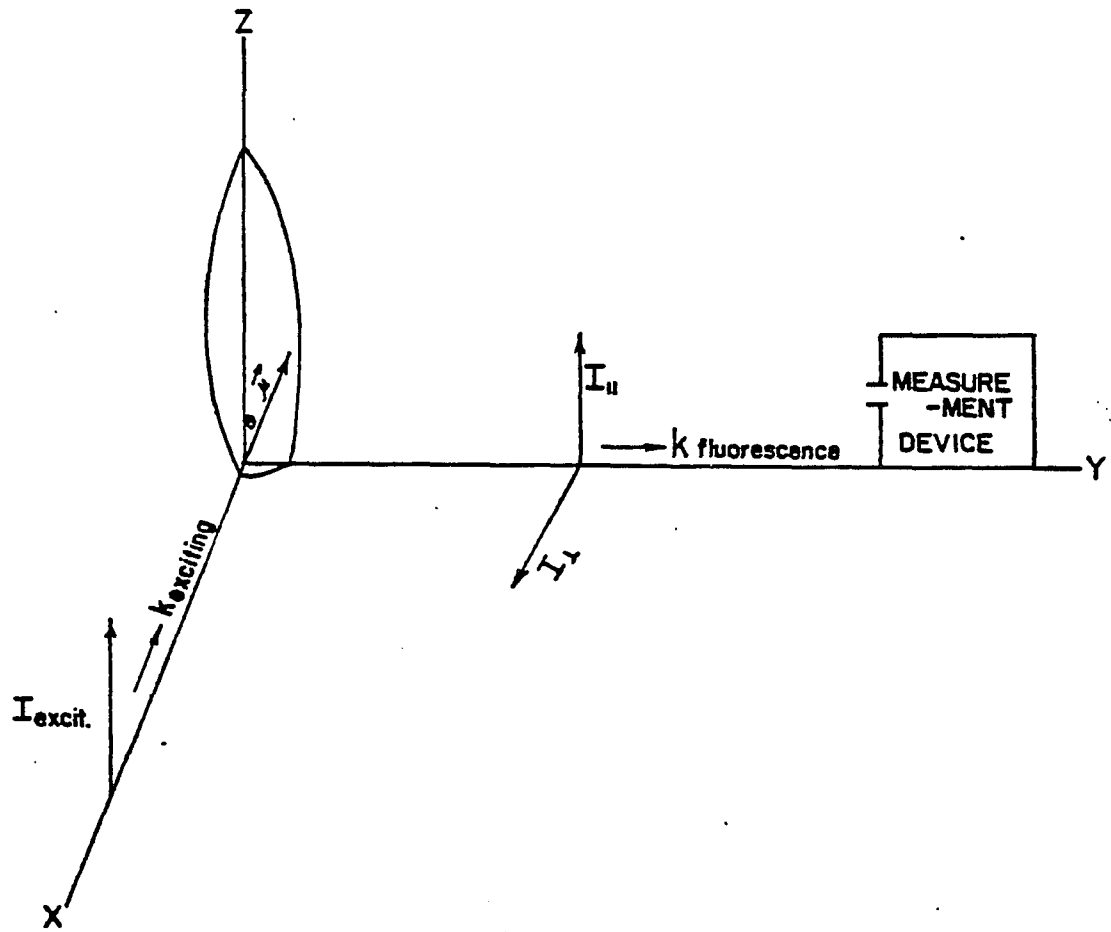

Figure 3.4: Geometry of Polarization Experiment.

In our experimental setup, we took measurements without polarizers. To obtain the correct expressions for the physical observables in that case, one notes that if a polarizer is set at some arbitrary angle α from the direction of parallel polarization, the observed fluorescence is:

$$I_{\alpha}(t) = \cos^2\alpha I_{11}(t) + \sin^2\alpha I_{+}(t) \qquad (3.4.14)$$

In the absence of polarizers, one averages over all possible angles to obtain the observed fluorescence:

$$I(t) = \frac{1}{2}(I_{11}(t) + I_{+}(t)) \qquad (3.4.15)$$

3.5 Energy Transfer to Randomly Distributed Acceptors--Infinite Domain

Many papers[1,2,11,14] dealing with energy transfer in photosynthetic systems note that the decays can be fit to a $e^{-at\Delta/6-kt}$ decay law, for $\Delta = 1,2,3$ corresponding to the dimension of the domain over which energy transfer occurs. Such decays are expected from a system consisting of a single, fluorescing donor surrounded by acceptor molecules in an infinite domain. The donor decays by two independent processes: transfer to acceptors or fluorescing. For at least two major reasons discussed later, including the small sizes of our samples and the lack of a single donor in a sea of nonfluorescing moieties, we discounted the use of this theory. We also feel it is frequently inappropriately applied in other systems, similar to our own. Its

frequent appearance, in the literature, however, prompts us to note its existence, describe its derivations and discuss its limitations.

The decay of an excited donor surrounded by acceptor molecules can occur either by the donor transferring its excitation to an acceptor or by the donor undergoing radiative or radiationless decay processes. The two decay channels are independent, allowing one to express the time evolution of decay into the product.

$F(t) = \phi(k_n,t)e^{-t/\tau_D}$ where τ_D is the donor specific decay rate and ϕ the decay function due to transfer of energy to the acceptors.

If a particular acceptor configuration K_n is characterized by n acceptors occupying the sites i_1 .... i_n of the host lattice, then

$$\phi(K_n,t) = \prod_{d=K_n} E_j(t) \qquad (3.5.1)$$

where E_j describes the decay of the donor excitation due to energy transfer to the acceptor site at j. For multipolar interactions,

$$E_j(t) = \exp\left[-(t/\tau)\left(\frac{d}{R_j}\right)s\right]$$

where s = 6 for dipole-dipole interactions and d is the nearest neighbor distance.

One may rewrite Equation (3.5.1) as

$$\phi(K_n,t) = \prod_{i=1}^{N} (1 - \Delta_i^n \ (1 - E_i(t))) \qquad (3.5.2)$$

where N is the number of lattice sites and

$$\Delta_i^n = \begin{cases} 1 & \text{if } i \in K_n \\ 0 & \text{else} \end{cases} \tag{3.5.3}$$

If p is the possibility of one of the N lattice sites being occupied by an acceptor, one can easily verify that $\langle \Delta_i^n \rangle = p$ and, hence,

$$\phi(p,t) = \prod_{i=1}^{N} (1 - p + pE_i(t)) \tag{3.5.4}$$

where again,

$$E_i = \exp\left[-\left(\frac{t}{\tau}\right)\left(\frac{d}{R_o}\right)s\right] \tag{3.5.5}$$

To evaluate ϕ one takes the natural logarithm of both sides, obtaining:

$$\ell n\phi(p,t) = \sum \ell n\{1 - p[1 - e^{-\left(\frac{t}{\tau}\right)\left(\frac{d}{R_j}\right)s}]\} = \sum_{k=1}^{\infty} \frac{p^k}{k} S_k(t) \tag{3.5.6}$$

where

$$S_k(t) = \sum_i \left[\left(1 - e^{-(t/\tau)\left(\frac{d}{R_j}\right)^s}\right)\right]^k \tag{3.5.7}$$

Because an infinite lattice is assumed, one can, in the continuum approximation evaluate S_k by converting the sum into the appropriate integral for one, two or three dimensions.

$$\Sigma h(R_i) \rightarrow \begin{cases} 2p \int_0^\infty h(R)dR & 1 \text{ dim} \\ 2\pi\rho \int_0^\infty h(R)Rdr & 2 \text{ dim} \\ 4\pi\rho \int_0^\infty h(R)R^2dr & 3 \text{ dim} \end{cases}$$

where p is the density of lattice points in the lattice considered; generally $p^{-1} = ud^{\Delta}$ where Δ is the dimension, d the nearest neighbor distance and u a number on the order of unity.

Evaluation of the integrals is clearly dependent on the dimensions of the lattice, and one obtains, to first approximation:

$$\phi(p,t) = \exp\left[-d^{\Delta}V_{\Delta}\ p\ \Gamma(1 - \tfrac{\Delta}{s})\ p\ (\tfrac{t}{\tau})^{\Delta/s}\right] \qquad (3.5.9)$$

or, taking into account the donor specific decay, $\frac{e^{-t/\tau_D}}{\tau}$

$$F(t) \sim \exp\left[-at^{\Delta/s} - \frac{t}{\tau_D}\right] \qquad (3.5.10)$$

For Forster interactions, s = 6 and the decays are $t^{1/6}$, $t^{1/3}$ and $t^{1/2}$ for one, two and three dimensions, respectively. The coefficient a is proportional to the volume of the surface in Δ dimension space, V_{Δ}, and the probability of a particular lattice site being occupied, p. It is comforting to note that as the dimension increases, the decay lifetime decreases due to the increase in both a and t ($t^{1/2}$ decay is faster than $t^{1/3}$ decay). As dimension increases, there are more acceptors to which the donor can transfer energy (for the same density). Because there are more avenues for deactivation of the excited state population, the decay lifetime decreases more rapidly. For the same reason, the lifetime decreases when the probability of a lattice site being occupied, p, increases.

As pointed out previously, the r = 2-5 curves in the Paillotin-Swenberg theory can be fit to a $t^{1/2}$ decay. In our research, we found

a relationship between the r = 0.05 to r = 0.5 curves and a $t^{1/3}$ decay. One should point out that the results derived in this section assume that the decay rates $(d/R_j)^s$ and thus the acceptor concentration and distances R_j remain constant in time. When singlet-singlet annihilation occurs, however, neither R_j nor the concentration of quenchers remains constant in time. The fact that the same decay kinetics can be described by mutually exclusive models, necessitates determining other experimental parameters to attempt to determine which model is appropriate.

We used transmission and relative quantum yield data to determine that exciton annihilation processes do not occur in the α, β and (αβ) subunits of PE. We then discounted the theory presented in this section because it assumes an infinite domain. In the case of the α, β, and (αβ) subunits, the dimensions of the sample are on the order of R_o, the Forster radius. It is specifically for these dimensions that the finite size of the domain is most pronounced. Examination of theoretical curves generated by Ediger and our laboratory indicates that a domain should not be approximated by the infinite results until its radius is at least ten times R_o ($R/R_o \geq 10$). Assuming R_o = 20-30 Å, one could not use the $t^{\Delta/s}$ time decays in a unit smaller than the hexamer. Another factor mitigating against the use of the $t^{\Delta/s}$ dependence is it derives from a model of one fluorescing donor transferring energy to a sea of nonfluorescing acceptors. Our data, and those of other investigators, suggest the possibility of more than one chromophore fluorescing. In addition, even those who postulate that only one chromophore fluoresces in these samples (denoted by 'f')

contend that it is the other nonfluorescing chromophores (denoted by 's') that transfer energy to the 'f' chromophore. This concept of $s \rightarrow f$ transfer is not accounted for in the $t^{\Delta/6}$ model which assumes the reverse energy pathway: a fluorescing donor transferring energy to nonfluorescing acceptors.

3.6 Summary

This chapter has presented the theories considered germane to the study of the picosecond fluorescence kinetics from photosynthetic algae. As will be seen in the following chapters, the fluence independent decays and transmission data offsetting the apparent decrease in quantum yield of the α, β and $(\alpha\beta)$ samples led us to conclude that annihilation processes are absent in these units. All the fluorescence kinetics could be fit by multi-exponential expressions. Such expressions are appropriate for chromophores in different environments fluorescing at distinct decay rates. We were intrigued by the fitting of our data to reasonable parameters of the small domain theory. As discussed in the research section, the small domain theory's assumption of a random distribution of chromophores apparently conflict with the geneticists' expectations that the distances between chromophores will be found to be the same from sample to sample. They base this on the biological fact that the chromophores are bound to definite amino acids in the protein. Though the assumption of fixed distances of the chromophores follows logically from previous experience, we stress that x-ray crystallography has yet

to be done on our samples. Not until such studies are made will the exact distances between chromophores, and whether they actually are, as expected, fixed be determined. As we will also see, the data can be fit to models assuming fluorescing 's' and 'f' chromophores with energy transfer occurring from the 's' to the 'f' moieties. These models are discussed in detail in the following chapters.

Notes

1. Paillotin, G., Swenberg, C. E., J. Breton, & Geacintov, N. E. (1979). Biophys. J., 25, 513.

2. Swenberg, C. E., Geacintov, N. E., & Pope, M. (1976). Biophys. J., 16, 1447.

3. Hogg, Robert V., & Craig, Allen T. (1978). Introduction to Mathematical Statistics, 4th ed. New York: Macmillan Publishing Co., Inc.

4. Melissinos, Adrian C. (1966). Experiments in Modern Physics. New York: Academic Press.

5. Swenberg, C. W., & Geacintov, N. E. (1973). In J. B. Birks, Ed., Organic Molecular Photophysics. Sussex, England: J. Wiley & Sons, Ltd.

6. Campillo, A. J., Shapiro, S. L., Kollman, V. H., Winn, K. R., and Hyer, R. C. (1977). Biophys. J., 16, 93.

7. Mauzerall, D. (1976). Biophys. J., 16, 87.

8. Mauzerall, D. (1976). J. Phys. Chem., 80, 2306.

9. Ediger, M. D., & Fayer, M. D. (1983). J. Chem. Phys., 78(s), 2518.

10. Ediger, M. D., Domingue, R. P., & Fayer, M.D. (1984). J Chem. Phys., 80(3), 1246.

11. Hahn, Steven W., & Zwansig, Robert (1978). J. Chem. Phys., 68, 1879.

12. Huber, D. L. (1979). Phys. Rev., B20, 2307, 5333.

13. Gochanour, C. R., Andersen, H. C., & Fayer, M. D. (1979). J. Chem. Phys., 70, 4254.

14. Blumen, A., & Manz, J. (1979). J. Chem. Phys., 71, 4694.

15. Dorf, Richard C. (1981). Modern Control Systems. Reading, MA: Addison-Wesley Publishing Co.

16. Stehfest, H. (1970). Commun. Assoc. Comput. Mach., 13, 47.

17. Tao, T. C. C. Doctoral dissertation.

18. Fleming, G. R., Morris, J. M., & Robinson, G. W. (1976). Chemical Physics, 17, 91.

19. Dagen, A. J., Alfano, R. R., & Swenberg, C. E. (1984). IEEE Journal of Quantum Electronics, QE-20(12), 1496.

Chapter 4

ANALYSIS OF FLUORESCENCE KINETICS AND ENERGY TRANSFER IN ISOLATED α SUBUNITS OF PHYCOERYTHRIN FROM NOSTOC sp.

In this chapter, the fluorescence decay profiles, relative quantum yield, and transmission of the phycoerythrin α subunit, isolated from the photosynthetic antenna system of Nostoc sp., and measured by single picosecond laser excitation is presented. The fluorescence decay profiles are found to be intensity independent for the intensity range investigated (4×10^{13} and 4×10^{15} photons-cm^{-2} per pulse). The decay profiles are fitted to a simple model assuming both chromophores absorb and fluoresce. The inferred total deactivation rates for the two chromophores, in the absence of energy transfer and when the effects of the response time of the streak camera and the finite pulse width are properly included, are 1.0×10^{10} s^{-1} and 1.0×10^{9} s^{-1} for the s and f chromophores, respectively, whereas the transfer rate between the two fluorophores is estimated to be 1.0×10^{10} s^{-1} giving an s → f transfer time on the order of 100 ps. Steady-state polarization measurements are found to be equal to those calculated using the rate parameters inferred from the kinetic model fit to the fluorescence decays. The apparent decrease in the relative fluorescence quantum yield and increase of the relative transmission with increasing excitation intensity is suggestive of ground state depletion and upper excited state absorption. Evidence suggests that

exciton annihilation is absent within isolated α subunits for the intensity range investigated (4×10^{13} to 4×10^{15} photons-cm^{-2} per pulse).

4.1 Introduction

Photosynthetic organisms have evolved a number of light harvesting antenna systems for the primary purpose of absorbing sunlight and transferring the absorbed energy to reaction centers. In red and blue-green algae, the light-harvesting system consists of an aggregation of phycobiliproteins, namely phycoerythrin, phycocyanin, and allophycocyanin, which collectively form the phycobilisomes. Each phycobiliprotein is composed of two dissimilar polypeptide chains, the α and β subunits, to which chromophores are covalently bound. The number and the chemical nature of the chromophores depend on the origin and spectroscopic class of the phycobiliproteins. For Nostoc sp. the α and β subunits of phycoerythrin have two and four chromophores, respectively. The α and β subunits assemble into aggregates, and the trimer form $(\alpha\beta)_3$ has dimensions of approximately a right circular disk of radius 60 A^{o} and height 30 A^{o}[1].

Fluorescence measurements on intact phycobilisomes have demonstrated that the route of energy migration within phycobilisomes occurs from phycoerythrin via phycocyanin to allophycocyanin.[2-4] The concept of energy transfer within the subunits is 14 years old. It was first introduced in the landmark papers of Teale and Dale.[5,6] Using steady state fluorescence spectra and polarization data, they developed the concept of 's' (sensitizing) chromophores transferring energy to 'f'

fluorescing chromophores within the subunits. Zickendraht-Wendelstadt et al.[7] used steady state measurements to show that both the 's' and 'f' chromophores of the α and β subunits and the monomer of Pseudanabaena W1173 fluoresce.

The investigation of this energy transfer for examining the picosecond fluorescence kinetics in isolated phycobiliproteins have led to apparently contradictory results. Kobayashi et al.[8] attributed the short-lived component of the biexponential decay in absorption kinetics in different aggregation states of C-Phycocyanin to the intraprotein energy transfer. They reported s → f transfer times of 56-84 picoseconds. In these higher aggregate forms ($(\alpha\beta)_3$ and larger), however, fluorescence and absorption kinetic measurements as a function of pulse intensity by Doukas et al.[9] indicated that the short decay component was caused by singlet-singlet annihilation effects. If 's' to 'f' transfer was occurring, its effects were masked by the bimolecular interactions. They contended that if s → f transfer existed it occurred in less than 12 ps. These two apparently contradictory interpretations of similar picosecond kinetic data have left the question of whether intraprotein energy transfer or other phenomena are being detected by these techniques. The purpose of this paper is to clarify this question by providing the first kinetic experimental evidence of s → f transfer by fitting an appropriate model to the fluorescence kinetics data from the α subunit.

In this chapter, the intramolecular energy transfer and fluorescence properties of the α subunit of phycoerythrin isolated from Nostoc sp. are characterized, using picosecond laser spectroscopy. In

contrast to experiments on intact phycobilisomes and isolated phycobiliproteins where it is well known that singlet-singlet annihilation occurs at high excitation intensities[10] the experiments reported herein indicate the absence of exciton fusion within the α subunit for the intensity range investigated (4×10^{13} to 4×10^{15} photons-cm^{-2} per pulse). This permits us to describe the kinetics by models assuming 's' to 'f' transfer. Our analysis represents the first attempt to computer simulate the energy transfer dynamics of the α subunit. We describe the α subunit as consisting of two fluorescing chromophores, with the 's' chromophore transferring energy to the 'f' chromophore. The 's' and 'f' chromophores are different spectroscopic forms of the phycoerythrobilin chromophore. It is concluded that the 's' and 'f' chromophores fluoresce with lifetimes in the absence of energy transfer of 100 ps and 1 ns, respectively. The s → f transfer time is estimated to be 100 ps.

4.2 Materials and Methods

The isolation of the α subunit is described in chapter 2, on page 54, and in references 11 and 12. The experimental arrangement used in the fluorescence kinetic measurements is shown in Figure 4.1.[13] The output of the Nd:glass laser consists of a train of 100 pulses. Pulses in the beginning portion of the train are approximately 8 ps in duration and are spaced 7 ns apart. A single pulse is selected from the train by applying a 5 ns, 8 kV pulse from a laser triggered spark gap to a Pockels cell situated between crossed polarizers. The

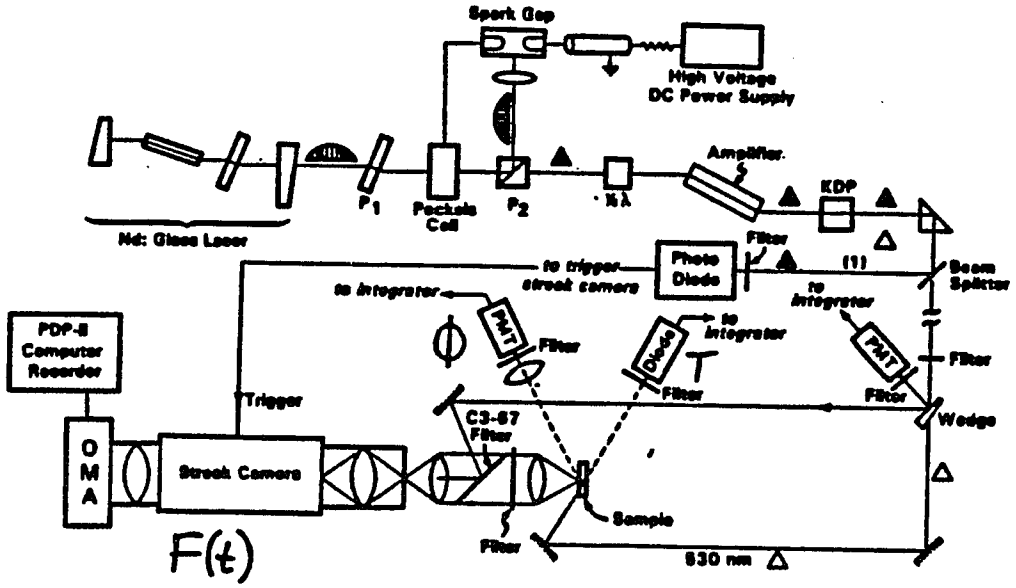

Figure 4.1(A). Schematic of experimental apparatus.

selected 1.06 μm pulse is frequency doubled to 6 ps, 0.53 μm pulse by passing the beam through a phase matched potassium di-hydrogen phosphate crystal. The sample is frontally excited and its fluorescence collected with f 1.25 optics, passed through a Corning 3-67 filter, and focused onto the entrance slit of the streak camera. The output from the phosphor screen of the streak camera is imaged onto an optical multichannel analyzer (OMA) video detector. The digitized trace is stored and processed on a Dec lab PDP 11/03 minicomputer. After normalization both in time and intensity for nonlinearities in the streak rate, the data were analyzed.

A fraction of the frequency doubled laser pulse is diverted along a separate path to the streak camera. This calibration pulse is well described by a Gaussian, $R(t) = I_o e^{-(t/\tau)^2}$ with τ = 25 ps on the 2.5 ns time scale and is used to determine the time resolution of the system for that sweep rate. On the 2.5 ns scale, the OMA displays the 6 ps laser pulse with an 8 channel width (FWHM). Because the full scale contains 500 channels each channel on this scale represents 5 ps. The excitation pulse is thus well described by a Gaussian with τ = 25 ps as shown in Figure 4.1(B). The 2.5 ns scale is used to measure the fluorescence decay kinetics. The 500 ps full scale sweep rate is used to measure the risetimes. The time resolution of the laser-streak camera system on this faster scale is less than 12 ps. The transmission and quantum yield data were obtained as explained in chapter 2, page 39. The digitized results permitted many shots in a particular intensity range to be examined, thereby resulting in

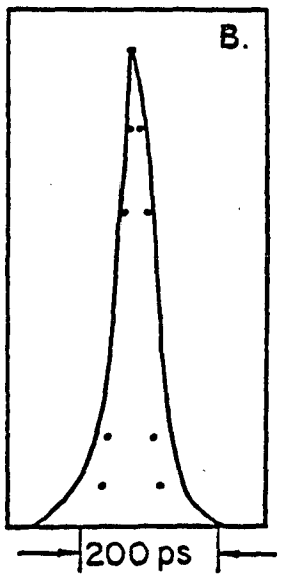

Figure 4.1(B): Response curve of the system (solid line) and fit to expression $R(t) = I_o \exp(-t^2/\tau^2)$ for τ = 25 ps (solid dots).

accurate quantum yield measurements. The intensity of the incident fluence was varied by placing appropriate neutral density filters in the excitation pathway. Experiments were performed on the α subunit suspended in 0.1 M potassium phosphate at pH 5. The sample OD at the excitation frequency was 0.48. All measurements were made at room temperature.

Absorption spectra were measured on a Cary 17D spectrophotometer. Fluorescence emission spectra were determined on a SLM 4800s spectrofluorimeter with corrections made for the grating and photomultiplier tube efficiency. Samples were diluted to an absorbance of 0.1 at the absorption maximum with 0.1 M potassium phosphate, pH 5.0, and were excited at 530 nm. The excitation and emission monochromator bandwidths were 8 and 2 nm, respectively. Fluorescence polarization spectra were measured with an Aminco-Bowman spectrofluorimeter equipped with a R446S (Hamamatsu TV) photomultiplier tube and two Glan-Thompson prism polarizers. Measurements and calculation of the degree of polarization were done as described by Grabowski and Gantt.[3,4] The excitation and emission monochromator bandpasses were 2.7 and 5.5 nm, respectively; the observation wavelength was at 585 nm. Samples were diluted to an absorbance of 0.17 at the absorption maximum with 0.1 M potassium phosphate buffer, pH 5.0.

4.3 Theoretical Background--Mirror Symmetry

The probability of a fluorescence transition from the o vibronic state of the excited electronic level u to the m vibronic level of the ℓ ground electronic state, is given by the Einstein A coefficient

$$A_{uo\to\ell m} = 8\pi\ h\nu^{3}_{uo\to\ell} n^{3}\ c^{-3}\ B_{uo\to\ell m} \qquad (4.3.1)$$

h is Plank's constant, n the index of refraction, c the speed of light; $\nu_{uo\to m}$ is the frequency of the transition where $\Delta E = h\nu_{uo\to\ell m}$ is the difference in energy between the two levels. $B_{uo\to\ell m}$ is defined by

$$B_{uo\to\ell m} = K|M_{uo\to\ell m}|^{2} \qquad (4.3.2)$$

where

$$M_{uo\to\ell m} = \langle\phi_{o}|M_{u\ell}|\phi_{\ell m}\rangle \qquad (4.3.3)$$

is the matrix element of the electric dipole moment $M_{u\ell}$ between the vibrational wavefunctions of the energy levels ϕ_{uo} and $\phi_{\ell m}$ $M_{u\ell}$ is defined by

$$M_{u\ell} = e\ \langle\psi_{u}|\sum_{i} Z_{i}\vec{r}_{i}|\psi_{\ell}\rangle \qquad (4.3.4)$$

where ψ_{ℓ} and ψ_{u} are the electronic wavefunctions of the two levels, r_{i} is the position vector of the i^{th} particle (electron or nucleus) of charge Z_{i} e in the molecule. Z_{i} = +1 for a proton, -1 for a electron and o for a neutron.

The corresponding equation for the $\ell o \to un$ vibronic absorption transition, which is the inverse of the fluorescence transition, is given by

$$M_{\ell o\to un} = \langle\phi_{\ell o}|M_{\ell u}|\phi_{un}\rangle \qquad (4.3.5)$$

by the nuclear configurations of the ground (ℓ) and excited (u) electronic states are sufficiently similar that the vibrational wavefunctions are the same in ℓ and u, that is

$\phi_o = \phi_{uo}$, $\phi_{\ell m} = \phi_{um}$, $\vec{M}_{u\ell} = M_{u\ell}$, then

$$\vec{M}_{uo\rightarrow \ell m} = \vec{M}_{\ell o\rightarrow um} \quad \text{and} \tag{4.3.6}$$

$$B_{uo\rightarrow \ell m} = B_{\ell o\rightarrow um} \tag{4.3.7}$$

It can be shown that the Einstein coefficient describing the fluorescence transition can also be given by

$$B_{uo\rightarrow \ell m} \alpha \frac{1}{n_f^3} \int \frac{F(\nu)d\nu}{\nu^3} \tag{4.3.8}$$

where n_f is the refractive index of the solvent over the fluorescence band described by $F(\nu)$. The absorption spectrum coefficient is given by

$$B_{\ell o\rightarrow um} \alpha \frac{1}{n_a} \int \varepsilon(\nu)\frac{\nu}{\nu} \tag{4.3.9}$$

where n_a is the refractive index of the solvent over the absorption band with extinction coefficient $\varepsilon(\nu)$. The deviation of the absorption spectrum from the mirror image of the fluorescence spectrum of the molecule is thus obtained by subtraction of the reflection of the modified fluorescence spectrum, $F(\nu)/\nu^3$ about the mirror symmetry

frequency ν_o, from the modified absorption spectrum $\varepsilon(\nu)/\nu$. The results are critically dependent on the value of ν_o chosen.

4.4 Results

Figure 4.2 shows the fluorescence and absorption spectra of the α subunit. The absorption spectrum exhibits a strong peak at ∿ 565 nm and a weaker band near 545 nm indicating absorption by 'f' and 's' chromophores, respectively. The measured extinction coefficient at 565 nm is 145,000 M^{-1} cm^{-1}. It is evident from Figure 4.2(A) that the fluorescence is Stokes shifted about 10 nm with its peak occurring at 575 nm. Assuming mirror symmetry between absorption and emission spectra for the 'f' chromophore allows the total absorption spectrum to be deconvoluted into bands for s and f chromophores. The bands obtained are shown in Figure 4.2(B); note that for $\lambda >> 580$ nm direct excitation of the 's' chromophore is negligible. The deconvolution of the absorption spectrum illustrated in Figure 4.2(B) is very similar to the α-subunit of Pseudanabaena W1173 absorption spectrum deconvolution reported by Zickendraht-Wendelstadt et al.[7] and Dale and Teale (1970). The absorption spectrum of the f-chromophore shown in Figure 4.2(B) and that reported by Zickendraht-Wendelstadt et al.[7] both show structure at short wavelengths near the 's'-chromophore absorption peak. At the laser excitation wavelength, 530 nm, the calculated ratio of the f to s absorption coefficients is 0.76.

The fluorescence decay profiles for high and low excitation intensity are illustrated in Figure 4.3. The shape of the fluorescence

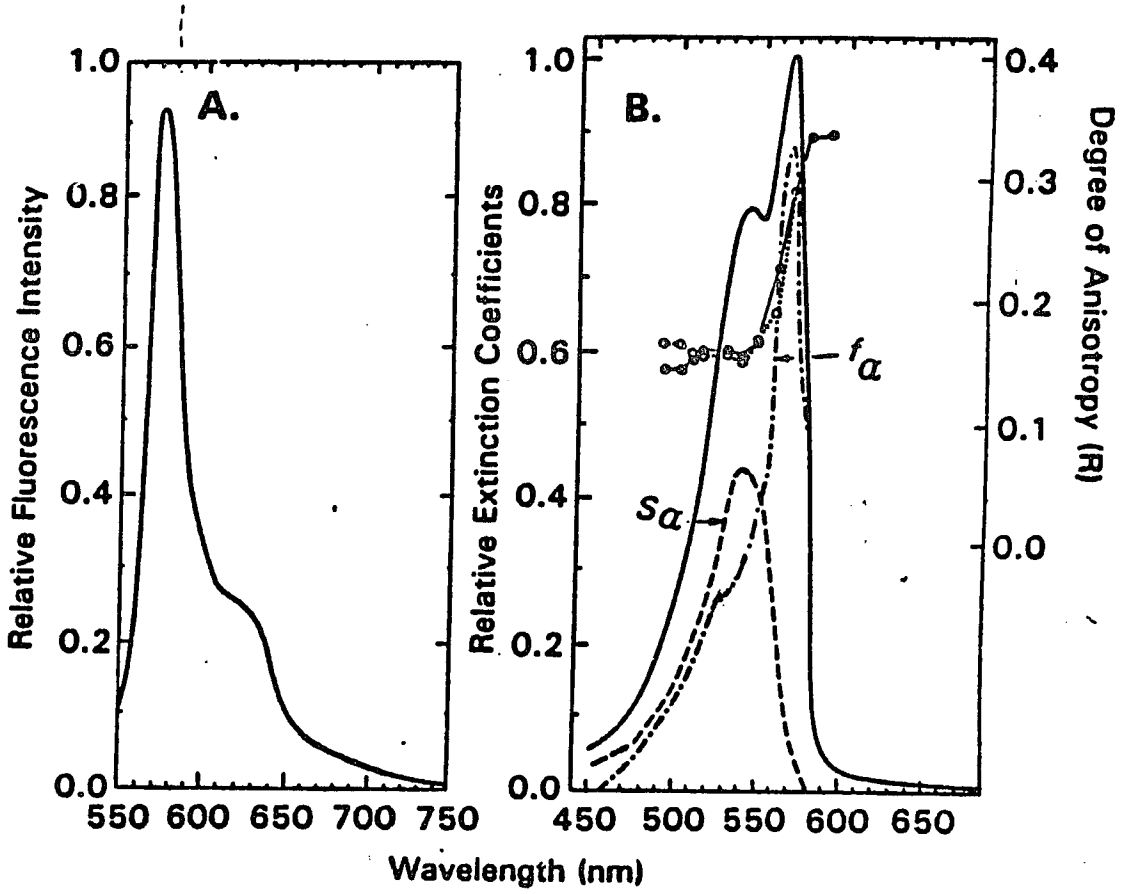

Figure 4.2(A): Fluorescence emission spectrum of α subunit. Excitation wavelength 530 nm.

(B) Absorption spectrum of the a subunit and the theoretical deconvolution of the spectrum into its 's' and 'f' components (see text). Theoretical predicted (R) polarization anisotropy (closed circles) derived by fit procedure as described in text (Equation 4.5.13); experimental polarization anisotropy values (open circles). The experimental and theoretical values of R for $\lambda > 580$ nm are identical within experimental error.

profiles was intensity-independent over the intensity range investigated (4×10^{13} to 4×10^{15} photons cm^{-2} per pulse). The decay profiles are doubly exponential with an overall e^{-1} time of approximately 1.1 nsec. The effect of adding a 2-59 filter in front of the streak camera on the time dependent emission is shown in Figure 4.4. The 2-59 filter transmits light of wavelengths beyond 590 nm only. In this case the decay exhibits single exponential behavior with a e^{-1} time of 1.1 nsec. In contrast to the decay profiles in the absence of the 2-59 filter (Figure 4.3 (A and B)), the kinetics display a slight rounding in the emission profiles for $t < 200$ psec when a 2-59 filter is present (Figure 4.4(A and B)). This slight change in shape during the first few hundred picoseconds is strong evidence for energy transfer from 's' to 'f' fluorophores. This is more evident in Figure 4.5, which displays the average of 10 fluorescence decay profiles, without (Figure 4.5A) and with (Figure 4.5B) the 2-59 filter. Shown in Figure 4.1(B) is the calibration response curve of the system on the 2.5 ns time scale. It is well described by the expression $R(t) = I_o \exp(-t^2/\tau^2)$ $\tau = 25$ ps. The curves in Figures 4.6A and 4.6B displays the rise portion of the actual experimental date acquired on the fast time scale without and with the presence of a 2-59 filter respectively.

In Figure 4.7 is shown the dependence of the relative (apparent) quantum yield and the ratio of transmitted light at high intensity to that at low intensity as a function of single pulse intensity. It is to be noted that the two curves are approximately

mirror images of each other with both breaking from unity at an incident fluence of approximately 3 to 4 x 10^{14} photon cm^{-2}.

4.5 Discussion

4.5a. Analysis of Time Dependence of Fluorescence

We analyze the data in terms of the model illustrated in Figure 4.8, where the 's' and 'f' chromophores within the α subunit are assumed fixed at a definite distance and orientation. Neglecting coherence effects (i.e., off-diagonal density matrix elements are set equal to zero) allows the rate equations to be written as

$$\frac{d\rho_s}{dt} = \alpha_s I(t) - (K_s + K_{sf})\ \rho_s(t) \qquad (4.5.1)$$

$$\frac{d\rho_s}{dt} = \alpha_f I(t) - K_f\ \rho_f(t) + K_{sf}\ \rho_s(t) \qquad (4.5.2)$$

where α_s and α_f are the absorption coefficients of the 's' and 'f' chromophores and I(t) is the normalized excitation pulse shape. The s → f transfer rate is denoted by K_{sf} and K_s and K_f are the total deactivation rate constants in the absence of energy transfer. Back transfer neglect is justified since the separation in the peaks of the absorption coefficients for 's' and 'f' chromophores imply an energy of activation on the order of 1000 cm^{-1}. A VAX 11/780 computer was used to numerically solve the differential equations describing energy

transfer. The equations were solved using a standard Runge-Kutta technique contained in the International Mathematics and Statistical Library (NBC Building, Houston, Texas). These programs are listed in the appendix.

$$F(t) = K_{sr}\,\rho_s(t) + K_{fr}\,\rho_f(t) \qquad (4.5.3)$$

where K_{sr} and K_{fr} are the radiation rates of the 's' and 'f' chromophores respectively. When the 2-59 filter is present only wavelengths beyond 590 nm are transmitted and the emission decay profile is given by

$$F(t) = CK_{sr}\,\rho_s(t) + (1-C)K_{fr}\,\rho_f(t) \qquad (4.5.4)$$

C indicates the contribution of the 's' chromophore emission to the fluorescence beyond 590 nm. Our deconvolution of the absorption spectra shows that C is very small.

The radiative rates of the 's' and 'f' chromophore were obtained from their respective deconvoluted absorption curves (see Figure 4.2(B)), by using the Einstein relationship

$$K_r = 2.88 \times n^2 \times 10^{-9} \int \frac{(2\tilde{\nu}_o - \tilde{\nu})^3}{\tilde{\nu}}\,\varepsilon(\tilde{\nu})\,d\tilde{\nu}\,sec^{-1} \qquad (4.5.5)$$

Here $\tilde{\nu}_o$ is the wavenumber at the mirror symmetry point, $\varepsilon(\tilde{\nu})$ is the absorption coefficient at wave number $\tilde{\nu}$, and n is the index of refraction. For the α subunit, n is approximately 1.5.[5,6] The integral was done numerically with a mesh size of 2 cm^{-1}. A 10 nm

Stokes shift was assumed between the peaks of the absorption and fluorescing curves of the 's' chromophore, as is the case of the 'f' chromophore. For the s chromophore, $\tilde{\nu}_o = 1.83 \times 10^4$ cm^{-1}, whereas for the f chromophore, $\tilde{\nu}_o = 1.75 \times 10^4$ cm^{-1}. With these assumptions the radiative value for the 's' and 'f' chromophores are calculated to be 2.1×10^8 sec^{-1} and 3.1×10^8 sec^{-1} respectively. These numbers are estimated to be accurate to within a factor of 2. The ratio (y) of the calculated radiative rates is therefore, $y = K_{fr}/K_{sr} = 1.5$.

The best fit to the decay kinetics (in the absence of the C.S. 2-59 filter) for y = 1.5 gives $K_s = 1.0 \times 10^{10}$ sec^{-1}, $K_{sf} = 1.0 \times 10^{10}$ sec^{-1} and $K_f = 1.0 \times 10^9$ sec^{-1}. These parameters correspond to an s fluorescence decay time in the absence of energy transfer of 100 ps and an 'f' fluorescence e^{-1} decay time of 1.0 ns. The s → f transfer rate is 100 ps. The parameters are accurate to within a factor of two. Doubling any single parameter yields a worse fit. The effects of doubling K_{sf} is shown in Figure 4.5.(A). The theoretical decay curves were fit to an average of 10 experimental fluorescence decays.

These same rate constants were used to fit the fluorescence kinetics in the presence of the C.S. 2-59 filter. Using Equation 4.5.4 a value of C equal to 0.10 was obtained. Again, the fit (illustrated in Figure 4.5(B)) is estimated to have an accuracy to within a factor of 2 for all rate constants. The excellent fit of this entire curve (including rise-times) using the same rate parameters as in Figure 4.5(A) strengthens our contention that the slight change in shape during the first few hundred picoseconds is due to energy

transfer. A value of τ = 25 ps provides a good fit to both the response curve (Figure 4.5(C)) and the rise time of the emission.

For Forster dipole-dipole transfer mechanism[19]

$$K_{sf} = K_s \left(\frac{R_o}{R}\right)^6 = \frac{1}{\tau_s}\left(\frac{R_o}{R}\right)^6 \qquad (4.5.6)$$

where τ_s is the lifetime of the donor ('s' chromophore) in the absence of transfer and R_o is the characteristic Forster distance for the process;

$$R_o^6 = \frac{(9000)(\ln 10)}{128\ \Pi^5\ Nn^4}\ \phi_s K^2\ J \qquad (4.5.7)$$

N is Avogadro's number per cubic centimeters, ϕ_s is the donor's emission yield in the absence of energy transfer (i.e., $\phi_s = K_{sr}/K_s = (2.1 \times 10^8/(1.0 \times 10^{10}) = .02$; see Table 4.1), n is the refractive index of the medium and J is the spectral overlap integral. We estimate $J = .16 \times 10^{-13}$ cm^6 assuming mirror symmetry for the 's' chromophore and a 10 nm Stoke shift between absorption and emission maximum for the donor. The orientation factor, K^2, is not known. In fact, a specific or average value of K^2 cannot be determined from the transfer depolarization factor alone. We therefore adopt the reasonable value of $K^2 = 1.0$.

With $K^2 = 1.0$, n = 1.5 (as approximated by Dale and Teale) and $\phi_s = 0.02$ equation (7) gives $R_o = 20$ Å. This implies that the distance

between the 's' and 'f' chromophores is $R = (K_s/K_{sf})^{1/6} R_o = 20$ Å. To compare this with the "size" of the molecule we note that the approximate volume of the $(\alpha\beta)_3$ unit is 3.4×10^5 A^3.[1] The α subunit molecular weight is 16,600 daltons which is slightly less than the β subunit which has a molecular weight of 19,500 daltons. If we assume the volume occupied by the α component is in the same ratio to the volume occupied by β component as is the ratio of their weights, and that both are spherical molecules[14] then the radius of the α subunit is approximately 25 Å. This value compares quite favorably with the theoretical R value of 20 Å; presumably the 's' and 'f' moieties can easily be accommodated within the interior of the α molecule.

The absolute fluorescence quantum yield for the α subunit as modelled in Figure 5.8, is defined as the ratio of the number of molecules fluorescing over the number of molecules initially excited.

$$\phi = \frac{\#\ \text{Fluorescing}}{\#\ \text{Initially excited}} \tag{4.5.8}$$

For an incident pulse intensity I, $\alpha_s I$ and $\alpha_f I$ are the number of excitons absorbed by the 's' and 'f' chromophores, respectively. The ratio $\frac{k_s}{k_s+k_{sf}}$ is the fraction of excitons created in the 's' not transferred, while $\frac{k_s}{k_s+k_{sf}}$ is the fraction transferred to the 'f' chromophores. As a result,

$$\frac{k_{sf}}{k_s+k_{sf}}\ \alpha_s I \tag{4.5.9}$$

is the number of photons emitted by the 's' chromophores.

$$\frac{k_{fr}}{k_f}\ \alpha_f + \frac{k_{sf}\ \alpha_s}{k_s+k_{sf}} \qquad (4.5.10)$$

is the fraction of excitons in the sea of 'f' chromophores that deexcite by fluorescing. Hence, the first term represents the photons emitted by those directly absorbed by the 'f' chromophores while the second term are the photons emitted by the excitons transferred from the 's' chromophores. Since the total number of excitons absorbed is $(\alpha_s + \alpha_f)I$, the quantum yield ϕ is given by:

$$\phi = \frac{\frac{k_{sf}\ \alpha_s}{k_s+k_{sf}} + \frac{k_{fr}}{k_f}\ \frac{\alpha_f\ (k_s + k_{sf}) + k_{sf}\ \alpha_s}{k_s + k_{sf}}}{\alpha_s + \alpha_f} \qquad (4.5.11)$$

which reduces to

$$\phi = \frac{K_{sr}}{1+x}\ \frac{K_f + K_{sf}\ (1+x)\ y + K_s xy}{K_f(K_s + K_{sf})} \qquad (4.5.12)$$

where $\times = \alpha_f/\alpha_s = 0.76$ and $y = K_{fr}/K_{sr} = 1.5$. For the parameters that best fit the experimental decay curves $\phi = 0.23$. The experimentally obtained value is 0.46 ± 0.06. The discrepancy may be accounted for by the estimation used in calculating K_{sr}, the radiative rate of the 's' chromophore. In particular use of the Einstein relationship to obtain the radiative rate of a chromophore whose fluorescence spectra is unknown (experimentally) is dependent on both the Stokes shift assumed

and use of mirror symmetry between absorption and emission spectra. If K_{sr} were 65% larger than that reported the theoretical value for the quantum yield would be within the error bars of the measured value of ϕ. The kinetics fits show that the value of ϕ (donor's emission yield in the absence of energy transfer) is accurate to within a factor of two. The value of K^2 is also estimated to be within a factor of two. Assuming J is accurate to within a factor of 1.5, R_o and hence R have an estimated accuracy of approximately 50%. This is quite reasonable for data obtained from kinetic fits. Most of the errors are due to the inherent approximations involved in obtaining the deconvoluted absorption spectra of each chromophore and use of Einstein's relationship to derive the radiative rates.

Table 4.1

Rate Constants (units s^{-1}) for the α subunit of Nostoc sp.
(See Figure 4.8)
Values in parentheses are times in (ps)

$K_s = 1.0 \times 10^{10}\ s^{-1}$ (100 ps)	$K_f = 1.0 \times 10^{9}\ sec^{-1}$ (1000 ps)
$K_{sr} = 2.1 \times 10^{8}\ s^{-1}$ (5000 ps)	$K_{fr} = 3.1 \times 10^{8}\ s^{-1}$ (3333 ps)

Transfer rate = $K_{sf} = 1.0 \times 10^{10}\ s^{-1}$ (100 ps)

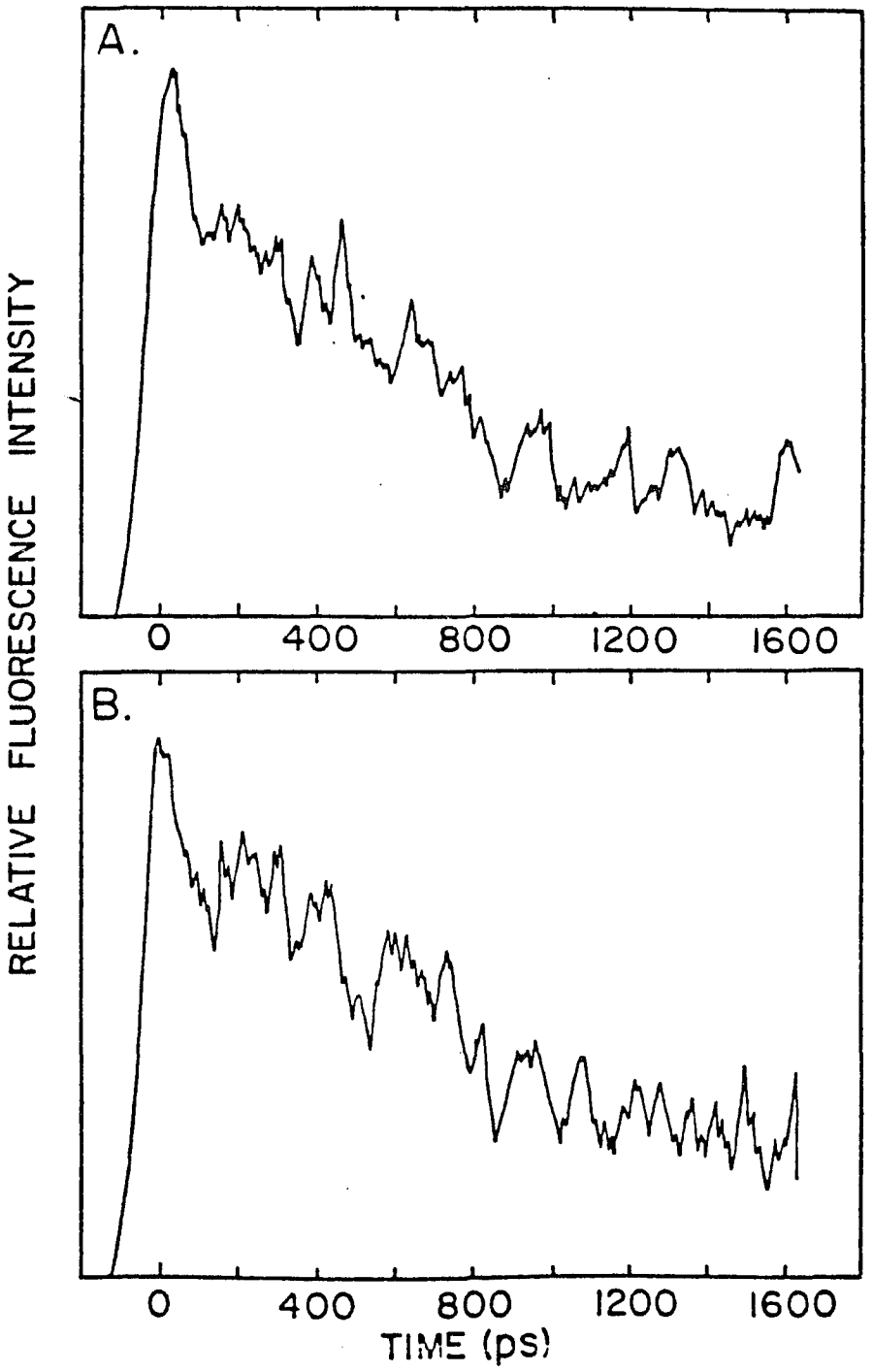

Figure 4.3(A): Fluorescence kinetic profile; excitation wavelength 530 nm, 3-67 filter, 200 psec per division. Incident fluence equal to 7.3×10^{13} photons-cm^{2}.

(B) Same as (A) but for fluence of 1.43×10^{15} photons-cm^{-2}

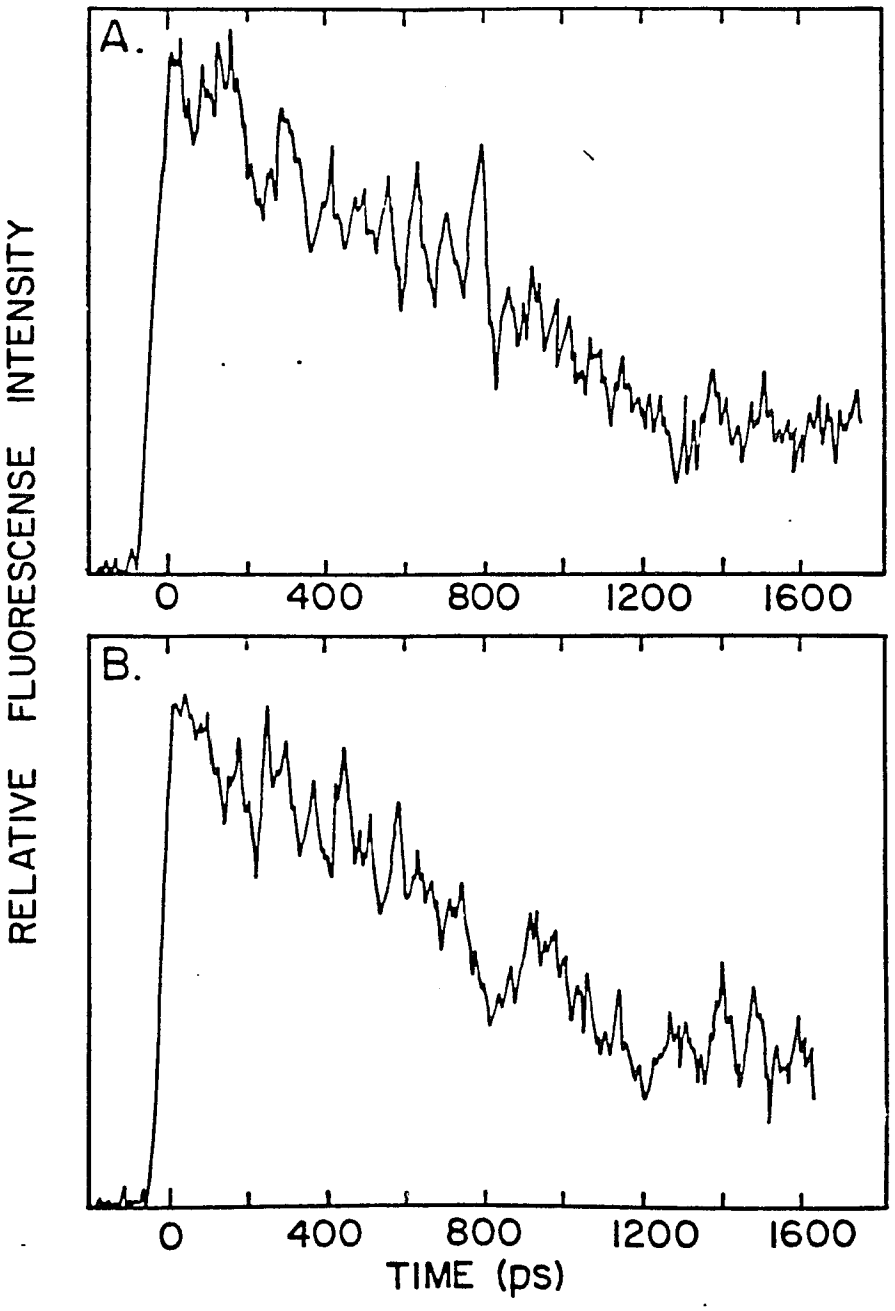

Figure 4.4: Fluorescence kinetic profile; excitation wavelength 530 nm, 2-59 and 3-67 filters, 200 psec per division.

(A) Incident fluence: 1.18×10^{14} photon-cm^{-2}

(B) Same as A but for incident fluence: 1.05×10^{15} photon-cm^{-2}.

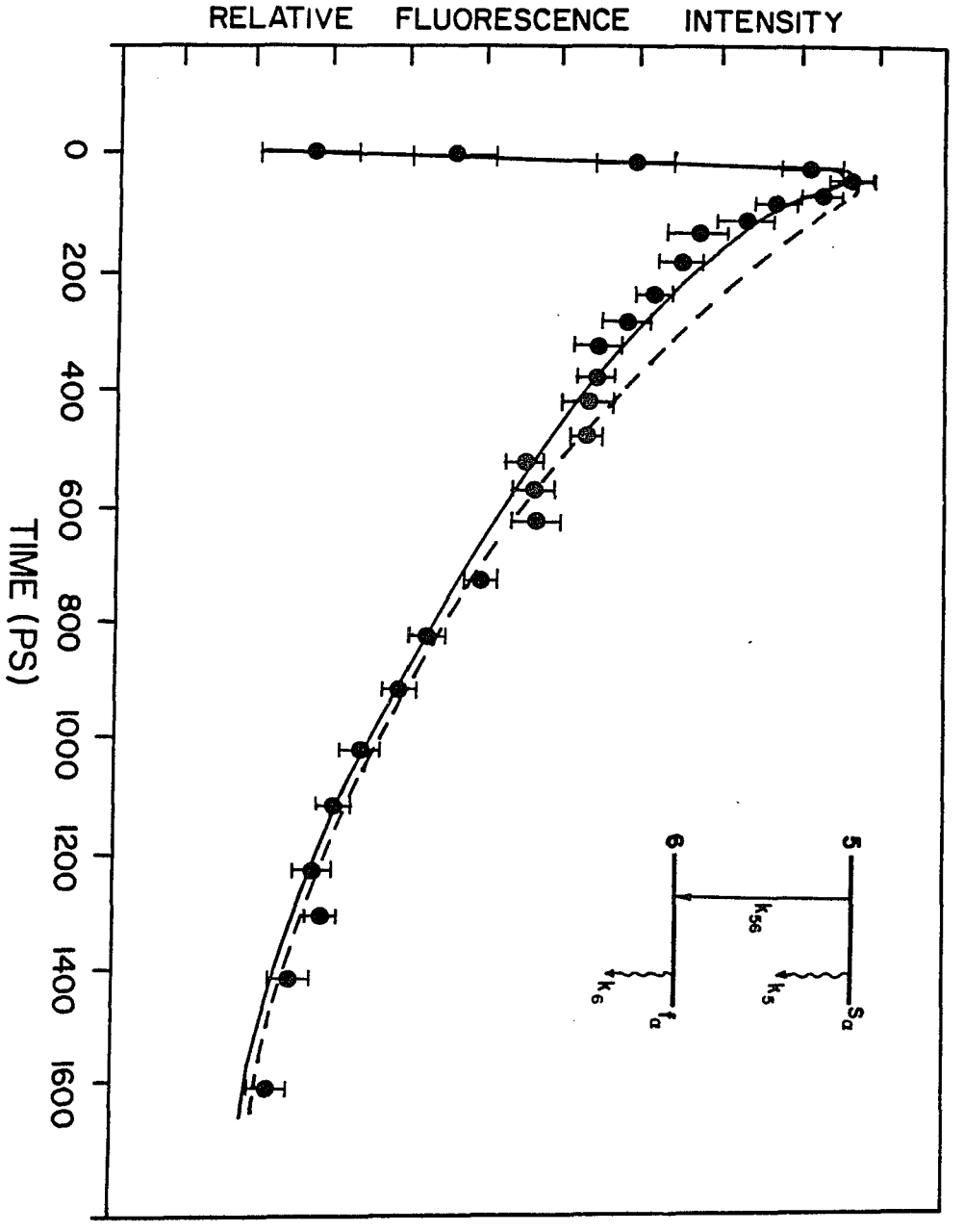

Figure 4.5(A): Average of 10 fluorescence decays; excitation wavelength 530 nm, incident fluence 7.3×10^{13} photon cm^{-2} with 3-67 filter. Solid line is best fit to Equation 4.5.3 with τ = 25 ps, $K_s = 1 \times 10^{10}\ s^{-1}$, $K_{sf} = 1 \times 10^{10}\ s^{-1}$, $K_f = 1 \times 10^{9}\ s^{-1}$ and $K_{sr}:K_{fr} = 0.8:1.2$. Dashed line is fit when K_{sf} is doubled. Error bars are shown for averaged fluorescence curve.

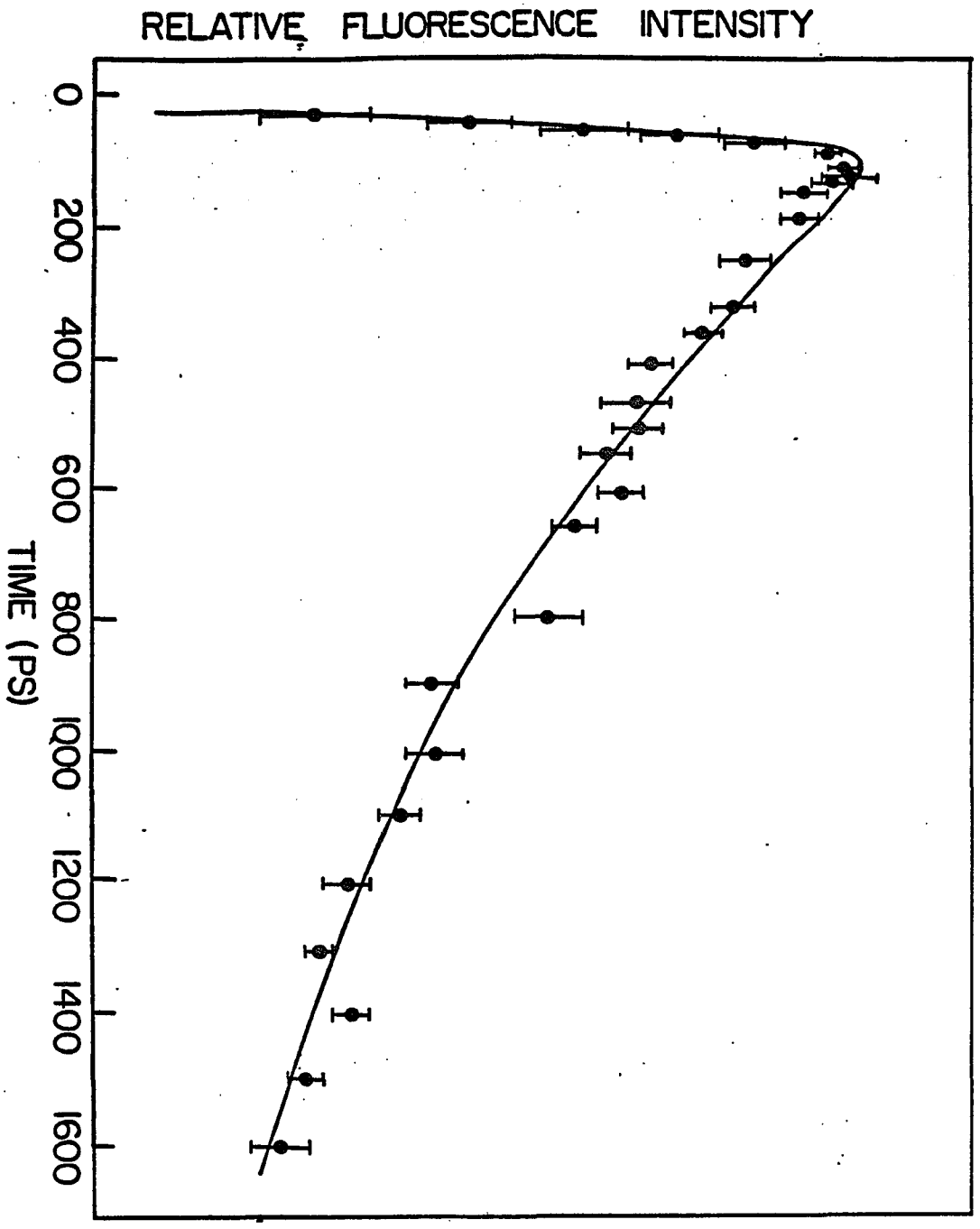

Figure 4.5(B). Decay profile in presence of 3-67 and 2-59 filter, solid line is fit to Equation 4.5.4 for same rate constants as in (A) with C = 0.1. Error bars are shown for averaged fluorescence curve.

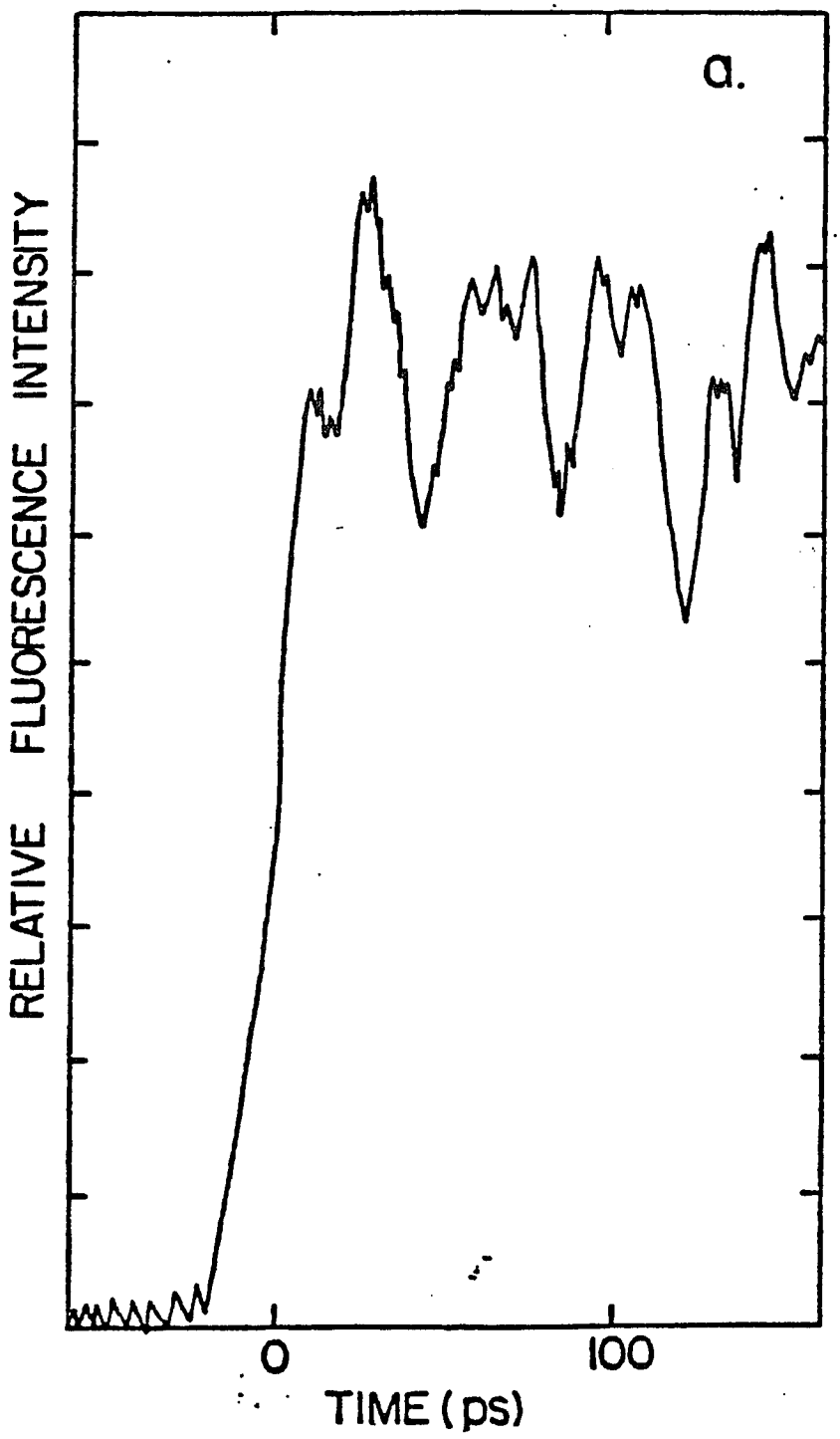

Figure 4.6(A). Fluorescence kinetics decays during the first 150 ps on the fast time scale without (A) and with (B) a C.S. 2-59 filter.

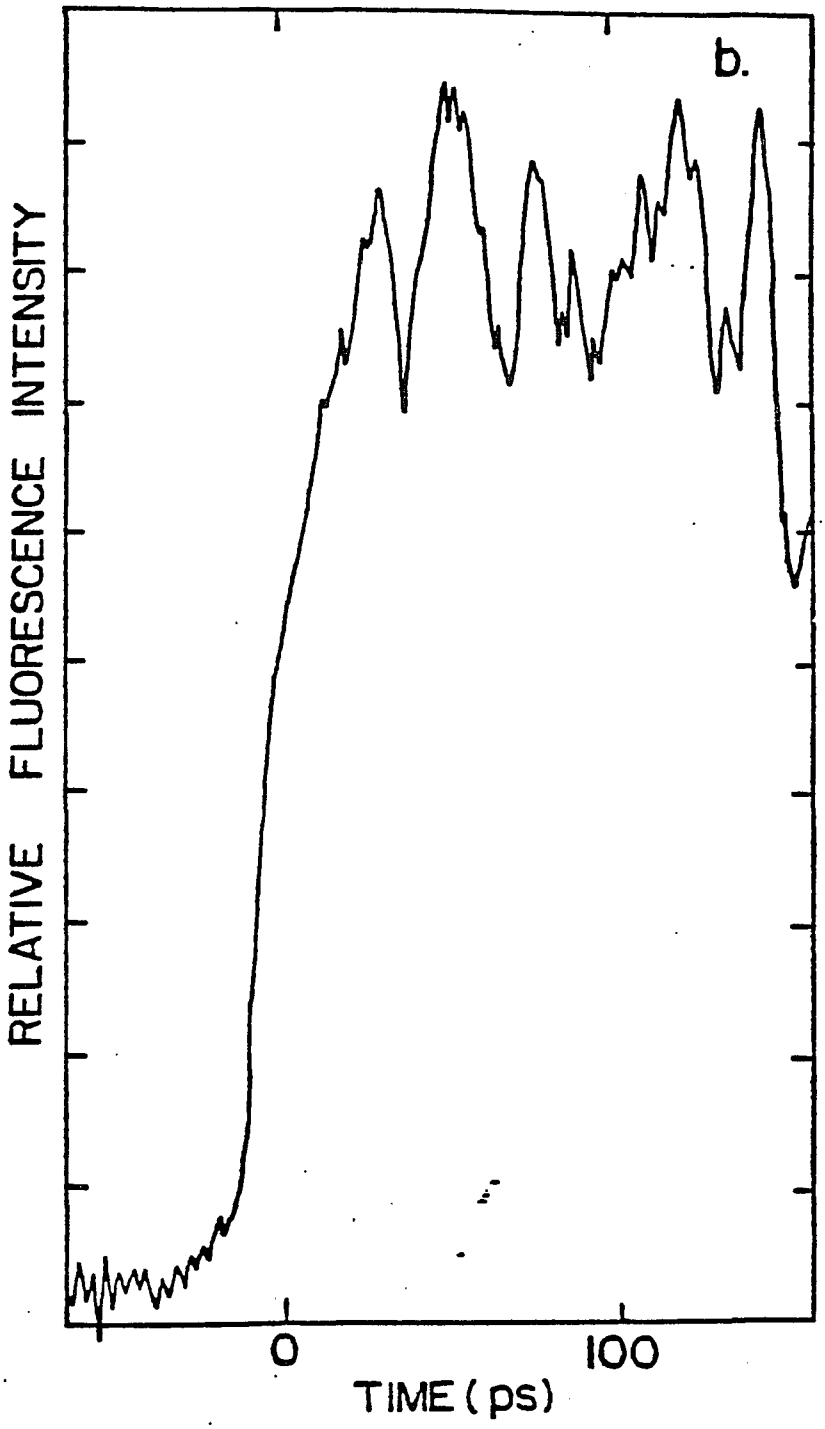

Figure 4.6(B). A C.S. 2-59 filter.

4.5b. Degree of Polarization Anisotropy

A characteristic feature of the measured anisotropy (R) reported in Figure 4.2(B) is the presence of very little structure and nearly constant value of 0.16 for wavelengths between 480 and 550 nm, its monotonic increase for $\lambda \tilde{\sim}$ 550-570 nm, and its saturation at 0.34 for λ > 580 nm. This functional behavior is similar to that reported by Zickendraht-Wendelstadt et al.[7] for the α subunit isolated from Pseudanabaena W1173 C-phycoerythrin. Consistency of the experimental values of R (=R_m) with the deconvoluted absorption spectrum is afforded by comparing R_m with the calculated weighted sum of the anisotropy (R_w) of the individual absorption band, i.e.:

$$R_w = \frac{\alpha_s(\lambda)R_s + \alpha_f(\lambda)R_f}{\alpha_s(\lambda) + \alpha_f(\lambda)} \qquad (4.5.13)$$

where R_s and R_f are the degree of anisotropy associated with direct excitation of the s and f chromophores respectively. Values of R_s and R_f were obtained as follows. For λ > 580 nm, $\alpha_s(\lambda)$ = 0 giving $R_w = R_f = 0.34$, the measured value of R. The value of R_s was inferred from $R_m = 0.16$ at 530 nm where $\alpha_f(\lambda)/\alpha_s(\lambda) = 0.76$. Values of R at other wavelengths were calculated using the deconvoluted spectral data given in Figure 4.2(B). It is evident that the agreement between R_w and R_m reported in Figure 4.2(B) indirectly supports the deconvolution procedure.

Further support for the kinetics and the measured anisotropy is provided by demanding consistency between calculated anisotropy (as a function of wavelength) utilizing the rate parameters inferred from fluorescence time-dependent measurements and the steady-state anisotropy data. The steady-state anisotropy can be written in terms of the dimer kinetic parameters[15] as:

$$R = 0.34 + \frac{z\, K_{fr}K_{sf}}{5\{xK_{fr}(K_s+K_{sf})+K_{sr}K_f+K_{fr}K_{sf}\}} \qquad (4.5.14)$$

where $x = \alpha_f(\lambda)/\alpha_s(\lambda)$ and $z = 3(\cos^2 \gamma - 1)$; γ is the angle formed by the emission dipole of the 's' chromophore and the absorption moment of the 'f' chromophore. The constant 0.34 denotes the value of the anisotropy at long wavelength. In adopting this value we have arbitrarily changed the theoretical limiting value of 0.4 to 0.34. This discrepancy arises from the slight differences in the absorption and emission transition moments of either the 's' and 'f' chromophores of both moieties. This point will not concern us here. Values of R, calculated by Equation 4.5.14 using the kinetic parameters given in Table 4.1 and the deconvoluted absorption spectra, fit the experimental data as well as, if not better than, those calculated using Equation 4.5.13. The inferred value of $\gamma = 59°$ is quite similar to the value of 49^o determined by Zickendraht-Wendelstadt et al.[7] for Pseudanabaena W1173. The difference in values is, as in the case of the absolute quantum yield, attributable to the inherent approximations in

obtaining the deconvoluted absorption spectra of each chromophore and use of Einstein's relationship to derive the radiative rates.

4.5c Analysis of the Dependence of the Apparent Quantum Yield and Transmission on Intensity

The apparent fluorescence quantum yield dependence on excitation intensity as shown in Figure 4.7 has a functional form similar to that predicted by exciton annihilation theories.[16,17] For the parameter selection of r = 0.05, Z = 0.5 and K = 8.76 x 10^8 s^{-1}, the exciton fusion theory of Paillotin et al.[17] fits the relative yield (defined as the integrated fluorescence intensity normalized to low excitation emission intensity) versus intensity, as indicated by the solid line in Figure 4.7. Without additional experimental data, such as time-dependence fluorescence measurements and transmission data over a broad excitation intensity range, this agreement is suggestive of exciton annihilation processes. The exciton theory of Paillotin et al.[17] does not include the nonlinear optical effects produced by ground state depletion or upper excited state absorption and is well known to be applicable only in cases where transmission is unchanged over the intensity domain measured[18] in contrast to the transmission results reported in Figure 4.7. Hence, the apparent decrease in the fluorescence yield cannot be attributed solely to singlet exciton fusion. Further evidence against exciton annihilation is the observation that the emission decay, although nonexponential over the excitation intensity domain studied, is independent of laser intensity. When exciton annihilation processes are operative, the fluorescence decay profiles are expected to be nonexponential and excitation

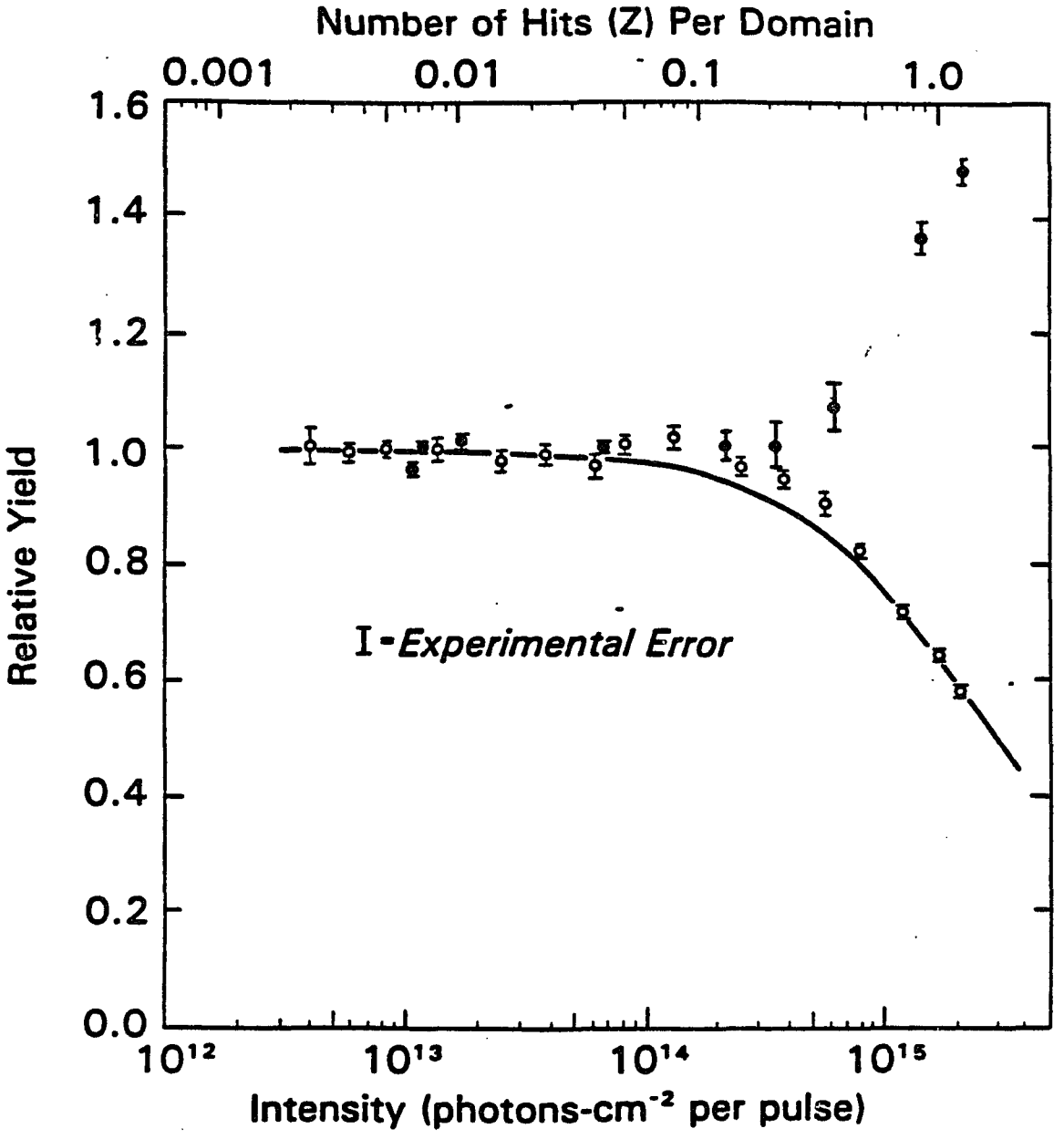

Figure 4.7: Relative fluorescence quantum yield and transmission as a function of laser single pulse intensity (photon cm^{-2}); 0 measured relative quantum yield, ● measured relative transmission. Solid line is fit of apparent relative flourescence quantum yield to Paillotin-Swenberg theory with r = 0.05.

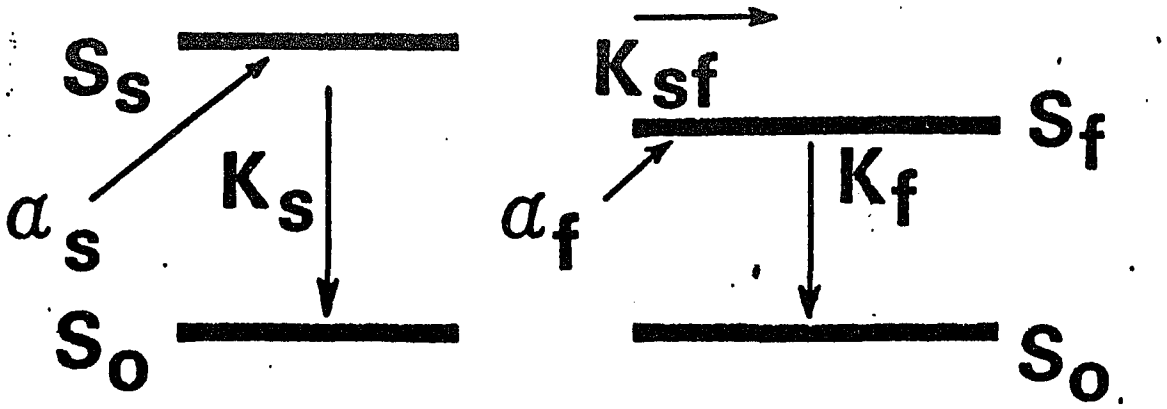

Figure 4.8: Two component model utilized for the analysis of fluorescence from the α subunit.

S_o denotes the electronic ground state and S_s and S_f are the first excited singlet states for s and f moieties, α_s and α_f are the absorption coefficients for these states. K_s and K_f are the total deactivation rates from the s and f chromophores in absence of energy transfer; K_{sf} is the energy transfer rate from s to f.

intensity dependent. We cannot, at this time, offer a quantitative explanation for the single laser pulse data reported in Figure 4.7. The observation that the relative transmission (T_R) and apparent fluorescence yield (ϕ_R) are approximately mirror reflections (about the unit axis) of each other is strongly suggestive of ground state depletion since a three level model, under steady-state excitation, gives $\phi_R = T_R^{-1}$ when the excitation intensity is less than the saturation intensity, defined as the incident intensity required to obtain a fluorescence yield decrease of 50% compared to low intensity yield. These remarks suggest that the major contribution to the apparent decrease in ϕ_R and the corresponding increase in T_R is ground state depletion although it does not rule out nonlinearities in T_R and ϕ_R due to upper excited state absorption. The absence of exciton annihilation allows the solutions of equations describing energy transfer to explain the decay kinetics by s → f transfer. In larger aggregates of α and β subunits bimolecular processes mask the observation of the s → f transfer process.

4.6 Summary

The time dependent fluorescence profiles, apparent quantum yield and transmission from the phycoerythrin α subunit isolated from Nostoc sp. have been measured over a wide excitation intensity range using a single pulse picosecond source. Kinetics of the fluorescence are quantitatively accounted for using a simple model that assumes both moieties (s and f) absorb and fluoresce. The kinetic parameters

characterizing the chromophores have been inferred. This experiment constitutes the first measurement of the s → f transfer in the α subunit. The Forster transfer critical distance (R_o) and the distance between the s and f moieties were calculated. The apparent decrease in the fluorescence yield is attributed to ground state depletion and upper excited absorption. The nonexponential intensity independent fluorescence decays are inconsistent with an exciton annihilation mechanism and are best accounted for in terms of the two component model. Our results strongly suggest that annihilation processes do not occur in isolated α-subunits for fluences less than 4×10^{15} photon-cm^{-2}. The absence of exciton fusion permits the quantitative analysis of the fluorescence kinetics to a model with s → f transfer with both chromophores fluorescing. The s → f time in the α unit is 100 ps. The determination of the intramolecular transfer rate is not possible in the larger aggregates where annihilation is known to occur unless investigations are performed at excitation fluence of less than 10^{10} photon-cm^{-2}.

Notes

1. Bryant, D. A., Guglielmi, G., Tandeau, N., deMarsac, A. M. Castets, & Cohen-Bazie, G. (1979). Arch. Microbiol., 123, 113.

2. Porter, G., Tredwell, C. J., Searle, C. F. W., & Barber, J. (1978). Biophys. J., 25, 513.

3. Grabowski, J., & Gantt, E. (1978a). Photochem. Photobiol., 28, 39.

4. Grabowski, J., & Gantt, E. (1978b). Photochem. Photobiol., 28, 47.

5. Teale, F. W. J., & Dale, R. E. (1970). Biochem. J., 116, 161.

6. Dale, R. E., & Teale, F. W. J. (1970). Photochem. Photobiol., 12, 99.

7. Zickendraht-Wendelstadt, B., Friedrich, J., & Rudiger, W. (1980). Photochem. Photobiol., 34, 367.

8. Kobayashi, T., Degenkolb, E. O., Bersohn, R., Rentzepis, P. M., MacColl, R., & Berns, D. S. (1979). Biochemistry, 18, 5073.

9. Doukas, A. G., Stefancic, V., Buchert, J., Alfano, R. R., & Zilinskas, B. A. (1981). Photochem. Photobiol., 34, 505.

10. Wong, D. F., Pellegrino, F., Alfano, R. R., & Zilinskas, B. A. (1981). Photochem. Photobiol., 33, 651.

11. Zilinskas, B. A., & Howell, D. A. (1983). Plant Physiol., 71, 379.

12. Troxler, R. R., Greenwald, L. S., & Zilinskas, B. A. (1980). J. Biol. Chem., 255, 9380.

13. Lu, P. Y., Yu, Z. X., Alfano, R. R., & Gersten, J. I. (1982). Phys. Rev., A26, 3610.

14. Morschel, E., Klaus-Peter Koller, & Wehrmeyer, Werner (1980). Arch. Microbiol., 125, 43.

15. Tanaka, F., & Mataga, N. (1980). Photochem. Photobiol., 29, 1091.

16. Swenberg, C. E., Geacintov, N. E., & Pope, M. (1976). Biophys. J., 16, 1447.

17. Paillotin, G., Swenberg, C. E., Breton, J., & Geacintov, N. E. (1979). Biophys. J., 25, 513.

18. Breton, J., & Geacintov N. E. (1980). Biochem. Biophys., 594, 1.

19. Forster, Th. W. (1965). In O. Sinanoglu, Ed., Modern Quantum Chemistry, pp. 93-137. New York: Academic Press.

Chapter 5

SPECTRAL AND TEMPORAL PROPERTIES OF THE β AND αβ SUBUNITS ISOLATED FROM NOSTOC sp. USING PICOSECOND LASER SPECTROSCOPY

In this chapter, the intensity dependence of the decay kinetics, relative quantum yield, and transmission of the β subunit and (αβ) monomer of PE isolated from Nostoc sp. as well as the steady-state absorption and fluorescence spectra are presented. These measurements are used to develop models describing the energy transfer pathways in these subunits. Exciton annihilation is shown not to occur in these units over the intensities (~10^{12} to ~10^{15} photons/cm^2) investigated. The data are fit to equations describing energy transfer between 's' and 'f' chromophores in the β subunit and the monomer. The transfer rates between the 's' and 'f' chromophores and their respective fluorescence decay rates in the absence of energy transfer are deduced from the chosen models. Part of the analysis on the α subunit is repeated, from the previous chapter, for completeness.

5.1 Introduction

A number of light harvesting antenna molecules have evolved in photosynthetic organisms for the primary purpose of absorbing sunlight and transferring the absorbed energy to reaction centers where photochemistry occurs. In red and blue-green algae, the light-harvesting system consists of an aggregation of phycobiliproteins, namely

phycoerythrin (PE), phycocyanin (PC), and allophycocyanin (APC), which collectively form the phycobilisomes (PBS). Each phycobiliprotein is composed of two dissimilar polypeptides the α and β subunits, to which chromophores are covalently bound. The number and the chemical nature of the chromophores depend on the origin and spectroscopic class of the phycobiliproteins. For Nostoc sp., the α and β subunits of phycoerythrin have two and four chromophores, respectively.[1] The α and β subunits assemble into aggregates and the trimer form $(\alpha\beta)_3$ has dimensions of approximately a right circular cylinder of radius 60A° and height 30A.[2] The basic unit of PE in the phycobilisome is a trimer $(\alpha\beta)_3$. Fluorescence measurements on intact phycobilisomes have demonstrated that the route of energy migration within phycobilisomes occurs from PE via PC to APC.[3-4] Several processes (fluorescence, internal nonradiative conversion, singlet-singlet exciton annihilation) compete for the excitation energy and thus affect the migration of the excitation energy.[5-17] Grabowski and Gantt[4] used steady-state measurements to provide the first estimates that the transfer time from PE to PC was on the order of 200-300 ps. The pioneering time resolved kinetic studies of Porter et al.[6] yielded the first direct measurements of the transfer times (70-120 ps) within PBS. The concept of energy transfer within the subunits of the phycobiliproteins is 14 years old. It was first introduced in the landmark papers of Dale and Teale.[9,10] Using steady-state fluorescence spectra and polarization data, they developed the concept of 's' (sensitizing) chromophores transferring energy to 'f' (fluorescing) chromophores within the subunits. Their data suggested that the 's' to 'f' transfer rate was approximately 2000

times the 's' fluorescence rate. Zickendraht-Wendelstadt et al.[11] used steady-state measurements to obtain the absorption spectra of the 's' and 'f' chromophores of the α and β subunits and monomer forms of PC isolated from Pseudanabaena W1173. They showed that both the 's' and 'f' chromophores fluoresce, though they did not obtain 's' → 'f' transfer times.

Similar attempts to follow this energy transfer by examining the picosecond fluorescence kinetics in isolated phycobiliproteins of both blue-green and cryptomonad algae have led to apparently contradictory results. Kobayashi et al.[15] attributed the short-lived component (picoseconds) of the two component decay they found in different aggregation states of C-phycocyanin to intraprotein energy transfer. They reported s → f transfer times of 56-84 picoseconds. In the higher aggregation states of Nostoc sp. $(\alpha\beta)_3$ and larger, however, fluorescence and absorption kinetic measurements as a function of pulse intensity by Doukas et al.[16] indicated that the short decay component was caused by singlet-singlet annihilation effects. If 's' to 'f' transfer was occurring, its effects were masked by the bimolecular interactions. They contended that if s → f transfer existed, it occurred in less than 12 ps. These two apparently opposing interpretations of similar picosecond fluorescence kinetic data have left the question of whether intraprotein energy transfer or other phenomena are being detected by these techniques. The purpose of this chapter is to clarify this question by providing the first direct evidence of s → f transfer by fitting models to the kinetics data.

In this chapter, the intramolecular energy transfer and fluorescence properties of the β and (αβ) subunits of phycoerythrin isolated

from Nostoc sp. are characterized using picosecond laser spectroscopy. This analysis, in addition to that performed on the α subunit of the same algae, represents one of the first attempts to computer simulate the energy transfer dynamics in these samples. Furthermore, from the fluorescence kinetics and the transmission data we show that exciton annihilation processes do not occur in these lower subunits at the laser excitation intensities studied (10^{12} to 10^{15}ph/cm^2). The absence of exciton fusion allows us to describe the kinetics by models assuming 's' to 'f' transfer. In contrast, our experimental evidence indicates the occurrence of annihilation in the higher aggregates of the biliproteins ($(\alpha\beta)_3$, $(\alpha\beta)_6$, $(\alpha\beta)_{12}$), which mask the 's' to 'f' transfer in the kinetics. Computer models are used here to deduce 's' to 'f' transfer rates, as well as the fluorescence rates of the 's' and 'f' chromophores, for the chosen models of the β and (αβ) units. Part of the analysis of the α subunit is included for completeness.[18]

The α subunit consists of two fluorescing chromophores, with the 's' chromophores transferring energy to the 'f' chromophore. Our model of the β subunit, for simplicity, assumes 2 's' and 2 'f' chromophores. The $s_\beta \rightarrow f_\beta$ transfer rates from each s_β to each f_β are assumed to be equal. In addition, the fluorescence rates in the absence of energy transfer of each of the s_β and each of the f_β chromophores are assumed equal. The monomer is assumed to consist of the same 's' and 'f' chromophores as in the separated α and β subunits, and its kinetics are compared with those of its isolated subunits.

5.2 Methods: Laser and Streak Camera System

The experimental arrangement used in the fluorescence kinetic measurements is shown in Figure 5.1. The output of Nd:glass laser consists of a train of 100 pulses. Pulses in the beginning portion of the train are approximately 8 ps in duration and are spaced by approximately 7 ns. A single pulse is selected from the train by applying a 5 ns, 8 KV pulse from a laser triggered spark gap to a Pockels cell situated between crossed polarizers. The selected 1.06 μm pulse was frequency doubled to a 6 ps, 0.53 μm pulse by passing the beam through a phase matched di-hydrogen phosphate crystal. The sample is frontally excited and fluorescence collected with f 1.25 optics, passed through a Corning 3-67 filter, and focused onto the entrance slit of the streak camera. The output from the phosphor screen of the streak camera was imaged onto an optical multichannel analyzer (OMA) video detector. The digitized trace was stored and processed using a Dec Lab PDP 11/03 minicomputer. The 2.5 ns scale was used to measure the fluorescence decay kinetics whereas a 500 ps full scale sweep rate was employed for fluorescence risetime measurements. A calibration pulse is sent along a path avoiding the sample. It is reflected from the Corning 3-67 filter into the camera. This pulse was used to characterize the laser pulse on the 2.5 ns scale. The pulse is well described by a Gaussian, $I = e^{-(t/\tau)2}$ where τ = 25 ps. On this scale, the OMA displays the 6 ps laser pulse with 5 channel width.

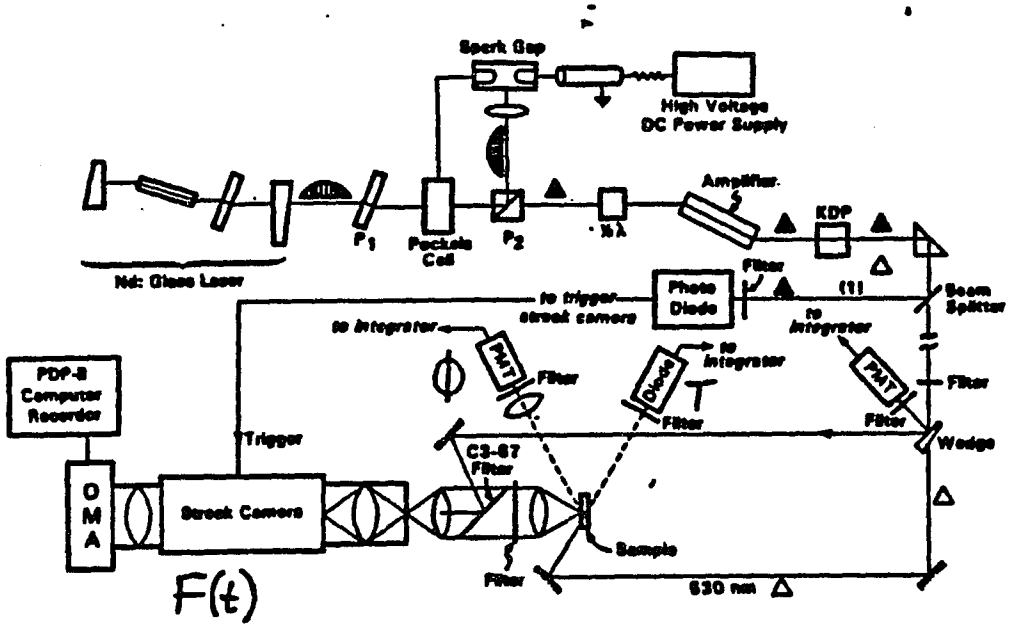

Figure 5.1: Experimental apparatus.

Because the full scale contains 500 channels, on the 2.5 ns scale this corresponds to 25 ps.

The isolation of the α, β subunits and (αβ) monomer are described on page 54. Quantum yield and transmission measurements were obtained as described in chapter 2, on page 39. The absorption and fluorescence spectra were obtained as explained in that chapter on page 56.

Results

5.3 Steady-State Fluorescence and Absorption Spectra

The steady-state absorption and fluorescence spectra of the β subunit and (αβ) monomer are shown in Figures 5.2 and 5.3, respectively. Figure 5.2(A) shows the absorption and fluorescence spectra of the β complex as a function of wavelength. The absorption peak of the β subunit occurs at 551 nm where its extinction coefficient is 315,000 $M^{-1}cm^{-1}$. The fluorescence peak for the β subunit is at 575 nm. The two spectra are nearly mirror images of each other and are similar to those reported by Zickendraht-Wendelstadt et al.[11] for the β subunit isolated from Pseudanabaena W1173. Figure 5.2 shows the 's_β' and 'f_β' components of the absorption spectra of the β subunit. The deconvolution technique, described later, assumes the β subunit contains 2 's' and 2 'f' chromophores. The absorption spectra of the 's_β' and 'f_β' spectra shown are each the summation of the spectra of the two chromophores contained in that class. The two spectra are nearly identical as a function of wavelength. Both have special peaks at about 550 nm. The deconvolution indicates it would be virtually

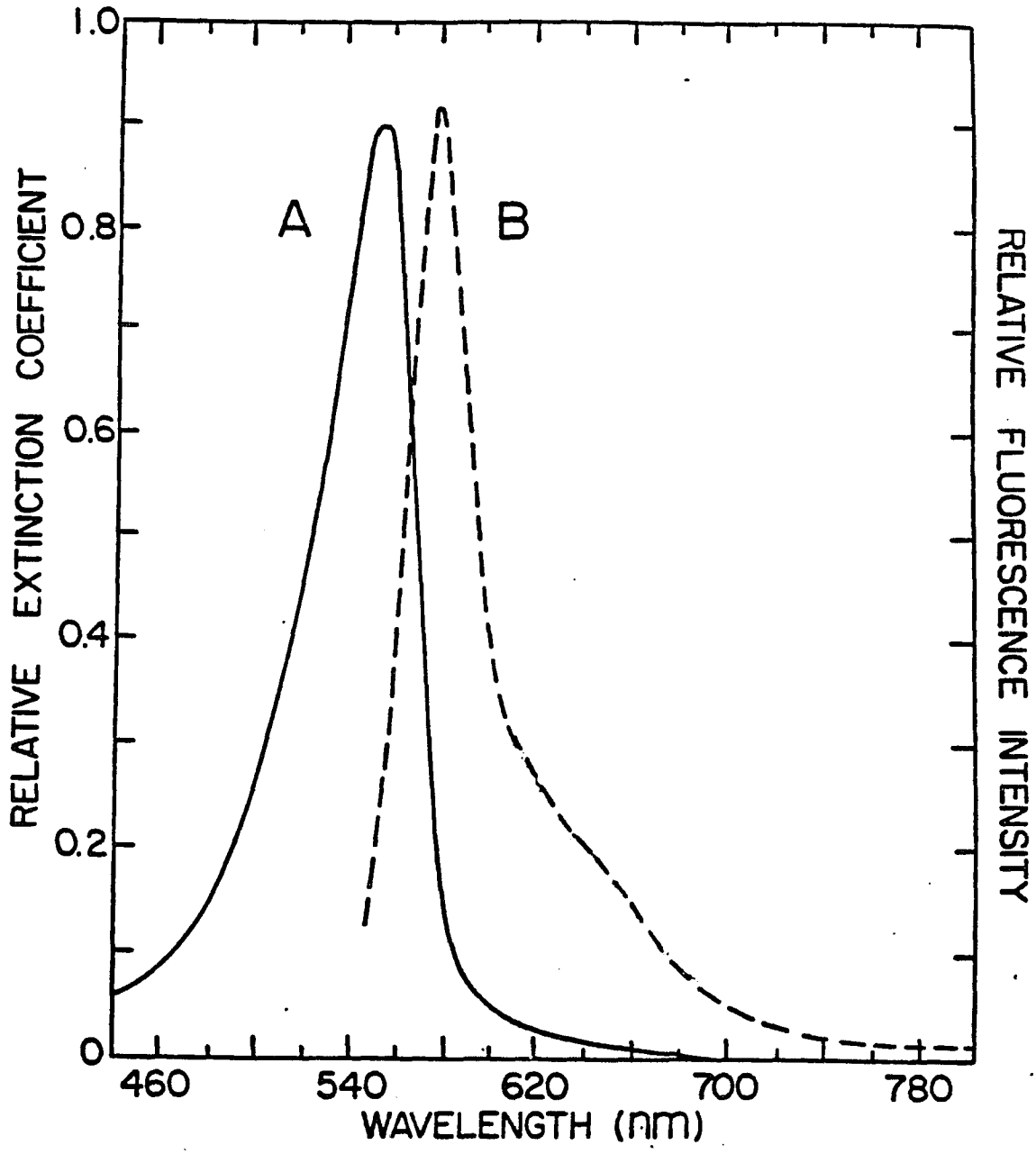

Figure 5.2(A): Absorption (solid line) and fluorescence (dashed line) spectra of β subunit.

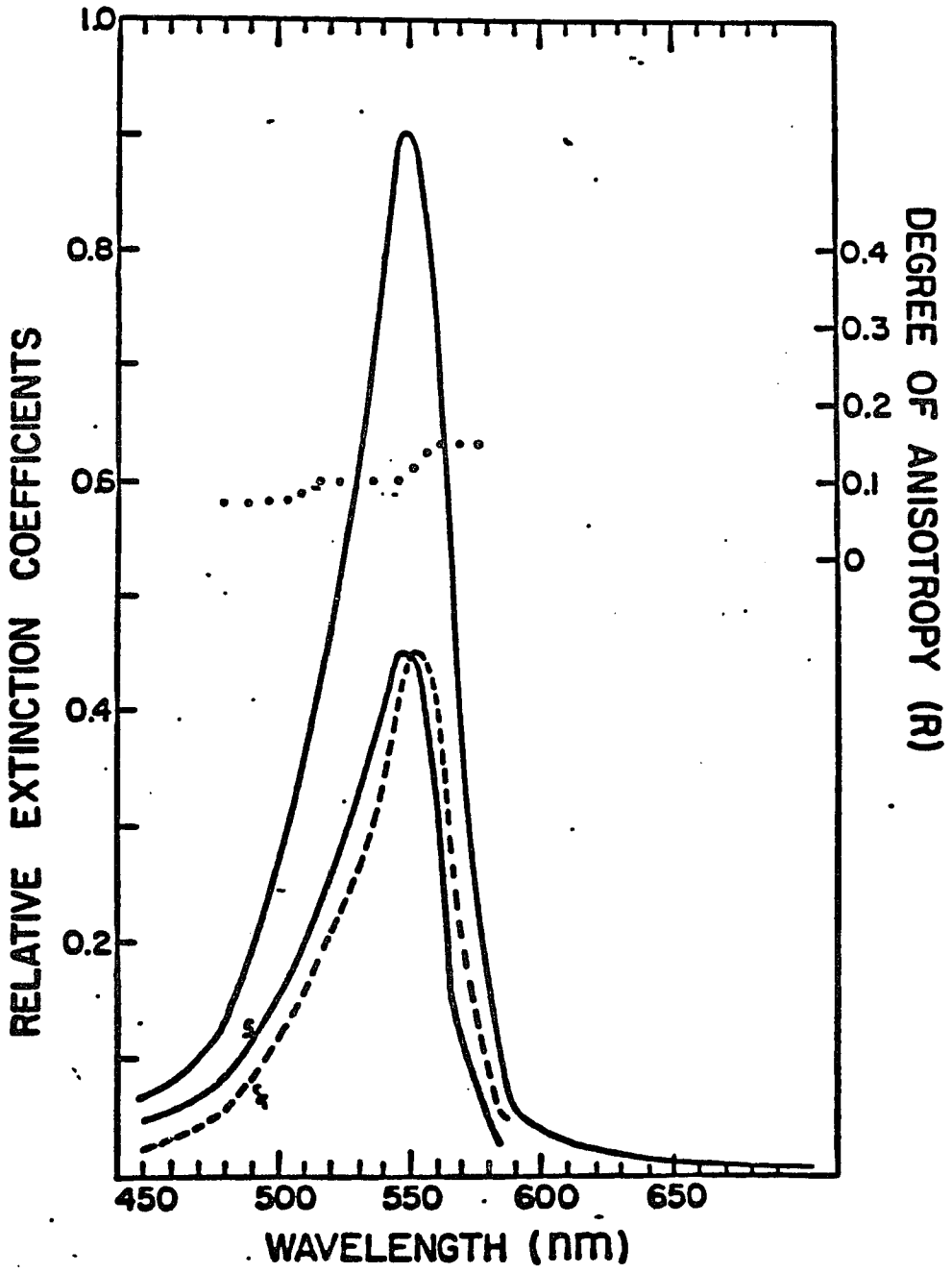

Figure 5.2(B): Deconvolution of β absorption spectra into its 's' and 'f' components assuming existence of 2's' and 2'f' chromophores. Solid line denotes the 's' components dashed line corresponds to 'f' components. Dots represent experimental steady-state polarization data, crosses (+) correspond to the theoretically obtained polarization data using the 's' and 'f' spectra.

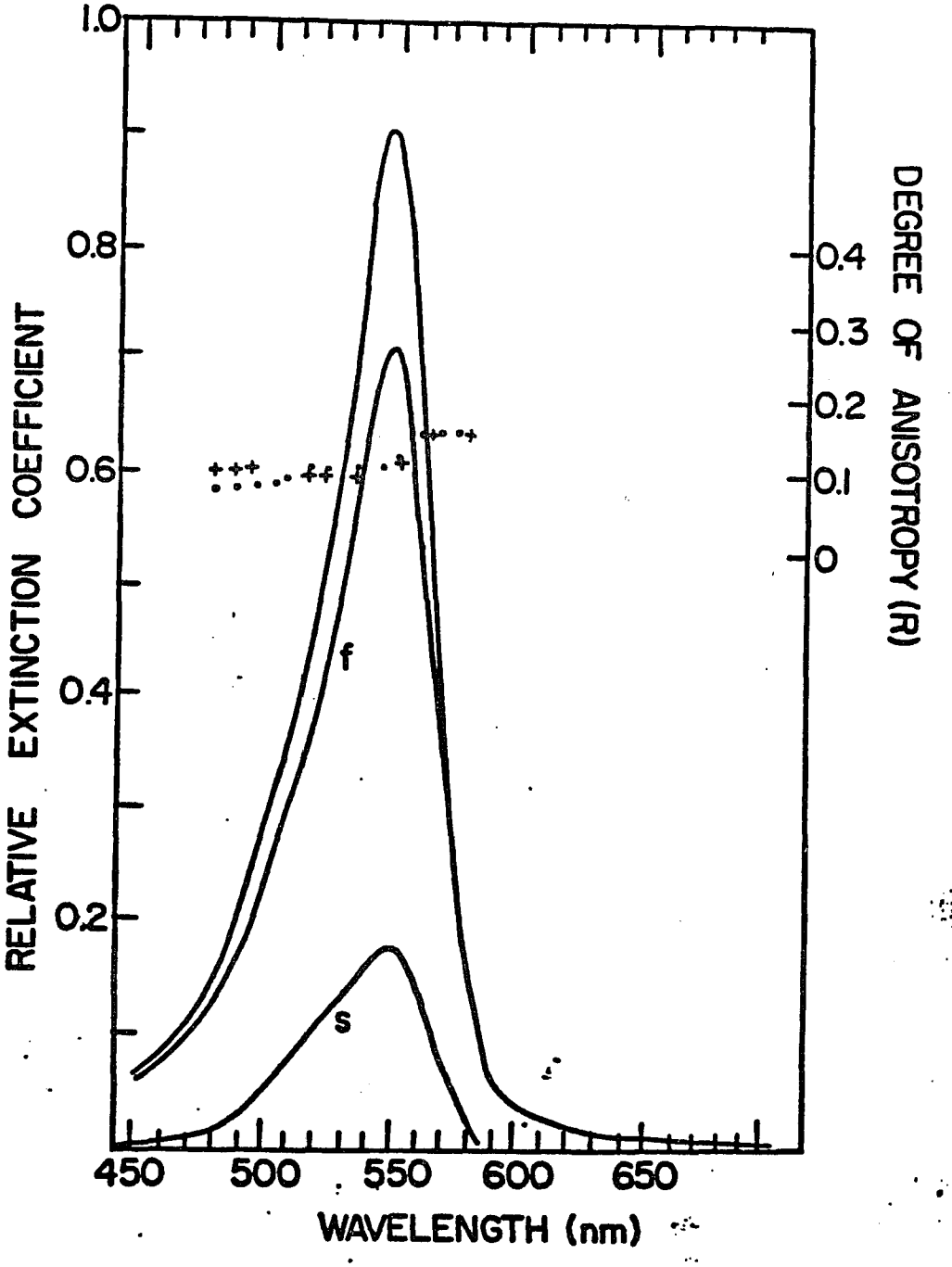

Figure 5.2(C): Deconvolution of β absorption spectra using mirror image of its fluorescence spectra. Dots correspond to experimental steady-state polarization dots, crosses (+) to the theoretically obtained polarization data using the 's' and 'f' spectra.

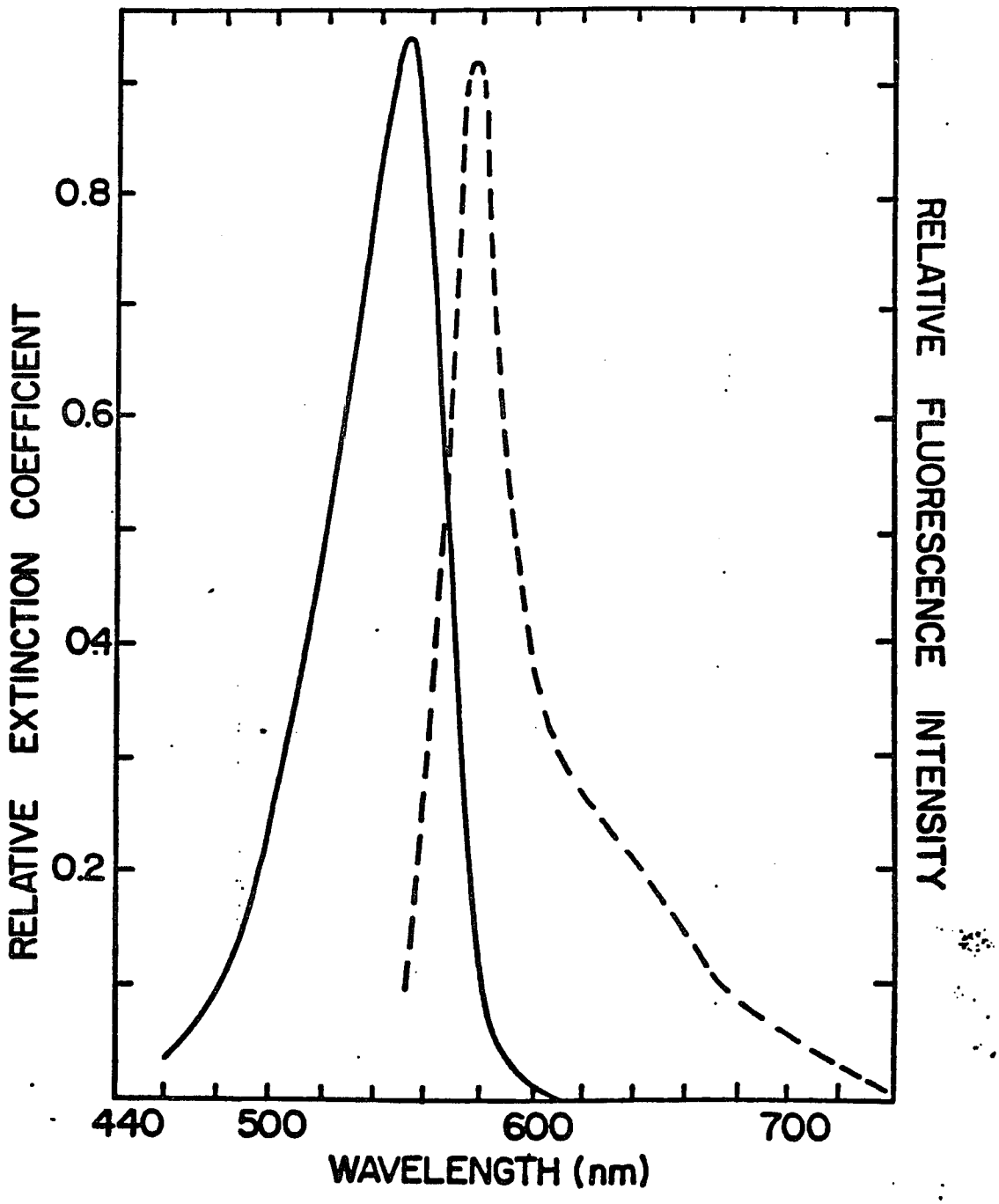

Figure 5.3A: Absorption (solid line) and fluorescence (dashed line) spectra of (αβ) monomer.

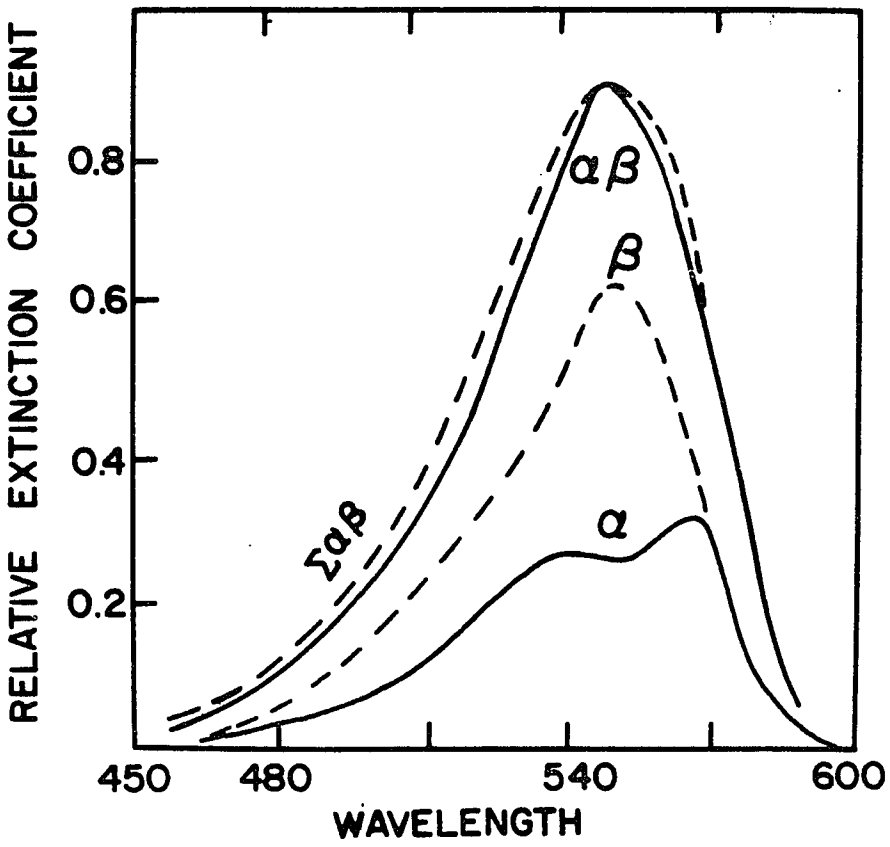

Figure 5.3(B): Absorption spectra α subunit (solid line) β, subunit (dashed line), (αβ) subunit (solid line) and summation of the α and β absorption spectra (dashed line).

impossible to spectrally isolate the fluorescence of the two chromophores. Indeed, we were unable to spectrally analyze the fluorescence with the use of filters looking at regions beyond 580 nm (2-59) filter), in the 580 nm region (580 NB) and below 560 nm (560 SP). The 2-59 filter is transparent to wavelengths beyond 580 nm. The 560 SP is transparent to wavelengths below 560 nm. The 580 NB filter is a narrow band filter permitting just wavelengths from 575 nm to 585 nm to pass. As explained later, the experimental polarization spectra (dots in Figure 5.2(B)) can be explained by using the deconvoluted spectra.

Because more than one 'f' chromophore is assumed, using the method of mirror images to deconvolute the R absorption spectrum into its 's' and 'f' components is inaccurate. Figure 5.2(C) shows the deconvolution one would obtain assuming the existence of one 'f_β' chromophore in the β subunit and using mirror images. The s_β chromophore never accounts for more than 20% of the absorption curve. Both peaks occur at about 550 nm. In addition, there is no 's_β' contribution past 580 nm, implying the kinetics should be able to be spectrally resolved. We were unable, however, to experimentally spectrally resolve the fluorescence kinetics of the subunit. As explained later, the theoretically obtained polarization data (crosses) using the 's_β' and 'f_β' spectra are nearly identical with the experimentally obtained spectra (dots).

Figure 5.3(A) displays the steady-state absorption (solid line) and fluorescence (dashed) line of the (αβ) monomer as a function of wavelength. The peak of the absorption curve occurs at 548 nm where

its measured extinction coefficient is 445, 000 M^{-1} cm^{-1}. The fluorescence spectra peaks at about 578 nm.

Figure 5.3(B) presents the addition of the absorption spectra of the isolated α and β subunits, and the absorption spectra of the (αβ) monomer. The figure shows that the addition of the spectra of the two isolated subunits is nearly identical with that of the aggregated monomer. As a result, one may assume that the absorption spectra of the chromophores in the isolated subunits do not change very much when they aggregate into the monomer.

Figure 5.4 displays the relative energy levels of the individual chromophores of the α and β subunits in the (αβ) monomer. As previously reported, the peak of the absorption spectra of the s_α chromophore occurs at about 540 nm. The peak of the f_α chromophore occurs at about 568 nm. Figure 5.2(B) shows the absorption spectra of the s_β chromophore occurs at about 548 nm, with that of the f_β chromophore red-shifted by about 5 nm. For simplicity, we label the s_β chromophores 1 and 2; chromophores 3 and 4 refer to the f_β chromophores; chromophore 5 is the s_α while the chromophore 6 refers to the f_α chromophore.

5.4 Fluorescence Kinetics and Relative Quantum Yield

Figure 5.5A shows the fluorescence kinetics of the α subunit,[18] reproduced in this paper for completeness. The shape of the fluorescence profile is intensity independent from 4 x 10^{13} to

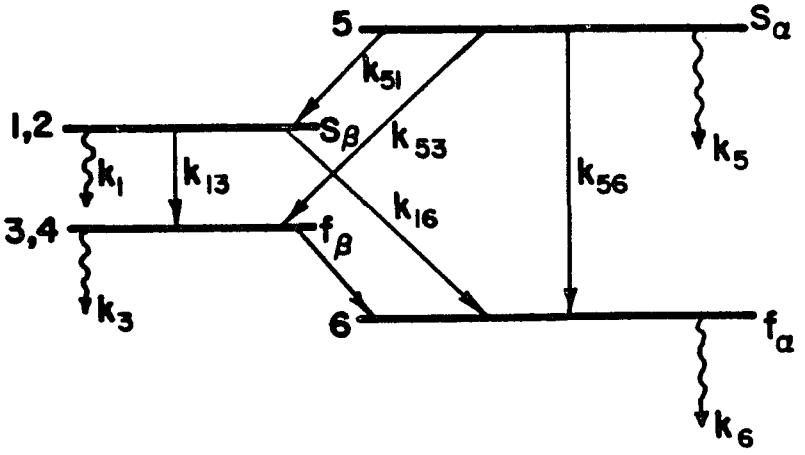

Figure 5.4: Relative energy levels of peaks of absorption spectra of the s and f chromophores of the α and β subunits when aggregated into the (αβ) monomer. s_β chromophores are numbered 1 and 2, f_β are 3 and 4. s_α is denoted as chromophore 5 and f_α as 6. Also shown are the energetically permissable transfer pathways which were considered in fitting the fluorescence kinetics.

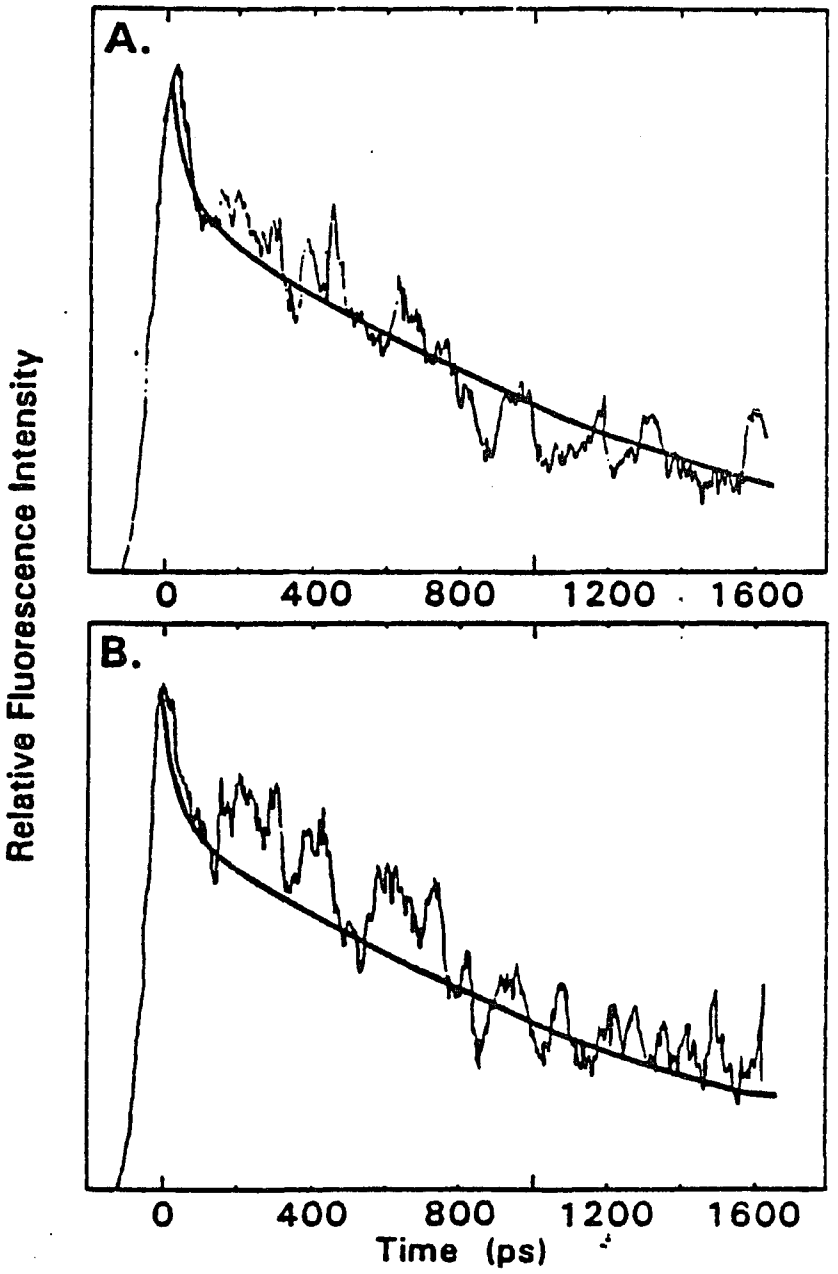

Figure 5.5A: Fluorescence kinetics of (α) subunit at low intensity (upper) and high intensity (lower) fit to Paillotin-Swenberg theory for r = 0.05, z = 0.5.

4×10^{15} photons/cm^2 per pulse. The decay profile is doubly exponential with an overall e^{-1} time of approximately 1.1 ns. It is well fit by $0.79 \exp(-k_1 t) + (0.19) \exp(-k_2 t)$ for $k_1 = 8.76 \times 10^8$ sec^{-1} and $k_2 = 3.68 \times 10^{10}$ sec^{-1}. This biexponential expression corresponds to $r = 0.05$ and $z = 0.5$ in the Paillotin formalism.[21] Figure 5.5B is the average of 10 curves.

The fluorescence kinetic profiles for the β subunit at high and low fluence are shown in Figure 5.6. The risetime of emission, measured on the 500 ps scale, was within the 12 ps resolution of the streak camera--OMA system on that time scale. The shape of the fluorescence profiles are fluence independent over the 40 field intensity range investigated (5×10^{13} to 3×10^{15} ph/cm^2 per pulse). The decay profiles can be fitted to a double exponential with an overall e^{-1} time of approximately 400 ps. It is well fit by $0.65 \exp(-k_1 t) + 0.35 \exp(-k_2 t)$ for $k_1 = 1.0 \times 10^9$ sec^{-1} and $k_2 = 2.2 \times 10^{10}$ sec^{-1}. This corresponds to $r = 0.1$ and $Z = 1.0$ in the Paillotin formalism.

Figure 5.7 displays the fluorescence decay profiles of the (αβ) monomer at high and low excitation intensities. The shape of the fluorescence decays is intensity independent over the intensity range investigated (4.0×10^{13} to 2×10^{15} ph/cm^2 per pulse). The decay is well described by a multiexponential ($r = 0.5$, $z = 5.0$ in the Paillotin formalism) with an e^{-1} time of approximately 200 ps. It is well

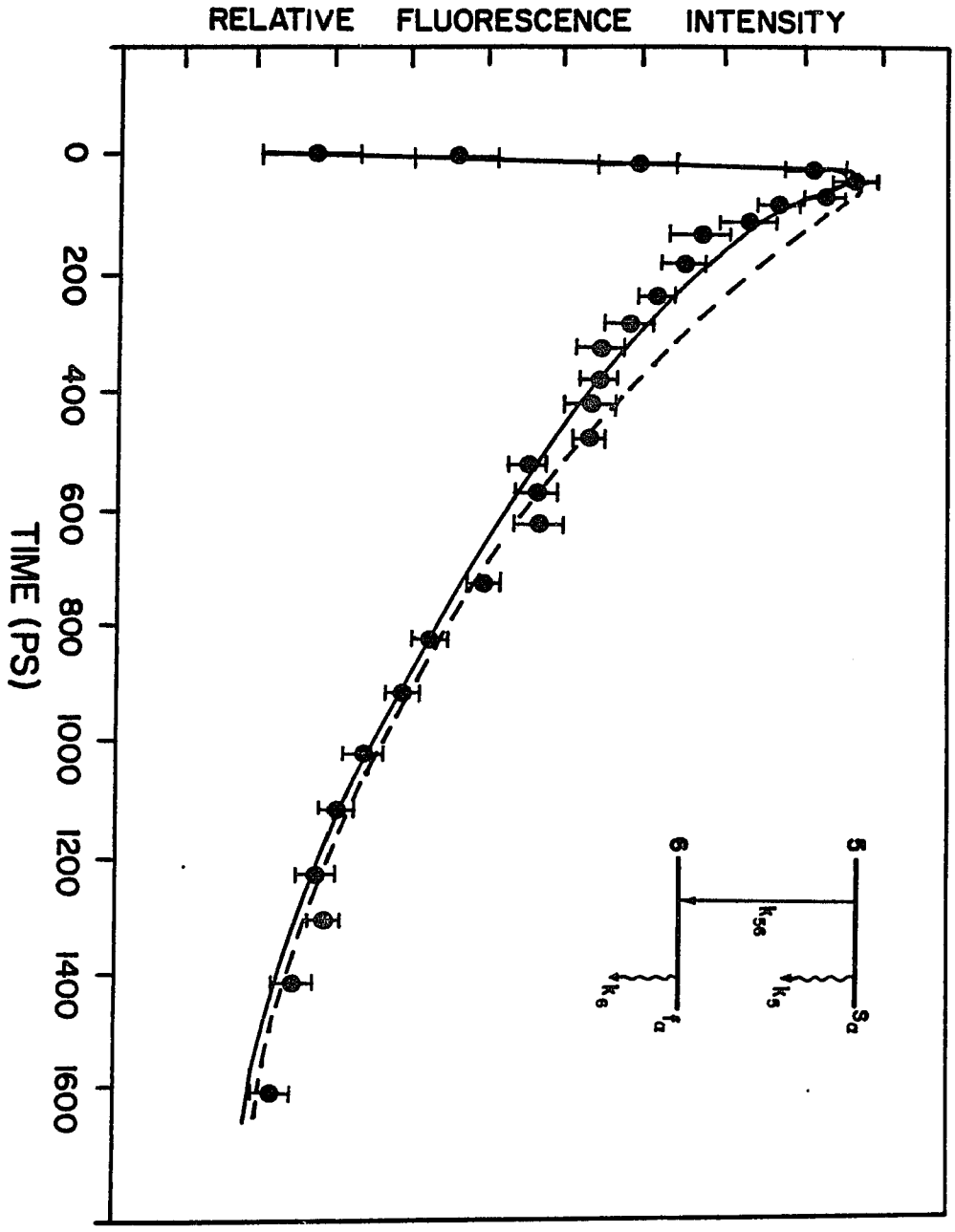

Figure 5.5B: Fluorescence kinetics of α subunit for k_{sr} = k_{fr} = 0.8:1.2. Solid line (curve 1) is for k_6 = 1.0 x 10^9 sec^{-1} k_{56} = 1 x 10^{10} sec^{-1}, and k_s = 1.0 x 10^{10}. Dashed line (curve 2) is result when k_{56} is doubled to 2 x 10^{10} sec^{-1}. Inset shows energy pathways and identification of chromophores. Average of 10 curves.

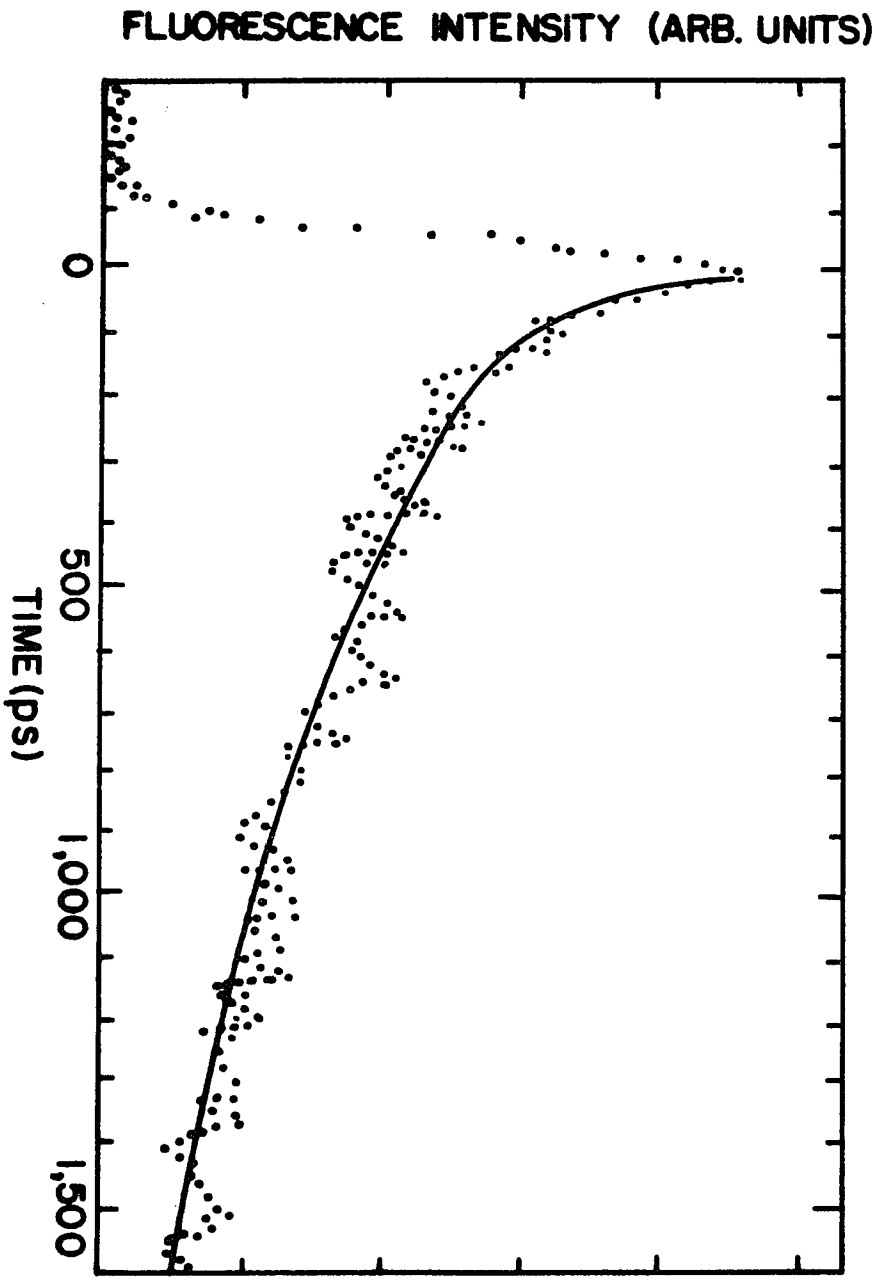

Figure 5.6A: Fluorescence kinetics of (β) subunit at low intensity (5.46×10^{13} photons-cm^2) fit to Paillotin-Swenberg theory for r = 0.1, z = 1.0.

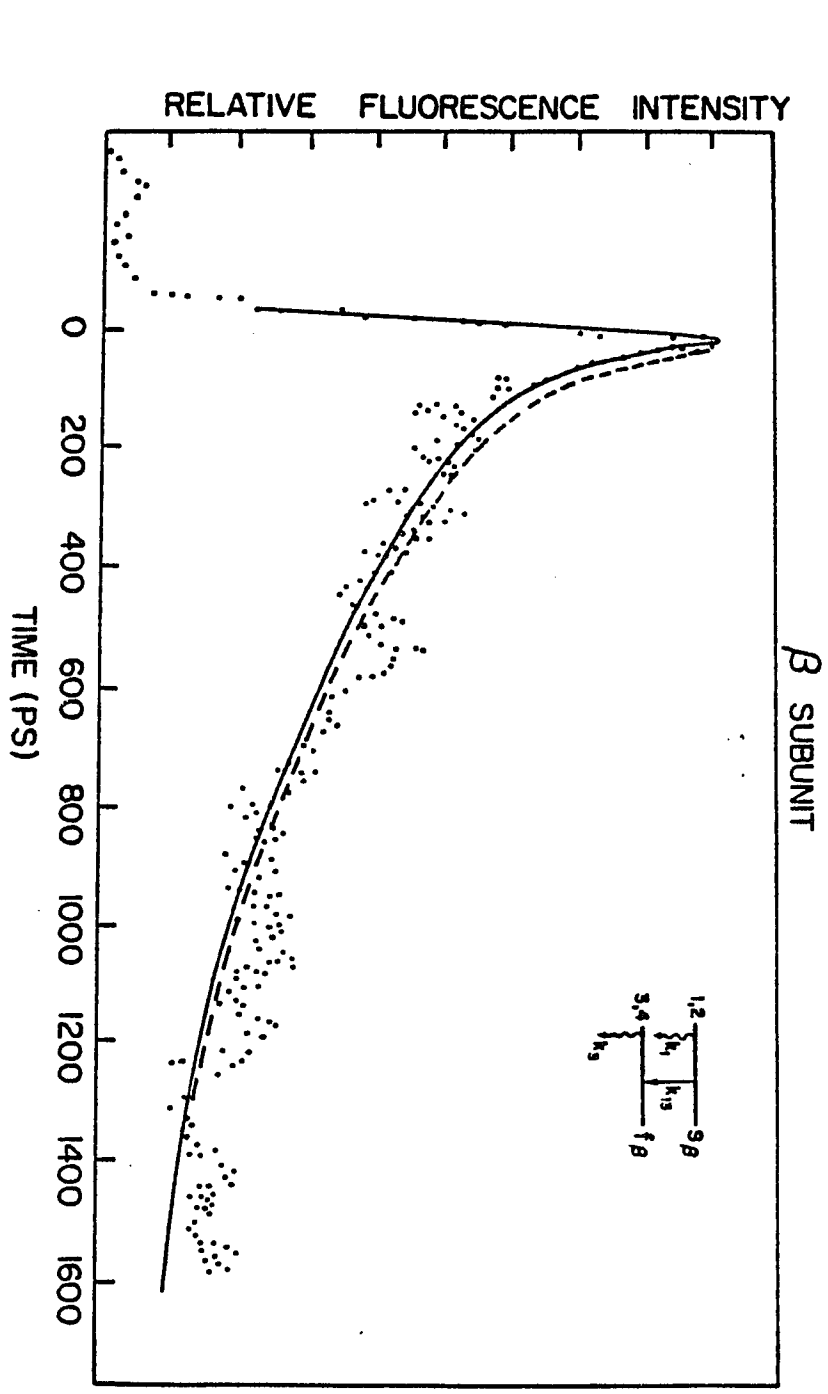

Figure 5.6B: Fluorescence kinetics of β subunit for $k_{sr} : k_{fr}$ = 1.0:1.0. Solid line (curve 1) is for $k_3 = k_4 = 1.2 \times 10^9$ sec^{-1}, $k_{13} = k_{23} = k_{14} = k_{24} = 1.5 \times 10^9$ sec^{-1} and $k_1 = k_2 = 1.5 \times 10^{10}$ sec^{-1}. Dashed line (curve 2) is result when $s_\beta \rightarrow f_\beta$ transfer rate is doubled to 3.0×10^9 sec^{-1}. Inset identifies chromophores and pathways. Intensity is 2×10^{15} photons-cm^{-2}.

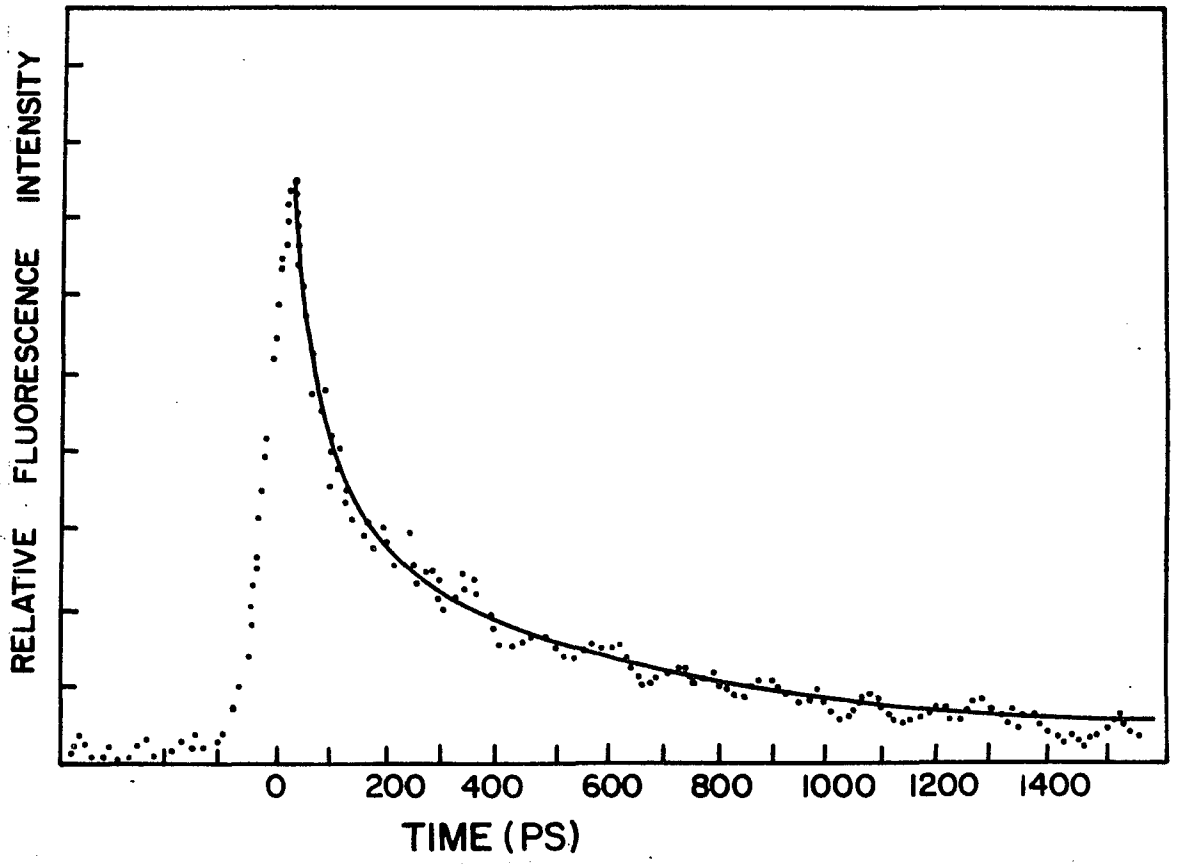

Figure 5.7A: Fluorescence kinetics of (αβ) monomer at low intensity (4×10^{13} photons-cm^{-2}) fit to Paillotin-Swenberg Theory for values r = 0.5, z = 5.0.

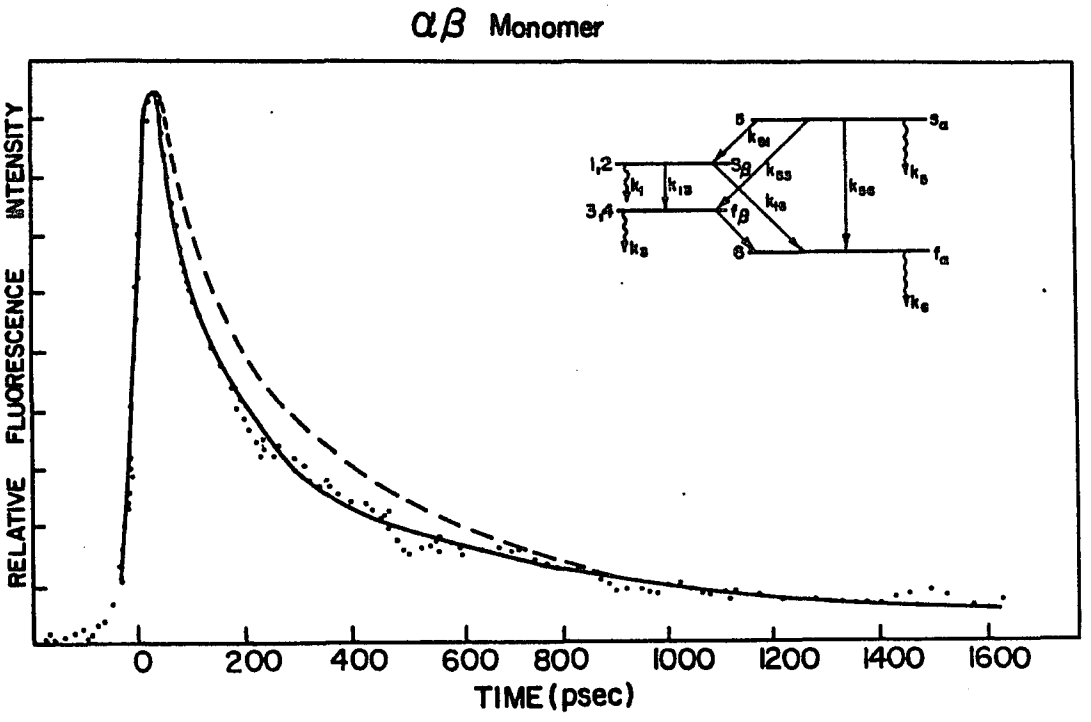

Figure 5.7B: Fluorescence kinetics of (αβ) monomer. Curve 1 (dashed line) for k^{β}_{sr}: k^{β}_{fr}: k^{β}_{sr} : k^{β}_{fr} = 1.0 : 1.0: 0.8: 1.2 and $k_{13} = 1.5 \times 10^{9}$ sec^{-1}, $k_{56} = 1.0 \times 10^{10}$ sec^{-1}, $k_{16} = 1 \times 10^{9}$ sec^{-1}, $k_{36} = 0$, $k_{51} = k_{53} = 3 \times 10^{9}$ sec^{-1}, $k_{6} = 1.2 \times 10^{9}$ sec^{-1}, $k_{5} = 1.0 \times 10^{10}$ sec^{-1}, $k_{1} = 1.5 \times 10^{10}$ sec^{-1}, $k_{3} = 8.0 \times 10^{9}$ sec^{-1}. Curve 2 (dashed line and circles) shows effect of letting $k_{3} = 4 \times 10^{9}$ sec^{-1}. Inset identifies chromophores and energy pathways. Intensity is 2.0×10^{15} photons-cm^{-2}.

described by $\Sigma A_i e^{-k_i t}$ for $A_1 = 0.27$, $A_2 = 0.36$, $A_3 = 0.23$, $A_4 = 0.10$ and $A_5 = 0.03$; $k_1 = 1.0 \times 10^9$ sec^{-1}, $k_2 = 6.0 \times 10^9$ sec^{-1}, $k_3 = 1.5 \times 10^{10}$ sec^{-1}, $k_4 = 2.8 \times 10^{10}$ sec^{-1}, and $k_5 = 4.5 \times 10^{10}$ sec^{-1}.

Figure 5.8 shows the relative quantum yield data and transmission data as a function of pulse intensity for the β and (αβ) units. As in the case of the α subunit, the transmission data in β and (αβ) are nearly the mirror image of the apparent quantum yield. The transmission curves in both units depart from the low intensity value at approximately 1.0 to 2 x 10^{14} photons/cm^2. The solid lines indicate the theoretical fits of the relative quantum yield using the formalism of Paillotin.[21] For β r = 0.1, and for (αβ) r = 0.5. The apparent excellent agreement between theory and experiment is deceptive as will be discussed later in this chapter.

5.5 Discussion: 's' and 'f' Absorption Spectra and Polarization

The separation of the absorption spectra of the β subunit into its 's' and 'f' components satisfies the following criteria:

1. The theoretical steady-state polarization dependence on wavelength agrees with the experimental polarization measurements and,

2. The ratio of the peak to the shoulder of the deconvoluted absorption curves is the same as that of the fluorescence curve.

Because the β subunit may contain more than one 'f' chromophore, using the method of mirror images to obtain the absorption spectra of

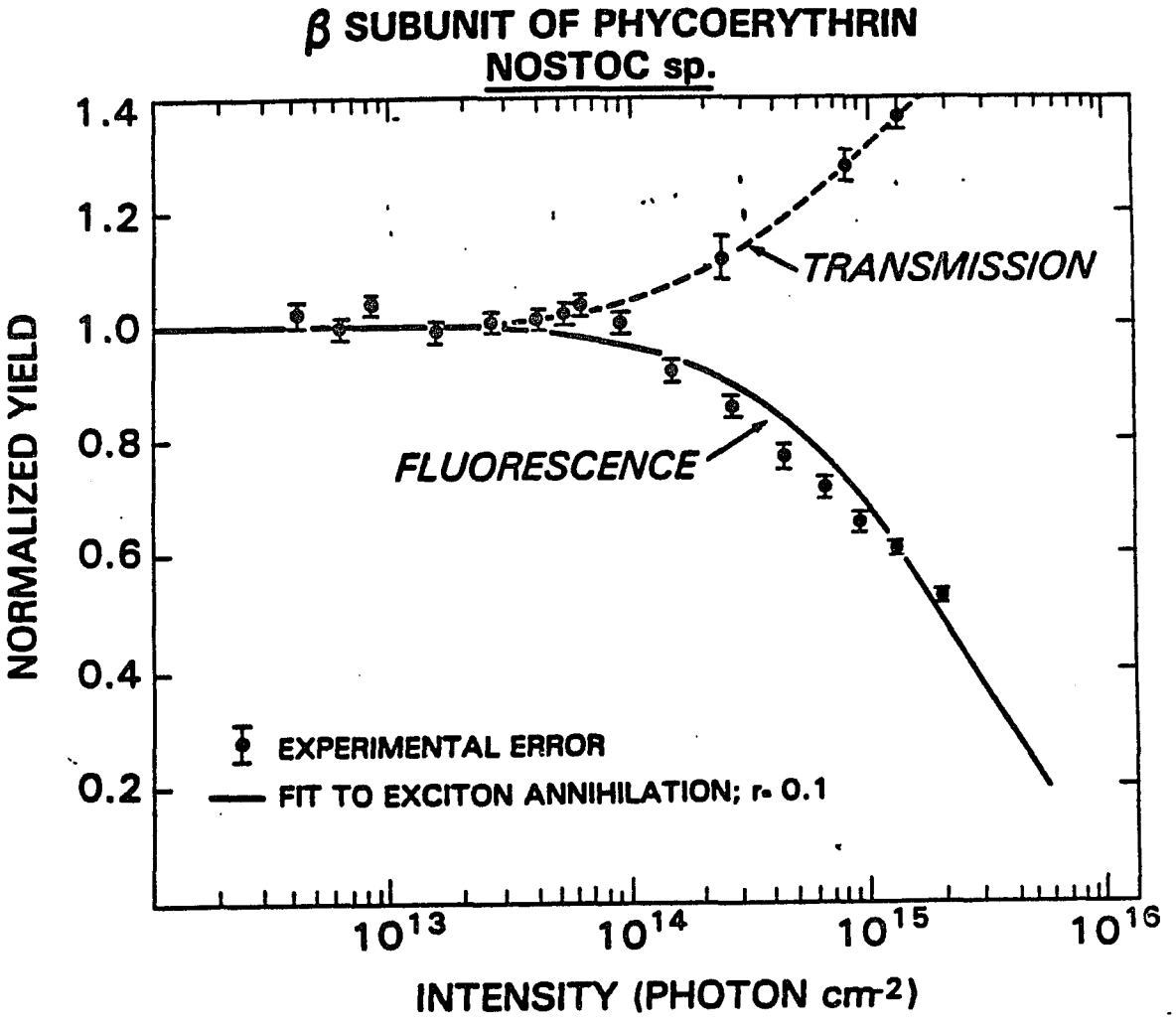

Figure 5.8A: Relative fluorescence quantum yield (solid line) and transmission data (dashed line) of (β) vs. pulse intensity. Solid line denotes fit of apparent quantum yield to Paillotin-Swenberg annihilation theory for r = 0.1.

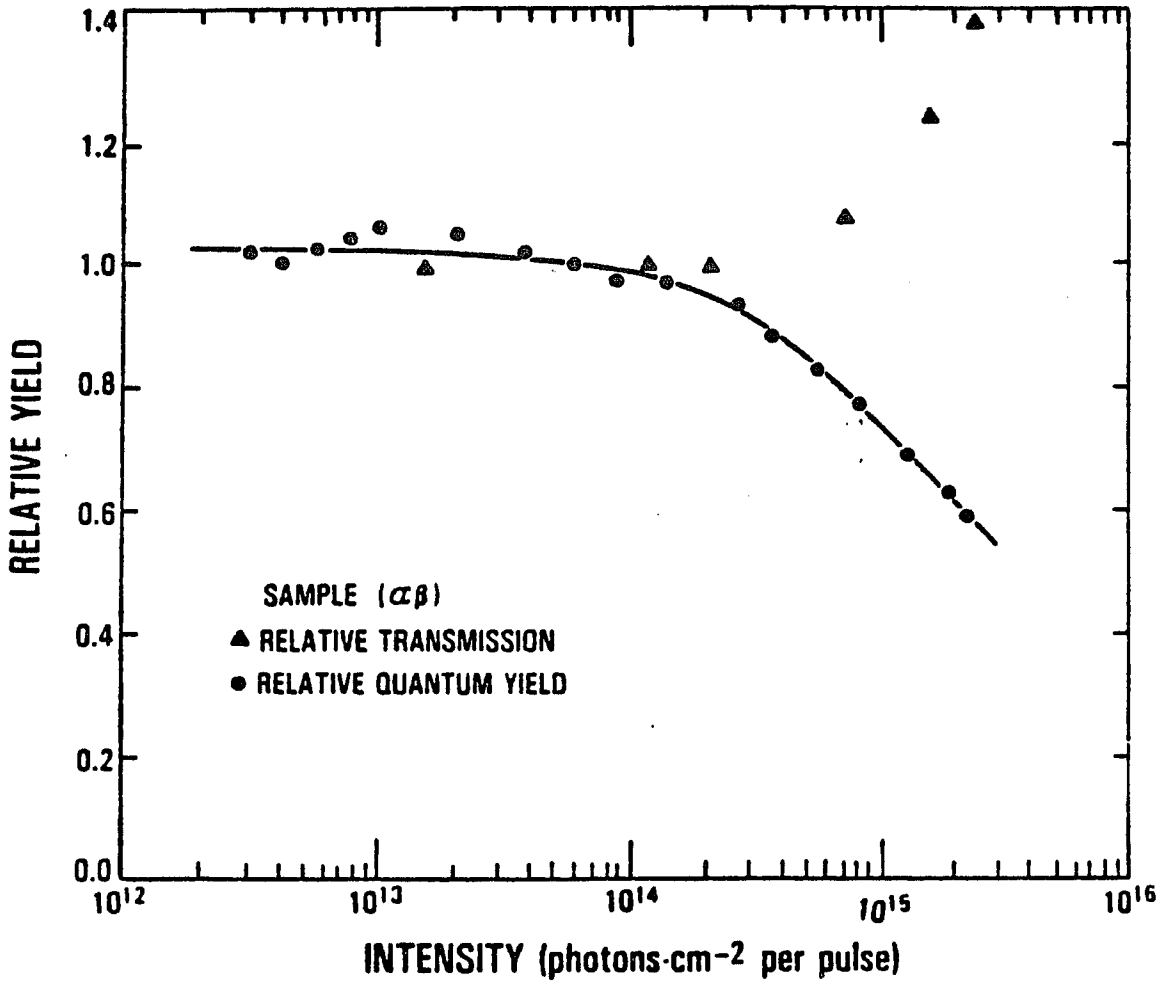

Figure 5.8B: Relative fluorescence quantum yield (solid dots) and transmission data (triangles) of (αβ) vs. pulse intensity. Solid line denotes fit of apparent quantum yield to Paillotin-Swenberg annihilation theory for r = 0.5.

the 's' and 'f' chromophore is inappropriate. For the sake of symmetry, we postulate the existence of two 's' and two 'f' chromophores in the β subunit. An implication of this assumption on the deconvolution as shown in Figure 5.2B, is that it is not possible to spectrally separate and analyze the fluorescence kinetics. This is consistent with the experimental evidence that the fluorescence kinetics do not change when different spectral regions of the fluorescence kinetics are examined. We examined the fluorescence for wavelengths beyond 580 nm, around 580 nm and below 560 nm. The kinetics were the same in all regions.

A characteristic feature of the measured anisotropy (R) shown in Figure 5.2(C) is the presence of very little structure and nearly constant value of 0.11 for wavelengths between 480 nm and 550 nm, its monotonic increase for $\lambda \sim$ 550-570 nm, and its saturation at 0.16 for $\lambda >$ 580 nm. Consistency of the experimental values (R_m) of R with the deconvoluted spectrum is afforded by comparing R_m with the calculated weighted sum of the anisotropy (R_w) of the individual absorption band, i.e.:

$$R_w = \frac{\sigma_s(\lambda)R_s + \sigma_f(\lambda)R_f}{\sigma_s(\lambda) + \sigma_s(\lambda)} \qquad (5.5.1)$$

where R_s and R_f are the degree of anisotropy associated with direct excitation of the s and f chromophores respectively. The values of $R_f = 0.15$ and $R_s = 0.01$ yield an excellent fit between the measured and theoretically obtained polarization points.

The α unit of this alga contains only two chromophores. As a result, if only one of them is assumed to be the f chromophore, the method of mirror images is appropriate (see reference 18 for details). We have conducted a complete study of the α subunit in the previous chapter.

5.6 Determination of the Radiative Rates

The fluorescence decays are determined by the populations of the excited states of chromophores as a function of time, and weighed by their respective radiative rates. Thus the fluorescence kinetics is described by:

$$F(t) = \sum k_i^r p_i(t) \qquad (5.9.1)$$

where k_i^r is the radiative rate of the i^{th} chromophore and $p_i(t)$ is the population of the excited state of the i^{th} chromophore. Inferring values for k_i^r is a difficult task for overlapping bands.

The radiative rates of the 's' and 'f' chromophores of each subunit were obtained from their respective deconvoluted absorption curves by using the Einstein relationships:

$$k_r = 2.88 \times n^2 \times 10^{-9} \int \frac{(2\tilde{\nu}_o - \tilde{\nu})^3}{\tilde{\nu}} \varepsilon(\tilde{\nu})\, d\tilde{\nu} \ \text{sec}^{-1} \qquad (5.9.2)$$

where $\tilde{\nu}_o$ is the wave number of the mirror symmetry point, $\varepsilon(\tilde{\nu})$ is the absorption coefficient at wave number $\tilde{\nu}$, and n is the index of

refraction. For the α and β subunits and (αβ) monomer n is approximately 1.5.

The radiative rates for the 's' and 'f' chromophores of the subunit was obtained by integrating under the appropriate absorption curves in Figure 5.2B. The integral was done numerically for every 2 cm^{-1} in wave number. The value of 1.78×10^4 cm^{-1} was used for the wave number of the mirror symmetry point, $\tilde{\nu}_o$. Because the 's' and 'f' absorption bands each correspond to two chromophores, the results were divided by two to obtain the radiative rate of each 's' and each 'f' chromophore in the subunit. Using this technique, the radiative rate of each chromophore in the subunit is approximately 2.6×10^8 sec^{-1}. The same method for the α subunit yields values of 2.1×10^8 sec^{-1} for the radiative rate of the 's_α' chromophore and 3.1×10^8 sec^{-1} for the radiative rate of the 'f_α' chromophore. We believe these numbers are accurate to within a factor of 2.0. The radiative rates of the various chromophores are, thus

$$k_1^r = k_2^r = k_3^r = k_4^r = 2.6 \times 10^8 \text{ sec}^{-1} \qquad (5.9.4)$$

$$k_5^r = 2.1 \times 10^8 \text{ sec}^{-1}$$

$$k_6^r = 3.1 \times 10^8 \text{ sec}^{-1}$$

where the number of the chromophore corresponds to those described in the Figure 5.4 caption. For the rest of this chapter, we shall use the following notation: k_{sr}^{α} for the radiative rate of the 's ' chromophore of the α, k_{fr}^{α} for the radiative rate of the 'f ' chromophore of the α

and similarly for the β subunit. Thus $k^{\alpha}_{sr} = 2.1 \times 10^{8}$ sec^{-1} $k^{\alpha}_{fr} = 3.1 \times 10^{18}$ sec^{-1} and $k^{\beta}_{sr} = k^{\beta}_{fr} = 2.6 \times 10^{8}$ sec^{-1}.

The simple addition of the absorption spectra of the isolated α and β subunits is virtually identical to the absorption spectra of the αβ monomer as Figure 5.3B illustrates. As a result, the spectra of the 's' and 'f' chromophores of the isolated units do not change greatly when aggregated into the monomer. Thus it is not unreasonable to assume that the radiative rates of each chromophore do not change significantly on aggregation into the monomer state. For the values obtained above, the relative ratios of various chromophores are:

$$k^{\beta}_{sr}:k^{\beta}_{fr}:k^{\alpha}_{sr}:k^{\alpha}_{fr} = (2.6 \times 10^{8}):(2.6 \times 10^{8}):(2.1 \times 10^{8}):(3.1 \times 10^{8}) \tag{5.9.5}$$

that is, 1:1:0.8:1.2. Similarly, the ratio of the radiative rates of the 's' and 'f chromophores of the α subunit is

$$k^{\alpha}_{sr}: k^{\alpha}_{fr} = 0.8:1.2 \tag{5.9.6}$$

The ratio of the radiative rates of the 's ' and 'f ' chromophores of the β subunit is, approximately,

$$k^{\beta}_{sr} : k^{\beta}_{fr} = 1.0:1.0 \tag{5.9.7}$$

Determining the radiative rates is highly dependent on the value of $\tilde{\nu}_o$ chosen. For the assumed absorption spectra, we estimate the radiative rates to be accurate to better than a factor of two.

5.7 Analysis of Fluorescence Kinetics

Figures 5.5, 5.6 and 5.7 display the fluorescence kinetics of the α, β and (αβ) units, respectively. In Figures 5.5A, 5.6A, and 5.7A, the kinetics are fit to the Paillotin annihilation theory.[21] The curves are fit from the peak. As described later, this theory is not appropriate for these subunits. All bimolecular theories predict a change in the fluorescence decay kinetics as a function of excitation intensity. The fluorescence kinetics of our samples are, however, intensity independent. The multiexponential fits are described in the results section and in the figure captions.

Figures 5.5B, 5.6B and 5.7B fit the entire fluorescence kinetic curves (including risetimes) to the appropriate energy transfer scheme, shown in the insets of the figures. The α subunit is fit to one s_α chromophore transferring energy to the f_α chromophore. Back transfer is neglected and both chromophores are assumed to fluoresce. For the β subunit each of two 's_β' chromophores is assumed to transfer excitation energy to each of two 'f_β' chromophores. All four chromophores fluoresce. The (αβ) scheme utilizes parameters inferred from the individual chromophores of the isolated α and β subunits. The order of the energy levels are from highest energy to lowest energy the s_α, s_β, f_β and f_α chromophores. Transfer is allowed from any chromophore to a lower energy chromophore and all six chromophores fluoresce. In all the complexes, the strengths of the fluorescence of each chromophore is weighted by its respective radiative rates.

The rate constants of all the subunits are summarized in Table 5.1.

5.8 Fluorescence Kinetics

5.8a. β Subunit

Figure 5.6B shows the fit of the fluorescence kinetics of the subunit to a model of two 's_β' and two 'f_β' chromophores. Energy transfer from each 's_β' chromophore to each 'f_β' chromophore is allowed. All chromophores are assumed to fluoresce. The insert shows the chromophore indices and the energy transfer scheme. Chromophores 1 and 2 refer to the 's_β' chromophores, while 3 and 4 refer to the 'f_β' chromophores. As described above the radiative rates of all the chromophores are equal. For reasons of symmetry, we set the fluorescence rates of the 's_β' chromophores in the absence of energy transfer equal ($k_1 = k_2$), as well as those of the 'f' chromophores ($k_3 = k_4$). The $s_\beta \rightarrow f_\beta$ transfer rate from each s_β to each f_β is set equal, and is denoted in the β unit by k_{13}.

The appropriate differential equations in the β subunit are:

$$p_1 = -k_1 p_1 - (k_{13} + k_{14})p_1 + \sigma_1 I = k_1 p_1 - 2k_{13} p_1 + \sigma_1 I$$

$$p_2 = -k_2 p_2 - (k_{23} + k_{24})p_2 + \sigma_2 I = - k_1 p_2 - 2k_{13} p_2 + \sigma_2 I$$

$$p_3 = k_{13} p_1 + k_{23} p_2 - k_3 p_3 + \sigma_3 I = + k_{13}(p_1 + p_2) - k_3 p_3 + \sigma_3 I$$

$$p_4 = k_{14} p_1 + k_{24} p_2 - k_4 p_4 + \sigma_4 I = k_{13}(p_1 + p_2) - k_3 p_4 + \sigma_4 I$$

where p_1 and p_2 denote the 's' chromophore excited state populations and p_3 and p_4 those of the 'f' chromophores. k_{ij} refers to the s → f transfer rate from chromophore i to chromophore j, k_i to the

fluorescence decay rate in the absence of energy transfer of chromophore i. The relative absorption coefficients σ_i are determined from the absorption curves at 530 nm. For the β subunit, $\sigma_1 = \sigma_2 = .275$ and $\sigma_3 = \sigma_4 = .225$. Direct excitation by the laser pulse of all the chromophores is suggested by the fast rise-times of the kinetics. If only the 's_β' chromophores were excited, a rise-time on the order of the s → f transfer time would be noticed. The pulse width of the laser pulse on the 2.5 ns time scale is described by $I(t) = e^{-(t/\tau)}$ for $\tau = 25$ ps. As explained above, we set $k_{13} = k_{14} = k_{23} = k_{24} = k_{12}$ and $k_3 = k_4 = k_3$ and $k_1 = k_2 = k_1$.

The expression for the fluorescence kinetics of the β subunit is given by

$$F(t) = k_{sr}^{\beta} (p_1(t) + p_2(t)) + k_{fr}^{\beta} (p_3(t) + p_4(t)) \qquad (5.10.2)$$

where the radiative rates k_{fr} are used to weight the contributions of the particular chromophore. The best fit to the β fluorescence kinetics is for the parameters $k_{13} = 1.5 \times 10^9$ sec^{-1}, $k_3 = k_4 = 1.2 \times 10^9$ sec^{-1} and $k_1 = k_2 = 1.5 \times 10^{10}$ sec^{-1}. The fluorescence of each chromophore is weighted by the radiative rates of the respective chromophore. These parameters correspond to a transfer rate from each 's' to each 'f' of approximately 666 ps. Both 'f' chromophores have fluorescent decay times in the absence of energy transfer of about 840 ps; those of the 's_β' have decay times of about 70 ps. Changing any rate parameter by a factor of two results in a fit totally outside of

the kinetics. The result of doubling the least sensitive parameter, k_{13}, is shown in the figure.

5.8b. α Subunit

The α subunit is fit to a model of two fluorescing chromophores, with the 's' chromophore (chromophore 5) transferring energy to the 'f' chromophore (chromophore 6). Though a complete analysis of this subunit is to be published,[18] we reproduce the kinetics fits for clarity and completeness in Figure 5.5b.

The equations for the α unit are:

$$p_5 = -(k_5 + k_{56})p_5 + \sigma_5 I \qquad (5.10.3)$$

$$p_6 = k_{56}\, p_5 - k_6 p_6 + \sigma_6 I$$

where p_5 and p_6 are the excited state populations of the 's' and 'f' chromophores, k_5 and k_6 are their respective fluorescence decay rates in the absence of energy transfer and k_{56} is the transfer rate from the 's' to 'f' chromophore. $(k_5 + k_{56})^{-1}$ is the total decay time of the 's' chromophore. The values of σ_i, the respective relative absorption coefficient at the excitation wavelength 530 nm are obtained from the deconvoluted spectra of the two chromophores. The 's_α' absorption coefficient σ_5 is .56, while σ_6 the 'f_α' absorption coefficient is .44 at 530 nm (see reference 17). The characteristics of the 25 ps

Gaussian laser pulse is accounted for by I (t). The fast rise-time of the kinetics, as in the β subunit, suggests direct excitation of both chromophores.

The expression for the observed fluorescence in the α subunit is

$$F(t) = k^{\alpha}_{sr}\, p_5(t) + k^{\alpha}_{fr}\, p_6(t) \qquad (5.10.4)$$

where k^{α}_{sr} and k^{α}_{fr} are the radiative rates on the 's' and 'f' chromophores respectively. The radiative rates weigh the contribution to the fluorescence of each chromophore.

Using the results obtained previously, $k^{\alpha}_{sr} : k^{\alpha}_{fr} = 0.8:1.2$. The best fit for this ratio is for the parameters $k_5 = 1.0 \times 10^{10}$ sec^{-1}, $k_6 = 1.0 \times 10^{9}$ sec^{-1} and $k_{56} = 1.0 \times 10^{10}$ sec^{-1}. The 's' fluorescence decay in the absence of energy transfer has a e^{-1} time of 100 ps and the 'f' fluorescence e^{-1} decay time is 1.0 ns. Both values are quite similar to those obtained in the β subunit. The 100 ps s → f transfer rate in the α subunit is considerably faster than that found in the subunit. Both rates are slower than those reported in higher aggregates where greater coupling amongst chromophores may result in faster transfer rates, or annihilation processes that mask s → f transfer and mislead investigators into thinking they are observing faster rates. The effects of doubling k_{56} is illustrated in the figure.

The kinetic parameters so obtained, when put into the expression for relative quantum yield derived in Dagen et al.[18], correspond to a value of $\phi = 0.23$. This value is in reasonable agreement to the reported experimental steady-state value of (0.46 ± .06). The

discrepancy can be accounted for by the fact that the mirror image deconvolution used in Dagen et al.[18] is an approximation that does not take into account the existence of other decay mechanisms. In addition, the determination of radiative rates using the Einstein relations is also an approximation.

5.8c (αβ) Monomer

Figure 5.7 shows the fluorescence kinetics of the (αβ) subunit. In studying the (αβ) monomer, we assumed the individual chromophores had the same energy levels as in the isolated α and β subunits. As a result, the s_α chromophore is at the highest energy level; the s_β chromophores and f_β chromophores and then f_α chromophore follow in decreasing order. As shown in the inset the numbering system is consistent with those used in the isolated α and β subunits. The s_β chromophores are numbered 1 and 2, f_β chromophores are numbered 3 and 4, the s_α chromophore is numbered 5 and the f_α chromophore is 6. The virtual identity of the summation of the absorption spectra of the α and β subunits with that of the monomer implies that the spectra properties of the individual chromophores is not changed when aggregated into the monomer.

The energetically permissible paths for energy transfer are from s_α to s_β, s_α to f_β, s_α to f_α, s_β to f_β, f_β to f_α and s_β to f_α. As depicted in Figure 5.7, we assumed the following simplifications.

$$k_{13} = k_{23} = k_{14} = k_{23} = k_{24} \ (s_\beta \text{ to } f_\beta \text{ transfer rate})$$

$$k_{16} = k_{26} = k_{26} \ (s_\beta \text{ to } f_\alpha \text{ transfer rate}) \qquad (5.10.5)$$

$k_{36} = k_{36} = k_{46}$ (f_β to f_α transfer rate)

$k_1 = k_1 = k_2$ (s_β fluorescence rate in absence of energy transfer)

$k_3 = k_3 = k_4$ (f_β fluorescence rate in absence of energy transfer

k_5 (s_α fluorescence rate in absence of energy transfer

k_6 (f_α fluorescence rate in absence of energy transfer

k_{56} (s_α to f_α transfer rate)

k_{51} (s_α to s_β transfer rate)

k_{53} (s_α to f_β transfer rate)

These simplifications are necessary to enable solving the equations with a minimum of parameters. The energy scheme is described by the following differential equations, which after inserting the above simplifications, reduce to the equations on the right.

$$\dot{p}_1 = -k_1p_1-k_{13}p_1-k_{14}p_1-k_{16}p_1+\sigma\ I_1 = -(k_1+2k_{13}+k_{16})p_1+k_{51}p_5+\sigma_1 I$$

$$\dot{p}_2 = -k_2p_2-k_{23}p_2-k_{24}p_2-k_{26}p_2+k_{51}p_5+\sigma_2 I = -(k_2+2k_{13}+k_{16})p_2+k_{51}p_5+\sigma_2 I$$

$$\dot{p}_3 = -k_3p_3-k_{36}p_3+k_{13}p_1+k_{23}p_2+k_{53}p_5+\sigma_3 I = -k_3p_3-k_{36}p_3+k_{13}(p_1+p_2) + k_{53}p_5+\sigma_3 I \qquad (5.10.6)$$

$$\dot{p}_4 = -k_4p_4-k_{46}p_4+k_{14}p_1+k_{24}p_2+k_{53}p_5+\sigma_4 I = k_3p_4-k_{36}p_4+k_{13}(p_1+p_2)+k_{53}p_5+\sigma_4 I$$

$$\dot{p}_5 = -(k_5+ k_{56}+2k_{51}+2k_{53})p_5+\sigma_5 I$$

$$\dot{p}_6 = -k_6p_6+k_{16}p_1+k_{26}p_2+k_{36}p_3+k_{46}p_4+k_{56}p_5+\sigma_6 I = -k_6p_6 +k_{16}(p_1+ p_2)+k_{36}(p_3+p_4)+k_{56}p_5+\sigma_6 I$$

The σ_i obtained from the absorption spectra, are

$$\sigma_1 = \sigma_2 = 0.18$$

$$\sigma_3 = \sigma_4 = 0.15$$

$$\sigma_5 = 0.19 \qquad (5.10.7)$$

$$\sigma_6 = 0.14$$

The ($\alpha\beta$) fluorescence kinetics is given by:

$$F^{\alpha\beta}(t) = k^{\beta}_{sr}(p_1(t) + p_2(t)) + k^{\beta}_{fr}(p_3(t) + p_4(t)) + k^{\alpha}_{sr}p_5(t) + k^{\alpha}_{fr}p_6(t) \qquad (5.10.8)$$

The decay kinetics were fit for values of the ratios of the radiative rates k_{sr}: k_{fr}: k_{sr}: k_{fr} = 1: 1: 0.8: 1.2.

This ratio corresponds to those values obtained by integration under the absorption curves, as described in the section on radiative rates. The decay kinetics were fit with the constraint that the $s_\alpha \rightarrow f_\alpha$ and $s_\beta \rightarrow f_\beta$ transfer rates have the same values in the monomer as they do in the isolated subunits. Thus we set $k_{56} = 1\text{x}10^{10}$ sec^{-1}(100 ps) and $k_{23} = 1.5\text{x}10^{9}$ sec^{-1}(666 ps). We found it is not possible to describe the kinetics using the same parameters found in the individual subunits. In particular, the fluorescence decay of the f_β chromophore

changes considerably when it aggregates into the monomer. There is also a slight increase in the nonradiative rate of the f_α chromophore.

The ($\alpha\beta$) kinetics are best fit, under the constraints listed above, for equal $s_\alpha \rightarrow s_\beta$ and $s_\alpha \rightarrow f_\beta$ transfer rates of 3×10^9 sec^{-1} (333 ps). That is, $k_{51} = k_{53} = 3 \times 10^9$ sec^{-1}. The best fit requires $k_{16} = 1 \times 10^9$ sec^{-1}; k_{16} is the $s_\beta \rightarrow f_\alpha$ rate. It is not a sensitive parameter. Satisfactory fits can be found for $k_{16} = 0$ by adjusting the f_β and f_α decay rates. The $f_\beta \rightarrow f_\alpha$ transfer rate is a more sensitive parameter. We found k_{36} must be zero. Though this transfer is energetically allowed, one must surmise that its nonexistence may be due to a large distance between these sets of chromophores in the monomer. Possibly, they appear on opposite surfaces of the monomer.

The most sensitive parameter is the decay rate of the f_β chromophore. We found the best fit requires $k_3 = k_4 = 8 \times 10^9$ sec^{-1}(125 ps), a considerable increase in the nonradiative rate than that reported for the isolated β subunit. The significance of this parameter can be understood by realizing that the short component of the ($\alpha\beta$) kinetics is due to the β subunit, while the long component is due to the f_α fluorescence. The ($\alpha\beta$) kinetics drops considerably faster than the β kinetics, and hence the fit requires an increase in the nonradiative rate of the f_β chromophore. It is interesting to note that fluorescence on the order of hundreds of ps has been observed in other monomers, and was attributed to the possibility of chromophore-chromophore interaction.[8] Our results would tend to substantiate those claims that chromophore-chromophore interactions result in a $\sim$125 ps component of the fluorescence and to identify it as resulting from the f_β chromophore.

The increase in the nonradiative rate may imply increased energy loss mechanisms, such as energy transfer to the protein. When aggregated into higher forms, such as the fast trimer, the greater coupling may result in energy transfer from f_β to other chromophores. The best fit also requires $k_6 = 1.2 \times 10^9$ sec^{-1} (83 ps). This represents a 20% increase in the f_α decay rate. Though the decay time of the f_β chromophores changes considerably, due to an increase in its nonradiative rate, the decay times of the other chromophores are approximately the same in the monomer as they are in the isolated α and β subunits. The $s_\alpha \rightarrow f_\alpha$ and $s_\beta \rightarrow f_\beta$ decay rates were constrained to be the same in the monomer as in the isolated subunits. The existence of $s_\beta \rightarrow f_\alpha$ transfer is ambiguous (k_{16}), though $f_\beta \rightarrow f_\alpha$ (k_{36}) transfer seems to be forbidden.

5.9 Quantum Yield and Transmission Data

Figure 5.8 shows the relative quantum yield and transmission data as a function of pulse intensity for the β and (αβ) units. The transmission curves in both units depart from the low intensity value at approximately 1 to 2 x 10^{14} photons/cm^2, and are approximately the mirror images of the quantum yield data. The β and (αβ) quantum yield dependence on excitation intensity has a functional form similar to that predicted by exciton annihilation theories. The curves are well fit for r = 0.1 in the β unit and r = 0.5 in the (αβ) complex which is seemingly suggestive of the occurrence of exciton annihilation processes. The Paillotin theory does not include the nonlinear optical effects produced by ground state depletion or upper excited state

absorption and is applicable only when the transmission is unchanged over the intensity domain measured, in contrast to the results reported in Figure 5.8. Further evidence against exciton annihilation is the intensity independent kinetics decay. Though the decays are non-exponential as predicted by annihilation theories, they do not display the intensity dependence predicted by the theory. As a result, we believe annihilation processes are not occurring in these samples over the intensity range investigated, in contrast to the results reported in the higher aggregates of these pigments ($(\alpha\beta)_3$ and $(\alpha\beta)_6$) (to be published). The observation that the apparent fluorescence yield (ϕ_R) and the relative transmission (T_R) are approximately mirror reflections (about the unit axis) of each other is strongly suggestive of ground state depletion, although upper excited state absorption may also be involved.

The absence of annihilation in these samples is probably due to the small number of excitons created at these intensities. For annihilation to occur, at least two excitons must be created. At the highest intensities investigated, the average number of 1.5 excitons are created in the α and β subunits. On the average, approximately two excitons are created in the $(\alpha\beta)$ at the highest intensity. Though we do not notice annihilation effects in the $(\alpha\beta)$, it is possible we are viewing the onset of such processes at the highest intensity and our experiments are too insensitive to notice it. Experiments at higher incident fluence for the moment will show whether we are indeed at the onset of such effects.

5.10 Conclusions

The fluorescence decay kinetics and steady-state absorption and fluorescence curves of the α, β and (αβ) units have been used to describe the possible energy transfer pathways in these units. Unlike the higher aggregates of these forms, rising transmission curves as a function of intensity and, in particular, the intensity-independent kinetics strongly suggest the absence of exciton annihilation in these units. The absence of annihilation is probably due to the small number of excitons created in these units at the intensities investigated. The lack of annihilation permits one to infer the possible energy transfer pathways and decay rates. In the isolated α subunit, an $s_\alpha \rightarrow f_\alpha$ transfer rate of 100 ps is reported. In the isolated β subunit, the $s_\beta \rightarrow f_\beta$ rate is 666 ps. These slower rates in the subunits are expected to increase when aggregated into higher complexes where greater coupling amongst the chromophores is expected. The fluorescence decay rates in the absence of energy transfer is 70 ps for the 's_β' chromophores, 100 ps for the 's_α' chromophores and 1 ns for the 'f' chromophores of both subunits. These decay rates are mostly unchanged when aggregated into the monomer, except for the f_β rate which decays at 125 ps. The f_α decay rate increases by 20% in the monomer. The $s_\alpha \rightarrow f_\alpha$ and $s_\beta \rightarrow f_\beta$ transfer rates in the monomer are constrained to be the same as in the isolated subunits. The exact transfer rate parameters can only be determined after other parameters, such as the radiative rates of the chromophores and the number of 's' and 'f' chromophores are determined experimentally. The importance of determining these rates have now been shown to be a key element in

unraveling the underlying energy transfer mechanisms in the lower subunits of photosynthetic algae. We believe that our first attempts at modelling the energy pathways in algae is a step in the right direction towards understanding these processes and is a harbinger of man's future understanding, and hopefully, harnessing of one of nature's most impressive phenomena.

Table 5.1

Summary of Rate Constants in α, β and (αβ) Units

(in units of 10^9 sec^{-1})

	$(s_\beta \rightarrow f_\beta)$	$(s_\beta \rightarrow f_\alpha)$	$(f_\beta \rightarrow f_\alpha)$	$(s_\alpha \rightarrow f_\alpha)$	$(s_\alpha \rightarrow f_\beta)$	$(s_\alpha \rightarrow s_\beta)$	s_β	f_β	s_α	f_α
	k_{13}	k_{16}	k_{36}	k_{56}	k_{53}	k_{51}	$k_1=k_2$	$k_3=k_4$	k_5	k_6
α	-	-	-	10	-	-	-	-	10	1
β	1.5	-	-	-	-	-	15	1.2	-	-
αβ	1.5	*	0	10	3	3	15	8	10	1.2

*Undetermined.

Notes

1. Zilinskas, B. A. unpublished results.

2. Bryant, D. A., Guglielmi, G., Tandea de Marsac, N., Castets, A. M., & Cohen-Bazire, G. (1979). Arch. Microbiol. 123, 113.

3. Grabowski, J., & Gantt, E. (1978). Photochem. Photobiol., 28, 39.

4. Grabowski, J., & Gantt, E. (1978). Photochem. Photobiol., 28, 47.

5. Govindjee, & Govindjee, R. (1975). In Govindjee, Ed., Bioenergetics of Photosynthesis. New York: Academic Press.

6. Porter, G., Tredwell, C. J., Searle, G. F. W., and Barber, J. (1978). Biochim. Biophys. Acta, 501, 232.

7. Searle, G. F. W., Barber, J., Porter, G., & Tredwell, C. J. (1978). Biochim. et Biophysica Acta, 501, 246.

8. Holzwarth, A. R., Wendler, J., & Wehrmeyer, W. (1983). Biochim. Biophys. Acta, 724, 388.

9. Dale, R. E., & Teale, F. W. J. (1970). Photochem. Photobiol., 12, 99.

10. Teale, F. W. J., & Dale, R. E. (1970). Biochem. J., 116, 161.

11. Zickendraht-Wendelstadt, Friedrich, B. J., & Rudiger, W. (1980). Photochem. Photobiol., 31, 367.

12. Wong, D., Pellegrino, F., Alfano, R. R., & Zilinskas, B. A. (1981). Photochem. Photobiol., 33, 651.

13. Mauzerall, D. (1978). Photochem. Photobiol., 28, 991.

14. Pellegrino, F., Wong, D., Alfano, R. R., & Zilinskas, B. A. (1981). Photochem. Photobiol., 34, 691.

15. Kobayashi, T., Degenkolb, E. O., Bersohn, R., Rentzepis, P. M., MacColl, R., & Berns, D. S. (1979). Biochemistry, 18, 5073.

16. Doukas, A. G., Stefancic, V., Buchert, J., Alfano, R. R., & Zilinskas, B. A. (1981). Photochem. Photobiol., 34, 505.

17. Hefferle, P., Nies, M., Wehrmeyer, W., & Schneider, S. (1983). Photobiochem. Photobiophys. 5(6), 41.

18. Dagen, A. J., Alfano, R R., Zilinskas, B. A., & Swenberg, C. E. To be published.

19. Zilinskas, B. A., & Howell, D. A. (1983). Plant Physiol., 71, 379.

20. Troxler, R. R., Greenwald, L. S., & Zilinskas, B. A. (1980). J. Biol. Chem., 255, 9380.

21. Paillotin, G., Swenberg, C E., Breton, J., & Geacintov, N. E. (1979). Biophys. J., 25, 513.

Chapter 6

SMALL AND INFINITE DOMAIN THEORIES APPLIED TO α AND β SUBUNITS AND THE (αβ) MONOMER

6.1 Introduction

Over the past 30 years energy transfer dynamics of excited electronic states has been extensively studied and applied to a wide range of processes in biological and chemical systems.[1-8] Most of the theoretical and experimental studies have been concerned with systems composed of chromophores randomly distributed in either solutions or solids of infinite spatial extent. There are however, many important molecular systems where the distributions of chromophores are limited to a small finite volume, e.g., the chlorophyll light harvesting pigments of the photosynthetic unit of green plants, chromophores incorporated into small micellar units, as well as polymers which are constrained to volumes of microscopic dimensions. Recently Ediger and Fayer[9] have constructed a theoretical formalism for calculating observables when electronic energy is transported among molecules confined to small volumes. Their results demonstrate that time-dependent observables can be significantly altered in small systems relative to their behavior for infinite systems. In particular the fluorescence kinetics, in the absence of bimolecular annihilation, are fluence independent and nonexponential. Ideal biological systems to study the properties of electronic energy transfer in small domains are

the α, β and (αβ) units of phycoerythrin isolated from the photosynthetic antenna system of the blue-green alga Nostoc sp. The phycoerythrobilin pigment is one component of the phycobilisomes, the well defined organelles on the exterior surface of the thylakoid membranes of these organisms. In trimer form phycoerythrin of blue-green algae occupies a volume approximated by a right circular disk of radius 60 A^{o} and height 30 A^{o} (10). The basic monomer of the pigment consists of two dissimilar polypeptide chains to which chromophores are covalently bound; these chains, called the α and β subunits, contain 2 and 4 chromophores and have molecular weights of 16,600 and 19,500 daltons respectively[11,12]. In this chapter we report the first picosecond fluorescence kinetic measurements of the phycoerythrobolin chromophores in the α, β and (αβ) unit of phycoerythrin. The nonexponential fluorescence kinetic profiles were fitted to the Green function theory of Ediger and Fayer for energy transfer in small volumes, and to the appropriate theory for an infinite domain. The apparent drawbacks of each approach are clearly stated.

6.2 Theoretical Review I--Small Domain Theory of Energy Transfer

Use of the Ediger-Fayer theory permits one to explain fluence independent nonexponential decay curves by attributing the particular shape of the curves to the effects of energy transfer in a small domain. The theory includes bimolecular processes and its attendant fluence dependent decay curves.

When energy transfer occurs amongst fluorescing molecules randomly located in a lattice, the ensemble average of the fluorescence

overall configurations must be considered. Though for any particular configuration of molecules the total decay is a single exponential, the result of the averaging of the different configurations is a non-exponential decay. As will be shown later and was discussed in 3.5, the decay from an infinite lattice obeys a $t^{\Delta/6}$ law where Δ is the dimension of the lattice. For the infinite lattice, the decay law is determined solely by the dimension, the configuration surrounding each molecule is identical.

In a finite volume, however, the configuration around each molecule is different. As a result, the size of the domain as well as the dimension, determine the decay kinetics. Molecules near the edge of a finite volume have fewer numbers of neighboring chromophores than those near the center. Therefore, the transport time away from the originally excited molecule averaged over all starting positions and chromophore configurations is slower than in an infinite volume of the same chromophore density. This difference in the deexcitation pathways of the molecule results in distinct fluorescence profiles for the cases of infinite and finite volumes.

As detailed in section 3.2, the model assumed in the Ediger-Fayer theory is a spherical volume of randomly distributed and oriented molecules. The sphere has radium R, volume Ω and N donor molecules with no traps. The configuration of the system, K, is characterized by the location of the N molecules (r_1, r_2, ... r_n). The probability $P_j(K,t)$ that the j^{th} molecule is excited at time t in configuration K, is given by

$$\frac{dp'_j}{d\tau} = \frac{p'_j}{\tau} + \sum_{i=1} w_{ji}[p'_i(k,t) - p'_j(K,t)] \qquad (6.2.1)$$

τ is the measured excited state lifeline, the same for all chromophores

w_{ji} is the transfer rate between molecules j and i. $w_{ji} = \frac{1}{\tau}\left(\frac{R_o}{rj_i}\right)^6$ where R_o is the Forster radius and dipole-dipole interactions are assumed for w_{ji}. The first term of the equation is a loss term due to the fluorescence of the molecule in the absence of energy transfer. The second and third terms are source and loss terms, respectively, describing energy transfer to and from all the other molecules p_j. The size of the domain is taken into account when the basic solution to this equation is integrated over the various configurations.

The transformation $p_j = p'_j\, e^{-t/\tau}$ eliminates the lifetime decay terms allowing Equation 6.2.1 to be rewritten as

$$\frac{d\vec{p}}{d\tau} = \vec{W} \cdot \vec{p} \qquad (6.2.2)$$

where $W_{ji} = w_{ji} - \delta_{ij} \sum_{\ell} w_{i\ell}$

The solution to Equation 6.2.2 is

$$\vec{p}(t) = e^{t\vec{W}}\vec{p}(o) \qquad (6.2.3)$$

where p(t) is the column vector containing the solution as a function of time and p(o) is the column vector containing the initial conditions

of the system. The Green's function of the system is defined as follows.

If $P(N,\Omega,r,t)$ is the ensemble average density of excitations then

$$P(N,\Omega,r,t) = \int dr'\ G(N,\Omega,r,r',t)P(N,\Omega,r',o) \tag{6.2.4}$$

where

$$G(N,\Omega,r,r',t) = G^{s}(N,\Omega,r,r't) + G^{m}(N,\Omega,r,r',t) \tag{6.2.5}$$

$$G^{s}(N,\Omega,r,r',t) = \Omega\ll\delta\ (r_1-r)\delta(r_1-r')[\exp(tW)_{11}] \tag{6.2.6}$$

$$G^{m}(N,\Omega,r,r',t) = (N-1)\Omega < \delta(r_2-r)\delta(r_1-r')[\exp(tW)_{12}] > \tag{6.2.7}$$

The brackets indicate the ensemble average

$$< A(K) > = \frac{1}{\Omega^{n}} \int_{\Omega} dr_1 \ \ldots \int_{\Omega} dr_n\ A(K) \tag{6.2.8}$$

$G^{s}(N,\Omega,r,r',t)$ is the term that appears on the diagonal of the solution matrix. $G^{m}(N,\Omega,r,r',t)$ are the diagonal terms. One then defines $G^{s}(N,\Omega,t)$ by:

$$G^{s}(N,\Omega,t) = \frac{1}{\Omega} \int dr \int dr' G^{s}(N,\Omega,r,r',t) \tag{6.2.9}$$

$G^{s}(N,\Omega,t)$ is obtained by integrating over both spatial variables. Because this term appears on the diagonal of the solution matrix,

$G^s(N,\Omega,t)$ represents the probability that the excitation is on the originally excited molecule at time t. Similarly, integrating $G^m(N,\Omega,r,r',t)$ over the spatial coordinates gives the probability that the excitation is not on the originally excited molecule. The effect of the small domain comes into play when the integration of Equation 6.2.9 is done over the finite domain size. It is helpful to remember that up to that integration, the theory used a standard approach to obtain the solution of a system of basic rate equations. The uniqueness of the theory is encompassed in the integration of Equation 6.2.9 over a finite domain of configurations.

In actuality, expressions like Equation 6.2.9 are not integrated over the finite volume. It is easier to deal with the Laplace transform, $G^s(N,\Omega,r,r',s)$, integrate over the finite volume and use an algorithm to numerically calculate the inverse Laplace transform to obtain $G^s(N,\Omega,t)$. It can be shown that the exact solution for a large number of particles is:

$$\tilde{G}^s(N,\beta,s) = \frac{1}{s}/\{1 + \frac{C_D}{\sqrt{s\tau}}(1-\frac{1}{N})f_2(\beta) + \frac{C_D^2}{s\tau}[(1-\frac{1}{N})(1-\frac{1}{N})(f_2(\beta)))^2-(1-\frac{2}{N})f_3(\beta)]\}$$

where $C_D = N\,(\frac{R_o}{R})^3$. It has been shown that this expression for a small domain reduces to the expected results when the dimensions are assumed to be infinite.

The expressions for $f_2(\beta)$ and $f_3(\beta)$ appear in the appendix. These expressions were substituted into Equation 6.2.9 and $G^s(N,\beta,t)$ was obtained by numerically taking the inverse Laplacian of the expression. The algorithm to numerically calculate the inverse

Laplacian also appears in the appendix. β is defined by the expression

$$\beta = \left(\frac{R}{R_o}\right)^3 \frac{\sqrt{s\tau}}{2}$$

As explained in section 3.4, depolarization of the fluorescence occurs in the Ediger-Fayer theory because a fluorescent molecule, which absorbs light at time t, transfer its excitation to other fluorescent molecules whose emission dipoles are randomly oriented. The net result is of a rotation, in time, of the transition dipole of the fluorescing molecule. As explained in that section, the expressions for I_{11} and I_+ are

$$I_{11}(t) = e^{-t/\tau_f} [1 + 2k\, G_s(N,\Omega,t)] \qquad (6.2.11)$$

$$I_+(t) = e^{-t/\tau_f} [1 - k\, G_s(N,\Omega,t)]$$

where I_{11} is the component of the fluorescence polarized along the direction of the polarization of the excitation pulse, and I_+ is the component of the fluorescence polarized perpendicular to the direction of the polarization of the excitation pulse. As also derived in that section, the observed fluorescence in the absence of polarizers is given by:

$$I(t) = (I_{11}(t) + I_+(t)) \qquad (6.2.12)$$

In our experimental set up, the fluorescence kinetics were measured without polarizers. Equation 6.2.12 was, therefore, used to fit our experimental kinetics data.

6.3 Theoretical Review II--Energy Transfer in an Infinite Domain

As detailed in section 3.5, many decay kinetics from photosynthetic systems are fit to an $e^{-at\Delta/6}-kt$ decay law where $\Delta = 1,2,3$ corresponds to the dimension over which energy transfer occurs. Decays obeying this laws are expected from a system consisting of a single, fluorescing donor surrounded by acceptor molecules in an infinite domain. The donor decays by two independent processes transfer to acceptors and fluorescing. Though, as will be explained later, we consider this theory inappropriate for our samples, its frequent use or maybe, more accurately, its misuse in the literature prompted us to fit the kinetics of the α,β and $(\alpha\beta)$ samples to the theory.

The time evolution of the decay of the donor may be expressed as the product of the functions of its two independent decay channels: ϕ, the decay function due to transfer of energy to the acceptors and $e^{-t/\tau D}$ where t_D is the donor specific decay rate. Hence

$$F(t) = \phi(K_n,t)e^{-t/\tau_D} \qquad (6.3.1)$$

where K_n refers to a particular configuration of n acceptors occupying sites i_1, i_2 ... i_n $\phi(K_n,t)$ for a particular configuration is given by

$$\phi(K_n,t) = \prod_{j=K_n} E_j(t) \qquad (6.3.2)$$

where E_j describes the decay of the donor excitation due to energy transfer to the acceptor at site j. For multipolar interactions,

$$E_j(t) = \exp[-(t/\tau)(\frac{d}{R_j})^s] \qquad (6.3.3)$$

where s = 6 for dipole-dipole interactions and d is the nearest neighbor distance. By clever mathematical manipulations, one can obtain the expression for $\phi(p,t)$ where ϕ is the probability of any one of the N lattice sites being occupied by an acceptor as:

$$\ell n \quad (p,t) = \sum_{k=1}^{\infty} \frac{p^k}{k} S_k(t) \qquad (6.3.4)$$

where

$$S_k(t) = \sum_j [1 - e^{-(t/\tau)(\frac{d}{R_j})^s}]^k \qquad (6.3.5)$$

In the case of an <u>infinite</u> lattice, one can approximate the summation S_k by the appropriate integral for one, two or three dimensions.

$$\sum h(R_i) \rightarrow \begin{cases} 2p \int_0^{\infty} h(R)dR & 1 \text{ dim} \\ 2\pi p \int_0^{\infty} Rh(R)dR & 2 \text{ dim} \\ 4\pi p \int_0^{\infty} R^2 h(R)\, dR & 3 \text{ dim} \end{cases} \qquad (6.3.6)$$

where p is the density of lattice points in the lattice considered. In general, $p^{-1} = ud^{\Delta}$ where Δ is the dimension, d the nearest neighbor distance and u a number on the order of unity.

Evaluation of the integrals is clearly dependent on the dimensions of the lattice, and one obtains, to first approximation:

$$F(t) \sim \exp[-at^{\Delta/s} - t/\tau_D] \qquad (6.3.7)$$

where $a = d^{\Delta}V_{\Delta}p\ p(1 - \frac{\Delta}{s})p(t/\tau)^{\Delta/s}$. V_{Δ} is the volume of the surface in Δ dimension space. For Forster interactions, s = 6 and the decays obey a $t^{1/6}$, $t^{1/3}$ and $t^{1/2}$ decay law for one, two and three dimensions, respectively. As dimension increases, the decay lifetime decreases due to the increase in a and t (a $t^{1/2}$ decay is faster than a $t^{1/3}$ decay). This is consistent with the physical fact that as the dimension increases, the donor has more acceptors to which to transfer its energy. The increased number of avenues for the deactivation of the excited state population, results in more rapid decays.

In the case of the α, β and αβ units of Nostoc sp., the dimensions of the sample are on the order of R_o, the Forster radius. It is specifically for these dimensions that the effects of the finite size of the domain is most pronounced. Examination of theoretical curves generated by Ediger and our laboratory, indicates that a domain cannot be approximated as being infinite until its radius is at least ten times R_o ($\frac{R}{R_o} \geq 10$). Assuming R_o = 20-30 Å, one could not use the $t^{\Delta/s}$ time decays in a unit smaller than the hexamer. Another argument against the use of the $t^{\Delta/s}$ dependence is that the model consists of one fluorescing donor transferring energy to a sea of nonfluorescing acceptors. It is believed that more than one chromophore fluoresces in our samples. Even those who postulate that only the 'f' chromophore fluoresces, still contend that it is the other nonfluorescing 's' chromophores that transfer energy to the 'f' chromophore, counter to the assumptions of the $t^{\Delta/s}$ model. Despite the arguments mitigating against the use of this theory, we present in this chapter, the fits of the α, β and (αβ) units to the $t^{\Delta/6}$ decay laws.

6.4 Results and Discussion

Figures 6.1, 6.2 and 6.3 show the fits of the decay kinetics of the α, β, and αβ to the $\exp[-at^{1/3}-kt]$ decay laws. Fits to the $t^{1/2}$ and $t^{1/6}$ laws could not be found. The $t^{1/3}$ law corresponds to two dimensional transport over an infinite lattice. For the α subunit, the kinetics are best fit for the values of the parameters $a = 6.4 \times 10^{2}$ $sec^{-1/3}$ and $k = 3.77 \times 10^{8}$ sec^{-1}. The β subunit is best described by the parameters $a = 1.27 \times 10^{3}$ $sec^{-1/3}$ and $k = 4.4 \times 10^{8}$ sec^{-1}. The (αβ) monomer kinetics is best fit by $a = 1.43 \times 10^{3}$ $sec^{-1/3}$ and $k = 1.0 \times 10^{9}$ sec^{-1}. As pointed out previously, a is proportional to the probability of a lattice site being occupied by an acceptor. It is noted with interest, and with stress put on remembering the apparent inappropriateness of this theory, that a is larger for the two larger units than in the α subunit. Presumably, a unit with more chromophores provides more acceptors and hence increases the probability of a site being occupied by an acceptor. The data also implies equal fluorescence decay rates for the α and β subunits fluorescing chromophore and a much faster decay rate for the 'f' chromophore of the (αβ) monomer. The reader is reminded, however, that the theory is probably inappropriate. Yet those who support the theory might be interested in the physical significance of the data.

Figures 6.4, 6.5, 6.5 show the fits of the decay kinetics of the α, β and (αβ) units to the small domain theory. The curves were fit to the expression

$$F(t) = (1 + CG^{S}(N,\Omega,t))e^{-kt} \qquad (6.4.1)$$

where $G^{S}(N,\Omega,t)$ refers to the probability at time t that the initially excited molecule is still excited. N is the number of chromophores in the sphere of volume Ω $G'(N,\Omega,t)$ is a function of both N, and R_o where R_o is the Forster critical radius and R the radius of the sphere approximating the domain k is the fluorescing rate of the chromophores, all of which are assumed to fluoresce. C is the second parameter of the two parameter fit. For α, the parameters resulting in the best fit to the decay kinetics are C = 0.4, k = 1.0 x 10^9 sec^{-1}, $\frac{R}{R_o} = 0.5$. For the four chromophore system, β, the parameters of the best fit are C = 0.4, k = 1.72 x 10^9 sec^{-1}, $\frac{R}{R_o} = 0.5$. For the α and β subunits, R is approximately 25 Å and 22 Å, respectively. For the ($\alpha\beta$) monomer, the best fit parameters are C = 0.4, k = 2.87 x 10^9 sec^{-1}, and $\frac{R}{R_o} = 1.0$. Assuming the same critical Forster radius, R_o, for all the units, it is interesting that the theory is consistent with the physical fact that the monomer is about twice as large as the α and β subunits. This fact is reflected in the doubling of the R/R_o ratio in the monomer.

The chromophores of the three units have definite orientations relative to each other and therefore in a strict sense violate the assumptions employed in deriving Equation 6.4.1. Either the fits to Equation 6.4.1 are fortuitous or for small R/Ro and N, the equation has a much broader range of applicability than the randomization of chromophore distances implies. This could be rationalized by assuming that few configurations contribute for $R/R_o \leq 1$ with N small.

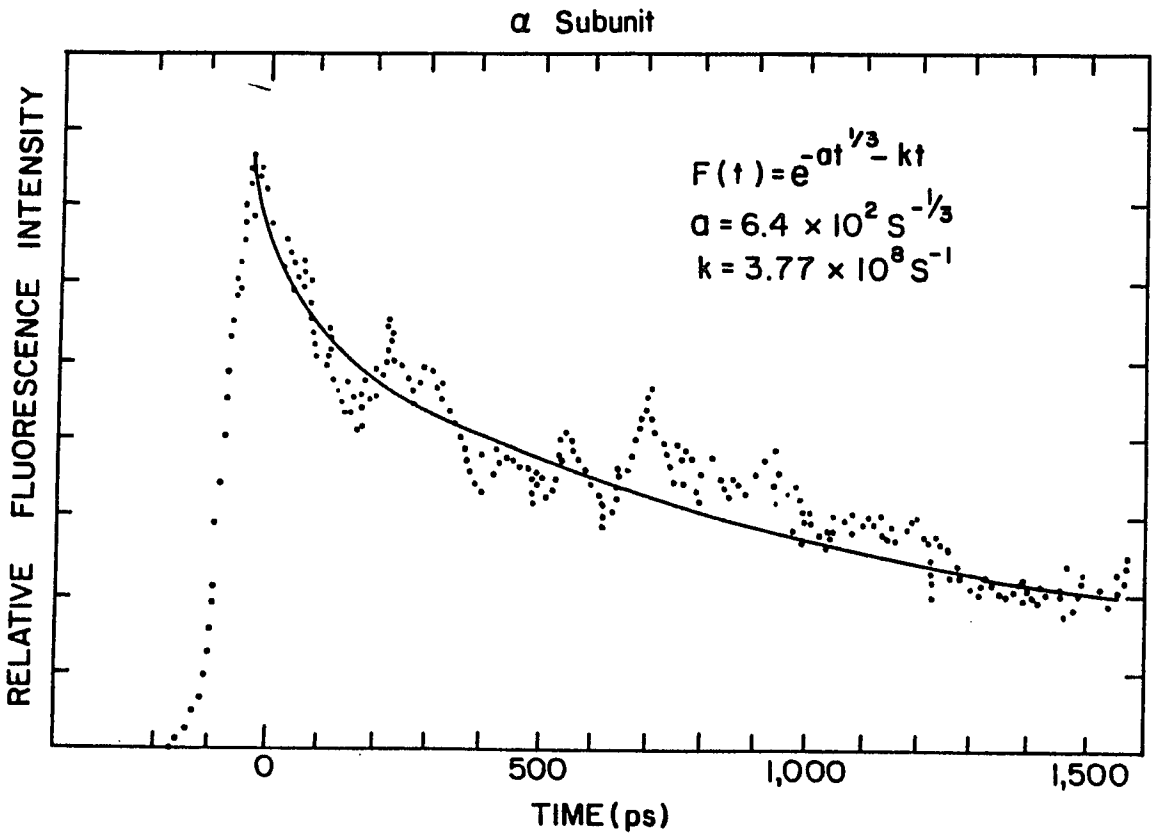

Figure 6.1: Fit of α subunit to $e^{-(at^{1/3}+kt)}$ for a = 6.4 x 10^2 $sec^{-1/3}$, k = 3.77 x 10^8 sec^{-1}.

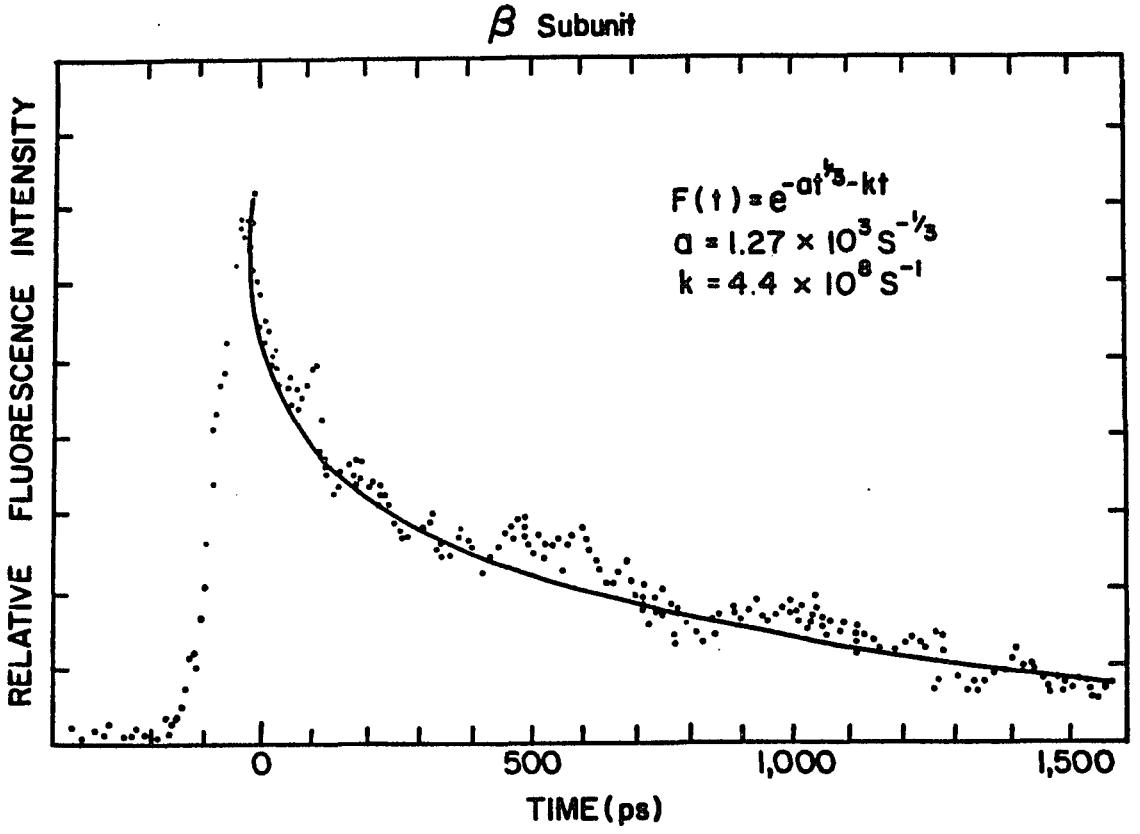

Figure 6.2: Fit of β subunit to $e^{-(at^{1/3}+kt)}$ for a = 1.27 x 10^3 $sec^{-1/3}$, k = 4.4 x 10^8 sec^{-1}.

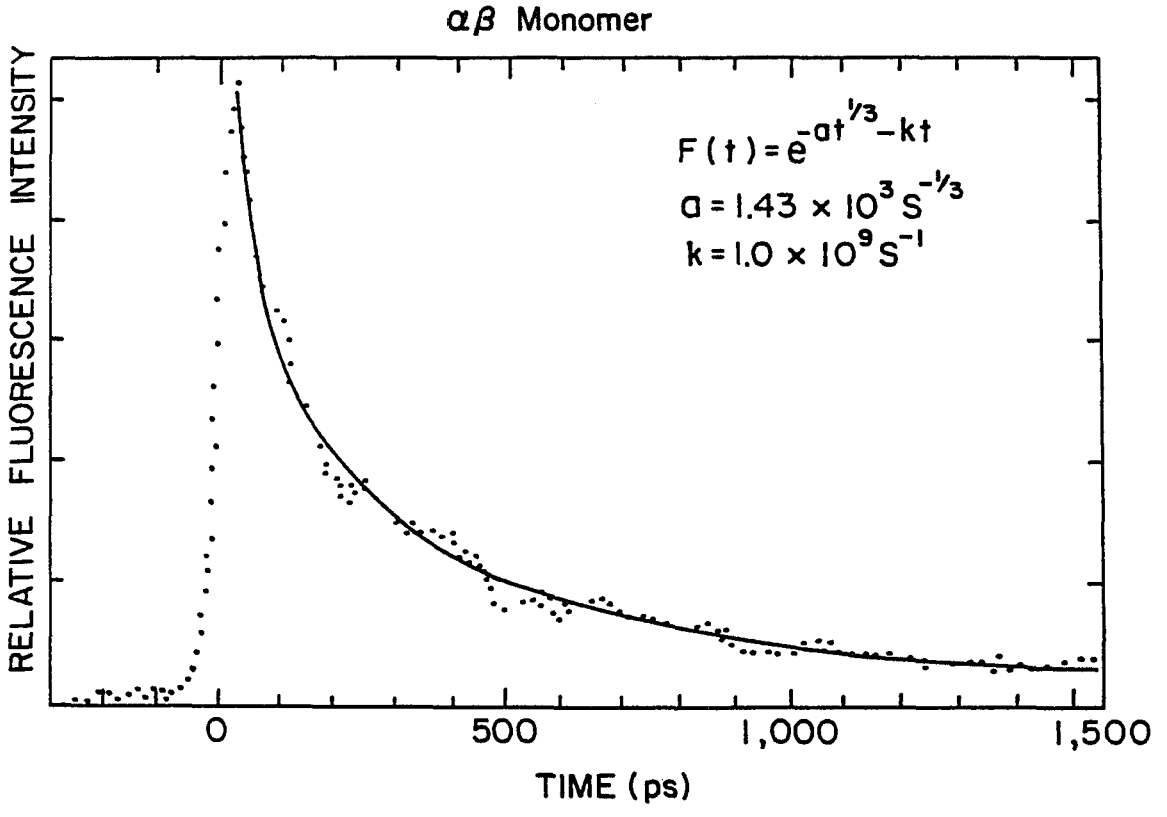

Figure 6.3: Fit of (αβ) monomer to $e^{-(at^{1/3}+kt)}$ for $a = 1.43 \times 10^{3}$ $sec^{-1/3}$, $k = 1 \times 10^{9}$ sec^{-1}.

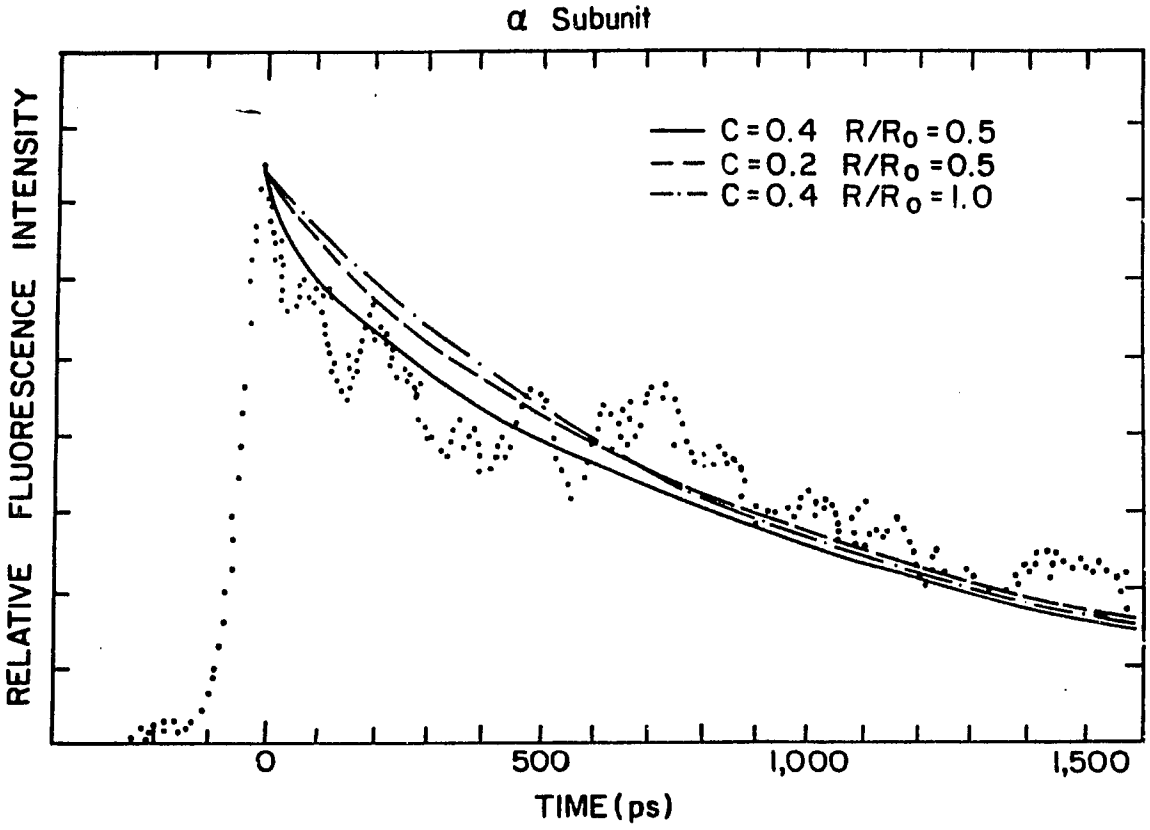

Figure 6.4: Fit of α subunit to $(1 + C\ G_s)e^{-kt}$ for $k = 1.0 \times 10^9\ sec^{-1}$, C and R/R_o according to legend.

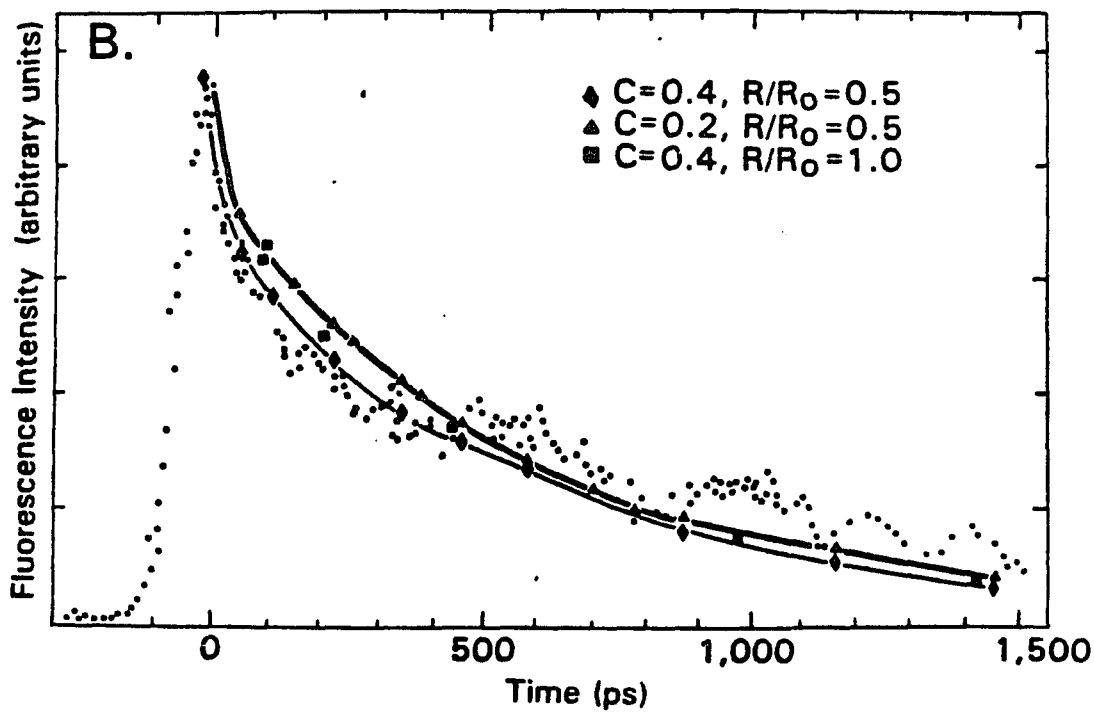

Figure 6.5: Fit of β subunit to $(1 + C\ G_s)e^{-kt}$ for $k = 1.72 \times 10^9\ sec^{-1}$, C and R/R_o according to legend.

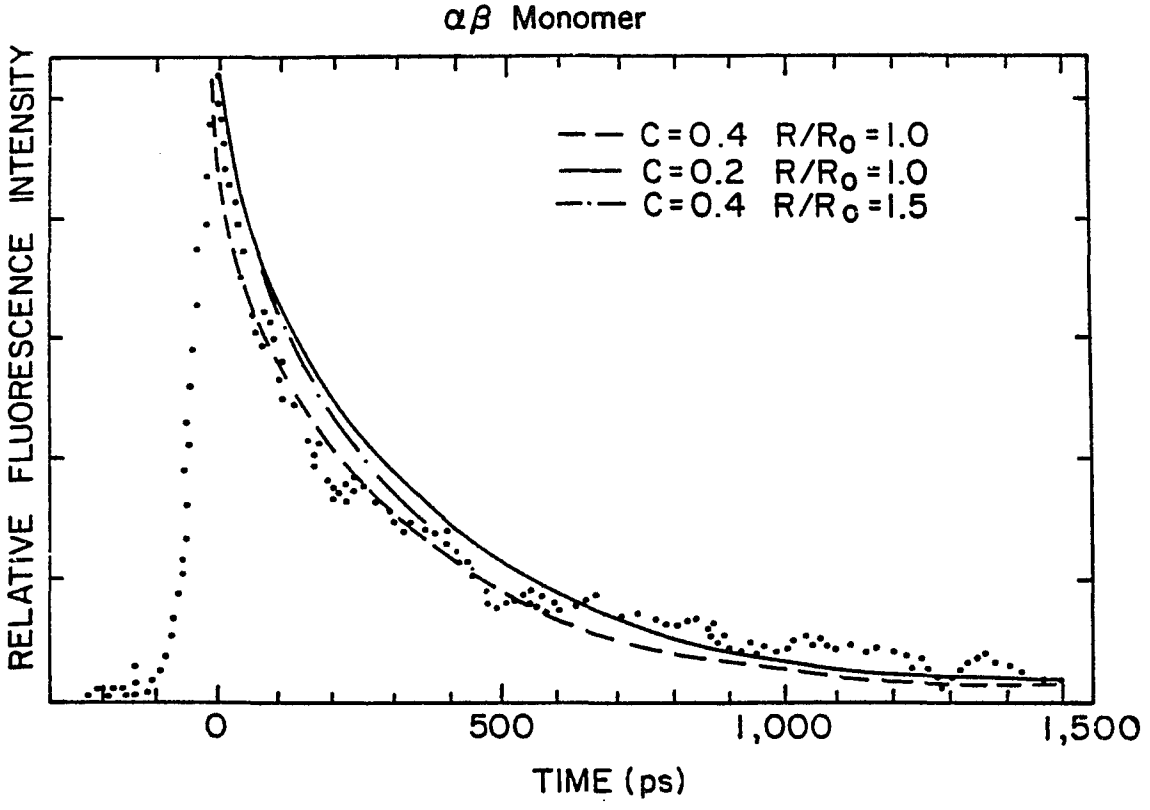

Figure 6.6: Fit of (αβ) monomer to $(1 + C\ G_s)e^{-kt}$ for $k = 2.87 \times 10^9\ sec^{-1}$, C and R/R_o according to legend.

6.5 Summary

This chapter presented fits of the α, β and (αβ) subunits kinetics to models, though apparently technically inappropriate, that have been described in the literature as pertaining to photosynthetic systems. The three units were fit to a model describing energy transfer in a finite domain and in an infinite domain. The relative smallness of the units with relation to the Forster radius invalidates the usage of the infinite domain theory. The small domain theory assumes random distributions of chromophores. Biologists strongly contend that chromophores cannot be randomly distributed. The lack of randomness has not been physically proved yet, however. Another possibility is that the small domain theory has a broader range of applicability than implied by the assumption of randomization. One may rationalize that few configurations contribute to $R/R_o \leq 1$ with the number of chromophores small.

Notes

1. Huber, D. L. (1979). Phys. Rev., 20, 2307; 20, 5333.

2. Blumen, A., & Manz, J. (1978). J. Chem. Phys., 68, 1879.

3. Forster, Th. (1949). Z. Naturforsch, 4a, 321.

4. Knox, R. S. (1975). In Govindjee, Ed., Bioenergetics of Photosynthesis, pp. 183-221. New York: Academic Press.

5. Hahn, S. W., & Zwanzig, R. (1978). J. Chem. Phys., 68, 1879.

6. Loring, R. F., Anderson, H. C., & Fayer, M. D. (1982). J. Chem. Phys., 76, 2015.

7. Lu, P. Y., Yu, Z. X., Alfano, R R., & Gersten, J. I. (1982). Phys. Rev., A26, 3610.

8. Porter, G., Tredwell, C. J., Seale, C. F. W., & Barber, J. (1978). Biochem. Biophys. Acta, 501, 232.

9. Ediger, M. D., & Fayer, M. D. (1983). J. Chem. Phys., 78, 2518.

10. Bryant, D. A., Guglielmi, G., deMarsac, N. T., Castets, A. M., & Cohen-Bazire, G. (1979). Arch. Microbiol., 123, 113.

11. Glazer, A. N. (1977). Mol. and Cellular Biochem., 18, 125.

12. Zickendraht-Wendelstadt, B., Friedrich, J., & Rudiger, W. (1980). Photochem. Photobiol., 31, 367.

Chapter 7

SUMMARY, CONCLUSIONS, FUTURE RESEARCH

7.1 Summary and Conclusions

This dissertation has examined the steady-state fluorescence and absorption spectra, relative quantum yield, transmission data and the picosecond time resolved fluorescence decays of the α, β and (αβ) units of phycoerythrin isolated from Nostoc sp. It has examined all of the theories used to explain picosecond phenomena from photosynthetic algae and has presented the first, complete computer analysis of energy transfer dynamics in these units. The s → f transfer rates, as well as the fluorescence decay rates of the various chromophores in the absence of energy transfer, were inferred by numerically solving the differential equations appropriate to the models used to describe the units.

As a result this dissertation has:

1. Shown the absence of annihilation processes in the α, β and (αβ) units over the intensity range investigated. We accomplished this by showing an increase in transmission through the sample, offsetting the drop in relative quantum yield. The intensity-independent fluorescence kinetics is another manifestation of the absence of these processes.

2. We have shown the experimental results expected when annihilation processes do occur. In addition, we generated the

theoretical curves that the fluorescence kinetics should fit, as a function of intensity in the presence of annihilation processes.

3. We have fit the fluorescence decay kinetics of all three units to differential equations describing s → f transfer. This represents the first computer simulation of energy transfer in a biological sample.

4. In the simpler α subunit, we have correlated the fluorescence kinetics parameters with the steady-state parameters. The reasonable agreement between the two measurements strengthens the justification of the applicability of our model.

5. We have provided a comprehensive account of all known applicable theories to the problem. We have shown their implications and limitations. The computer simulations represents our original contribution to theoretical approaches that are germane to the problem.

The apparent quantum yield and fluorescence decay profiles of the α subunit were measured over a wide intensity range (4×10^{13} to 4×10^{15} photons-cm^{-2} per pulse). The shapes of the fluorescence decay profiles were found to be intensity independent over the range investigated. Though the apparent quantum yield decreased as the intensity of the excitation pulse increased, the relative transmission increased as an approximate mirror reflection of the quantum yield. These observations suggest that the major contribution to the apparent decrease in quantum yield and the corresponding increase in transmission is ground state depletion, although upper excited state absorption can also not be ruled out. The observations do indicate the

absence of bimolecular singlet-singlet exciton annihilation processes in the α subunit.

The absence of annihilation processes in the α subunit permit describing the kinetics by a model in which both chromophores absorb and fluoresce and energy transfer occurs from one (the 's' chromophore) to the other (the 'f' chromophore). The appropriate differential equations describing this model were numerically solved. The relative absorption coefficients of the 's' and 'f' chromophore of the excitation wavelength (530 nm) were obtained by deconvoluting the absorption spectra of the α subunit into its 's' and 'f' components using mirror images. The deconvolution was verified by comparing experimental steady-state polarization data with the theoretical points attained using the derived spectra. The deconvoluted spectra were also used to obtain the radiative rates of each chromophore by integrating under each absorption spectra curve using the Einstein relations. These radiative rates were used to weight the contribution of each chromophore to the total fluorescence.

The inferred total deactivation rates for the 2 chromophores, in the absence of energy transfer and when the effects of the response time of the streak camera and the finite pulse width are properly included, are 1×10^{10} sec^{-1} (100 ps) and 1×10^{9} sec^{-1} (1 ns) for the 's' and 'f' chromophores, respectively. The s → f transfer rate was inferred to be 100 ps. The inferred kinetic parameters were used to obtain the Forster transfer radius, R_o. This value was found to be $R_o = 20\text{Å}$. As a result, the distance between the two chromophores in

the subunit is found to be 20 Å, consistent with the 25 Å radius of the α subunit.

Similar rate equations were solved in modelling the four chromophore β system and the six chromophore (αβ) monomer. In both units, all chromophores were assumed to absorb and fluoresce. The β subunit was assumed to consist of 2 's' and 2 'f' chromophores; the (αβ) monomer energy level scheme was shown to be similar to that obtained by aggregating the isolated α and β subunits into the monomer. This was shown by displaying the similarity between the addition of the absorption spectra of the α and β subunits and the (αβ) monomer.

Though the complexity of the β system (more than one 's' chromophore) forbids the use of mirror images, a deconvolution of the absorption spectra was obtained consistent with the experimental steady-state polarization data. These spectra were used to obtain the radiative rates of the four chromophores, as well as their relative absorption coefficients at the excitation wavelength. By solving the appropriate differential equations, the kinetic parameters of the β subunits were inferred. Our analysis showed that the rates of fluorescence decay in the absence of energy transfer is 1.5×10^{10} sec^{-1} (66 ps) for the 's' chromophores and 1.2×10^{9} sec^{-1} (833 ps) for the 'f' chromophores. The s→ f transfer rate was inferred to be 666 ps. As in the α subunit, mirror image quantum yield and transmission data--as well as intensity independent decay profiles--indicated the absence of annihilation processes. The absence of these bimolecular processes permitted the modeling of the subunit as each of 2 's' chromophores transferring energy to each of 2 'f' chromophores

with all 4 chromophores fluorescing and absorbing with the rates mentioned above. The rates indicate a low efficiency (10%) of transfer between the s and f chromophores in the β subunit.

In studying the (αβ) monomer, the individual chromophores were assumed to have the same energy levels as in the isolated α and β subunits. Energy transfer was permitted from chromophores of higher energy to those of lower energy. All chromophores were also assumed to have the same radiative rates and relative absorption coefficients as in the isolated subunits. The $s_\alpha \rightarrow f_\alpha$ and $s_\beta \rightarrow f_\beta$ transfer rates were constrained to be the same as those found in the isolated α and β subunits. We, therefore, set the $s_\alpha \rightarrow f_\alpha$ rate at 1×10^{10} sec^{-1} and the $s_\beta \rightarrow f_\beta$ rate at 1.5×10^9 sec^{-1}. Under these constraints, we found the best fit occurred for equal $s_\alpha \rightarrow s_\beta$ and $s_\alpha \rightarrow f_\beta$ transfer rates of 3×10^9 sec^{-1} (333 ps). The $s_\beta \rightarrow f_\alpha$ transfer rate was found to be 1×10^9 sec^{-1}, though this parameter is not sensitive. The existence of energy transfer from s_β to f_α chromophores could not, therefore, be uniquely determined. The $f_\beta \rightarrow f_\alpha$ decay rate was found to be more sensitive. Though energetically permitted, the decay profiles could be fit only when transfer from the f_β to f_α chromophores was forbidden. One may surmise that the distance between these two sets of chromophores may be too large to permit energy transfer.

We found a dramatic increase in the f_β decay rate. The best fit required the f_β chromophore decay at 8×10^9 sec^{-1}, representing a considerable increase in its nonradiative rate when compared to its rate in the isolated β subunit. This dramatic increase is reflected in a faster decay profile in the (αβ) monomer than in the β subunit. The

best fit also required a 20% increase in the f_α decay rate. The deduced rates of s → f transfer in the α, β and (αβ) complexes are slow compared to those reported in the trimer and hexamer. The trimer and hexamer are the forms in which PE is found as a functional unit in nature. Apparently, certain as yet unexplained changes occur in the formation of the trimer and hexamer which result in more efficient energy transfer. This may explain why these higher aggregates are the functional forms found in nature.

The decay profiles of the three samples were also fit to the Paillotin-Swenberg annihilation theory, and theories assuming energy transfer over an infinite lattice and over a finite domain. Though annihilation processes are not occurring over the intensity range investigated, the Paillotin-Swenberg fits provide good multiexponential fits to the data. In general, multiexponential fits are considered state of the art in this field. The α subunit is fit to the parameters $r = 0.05$, $z = 0.5$ for $k_o = 8.76 \times 10^8$ sec^{-1}. The fit is biexponential with $A_o = .79$, $A_1 = .19$ and $k_1 = 3.6 \times 10^9$ sec^{-1} k_o. The β subunit is fit to $r = 0.1$, $z = 1.0$, a biexponential with $A_o = .65$, $A_1 = .35$, $k_o = 1.0 \times 10^9$ sec^{-1} and $k_1 = 22\ k_o$. The αβ monomer is best fit for $r = 0.5$, $z = 5.0$. This is a multiexponential with $A_o = 0.27$, $A_1 = 0.36$, $A_2 = 0.23$, $A_3 = 0.10$ and $A_4 = 0.03$. The corresponding decay rates are $k_o = 1 \times 10^9$ sec^{-1}, $k_1 = 6\ k_o$, $k_2 = 15\ k_o$, $k_3 = 28\ k_o$ and $k_5 = 45\ k_o$. Though the Paillotin-Swenberg theory is inappropriate to our subunits, it is interesting that the values of r, related to the domain size of migration of excitons, increases as the size of the units increase.

The fluorescence kinetics of the three units were also fit to a $t^{1/3}$ decay law. This corresponds to the decay expected from a fluorescing acceptor in an infinite two dimensional sea of donors. The decay corresponding to energy transfer in one ($t^{1/6}$) and three ($t^{1/2}$) dimensions were found not to fit the data. The smallness of the units, however (on the order of the Forster radius, R_o), invalidates the use of an infinite domain theory. As a result, we also fit the data to a theory taking into account the finite size of the domain.

The small domain theory assumes a random distribution of chromophores in a finite size domain. We found fits to the kinetic data that appear consistent with the actual sizes of the units. The ratio of the radius R of the units to the Forster radius R_o were found to be 0.5 for the α and β subunits and 1.0 for the ($\alpha\beta$) monomer. These fits may be fortuitous or for small values of R/R_o and N, the theory has a broader range of applicability than the randomization of chromophore distances implies. This can be rationalized by assuming that few configurations contribute for $R/R_o < 1$ and N small. Also, though highly unlikely, the possibility of some slight randomization of chromophores has not been visibly disproved yet through x-ray crystallography.

7.2 Future Research

This dissertation has provided the first computer model of energy transfer within a photosynthetic system. There are many other areas that need similar thorough and complete computer and mathematical analyses. Amongst the areas needing further exploration:

1. The "size effects" of units on annihilation processes. At what stage of aggregation do bimolecular processes begin to play a role? Our preliminary data indicates that annihilation processes begin to be seen in the trimer. If annihilation processes do indeed occur in these units, one should determine whether, and to what extent, the Paillotin-Swenberg theory is appropriate.

2. How many 's' and how many 'f' chromophores really do exist? What are the actual energy pathways? What are the absorption and fluorescence spectra of each chromophore? What are their radiative rates? Physical means of isolating the radiative rates of the chromophores would be very useful in improving the accuracy of models as presented in this dissertation. This crucial task is non-trivial because the chromophores do not exhibit the same characteristics in the denatured state as they do in vivo.

3. Research is needed into the physical location of the chromophores. Is there some, albeit small, degree of randomness? Physical evidence is required to determine that models that seem to fit the data are indeed incorrect.

4. This dissertation focussed on the blue-green alga Nostoc sp. It might be of interest to obtain comparable data from red algae and other biological systems.

The mechanisms of energy transfer in photosynthetic systems--one of the most efficient forms of energy transfer in nature--still remains a major mystery. Much more research is required in order to understand and hopefully, eventually harness one of nature's most impressive phenomena.

APPENDIX

This program plots the decay kinetics for the Paillotin-Swenberg annihilation theory.

```
      DOUBLE PRECISION Z,APK1,ZDIF,SUM,DIF,APK,ZSUM,X,A(20)
      DOUBLE PRECISION RK,B0,T,P1,P2,B1,R,B2,B3,B4,B5,B6,B7,B8,B9
      DOUBLE PRECISION B10,B11,P3,P4,P5,P6,P7,P8,P9,P10,P11,P12,ZMULT
      DOUBLE PRECISION PAR,ZK,P,A0,AMULT,Y
      DIMENSION IBUF(500)
      DATA A IBUF/500*0/
      DATA A(20)/20*0.D0/
      SUM=1.D-37
 4    TYPE 1
 1    FORMAT(1X,'INSERT R AND Z IN D FIELD NOTATION')
      ACCEPT 2,R,Z
 2    FORMAT (2D23.9)
      K=0
      IP=0
      DO 100 I=1,12
      DO 517,LA=1,2500
      ZMULT=1.0
      M=K+1
      DO 107, L=1,M
      PAR=Z/(R+IP+L)
      ZMULT=(PAR*ZMULT)
107   CONTINUE
      ZK=FLOAT(K)
      CALL PCOMK(ZK,IP,AMULT,P)
      APK=((-1)**K)*AMULT
      APK1=(APK)*ZMULT*((R+2*IP+1)/Z)
      ZSUM=SUM
      SUM=APK1+SUM
      X=DABS(APK1)
      IF (X.LT.1.D-17) GO TO 70
      K=K+1
517   CONTINUE
 70   CONTINUE
      IF (I.EQ.1) GO TO 95
      A(I-1)=SUM
      GO TO 96
 95   A0=SUM
 96   IP=IP+1
      K=IP
100   SUM=1.D-37
      TYPE 190,A0
190   FORMAT(1X,'A0=',D23.9)
      DO 800 J=2,12
      TYPE 210,J=1,A(J-1)
210   FORMAT(1X,'J-1 IS',I4,2X,'A(J-1)=',D23.9)
```

```
800     CONTINUE
  5     TYPE 240
240     FORMAT('ENTER K')
        ACCEPT 17,RK
 17     FORMAT(D23.9)
        TYPE 53
 53     FORMAT(1X,'STANDBY WHILE I CALCULATE')
600     TYPE 400
400     FORMAT(1X,'INSERT CH. # FROM WHERE GRAPH SHOULD START')
        ACCEPT 401,IZ
401     FORMAT(I4)
        TYPE 402
402     FORMAT(1X,'MAX FOR K*T=?')
        ACCEPT 403,RK1
403     FORMAT(D10.4)
        DO 650,IH=1,500
650     IBUF(IH)=0
        IBUF(IZ)=230
        DO 10,ID=IZ+1,500
        Z4=(RK1/500.)
        T=(Z4)/RK+((ID-(IZ+1))*((Z4)))/RK
        P1=RK*T
        P2=2.*(1.+R)/R)*RK*T
        P3=3.*((2.+R)/R)*RK*T
        P4=4.*((3.+R)/R)*RK*T
        P5=5.*((4.+R)/R)*RK*T
        P6=6.*((5.+R)/R)*RK*T
        P7=7.*((6.+R)/R)*RK*T
        P8=8.*((7.+R)/R)*RK*T
        P9=9.*((8.+R)/R)*RK*T
        P10=10.*((9.+R)/R)*RK*T
        P11=11.*((10.+R)/R)*RK*T
        P12=12.*((11.+R)/R)*RK*T
        IF(P1 .GT. 85.) GO TO 11
        BO=AO/DEXP(P1)
        IF(P2 .GT. 85.) GO TO 21
        B1=A(i)/DEXP(P2)
        IF(P3 .GT. 85.) GO TO 31
        B2=A(2)/DEXP(P3)
        IF(P4 .GT. 85.) GO TO 41
        B3=A(3)/DEXP(P4)
        IF(P5 .GT. 85.) GO TO 51
        B4=A(4)/DEXP(P5)
        IF(P6 .GT. 85.) GO TO 61
        B5=A(5)/DEXP(P6)
        IF(P7 .GT. 85.) GO TO 71
        B6=A(6)/DEXP(P7)
        IF(P8 .GT. 85.) GO TO 81
        B7=A(7)/DEXP(PB)
        IF(P9 .GT. 85.) GO TO 91
        BB=A(8)/DEXP(P9)
```

```
      IF(P10 .GT. 85.) GO TO 101
      B9=A(9)/DEXP(P10)
      IF(P11 .GT. 85.) GO TO 111
      B10=A(10)/DEXP(P11)
      IF(P12 .GT. 85.) GO TO 121
      B11=A(11)/DEXP(P12)
      GO TO 52
 11   B0=0.
 21   B1=0.
 31   B2=0.
 41   B3=0.
 51   B4=0.
 61   B5=0.
 71   B6=0.
 81   B7=0.
 91   B8=0.
101   B9=0.
111   B10=0.
121   B11=0.
 52   IBUF(ID)=IFIX(230.*(B0-B1+B2-B3+B4-B5+B6-B7+B8-B9+B10-B11))
 10   CONTINUE
      TYPE 124
124   FORMAT(1X,'1 FOR DATA, 2 FOR GRAPH')
      ACCEPT 125,IN
125   FORMAT(I2)
      GO TO (130,150)IN
130   TYPE 131
131   FORMAT(1X,'INSERT CHANNELS BET WHICH WANT DATA LISTED')
      ACCEPT 132,IB,IF
132   FORMAT(2I4)
      DO 20,JA=IB,IF
      T=.004/RK+((JA-1)*(.004))/RK
      TYPE 200,JA,T,IBUF(JA)
200   FORMAT(1X,'I,T,IBUF',I8,D23.9.IB)
 20   CONTINUE
150   CALL PLOT55(2,1+512+2+4,)
      CALL PLOT55(1,0,)
      CALL PLOT55(3,-500,IBUF)
      TYPE 160
160   FORMAT(1X,'1 TO ENTER NEW PARAMETERS OR 2 FOR LISTING OF DATA')
      ACCEPT 161,IA
161   FORMAT(I3)
      GO TO(4,130)IA
      STOP
      END
      SUBROUTINE PCOMK(ZK,IP,AMULT,P)
      DOUBLE PRECISION ZK,AMULT,P,Y
      AMULT=1.DOO
      P=FLOAT(IP)
      IF(IP .EQ. 0) GO TO 120
      DO 900,IC=1,IP
```

```
      Y=ZK/P
      AMULT=Y*AMULT
      ZK=ZK-1
      P=P-1
900   CONTINUE
      GO TO 137
120   AMULT=1.DOO
137   CONTINUE
      RETURN
      END
```

This Algorithm computes the inverse Laplacian of the function P. The result is contained in FA. T is the time. (From H. Stehfest, Communications of the ACM (1970), 13, 47).

```
      INTEGER SN
      DIMENSION G(21),H(20),V(20)
      N=10
      G(1)=1.
      NH=N/2
      DO5 I=2,N+1
 5    G(I)=G(I-1)*(I-1)
      H(1)=2./G(NH)
      DO 10 I=2,NH
10    H(I) = (FLOAT (I)**NH)*G((2*I)+1)/(G(NH-I+1)*G(I+1)*G(I))
      SN = -1
      DO 15 I=1,N
      V(I) =0.
      K = INT(I+1)/2)
      J=NH
      IF(I .LT. NH)J=I
      DO 20 II=K,J
20    V(I)=V(I)+H(II)/(G(I-II+1)*G((2*II-1)+1))
      V(I)=SN*V(I)
15    SN=-SN
      B=ALOG(2.)
      FA=0.0
      A=B/T
      DO 25 I=1,N
      Y=FLOAT(I)*A
      S=P(Y,CD,BE,N,Z,T,TP)
25    FA=FA+V(I)*S
      FA=A*FA
      RETURN
      END
```

The functions listed below for $f_2(\beta)$ and $f_3(\beta)$ result in an error of less than 0.01 in the small domain theory function, $G_s(t)$ The ranges overlap significantly because the algorithm used for the inverse Laplace transform is extremely sensitive to discontinuities. The overlapping ranges allow each time point to be calculated from s values obtained from only one of the following equations:

$$f_2(\beta) = 0.70812\beta - 0.04373\beta^2 - 2.9191\beta^3 + 6.6524\beta^4 - 4.793\beta^5 \quad (10^{-4}<\beta<0.4)$$

$$f_2(\beta) = 0.083779 - 0.73208\beta^{1/3} + 2.0837\beta^{2/3} - 1.3943\beta + 0.31104\ ^{4/3} \quad (0.1<\beta<4)$$

$$f_2(\beta) = 1.1107\ [0.012335 + 0.98767\ (1 - 0.3344\beta^{-0.3444})^{2.907}] \quad (\beta>1)$$

$$f_3(\beta) = 2.752 \times 10^{-8}\beta + 0.33294\beta^2 + 0.043868\beta^3 - 4.3816\beta^4 + 15.685\beta^5 - 24.328\beta^6 + 14.449\ \beta^7 \quad (10^{-4}<\beta<0.4)$$

$$f_3(\beta) = 0.01303 = 0.10578\beta^{1/2} + 0.26187\beta - 0.079933\beta^{3/2} - 0.020128\beta^2 + 0.010583\beta^{5/2} \quad (0.1<\beta<3.2)$$

$$f_3(\beta) = 10^{-4}\ (-864.02 + 1754.2\beta^{1/2} - 49.632\beta - 47.12\beta^{3/2} + 5.6253\beta^2) \quad (0.8<\beta<22.4)$$

$$f_3(\beta) = 0.80555\ [0.012335 + 0.98767\ (1 - 0.602\beta^{-0.344})^{2.907}]\ \beta>5.6$$

The following programs come from the International Mathematics and Statistics Library (IMSL). The IMSL is headquartered in the NBC Building in Houston, Texas. Both programs were used in both single and double precision modes to insure the accuracy of the results. DGEAR uses a multi-step Adams method, while DVERK uses the Runge-Kutta technique. DGEAR keeps the error in going from an assumed perfect answer to the next step within the tolerance specified by TOL. DVERK keeps the calculated answer at each point to within tolerance (specified by TOL) of the actual answer at that point. The programs were run on a VAX 11/780 and rerun on an IBM 3033. The calls to plotting routines are those for a CALCOMP pen plotter. This program calculates the decay kinetics for the α subunit (Runge-Kutta).

```
      INTEGER N,IND,NW,IER,K
      DOUBLE PRECISION Y(2),C(24),W(2,9),XEND,H,K1,SI1,SI2,K12,K2
      DOUBLE PRECISION ANS,KRF,KRS,TOL,X
      DOUBLE PRECISION XX(2002),YY(2002),YMAX,XARRAY(2002),KA1
      COMMON K1,K2,K12,SI1,SI2
      EXTERNAL FCN1
      NW=2
      N=2
      X=-100.DO
      Y(1)=0.DO
      V(2)=0.DO
      TOL=0.001DO
      IND=1
      WRITE (6,3)
  3   FORMAT (IX, 'INPUT KS,KF,KSF')
      READ(1,*)KA1,K2,K12
      K1=KA1+K12
      KRS=.67
      KRF=1.
      WRITE(6,600)
600   FORMAT(IX,'ENTER C1,C2')
      READ(1,*)C12,C13
```

```
      DO 10 K=1,2000.1
      XEND=DFLOAT(K-100)
      CALL DVERK(N,FCN1,X,Y,XEND,TOL,IND,C,NW,W,IER)
      IF (IER.GT.0 .OR. IND.LT.0)GO TO 20
      ANS=C12*Y(1)+C13*Y(2)
      YY(K)=ANS*.71
 10   CONTINUE
      DO 9 KK=51,300,1
      WRITE(6.7)KK-100,YY(KK)
  7   FORMAT(15,F12.8)
  9   CONTINUE
      DO 19 I=1,2000
      XARRAY(I)=FLOAT(I)
 19   CONTINUE

      DO 18,KK1=300,2000,100
      WRITE(6,111)KK1-100,YY(KK1)
111   FORMAT(I5,F12.8)
 18   CONTINUE
      WRITE(6,400)K1,K2,K12
400   FORMAT(1X,'K1=',F8.5,'K2=.F9.5,'KSF=',F9.5)
 20   CONTINUE
      WRITE(6,*)IER,IND
      CALL PLBEG7
      CALL PLOT (0.5,0.5,-3)
      CALL SCALE(XARRAY,8.85,2000,1)
      CALL SCALE(YY,5.0,2000,1)
      CALL AXIS7(.0,.0,'TIME',-4,17.5,0.,XARRAY(2001),XARRAY(2002))
      CALL AXIS7(0.0,0.0,'F',-1,5.0,90.,YY(2001),YY(2002))
      CALL FLINE(XARRAY,YY,200,1,0.0)
      CALL TINPUT(IDUM)
      CALL PLEND7(15.)
      STOP
      END

      SUBROUTINE FCN1(N,X,Y,YPRIME)
      INTEGER N
      COMMON K1,K2,K12,SI1,SI2
      REAL Y(N),YPRIME(N),X,K1,K2,K12,SI1,SI2
      IF (X .LT. (-100.D0)) S=0.D0
      IF (X .GE. (-100.D0).AND.X.LE.100.D0)S=DEXP((-(X**2))/(625.D0))
      IF (X. GE.(100.D0)) S=0.D0
      YPRIME(1)=(-(K1))*Y(1)+.SI5*S
      YPRIME(2)=.SI6*S+K12*Y(1)-((K2)*Y(2))
      RETURN
      END
```

This program calculates the decay kinetics for the monomer (Runge-Kutta).

```
      INTEGER N,IND,NW,IER,K
      REAL Y(6),C(24),W(6,9),X,TOL,K1,SI1,SI2,XEND
      REAL K12,K2,K3,K4,SI3,SI4,ANS,XARRAY(2002)
      REAL K5,K6,K16,K36,K56,SI5,SI6,KRSA,KRFA,KRSB,KRFB,K51,K52
      REAL XX(2400),YY(2002),YMAX,K1A,K2A,K3A,K4A,K5A,K6A
      COMMON K1,K2,K12,SI1,SI2,K3,K4,SI3,SI4,K5,K6,K16,K36,K56,SI5,SI6
      COMMON K51,K52
      EXTERNAL FCN1
      NW=6
      READ (1,*)SI1,SI2
      READ (1,*)SI3,SI4
      READ (1,*)SI5,SI6
      N=6
      X=-100.
      Y(1)=0.
      Y(2)=0.
      Y(3)=0.
      Y(4)=0.
      Y(5)=0.
      Y(6)=0.
      TOL=0.0001
      IND=1
      WRITE(6,3)
    3 FORMAT(IX,'INPUT K1A,K3A')
      READ(1,*)K1A, K3A
      DO 1000 IA=1,2000
      XARRAY(IA)=FLOAT(IA)
 1000 CONTINUE
      K56=.01
      K12=.0015
      WRITE(6,4)
    4 FORMAT(1X,'INPUT K5A,K6,K16,K36,K51,K52')
      READ(1,*)K5A,K6,K16,K36,K51,K52
      K1=K1A+K12+K12+K16
      K2=K1
      K3=K3A+K36
      K4=K3
      K5=K5A+K56+K51+K51+K52+K52
      KRSB=1.
      KRFB=1.
      KRSA=.8
      KRFA=1.2
```

```
  5  FORMAT(5(F12.8))
  8  FORMAT(7(F12.8))
     DO 10 K=1,2000.1
     XEND=FLOAT(K-100)
     CALL DVERK(N,FCN1,X,Y,XEND,TOL,IND,C,NW,W,IER)
     IF(IER.GT.0.OR.IND.LT.0)GO TO 20
     Z1=Y(1)+Y(2)
     ANS=(KRSB*Z1)+(KRFB*(Y(3)+Y(4)))+(KRSA*Y(5))+(KRFA*Y(6))
     YY(K)=ANS
 10  CONTINUE
     WRITE(6,100)K1,K2,K12
100  FORMAT(1X,'K1',F8.5,'K2=',F8.5,'K12=',F8.5)
     WRITE (6,101)K3,K4
101  FORMAT (1X,'K3=',F8.5,1X,'K4=',F8.5)
     WRITE(6.102)K5,K6,K56
102  FORMAT (IX,'K5=',F8.5, 'K6=',F8.5,'K56=',F8.5)
     WRITE(6,103)K16,K36,K51,K52
103  FORMAT(IX,'K16=',F8.5,1X,'K36=',F8.5,'K51=',F8.5,'K52=',F8.5)
     WRITE(6,105)K1A,K3A,K5A
105  FORMAT(1X,'K1A=',F8.5,'K3A=',F8.5,'K5A=',F8.5)
     DO 9 KK=51,162,1
     WRITE(6.7)KK-100,YY(KK)
  7  FORMAT(I5,F12.8)
  9  CONTINUE

     DO19 KK=I,2000,100
     WRITE (6,17)KK-100,YY(KK)
 17  FORMAT(15,F12.8)
 19  CONTINUE
     CALL TINPUT(IDUM)
     CALL PLBEG7
     CALL PLOT(0,0.5,-3)
     CALL SCALE(XARRAY,11.,2000,1)
     CALL SCALE(YY,8.5,2000,1)
     CALL AXIS7(0.,0.,'TIME',-4,11.,0.,XARRAY(2001),XARRAY(2002))
     CALL AXIS7(0.,0.,'F',-1,8.5,90.,YY(2001),YY(2002))
     CALL FLINE(XARRAY,YY,2000,1,0,0)
     CALL TINPUT (IDUM)
     CALL PLEND7(15.)
     WRITE(6.*)IND,IER
     STOP
  20 CONTINUE
     WRITE(6,*)IND,IER
     STOP
     END

     SUBROUTINE FCN1(N,X,Y,YPRIME)
     INTEGER N
     COMMON K1,K2,K12,SI1,SI2,K3,K4,SI3,SI4,K5,K6,K16,K36,K56,SI5,SI6
     COMMON K51,K52
     REAL SI5,SI6,K51,K56,K36,K16,K6,K5,SI4,SI3,K4,K3,SI2,SI1,K12
```

```
      REAL K2,K1,X,YPRIME(N),Y(N),K52
      IF(X.LE.(-100.0)S=0
      IF(X.GE.(-100.0).AND.X.LE.100.)S=EXP((-X**2)/(625.))
      IF(X.GE.100.0)S=0
      YPRIME(1)=(-(K1))*Y(1)+SI1*S+(K51*(Y(5)))
      YPRIME(2)=(-(K2))*Y(2)+SI2*S+(K51*Y(5))
      YPRIME(3)=(-(K3))*Y(3)+SI3*S+(K12*(Y(1)+Y(2)))+(K52*(Y(5)))
      YPRIME(4)=(-(K4))*Y(4)+SI4*S+(K12*(Y(1)+Y(2)))+(K52*(Y(5)))
      YPRIME(5)=(-(K5))*Y(5)+SI5*S
      YPRIME(6)=(-(K6))*Y(6)+SI6*S+(K16*(Y(1)+Y(2)))+(K36*(Y(3)+Y(4)))
     1 +K56*Y(5)
      RETURN
      END
```

This program calculates the decay kinetics for the α subunit (Adams method).

```
      INTEGER N,METH,MITER,INDEX,IWK(2),IER,K
      REAL Y(2),WK(35),X,TOL,XEND,H,K1,SI1,SI2,K12,K2,KRS,KRF,ANS
      REAL XX(2002),YY(2002),YMAX,XARRAY(2002),KA1
      COMMON K1,K2,K12,SI1,SI2
      EXTERNAL FCN, FCNJ
      M=2000
      N=2
      X=-100.
      Y(1)=0.
      Y(2)=0.
      TOL=0.00001
      H=0.00001
      METH=1
      MITER=0
      INDEX=1
      WRITE (6,3)
    3 FORMAT(1X,'INPUT KS,KF,KSF')
      READ(1,*)KA1,K2,K12
      K1=KA1+K12
      KRS=.67
      KRF=1.
      WRITE(6,600)
  600 FORMAT(1X,'ENTER C1,C2')
      READ(1,*)C12,C13

      DO 10 K=1,2000,1
      XEND=FLOAT(K-100)
      CALL DGEAR(N,FCN,FCNJ,X,H,Y,XEND,TOL,METH,MITER,INDEX,IWK,WK,IER)
      IF( IER.GT.128)GO TO 20
      ANS=C12*Y(1)+C13*Y(2)
      YY(K)=ANS*.71
   10 CONTINUE
      DO 9 KK=51,300.1
      WRITE(6,7)KK-100,YY(KK)
    7 FORMAT(I5,F12.8)
    9 CONTINUE
      DO 19 I=1,2000
      XARRAY(I)=FLOAT(I)
   19 CONTINUE

      DO 18,KK1=300,2000,100
      WRITE(6,111)KK1-100,YY(KK1)
  111 FORMAT(I5,F12.8)
```

```
 18  CONTINUE
     WRITE(6,400)K1,K2,K12
400  FORMAT(1X,'K1=',F8.5,'K2=',F9.5,'KSF=',F9.5)
 20  CONTINUE
     CALL PLBEG7
     CALL PLOT (0.5,0.5,-3)
     CALL SCALE(XARRAY,8.85,2000,1)
     CALL SCALE(YY,5.0,2000,1)
     CALL AXIS7(.0,.0,'TIME',-4,17.5.0.,XARRAY(2001),XARRAY(2002))
     CALL AXIS7(0.0,0.5,'F',-1,5.0,90.,YY(2001),YY(2002))
     CALL FLINE(XARRAY),YY,2000,1,0,0)
     CALL TINPUT(IDUM)
     CALL PLEND7(15.)
     STOP
     END

     SUBROUTINE FCN(N,X,Y,YPRIME)
     INTEGER N
     COMMON K1,K2,K12,SI1,SI2
     REAL Y(N),YPRIME(N),X,K1,K2,K12,SI1,SI2
     IF (X .LT. (-100.)) S=0.0
     IF (X.GE.(-100.).AND.X.LE.(100.0))S=EXP((-X**2)/(625.0))
     IF (X.GE.100.)S=0.0
     YPRIME(1)=(-(K1))*Y(1)+.SI5*S
     YPRIME(2)=.SI6*S+K12*Y(1)-((K2)*Y(2))
     SUBROUTINE FCNJ(N,X,Y,PD)
     INTEGER N
     REAL Y(N),PD(N,N),X
     RETURN
     END
```

This program calculates decay kinetics of β subunit (Adams Method).

```
      INTEGER N,METH,MITER,INDEX,IWK(4),IER,K
      REAL Y(4),WK(76),X,TOL,XEND,H,K1,SI1,SI2
      REAL K12,K2,K3,K4,SI3,SI4,ANS,XARRAY(2002)
      REAL KRSB,KRFB
      REAL XX(2400),YY(2002),K1A,K2A,K3A,K4A
      COMMON K1,K2,K12,SI1,SI2,K3,K4,SI3,SI4

      EXTERNAL FCN,FCNJ
      M=2000
      N=4
      X=-100.
      Y(1)=0.
      Y(2)=0.
      Y(3)=0.
      Y(4)=0.
      TOL=0.0001
      H=0.0001
      METH=1
      MITER=0
      INDEX=1
      WRITE (6,3)
   3  FORMAT(1X,'INPUT K1A,K3A')
      READ(1,*)K1A, K3A
      DO 1000 IA=1,2000
      XARRAY(IA)=FLOAT(IA)
1000  CONTINUE
      K1=K1A+K12+K12
      K2=K1
      K3=K3A
      K4=K3
      KRSB=1.
      KRFB=1.
   5  FORMAT(5(F12.8))
   8  FORMAT(7(F12.8))
      DO 10 K=1,200.1
      XEND=FLOAT(K-100)
      CALL DGEAR(N,FCN,FCNJ,X,H,Y,XEND,TOL,METH,MITER,INDEX,IWK,WK,IER)
      IF(IER.GT.128)GO TO 20
      Z1=Y(1)+Y(2)
      ANS=(KRSB*Z1)+(KRFB*(Y(3)+Y(4)))
      YY(K)=ANS
```

```
 10  CONTINUE
     WRITE (6,100)K1,K2,K12
100  FORMAT(1X,'K1=',F8.5,'K2=',F8.5,'K12=',F8.5)
     WRITE (6,101)K3,K4
101  FORMAT(1X,'K3=',F8.5,1X,'K4=',F8.5)
 12  DO 9 KK=51,162,1
     WRITE(6,7)KK-100,YY(KK)
  7  FORMAT(I5,F12.8)
  9  CONTINUE

     DO19 KK=I,2000,100
     WRITE (6.17)KK-100,YY(KK)
 17  FORMAT(I5,F12.8)
 19  CONTINUE
     CALL TINPUT(IDUM)
     CALL PLBEG7
     CALL PLOT(0,0.5,-3)
     CALL SCALE(XARRAY,11.,2000,1)
     CALL SCALE(YY,8.5,2000,1)
     CALL AXIS7(0.,0.,'TIME",-4,11.,0.,XARRAY(2001),XARRAY(2002))
     CALL AXIS7(0.,0.,'F',-1,8.5,90.,YY(2001),YY(2002))
     CALL FLINE(XARRAY,YY,2000,1,0,0)
     CALL TINPUT(IDUM)
     CALL PLEND7(15.)
     STOP
 20  CONTINUE
     STOP
     END

     SUBROUTINE FCN(N,X,Y,YPRIME)
     INTEGER N
     COMMON K1,K2,K12,SI1,SI2,K3,K4,SI3,SI4
     REAL SI4,SI3,K4,K3,SI2,SI1,K12
     REAL K2,K1,X,YPRIME(N),Y(N)
     IF(X.LT.(-100.0))S=0.0
     IF(X.GE.(-100.0).AND.X.LE.(100.0).S=EXP((-X**2)/(625.0)
     (F(X.GE.100.0)S=0.0
     YPRIME(1)=(-K1))*Y(1)+SI1*S
     YPRIME(2)=(-K2))*Y(2)+SI2*S
     YPRIME(3)=(-(K3))*Y(3)+SI3*S+(K12*(Y(1)+Y(2)))
     YPRIME(4)=(-(K4))*Y(4)+SI4*S+(K12*(Y(1)+Y(2)))
     RETURN
     END

     SUBROUTINE FCNJ(N,X,Y,PD)
     INTEGER N
     REAL Y(N),PD(N,N),X
     RETURN
     END
```

This program computes decay kinetics for monomer (Adams Method).

```
      INTEGER N,METH,MITER,INDEX,IWK(6),IER,K
      REAL Y(6),WK(103),X,TOL,XEND,H,K1,SI1,S12
      REAL K12,K2,K3,K4,SI3,SI4,ANS,XARRAY(2002)
      REAL K5,K6,K16,K36,K56,SI5,SI6,KRSA,KRFA,KRSB,KRFB,K51,K52
      REAL XX(2400),YY(2002),YMAX,K1A,K2A,K3A,K4A,K5A,K6A
      COMMON K1,K2,K12,SI1,SI2,K3,K4,SI3,SI4,K5,K6,K16,K36,K56,SI5,SI6
      COMMON K51,K52
      EXTERNAL FCN,FCNJ
      M=2000
      N=6
      X=-100.
      READ(1,*)SI1,SI2
      READ(1,*)SI3,SI4
      READ(1,*)SI5,SI6
      Y(1)=0.
      Y(2)=0.
      Y(3)=0.
      Y(4)=0.
      Y(5)=0.
      Y(6)=0.
      TOL=0.0001
      H=0.0001
      METH=1
      MITER=0
      INDEX=1
      WRITE (6,3)
    3 FORMAT(1X,'INPUT K1A,K3A')
      READ(1,*)K1A, K3A
      DO 1000 IA=1,2000
      XARRAY(IA)=FLOAT(IA)
 1000 CONTINUE
      K56=.01
      K12=.0015
      WRITE(6,4)
    4 FORMAT(1X,'INPUT K5A,K6,K16,K36,K51,K52')
      READ(1,*)K5A,K6,K16,K36,K51,K52
      K1=K1A+K12+K12+K16
      K2=K1
      K3=K3A+36
      K4=K3
      K5=K5A+K56+K51+K51+K52+K52
      KRSB=1.
      KRFB=1.
      KRSA=.8
      KRFA=1.2
    5 FORMAT(5(F12.8))
```

```
  8  FORMAT(7(F12.8))
     DO 10 K=1,2000,1
     XEND=FLOAT(K-100)
     CALL DGEAR(N,FCN,FCNJ,X,H,Y,XEND,TOL,METH,MITER,INDEX,IWK,WK,IER)
     IF(IER.GT.128)GO TO 20
     Z1=Y(1)+Y(2)
     ANS=(KRSB*Z1)+(KRFB*(Y(3)+Y(4)))+(KRSA*Y(5))+(KRFA*Y(6))
     YY(K)=ANS
 10  CONTINUE
     WRITE (6,100)K1,K2,K12
100  FORMAT(1X,'K1=',F8.5,'K2=',F8.5,'K12=',F8.5)
     WRITE (6,101)K3,K4
101  FORMAT(1X,'K3=',F8.5,1X,'K4=',F8.5)
     WRITE (6,102)K5,K6,K56
102  FORMAT(1X,'K5=',F8.5,'K6=',F8.5,'K56=',F8.5)
     WRITE(6,103)K16,K36,K51,K52
103  FORMAT(1X,'K16=',F8.5,1X,'K36=',F8.5,'K51=',F8.5,'K52=',F8.5)
     WRITE(6,105)K1A,K3A,K5A
105  FORMAT(1X,'K1A=',F8.5,'K3A=',F8.5,'K5A=',F8.5)
     DO 9KK=51,162,1
     WRITE(6,7)KK-100,YY(KK)
  7  FORMAT(15,F12.8)
  9  CONTINUE
     DO19 KK=I,2000,100
     WRITE (6,17)KK-100,YY(KK)
 17  FORMAT(15,F12.8)
 19  CONTINUE
     CALL TINPUT(IDUM)
     CALL PLBEG7
     CALL PLOT(0,0.5,-3)
     CALL SCALE(XARRAY, 11.,2000,1)
     CALL SCALE(YY,8.5,2000,1)
     CALL AXIS7(0.,0.,'TIME',-4,11.,0.,XARRAY(2001),XARRAY(2002))
     CALL AXIS7(0.,0.,'F',-1,8.5,90.,YY(2001),YY(2002))
     CALL FLINE(XARRAY,YY,2000,1,0,0)
     CALL TINPUT(IDUM)
     CALL PLEND7(15.)
     STOP
 20  CONTINUE
     STOP
     END

     SUBROUTINE FCN(N,X,Y,YPRIME)
     INTEGER N
     COMMON K1,K2,K12,SI1,SI2,K3,K4,SI3,SI4,K5,K6,K16,K36,K56,SI5,SI6
     COMMON K51,K52
     REAL SI5,SI6,K51,K56,K36,K16,K6,K5,SI4,SI3,K4,K3,SI2,SI1,K12
     REAL K2,K1,X,YPRIME(N),Y(N),K52
     IF(X.LT.(-100.0))S=0.0
     IF(X.GE.(-100.0).AND.X.LE.(100.))S=EXP((-X**2)/(625.0))
     IF(X.GE.(100.0))S=0.0
```

```
      YPRIME(1)=(-(K1))*Y(1)+SI1*S+(K51*(Y(5)))
      YPRIME(2)=(-(K2))*Y(2)+SI2*S+(K51*Y(5))
      YPRIME(3)=(-(K3))*Y(3)+SI3*S+(K12*(Y(1)+Y(2)))+(K52*(Y(5)))
      YPRIME(4)=(-(K4))*Y(4)+SI4*S+(K12*(Y(1)+Y(2)))+(K52*(Y(5)))
      YPRIME(5)=(-(K5))*Y(5)+SI15*S
      YPRIME(6)=(-(K6)*Y(6)+SI6*S+(K16*(Y(1)+Y(2)))+(K36*(Y(3)+Y(4)))
     1   +K56*Y(5)
      RETURN
      END

      SUBROUTINE FCNJ(N,X,Y,PD)
      INTEGER N
      REAL Y(N),PD(N,N),X
      RETURN
      END
```

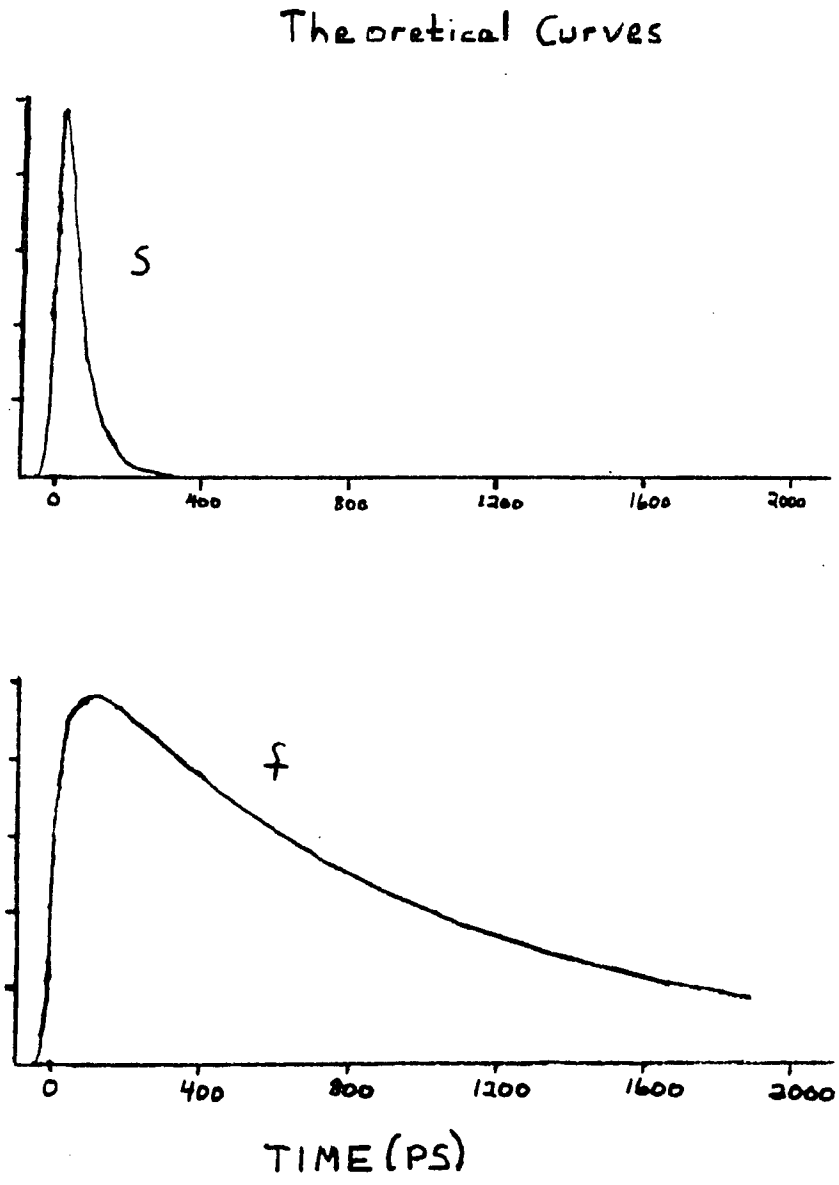

Figure A-1. Decay kinetics of s (upper curve) and f (lower curve) chromophores of α subunit.

REFERENCES

Barber, J. (1978). Rep. Prog. Phys. 41, 78.

Blumen, A., & Manz, J. (1978). J. Chem. Phys., 68, 1879.

Bradley, D. J., Higgins, J. F., & Key, M. H. (1971). Applied Physics Letters, 16, 53.

Bradley, D. J., Liddy, B., & Sleat, W. E. (1971). Optics Communications, 2, 391.

Breton, J., & Geacintov, N. E. (1980). Biochem. Biophys., 594, 1-32.

Brigand, D. A., Guglielmi, G., deMarsac, N. T., Castets, A. M., & Cohen-Bazire, G. (1979). Arch. Microbiol., 123, 113.

Bryant, D. A., Guglielmi, G., deMarsac, N. T., Castets, A. M., & Cohen-Bazire, G. (1979). Arch. Microbiol., 123, 113.

Campillo, A. J., Shapiro, S. L., Kollman, V. H., Winn, K. R., and Hyer, R. C. (1977). Biophys. J., 16, 93.

Clayton, Roderick K. (1980). Photosynthesis: Physical Mechanisms and Chemical Patterns. Cambridge: Cambride University Press.

Conwell, E. M. (1973). IEEE J. of Quan. Electron, QE-9, 867.

Dagen, A. J., Alfano, R. R., & Swenberg, C. E. (1984). IEEE Journal of Quantum Electronics, QE-20(12), 1496.

Dagen, A., Alfano, R. R., & Schiller, N. H. (1982). Picosecond Streak Cameras. International Encyclopedia of Optical/Electro-Optical Laser Technology.

Dale, R. E., & Teale, F. W. J. (1970). Photochem. Photobiol., 12, 99.

DeMaria, A. J., Glenn, Jr., W. H. Brienza, M. J., & Mack, M. E. (1969). Proceed. of IEEE, 57, 2.

Dorf, Richard C. (1981). Modern Control Systems. Reading, MA: Addison-Wesley Publishing Co.

Doukas, A. G., Stefancic, V., Buchert, J., Alfano, R. R., & Zilinskas, B. A. (1981). Photochem. Photobiol., 34, 505.

Ediger, M. D., & Fayer, M. D. (1983). J. Chem. Phys., 78(S), 2518.

Ediger, M. D., Domingue, R. P., & Fayer, M.D. (1984). J. Chem. Phys., 80(3), 1246.

Engelmann, T. W. (1881). Bot. Zeitung, 34, 441.

Engelmann, T. W. (1884). Bot. Zeitung, 42, 81.

Fleck, J. A. (1970). Phys. Rev. B1., 128, 84.

Fleming, G. R., Morris, J. M., & Robinson, G. W. (1976). Chemical Physics, 17, 91.

Forster, Th. W. (1965). In O. Sinanoglu, Ed., Modern Quantum Chemistry, pp. 93-137. New York: Academic Press.

Forster, The. (1949). Z. Naturforsch, 40, 321.

Gantt, E. (1981). Ann. Rev. Plant Physiol., 32, 327.

Gantt, E., Lipschultz, C. A., & Zilinskas, B. (1976). Biochemica et Biophysica Acta, 430, 375.

Glazer, A. N., Fang, S., & Brown, D. M. (1973). Journal of Biological Chemistry, 248, 5679.

Glazer, A. N. (1977). Mol. and Cellular Biochem., 18, 125.

Gochanour, C. R., Andersen, H. C., & Fayer, M. D. (1979). J. Chem. Phys., 70, 4254.

Govindjee, & Govindjee, R. (1975). In Govindjee, Ed., Bioenergetics of Photosynthesis. New York: Academic Press.

Grabowski, J., & Gantt, E. (1978). Photochem. Photobiol., 28, 39.

Grabowski, J., & Gantt, E. (1978). Photochem. Photobiol., 28, 47.

Green, B., & Alfano, R. R. (1977). Optics Communications, 20, 305.

Green, B., Liu, J. C., & Alfano, R. R. (1977). Optics Communications, 22, 119.

Grant, M., Schiller, N. H., & Alfano, R. R. (1977). Physics Teacher, 15, 369.

Hahn, S. W., & Zwanzig, R. (1978). J. Chem. Phys., 68, 1879.

Hefferle, P., Nies, M., Wehrmeyer, W., & Schneider, S. (1983). Photobiochem. Photobiophys., 5, 325.

Hogg, Robert V., & Craig, Allen T. (1978). Introduction to Mathematical Statistics, 4th ed. New York: Macmillan Publishing Co., Inc.

Holzwarth, A. R., Wendler, J., & Wehrmeyer, W. (1983). Biochimica et Biophysica Acta, 724, 388.

Huber, D. L. (1979). Phys. Rev., 20, 2307; 20, 5333.

Klauder, J. R., Duguay, M. A., Giordmaine, J. A., & Shapiro, S. L. (1968). Applied Physics Letters, 13, 174.

Kleinman, D. A. (1962). Physical Review, 128(4), 1761.

Knox, R. S. (1975). In Govindjee (Ed.), Bioenergetics of Photosynthesis, pp. 183-221. New York: Academic Press.

Kobayashi, T., Degenkolb, E. O., Bersohn, R., Rentzepis, P. M., MacColl, R., & Berns, D. S. (1979). Biochemistry, 18, 5073.

Lu, P. Y., Ho, P. P., & Alfano, R. R. (1979). IEEE J. of Quan. Electron, QE-15, 406.

Mauzerall, D. (1976). Biophys. J., 16, 87.

Mauzerall, D. (1976). J. Phys. Chem., 80, 2306.

Mauzerall, D. (1978). Photochem. Photobiol., 28, 991.

Morschel, E., Klaus-Peter Koller, & Wehrmeyer, Werner (1980). Arch. Microbiol., 125, 43.

Melissinos, Adrain C. (1966). Experiments in Modern Physics. New York: Academic Press.

Morschel, E., Koller, K.-P., Wehrmeyer, W., & Schneider, H. (1977). Cytobiologie, 16, 118.

Paillotin, G., Swenberg, C. E., Breton, J., & Geacintov, N. E. (1979). Biophys. J., 25, 513.

Pellegrino, F., Wong, D., Alfano, R. R., & Zilinskas, B. A. (1981). Photochem. Photobiol., 34, 691.

Porter, G., Tredwell, C. J., Seale, C. F. W., & Barber, J. (1978). Biochem. Biophys. Acta, 501, 232.

Porter, G., Tredwell, C. J., Searle, C. F. W., & Barber, J. (1978). Biophys. J., 25, 513.

Schiller, N. H., Dagen, A., & Alfano, R. R. (1982). Photonics, 16(1), 56.

Schiller, N. H., Tsuchiya, Y., Inuzuka, E., Suzuki, Y., Kamiya, K., Iida, H., & Alfano, R. R. (1980). Opt. Spec., 14, 55.

Searle, G. F. W., Barber, J., Porter, G., & Tredwell, C. J. (1978). Biochim. et Biophysica Acta, 501, 246.

Shapiro, S. L. (1968). Applied Physics Letters, 13, 19.

Smith, P. W., Duguay, M. A., & Ippen, E. P. (1975). Process in Quan. Electron, 3, 107.

Stehfest, H. (1970). Commun. Assoc. Comput. Mach., 13, 47.

Switalski, S. C., & Sauer, K. (1981). Photochem. Photobiol. 40, 423.

Swenberg, C. E., Geacintov, N. E., & Pope, M. (1976). Biophys. J., 16, 1447.

Swenberg, C. W., & Geacintov, N. E. (1973). In J. B. Birks, Ed. Organic Molecular Photophysics. Sussex, England: J. Wiley & Sons, Ltd.

Tanaka, F., & Mataga, N. (1980). Photochem. Photobiol., 29, 1091.

Tao, T. C. C. Doctoral dissertation.

Teale, F. W. J., & Dale, R. E. (1970). Biochem. J., 116, 161.

Troxler, R. R., Greenwald, L. S., & Zilinskas, B. A. (1980). J. Biol. Chem., 255, 9380.

Wendelstadt, B., Friedrich, J., & Rudiger, W. (1980). Photochem. Photobiol., 31, 367.

Wendler, J., Holzwarth, A. R., & Wehrmeyer, W. (1984). Biochimica et Biophysica Acta, 765, 58.

Wong, D. F., Pellegrino, F., Alfano, R. R., & Zilinskas, B. A. (1981). Photochem. Photobiol., 33, 651.

Yariv, A. (1975). Quantum Electronics, 2nd ed. New York: John Wiley.

Yariv, A. (1976). Optical Electronics, 2nd ed. New York: Holt, Rinehart and Winston.

YaShelev, M., Richardson, M. C., & Alcock, A. J. (1971). Applied Physics Letters, 18, 354.

Zickendraht-Wendelstadt, Friedrich, B. J., & Rudiger, W. (1980). Photochem. Photobiol., 31, 367.

Zilinskas, B. A., & Howell, D. A. (1983). Plant Physiol., 71, 379.